APART

A thesis by Jeroen Bominaar

Air Photolysis And Recombination Tracking

een wetenschappelijke proeve op het gebied
van de Natuurwetenschappen, Wiskunde en Informatica

Proefschrift

ter verkrijging van de graad van doctor
aan de Radboud Universiteit Nijmegen,
op gezag van de rector magnificus prof. mr. S.C.J.J. Kortmann
volgens besluit van het College van Decanen
in het openbaar te verdedigen op
dinsdag 9 september 2008
om 13.30 uur precies

door

Jeroen Bominaar

geboren op 20 juni 1979
te Roosendaal en Nispen

Voorwoord

Bijna zes jaar geleden, tijdens mijn externe stage bij Philips, was ik aan het zoeken naar een vervolg op mijn studie. Mijn afstudeeronderzoek bij de Foto-akoestiekgroep had ik al helemaal afgerond en ter oriëntatie was ik ook nog wat aan het snuffelen in het bedrijfsleven. Toch wilde ik graag nog wat meer van het wetenschappelijk onderzoek meekrijgen. Tot dan toe had ik al gemerkt dat onderzoek aan mensen compleet onvoorspelbaar is en daarom had ik behoefte aan wat hardere wetenschap. Bij het uitzoeken van mijn afstudeeronderzoek was ik ook eens op de Graalburcht bij Nico Dam geweest. Het toegepaste onderzoek wat daar werd gedaan leek me wel wat en zo werd ik gelukkig aangenomen op het Molecular Tagging Velocimetry project.

Het lab was al redelijk vertrouwd, omdat Iris hier ook al haar stage aan het doen was. Geleidelijk aan leerde ik al mijn collega's kennen. Van Thijs leerde ik de eerste kneepjes van het vak in het Diesellab, waar we recordvermogens uit de excimerlaser haalden, stikstoftenten bouwden en dubbelzinnige opmerkingen maakten. In the meantime, Coralie performed miracles in the windtunnel lab on the APART technique. When I saw what she could do, I immediately moved into her office and her lab. I learned a lot about science and French culture from her. Coralie, thanks for all your help and interest. I still enjoy visiting you and your family in Baisieux.

In het eerste jaar kwam ik erachter dat niet alleen het bestuderen van mensen onvoorspelbaar en onbetrouwbaar is. Lasers bleken minstens zo erg te zijn. Gelukkig leerde ik al snel dat er een lasertovenaar op het lab rondloopt. Nico heeft vele malen mijn lasers doorgelicht, gerepareerd en uitgelijnd. Nico, ik ben je dankbaar voor alle tijd die je hebt gestoken in mijn experimenten. Ook onze gesprekken over quantummechanica, jouw scheikundekindjes en paddenstoelen waren erg verfrissend. Je hebt me geleerd om niet alles te geloven wat er gezegd wordt. Helaas maakte je dat bij wetenschappelijke discussies erg moeilijk, omdat je meestal toch gelijk had.

Met een klein groepje collega's zaten we in ons eigen gebouwtje wat vele functies had, zoals spinnenhuis, bakoven, gevangenis, lawaaihok en gifgasfabriek. Toch hebben we het goed naar onze zin gehad en veel binnen en buiten het lab samen gedaan. Thijs, Kasper, Bas en de beide Arjans, bedankt voor de foute discussies, maandagochtendgrappen, filmpret en fysische ondersteuning. Verder zijn we ook nog regelmatig versterkt door studenten. Ook hen wil ik bedanken voor de leuke tijd.

Het enthousiasme van Willem van de Water was grenzeloos. Willem kwam ons regelmatig bezoeken en voerde dan discussies waar iedereen bij betrokken raakte, of je het nu wilde of niet. Toch heb ik daar veel van geleerd en spoorde dat me altijd aan tot net iets verder kijken. Na Coralie is Mira ons nog een tijdje komen versterken. Mira, I enjoyed all the fun stuff we did together, such as the colorful droplet sprays and the setup we built outside in the sun.

Natuurlijk kon vrijwel geen van die opstellingen gerealiseerd worden zonder de hulp van Arjan van Vliet. Arjan, ook al ben je bang van lasers, je hebt mij ook vaak de stuipen op het lijf gejaagd: boren boven een kwetsbare opstelling, alarmerende geluiden maken, of dreigen met het verschuiven van uitgelijnde spiegels of om op lasers te gaan staan. Bedankt voor al je constructies die je vaak nog op het laatste moment in elkaar moest draaien. De hulp van andere technici is ook onontbeerlijk geweest: Leander, Cor en

Peter, bedankt! Buiten de experimenten in het lab moesten er nog veel andere zaken geregeld worden. Ine staat daarvoor altijd voor ons klaar en daar ben ik haar dan ook heel dankbaar voor. Ook Erna en Magda hebben mij vaak geholpen. Hen en de rest van de afdeling wil ik dan ook bedanken voor deze tijd.

Aan het eind van deze periode van viereenhalf jaar waren er nog een aantal moeilijke puzzels, die opgelost moesten worden. Nico heeft me daar heel veel bij geholpen, maar ook Hans heeft een aantal heel nuttige tips gegeven. Hans, ik ben je niet alleen dankbaar voor de mogelijkheid om dit onderzoek te doen. Ook je continue interesse voor het onderzoek en je kritische blik hebben mij erg gestimuleerd. Mijn proefschrift is duidelijk beter geworden door jouw verbeteringen (ook al vond ik het verbeteren niet altijd even leuk).

Nu het schrijven van mijn proefschrift vrijwel is afgerond, werk ik al een jaar bij ASML in Veldhoven. Ondanks dat ik een leuke en interessante promotie heb gehad, is mijn voorkeur uiteindelijk toch uitgegaan naar het bedrijfsleven. Hierdoor ben ik samen met Iris naar Valkenswaard verhuisd: een Brabants dorp met Limburgse eigenschappen. Tot slot wil ik mijn familie en Iris bedanken dat ze altijd geïnteresseerd bleven voor mijn onderzoek en me altijd hebben gesteund in mijn keuzes.

Mijn boekje is nu af, maar voor u, de lezer, begint het lezen pas. Er is genoeg keus: voor diegene met het meeste geduld en fysische ervaring zijn er de eerste acht hoofdstukken. Voor de lezer met wat minder natuurkundeachtergrond hoop ik dat mijn vereenvoudigde beschrijving het allemaal wat begrijpelijk maakt. Ik wens u in ieder geval heel veel leesplezier.

Jeroen

Contents

Chapter 1

Introduction

1.1 Measuring flow velocities

The determination of flow characteristics is important to many different fields of fundamental and applied research. Companies designing and building cars need to know exactly how the shape of their car influences the interaction of the car with the air that it moves through in order to improve fuel consumption and reduce friction. For the construction of aircraft the knowledge of the air flow structure around wings and engines is maybe even more important, since this information will keep planes in the air. Even machines designed to travel to and through space need to be optimized and tested in flow measurement facilities.

Also in the production of devices that are not directly concerned with transport it is important to gain understanding on the flow around and within them. The recent awareness of climatic change sparked interest on renewable energy sources, such as wind energy. To optimize the blades of a wind turbine, all losses need to be minimized and careful study on flow patterns around such a turbine is necessary. The process of combustion in large gas turbines or smaller engines is also driven by flows and especially the mixing of fuels and oxidizers. When the construction is made such that mixing is optimal, the combustion will result in the highest efficiency and lowest toxic output.

Fundamentally, the study of the process of mixing mostly concerns the study of turbulence, which is a classical problem that is not solved yet. Many studies in literature aim at describing turbulence characteristics in various systems in order to get a better understanding and to improve numerical models. It is therefore important to develop and use flow measuring techniques that follow the flow and turbulent structure as faithfully as possible and thereby disturb it as little as possible. Nowadays many different techniques are available that are used in commercial facilities and academic studies, all having their advantages and disadvantages. The available techniques can be divided into three groups; the mechanical, the opto-mechanical and the all-optical techniques.

1. Mechanical techniques

   Usually, mechanical techniques consist of adding a probe to the flow at the exact location where the flow velocity needs to be measured. A Pitot tube detects pressure differences between the flow and still air and after calibration it is possible to relate

this pressure difference to a velocity. Another velocity measurement device is the hotwire, which also needs to be calibrated. A current is run through a very thin wire, thereby heating the wire. The flow that is directed perpendicular to the wire, will tend to cool it down. The change of wire resistance due to this cooling can be measured and is related to the flow velocity. Velocities at surfaces of objects can also be measured by coating the surface with pressure sensitive paint. Under proper illumination, this paint will emit radiation, the wavelength of which depends on the pressure that is applied to the surface. By imaging the radiation from the surface one can get information on the velocity field at the surface.

2. Opto-mechanical techniques

There are two major flow velocity measurement techniques that consist of adding small particles to the flow and following the displacement of these particles by illuminating them with a lamp or a laser. One of these techniques is called particle image velocimetry (PIV), where the particles are illuminated stroboscopically and consecutive images reveal the displacements of the particles or ensembles of particles. To each displaced particle over time a velocity vector can be assigned resulting in a two-dimensional or even three-dimensional (when a stereoscopic setup of two cameras is used) velocity field. In the second technique, Laser Doppler Anemometry (LDA), the radiation scattered by the moving particles is Doppler-shifted. Together with the original electromagnetic radiation an interference pattern is created that can accurately represent the local velocity of the particles.

3. All-optical techniques

This type of technique does not require the seeding of small particles, but relies on light scattering off the molecules making up the flow themselves. Like in the previous class, methods exist that either follow groups of labelled molecules in time (Molecular Tagging Velocimetry; MTV), or that exploit the Doppler shift in light scattering by moving molecules (Filtered Rayleigh Scattering; FRS). FRS requires a narrow-band laser for illumination and sophisticated spectral filtering, because the Doppler shifts are generally very small (with respect to the frequency of the incident light). In MTV, molecules are tagged and followed, which makes it a more complex, but also less intrusive technique than the first two techniques. The details of this type of techniques will be discussed later in this chapter.

This thesis is concerned with an all-optical technique for local velocity measurements in air flows. With this technique, developed in our lab, we hope to fill a gap in applications. The development of the all-optical techniques was partly induced by the existence of several shortcomings with the first two types of techniques:

- One important effect of adding probes or particles to the flow is that they may influence the flow: the measurement device monitors a flow that is different from what it would be if the device were not there. The mechanical techniques consist of placing a relatively large object close to the point of interest. The flow is disturbed and the gas needs to follow a path around the object. Seeding particles change the density and composition of the gas. Small flow openings can also be clogged by

the particles, thereby blocking free pathways. Furthermore, it may be difficult to apply the techniques in special environments (e.g. combustion) or setups (delicate engines), because the seeded particles might not survive or they might damage the equipment.

- In particle-based techniques the seeds may be large relative to the flow structures. Especially in very small-scale turbulence, the velocity changes in size and direction are too large for the particles to follow. Drag and inertia decrease the accuracy and alter flow field results.

- Since seeding of particles in practice needs to occur locally, it is difficult to obtain uniform seeding. Of course the use of too few particles makes the measurement inaccurate, but too many particles may alter flow properties. Besides that, certain places in a flow may be hard to reach for the seeding particles. An example of this is the area behind an object, where wake flows may be important.

- Some of the particle based techniques detect the passing-by of particles past one point or volume in the flow. This way a bias for fast moving particles may occur, which necessitates corrections. This bias is caused by the fact that, in unit time, more fast particles move past the measurement volume, thereby raising the measured velocity with respect to the actual velocity.

- Finally, a density mismatch, which can cause the separation of the particles in the flow and the flow itself can also be problematic in flow measurements.

These issues can all be solved by creating molecular tracers and following them along their course. Since the molecules actually make up the flow, they will faithfully follow it and not perturb it. When the creation of these tracers can be performed at any position in the flow, it will also be possible to probe hard to reach places in the setup with particles. Finally, the bias problem will be circumvented by following the displacement of an ensemble of molecules (Lagrangian measurement) instead of measuring the velocity of molecules passing by (Eulerian measurement).

1.2   MTV

The class of techniques that use a molecular tracer for velocity measurements is also called molecular tagging velocimetry (MTV). The basis of this all-optical technique consists of two steps. In the first step an ensemble of molecules (for instance a line or a grid) is labelled, such that it is different from the carrier gas. This ensemble will then move with the flow and experience the same flow characteristics. The second step then visualizes the tagged molecules, which gives information on the location of the molecules. With the initial position known, a velocity can be assigned to each characteristic point on the ensemble. By writing a line, only the velocity in one dimension can be determined. A grid will give two dimensions, while a stereoscopic detection setup with two cameras can even result in a three-dimensional velocity field.

Molecular tagging velocimetry is a molecular technique, which means that molecules must be labelled in some way or another, in practice by locally changing either the chemical composition of the medium, or the internal energy of existing molecules. In most of the MTV techniques, the first step involves the photodissociation of seeded or already present molecules. Existing molecules are broken into pieces, which sometimes recombine to form a new species. Other techniques consist of changing the energy level population of existing molecules to be able to distinguish them. The second step then uses standard methods of molecular spectroscopy to distinguish the labelled species from background molecules. Visualization is performed by irradiation, using a laser beam with a well-chosen wavelength such that only the labelled molecules will fluoresce (laser induced fluorescence; LIF). This fluorescence can be imaged on a camera and with the original tag position known, velocity information can be extracted. Some MTV techniques use phosphorescent molecules, so that the first and second step are combined. Where fluorescence lifetimes are in the order of nanoseconds, phosphorescence may last several microseconds to even seconds. The tracers will keep on radiating over the course of their displacement and consecutive images can be made without an extra visualization laser.

The MTV technique that was developed in this lab and which is the basis for this thesis is called Air Photolysis And Recombination Tracking (APART). Figure 1.1 schematically shows how APART works. As can be deduced from the title, the tagging principle is based on the photolysis of air after which the products recombine. Some other MTV techniques require seeding of special molecules in the flow. In APART, however, we use ambient oxygen and nitrogen to create the required tracers. The two steps in this APART technique are the following:

1. An ArF excimer laser with a wavelength of 193 nm is focused in air (usually perpendicular to the main flow direction) using a spherical lens. In a line along the focus the air is excited, ionized and dissociated and the stable molecule nitric oxide (NO) is created. This line of molecules moves with the flow and wrinkles in the presence of velocity fluctuations.

2. NO can be excited using radiation at 226 nm after which it fluoresces. The 226 nm is provided by a dye laser pumped by a Nd:YAG laser. The fluorescence from the NO molecules induced by this laser (LIF) can be imaged onto an Intensified CCD (ICCD) camera and from the difference between the initial line and the displaced line a velocity can be calculated for each point on the line. An example of an APART picture can be seen in Fig. 1.2.

The goal of this research consisted of two parts. First, the applicability of APART at conditions which are of importance in practical situations, such as at high temperatures or high pressures, needed to be studied. Second, the fundamentals behind the technique, the creation of nitric oxide from air, was still largely unknown. In order to improve the signal-to-noise ratio a better understanding was necessary, such that a more accurate optimization could be performed.
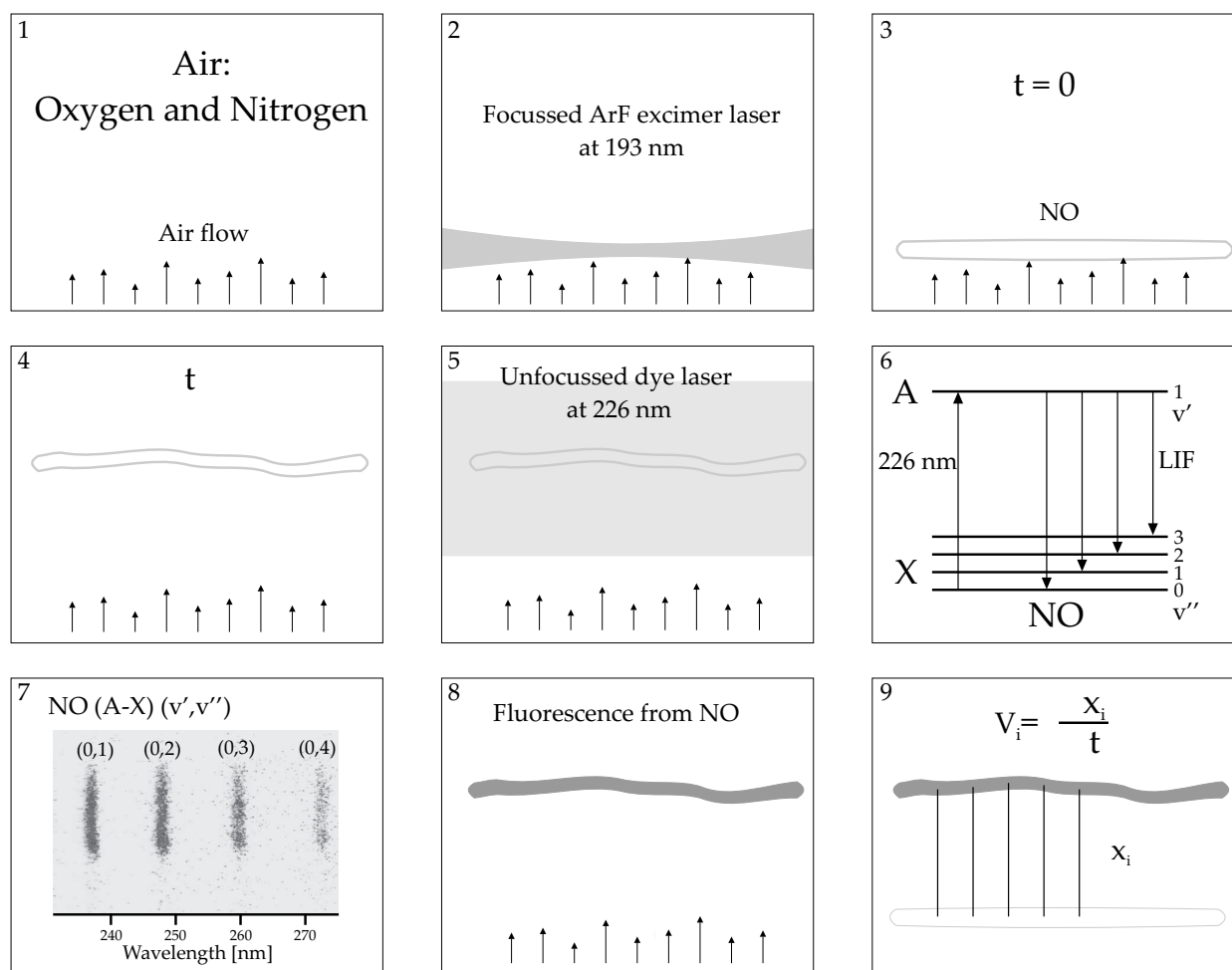
Figure 1.1: *Schematic depiction of APART. Panel 1: The studied air flow is placed in an ambient environment. Panel 2: The ArF excimer laser at 193 nm is focused in a narrow line perpendicular to the flow direction. Panel 3: From the oxygen and nitrogen in the air, nitric oxide molecules are created along the focus. Panel 4: The distribution of NO molecules is transported with the flow and any fluctuations in the flow alter the shape of the line. Panel 5: A dye laser at 226 nm is directed counter-parallel to the excimer laser and over the displaced NO molecules. Panel 6: The NO molecules are electronically excited from the $X^2\Pi$ ground state to the $A^2\Sigma^+$ state. Relaxation back to different vibrational states of the ground state results in fluorescence lines. Panel 7: The characteristic wavelength of NO LIF as seen by a spectrograph. Panel 8: The emission wavelengths from Panel 7 result in a radiating line of NO molecules, which can be imaged on a CCD camera. Panel 9: Together with the original position of the line and the time delay between the "write" excimer laser and the "read" dye laser the average velocity on every point of the line can be extracted.*
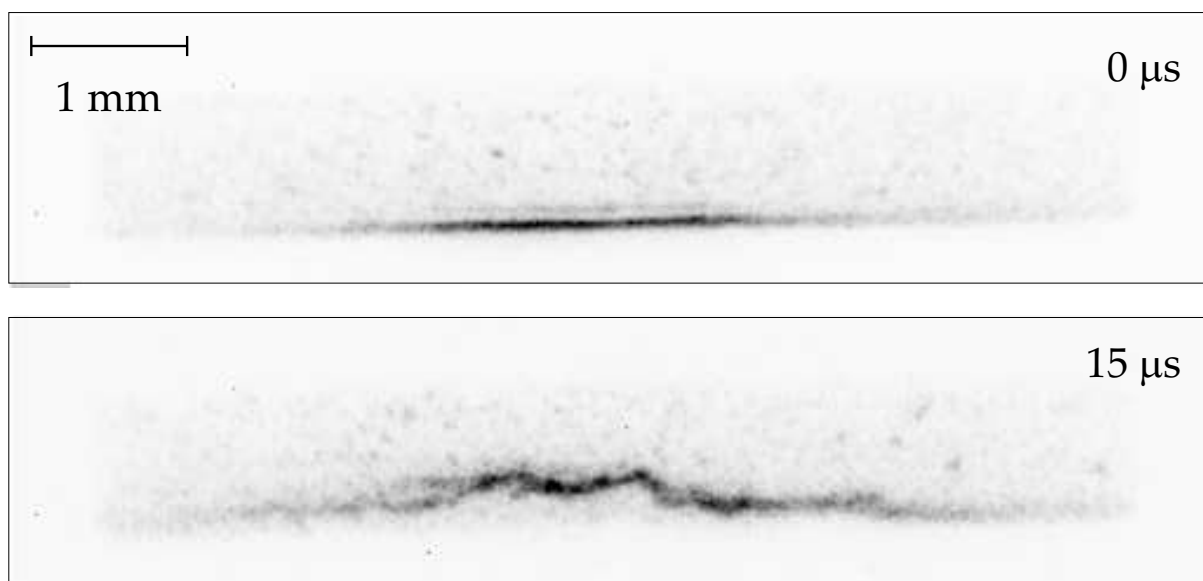
Figure 1.2: *Typical example of APART images written in air using a pressurized jet to create turbulence.*

1.3   This thesis

This thesis is divided into several chapters. In Chapter 2 a description is given of all the equipment used in the experiments as well as the basic setup for APART. The working distance was varied in order to investigate the possible range of applications, especially in view of the possible use in large facilities, such as the wind tunnels of DNW (German-Dutch Windtunnels). The temperature rise caused by the excimer laser was also studied in order to gain more insight in the intrusiveness of APART.

The applicability of APART was tested in different environments in the following experimental chapters. Chapter 3 describes the application of APART in a high pressure cell, in order to obtain information on the optimal gas composition at different pressures in preparation of high pressure experiments in this lab. The pressure was varied between 1 and 80 bar and the gas composition was modified by decreasing the oxygen percentage relative to the nitrogen percentage.

In Chapter 4 another environment was studied, where a laminar flame and a turbulent flame were investigated at different positions in the flame. The velocities and velocity fluctuations were measured as well. Again this study was performed to test the behavior of APART in a more extreme environment.

The second part of the thesis, which has a more spectroscopic nature, describes the study on the mechanism behind the APART technique. The creation of NO is a complex process and due to the use of a focused laser a large amount of energy is available to a small volume of air, leading to multiphoton processes and heating. To optimize the APART technique we need to know what exactly is happening in the focus, so the parameters can be tuned such that an optimal amount of NO with a minimum of excess energy
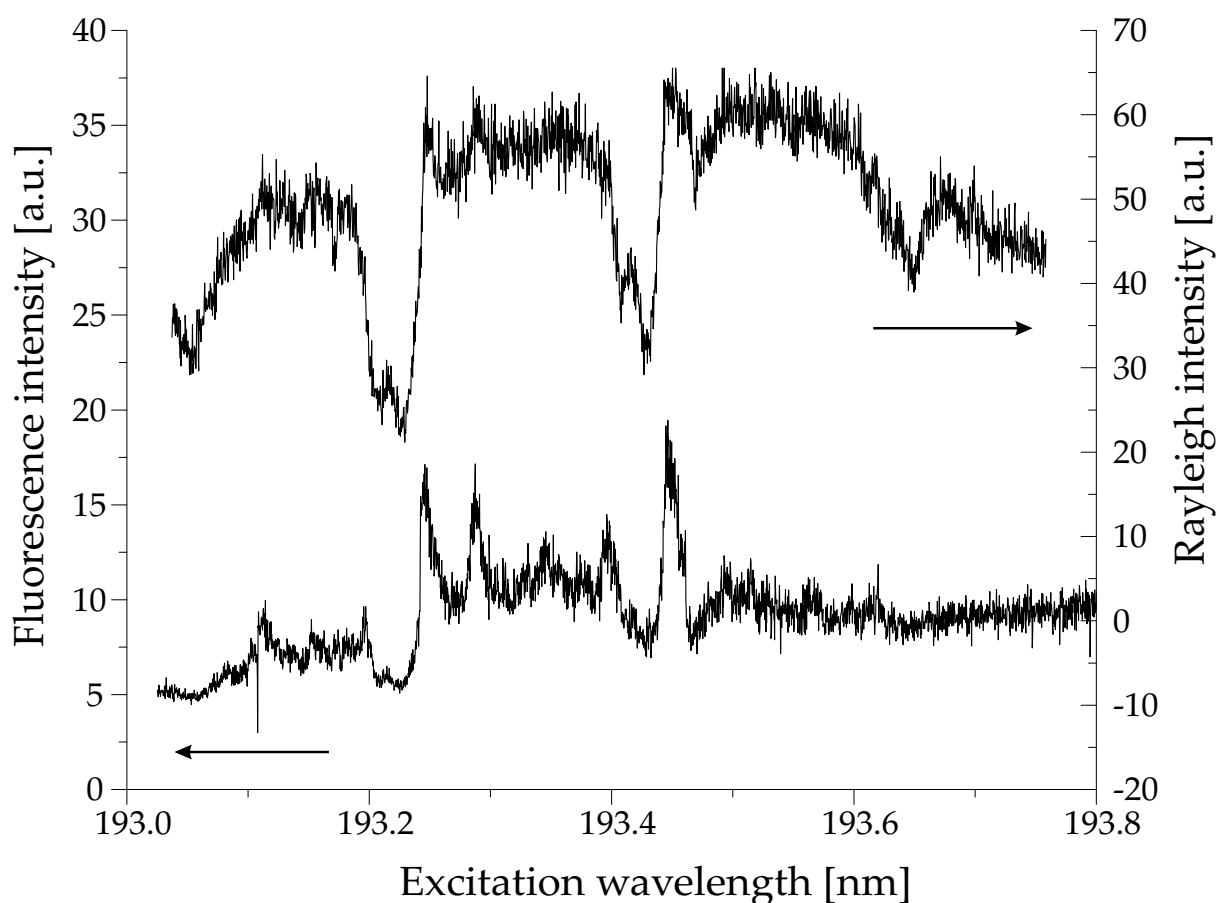
Figure 1.3: *An excitation spectrum of the creation of nitric oxide by the 193 nm excimer laser. The upper plot is the Rayleigh scattering signal at 193 nm and the lower plot is an accumulation of the NO fluorescence signal at 236 nm, 247 nm and 258 nm, both as a function of excimer laser wavelength.*

is created.

The most accessible way to vary parameters is to scan the wavelength of the tunable excimer laser over a small wavelength range of approximately 193.0 nm–193.8 nm and to measure the resulting laser induced fluorescence of NO. Figure 1.3 shows the amount of created nitric oxide as a function of excimer laser wavelength. The maxima in the lower plot demonstrate that the efficiency of NO creation increases for certain wavelengths. The relatively high background, however, indicates that several pathways play a role, at least one of which is wavelength-independent in that range. The description of this problem has been separated into three chapters.

In Chapters 5 and 6 we describe the characteristics of pure nitrogen and pure oxygen, respectively, in a focused excimer laser beam, to understand the photodynamics of the only two species involved in the NO creation.

The combination of the two species, oxygen and nitrogen and their laser induced

chemical interplay leading to nitric oxide is given in Chapter 7. A spectroscopic peculiarity is discussed as well as chemical reaction mechanisms involved.

Finally an Outlook is given in Chapter 8, and appendices give more information on different MTV techniques and describe this thesis for people without specific knowledge about its contents and basics.

Chapter 2

Experimental

2.1 Introduction

To apply APART in an air environment there is a necessary minimal amount of equipment.

A typical APART setup is shown in figure 2.1. The write laser is an ArF excimer laser (λ = 193 nm), which is focused through a quartz lens and creates the NO from the air. It was shown to be impossible to apply a KrF laser at 248 nm or a tripled Nd:YAG laser at 355 nm to create nitric oxide. A short time delay after writing (controlled by the delay generator) the read laser is fired counter-parallel to the write laser and at that same instant a digital camera images the resulting fluorescence and displays it on a computer.

Below, descriptions of the most relevant equipment used in this study are given. Furthermore, some fundamental issues related to the APART setup will be discussed. These include a study on the working distance of the technique, a discussion on the temperature increase due to APART and the creation of multiple points instead of a line.

2.2 Setup

2.2.1 Excimer Laser

In the write process of APART nitrogen and oxygen molecules in the air are turned into nitric oxide molecules, through a photosynthesis process. A tunable argon-fluoride excimer laser (Lambda-Physik EMG 150 MSCT) at 193 nm was employed for this creation process. This laser has a gas filling of argon, fluor, and helium in an oscillator tube and an amplifier tube. The wavelength of the oscillator output can be tuned between approximately 51650 cm^{-1} and 51850 cm^{-1} using a grating. This output can then be fed into the amplifier tube. The amplifier output consists of the amplified, narrow-bandwidth input plus a broadband component due to amplified spontaneous emission arising within the amplifier itself. In terms of energy the total power is split about evenly between these two components [1]. The energy of the excimer laser was nominally around 60 mJ/pulse. For the write process a large amount of energy is needed, even if only a small fraction is used in the actual creation of NO. If the laser is not focused the technique will not work, since the creation of nitric oxide involves one or several multi-photon interactions with N_2 and
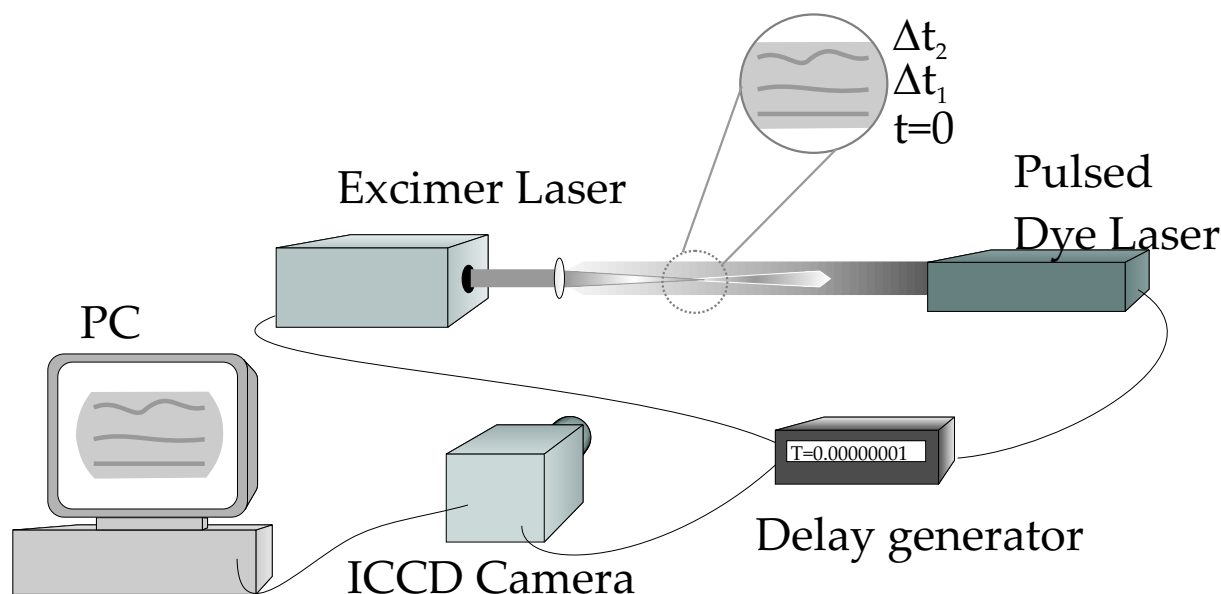
Figure 2.1: *Typical APART setup with all required equipment.*

O$_2$ (see Chapter 7). Under typical working conditions, the pulse energy is approximately 20 mJ or more.

The ArF excimer laser that was used, can be tuned to different wavelengths in a short range around 193 nm. This tunability is not crucial for application in APART, but it is important in the optimization of the technique. Choosing the right wavelength results in an increased amount of nitric oxide. The details will be explained in Chapter 6.

2.2.2 Nd:YAG-pumped Dye Laser

To visualize NO we need radiation at 226 nm. At this wavelength ground state nitric oxide (X$^2\Pi$) can be excited to an electronically excited state (A$^2\Sigma^+$). This transition is also known as the γ system [2]. To create this wavelength an elaborate setup is required (see Fig. 2.2). First a Nd:YAG laser system (Spectra-Physics Quanta-Ray Pro 250-10) operating at 1064 nm is frequency-doubled using a KD*P crystal. An injection seeder (model 6350 Spectra-Physics) installed in the Nd:YAG laser creates a temporally smooth Gaussian-shaped laser beam in a single longitudinal mode of the laser cavity. Mixing the resulting 532 nm beam with the remaining 1064 nm radiation using a BBO crystal results in frequency-tripled radiation at 355 nm. The residual green light is coupled into a dye laser system (PrecisionScan Sirah) operated on DCM dye, where an oscillator and two amplifiers convert the green radiation to red laser light (approximately 622 nm), with a linewidth of 0.002 nm. A BBO mixing crystal finally converts collinearly aligned beams at 622 nm and 355 nm into radiation with a wavelength of 226 nm. The final step in the system is a combination of four Pellin-Broca prisms which filters out all remaining radiation except at 226 nm. The average output power at 226 nm was approximately 7 mJ/pulse.

The choice of the read laser is governed by the absorption wavelength of nitric oxide,
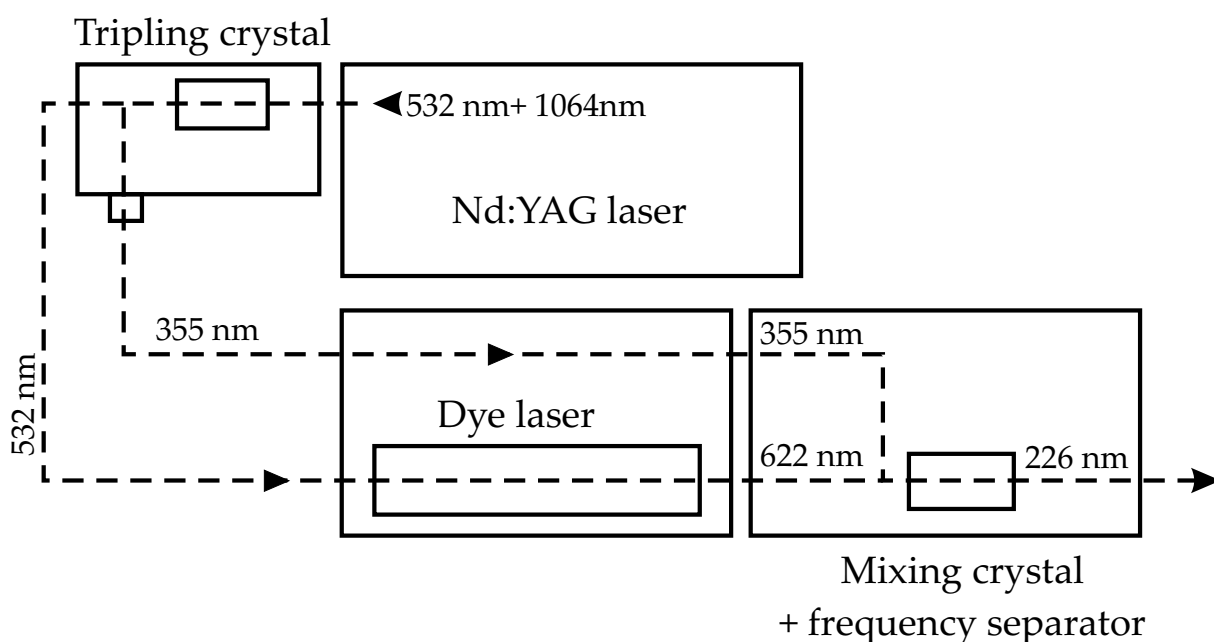
Figure 2.2: *Schematic drawing of the laser setup to acquire 226 nm radiation (mirrors omitted).*

which has a strong absorption at 226 nm (see Fig. 2.3). The γ-bands of NO are spectroscopically well-known, and they are frequently used for NO visualization in laser diagnostics [3–5]. It is important to note that this visualization process is linear in laser intensity and there is no need for focusing. However, it does help to have more energy, since this gives higher fluorescence levels and thus helps to improve the signal-to-noise ratio of the technique. Focusing the laser beam will of course also increase the fluorescence intensity. The drawback to this, however, is that overlapping the two beams (write and read lasers) in space, becomes more difficult and in the presence of a flow, the created NO line can more easily move out of the read laser beam.

2.2.3 ICCD Camera

Since most of the radiation in the APART experiment is in the ultraviolet a detector is needed that is sensitive at these short wavelengths. A typical charge coupled device (CCD) camera will only measure radiation in the visible and the infrared. An intensified CCD (ICCD) camera is a normal CCD camera with an image intensifier mounted in front of the chip. An intensifier consists of a photocathode where incoming photons are converted into electrons, which are subsequently multiplied by a multichannel plate (MCP). The electrons then arrive at a phosphor plate that emits photons in the wavelength range detectable by the CCD chip. This way it is possible to detect weak ultraviolet radiation. Another important reason to utilize this intensifier is the gating capability. The intensifier can be gated or triggered to open and close within 5 ns or more. This means that with the correct timing, short laser pulses (in the order of 20 ns) can be imaged exactly in time onto the camera and all radiation that is not inherent to the laser can be rejected by this
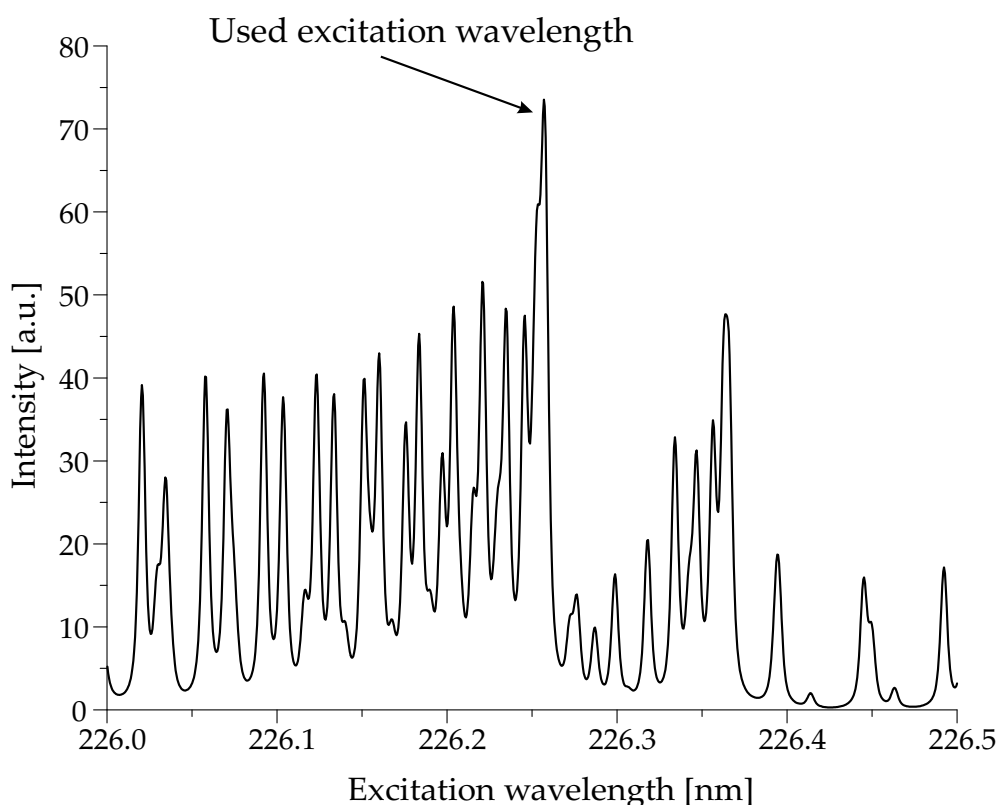
Figure 2.3: *The excitation spectrum of nitric oxide around 226.25 nm. At the excitation wavelength that was used in the experiments a concatenation of several transitions occur as indicated in this plot.*

gating. For the APART experiment gating is crucial since the radiation only lasts tens of nanoseconds and ambient light and radiation from the write laser need to be filtered out for a higher signal-to-noise ratio. The cameras used in the experiments are both from Princeton Instruments. One is an ICCD detector with an array of 512×512 pixels, which is cooled by Peltier elements. The heat transport away from the elements is accomplished by water flushing. To avoid condensation of water on the camera optics, the camera also needs to be flushed by nitrogen gas. The camera is controlled by a controller (ST-138) and the intensifier is gated using a programmable pulse generator (PG-200). The other camera is a PIMAX II ICCD detector (1024×1024 pixels, cooled by Peltier elements). It is controlled by an ST-133 controller with pulse generator (PTG). The objective that was used was a 105 mm objective (Nikon UV-Nikkor). A UV-notch filter at 226 nm was used to block the Rayleigh scattering from the pulsed dye laser.

2.2.4 Spectrograph

A device that was used extensively to study the fundamental aspects of APART is the spectrograph. It was also used for pre-optimization of APART, since N_2^+ fluorescence created by the excimer laser only is proportional to the NO LIF intensity induced by
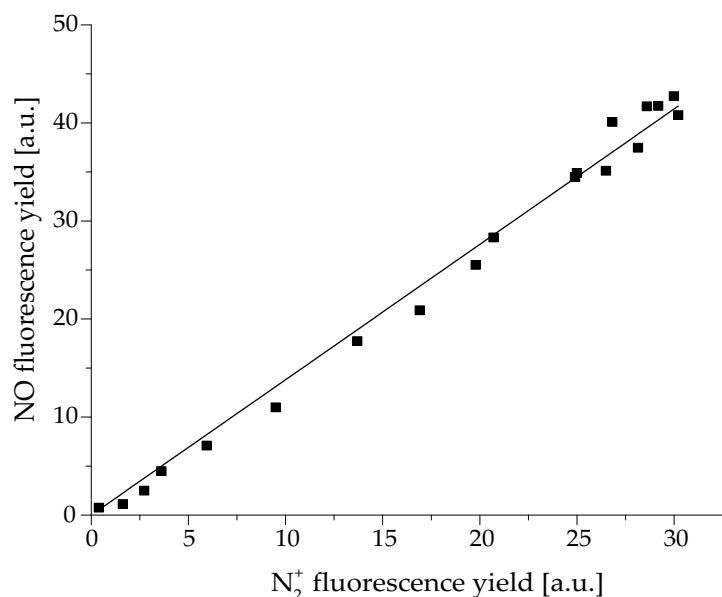
Figure 2.4: *Relation between N_2^+ fluorescence from the integrated emission intensity of the B-X (0,0) emission band and NO fluorescence induced by the dye laser measured from an integrated CCD image. Both datasets were corrected for background signal, and the fluorescence intensities were varied by changing the voltage of the amplifier tube of the excimer laser. The dye laser intensity (used for NO) was kept constant. The line is a linear fit through the origin.*

the dye laser as can be seen in Fig. 2.4. An objective images the incident radiation onto the entrance slit (adjustable between 0 and 3 mm) of an imaging spectrograph, which is equipped with an ICCD camera on its exit port. A set of mirrors and one grating on an adjustable three-grating turret separates the individual wavelength components of the incident radiation. This way, the spectrograph produces one image of the entrance slit for each individual wavelength component in the incident radiation. The position of every image on the ICCD camera is directly related to the wavelength. By rotating the grating a small wavelength range of the incident radiation can be selected to be imaged onto the camera. The spectrograph used in our experiments (ARC SpectraPro 300i) has three gratings with 150, 1200 and 2400 grooves/mm, respectively. The calibration of the wavelengths of the spectrograph was performed using a mercury lamp and the prominent lines at 254 nm and 577 nm. This resulted in an error of approximately 0.5 nm.

At maximum slit width a large amount of radiation is transmitted through the spectrograph to the CCD camera, thereby increasing the signal-to-noise ratio. There will, however, be spatial information included in the image, which then gives a convoluted picture of spatial dimensions and wavelength. By decreasing the slit width the contribution from individual wavelength components is increased, while the detected radiation intensity is diminished. Of course this depends on the width and the monochromaticity of the source. The size of a perfectly monochromatic point source will not change in size and intensity on the CCD chip while the slit width is changed. A more detailed descrip-
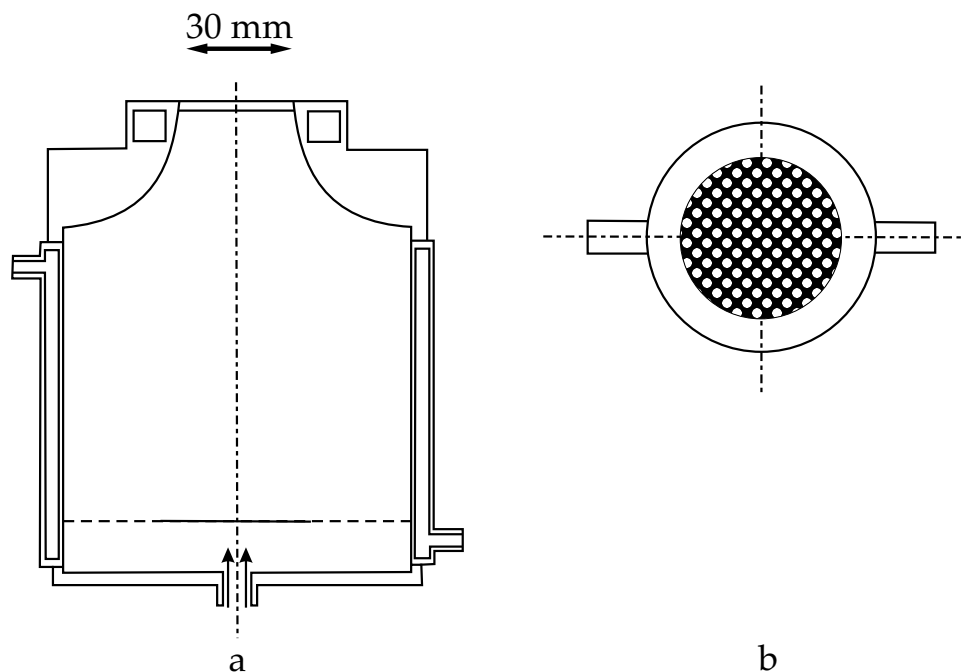
Figure 2.5: *The general purpose laminar flow generator used in spectroscopic gas flow experiments (a = side view, b = top view). Different gases can be flown through the large exit resulting in laminar flows of, for instance, pure oxygen or nitrogen.*

tion of this principle was given by Tolboom *et al.* [6]. Usually the slit width was set to 50 μm, resulting in a wavelength resolution of 0.1 nm.

2.2.5 Delay Generator

The heart of the entire setup is a digital delay/pulse generator (SRS DG535). This device controls the exact timing between the flash lamps and the Q-switch of the dye laser system, it triggers the excimer laser and it tells the cameras when to gate. The exact gate width of the intensifier and the exposure time of the camera are controlled by the corresponding pulser and camera software, respectively.

2.2.6 Test environments

Some of the performed experiments consisted of a wavelength resolved analysis of the emission from the excimer laser focus in nitrogen, oxygen and air. We used a general purpose laminar flow generator (see figure 2.5) to employ a steady flow with large outflow diameter. The diameter of the outflow opening is 30 mm and the hole diameter and pitch are 0.4 mm and 0.6 mm, respectively. A more detailed description of this flow generator and its specific use in combustion can be found in the thesis by Evertsen [7].
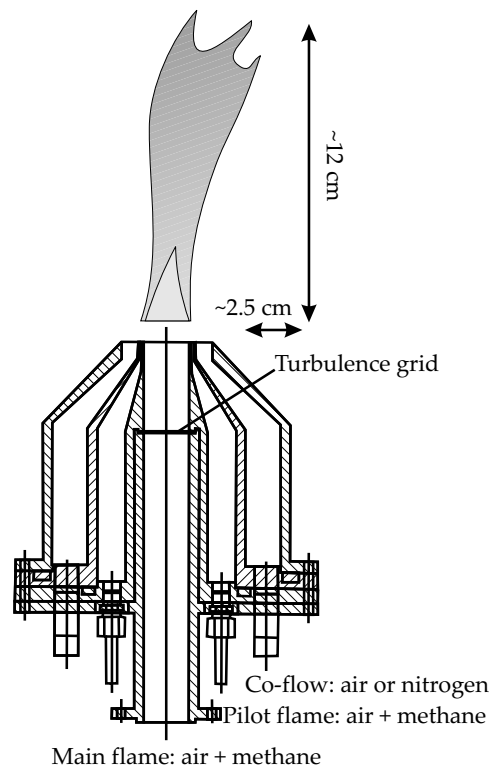
Figure 2.6: *A schematic drawing of the burner that was used. The pilot flame stabilizes the main flame and is also used to ignite it. The co-flow can be used to reduce lateral movements but was not used in our experiments. The diameter of the exit of the main flame is 25 mm.*

Other experimental environments consist of a high pressure cell and a special turbulent flame generator. The high pressure cell is a cylindrical steel body where two quartz windows are placed opposite to each other and another pair placed opposite but perpendicular to the first pair. This way laser beams can be directed through the cell, while at the same time two cameras can observe the laser beams perpendicular to their propagation direction. The volume of the cell is $10\,\ell$ and it can be filled separately with nitrogen and oxygen at pressures ranging from 1 bar up to 80 bar. The turbulent flame generator (Fig. 2.6) consists of an inner main flow, and an outer co-flow to ignite and stabilize the main flame. A grid with tiny holes provides the turbulence in the flow.

2.3   Working Distance

2.3.1   Background

To study the applicability of APART in large facilities, the working distance has to be investigated. Most of the experiments with APART have been performed with a working distance of approximately 25 cm [8, 9]. This means that the focusing lens of the excimer

beam has a focal distance of 25 cm and the camera is positioned at 25 cm distance from this focus. For an experiment in a large wind tunnel these distances are too small since the camera as well as the required optics should be placed outside the wind tunnel, in order not to perturb the flow.

At first sight, increasing the working distance might be expected to decrease only the light collection efficiency of the visualization system ($\sim 1/r^2$), which could in principle be countered by larger f/number optics. The pitfall, however, is in the writing step, with its non-linear dependence on laser intensity. On the one hand there is a relation [10] between focal distance f and waist diameter w_0,

$$w_0 = \frac{f\lambda}{\pi w_s} \quad , \tag{2.1}$$

with w_s the beam size at the lens. Although this relation strictly holds for Gaussian beams, we expect a similar relation for the beam of an excimer laser. On the other hand the increased path length through ambient air will result in less available laser power in the probe volume, due to absorption in the Schumann-Runge bands of ambient O_2.

In one experiment we performed APART on a simple compressed air device (commonly used to flush hoses) using three different lenses (25 cm, 50 cm and 100 cm) and three different camera positions ($\sim$25 cm, $\sim$50 cm and $\sim$100 cm away from the focus).

2.3.2   Results

Figure 2.7 shows some typical pictures of the measurements performed at different working distances. At the applied laser power (60 mJ/pulse at the exit of the excimer laser) the intensity of the focus of the 100 cm lens is still high enough to create NO. As can be seen in the figure the longer depth of focus of this lens also results in a longer line of NO molecules. If a Gaussian beam is assumed, the width (w) of the beam at any distance (z) from the focus is given by:

$$w(z) = w_0\sqrt{1 + \left(\frac{\lambda z}{\pi w_0^2}\right)^2} \quad , \tag{2.2}$$

where w_0 is the size of the laser beam in the focus and λ is the laser wavelength. The distance over which the size of the beam width increases by a factor of $\sqrt{2}$ compared to the minimum size is called the depth of focus, or Rayleigh length (z_r) and is defined by

$$z_r = \frac{\pi w_0^2}{\lambda} \quad . \tag{2.3}$$

If the focal distance is increased by a factor of two the Rayleigh length will increase by a factor of four. The beam waist size, however, scales proportional to the focal distance.

To determine if there is a relation between the scaling of the Rayleigh length and the written NO line, we measured the length of the NO line for the three different lenses and at two different camera positions for a delay time of 3 μs (almost no movement). Although not really necessary for the present purpose, a small flow was applied to avoid pile-up of photochemistry products. The experiment was performed by first setting up
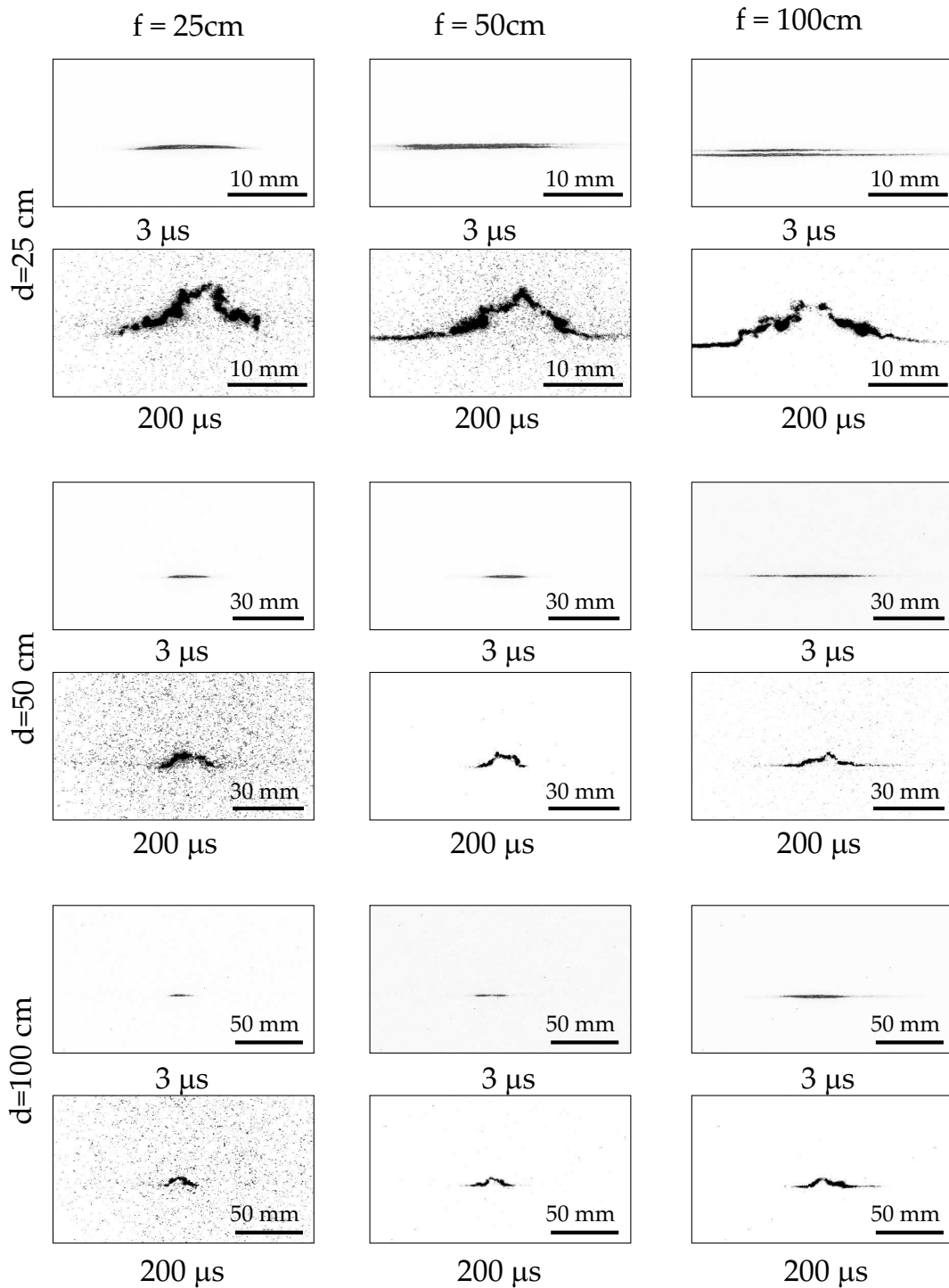
Figure 2.7: *Results of the APART measurements on a pressure gun. For every focal length and camera distance one measurement at a delay of 3 μs was taken and one measurement at a delay of 200 μs. The double line that can be seen in the upper right picture (f = 100 cm, d = 25 cm and a delay of 3 μs) is caused by a smudge on the output window of the excimer laser resulting in a hole in the center of the beam.*

Table 2.1: *Measurements of line lengths of initial written lines for different focal distances and camera positions. The lengths at a camera position of 50 cm and a focal distance of 25 cm and 50 cm are similar possibly because the tilt angle of the lenses was not the same.*

camera position [cm]	focal distance [cm]	line length [mm]
50	25	12 ± 1
50	50	12 ± 1
50	100	27 ± 3
100	25	14 ± 1
100	50	24 ± 2
100	100	35 ± 3

the experiment at one camera position while replacing the lens three times. Each time the lens was tilted to adjust the intensity, but such that no optical breakdown occurred. This was repeated for each of the three camera positions. By performing the experiment in this order we added an uncertainty to the tilting angle of the lenses for the different camera positions. The tilting was done by hand; when no visible breakdown was present, we secured the lens. It is difficult to do this in a reproducible way, because this angle depends on laser power and dust particles present in the focus.

The results of these measurements are given in Table 2.1. The line length was deduced by fitting Gaussian functions through all lines after having been accumulated vertically. The FWHM of this fit served as a measure for the line lengths. In general, the line length increases less than linear to the focal distance and the beam waist size and not quadratically like the Rayleigh length. This indicates the existence of a threshold intensity for NO formation, since the NO line length depends on the width of the beam. The flux (amount of photons n_p per cm^2) ϕ depends on the beam waist as

$$\phi = \frac{2n_p}{w^2} \quad , \tag{2.4}$$

assuming a rectangular beam where the width w of the beam is half of the height. Using Eq. 2.2 the position along the laser beam z as a function of beam width w is obtained:

$$z = \frac{\pi w_0}{\lambda}\sqrt{w^2 - w_0^2} \quad . \tag{2.5}$$

Since the minimum flux needed to create NO is related to a maximum beam width a crude estimate of the line length ($l = 2z_{\max}$) at maximum beam width as a function of focal distance can be deduced using Eq. 2.1:

$$l = 2\frac{f}{w_s}\sqrt{w_{\max}^2 - \frac{f^2\lambda^2}{\pi^2 w_s^2}} \tag{2.6}$$

Using $w_{\max} \gg f\lambda/\pi w_s$ we can neglect the second term in the square root, after which the following relation is obtained

$$l = 2\frac{f w_{\max}}{w_s} \quad , \tag{2.7}$$

which indicates that the length of the line scales proportional with the focal distance.

Using the data from Table 2.1 and Eq. 2.7 we can calculate the maximum waist diameter at which NO is formed at the used energy of 60 mJ/pulse. For $w_s = 1$ cm this value amounts to $w_{\mathrm{max}} = 0.20 \pm 0.06$ mm.

2.3.3   Conclusion

The measurements prove that a working distance of at least 100 cm is feasible. When using a lens with a longer focal distance the line of NO molecules gets longer and thicker. The stretching of the line goes proportional with focal length and not with Rayleigh length. For larger focal distances the focus might become too wide to still have enough laser intensity to create NO. The maximum beam waist should not exceed the limit of 0.2 mm. Using Eq. 2.2 it follows that a lens is needed with a focal distance of more than 32 m to receive a beam waist larger than 0.2 mm (at $w_s = 1$ cm). Before we reach such lengths, however, the absorption of oxygen along the beam path will play a more dominant role in limiting the NO creation. Moreover, it should be mentioned that an excimer laser beam does not behave like a pure Gaussian beam. This means that the beam size is approximately twice as large as expected from Gaussian theory. Therefore a better estimate of the maximum focal distance would be at a maximum beam waist of 0.1 mm, which corresponds to a maximum focal distance of 17 m.

2.4   Temperature

2.4.1   Introduction

Focusing a laser beam in a small volume of air should in principle not effect the gas as long as the light is not absorbed. In the case of an excimer laser, however, the Schumann-Runge bands of oxygen will very efficiently absorb the incoming photons thereby raising the local temperature. By tuning the laser wavelength away from the oxygen absorption lines, this effect will decrease. The NO creation efficiency, however, is found to depend strongly on wavelength as well (Chapter 1).

Knowledge of the temperature in the focus of the excimer laser beam is very important, because it gives information on the creation process, but also may put a limit on the intrusiveness of the technique. If there is a very strong increase of the temperature, this will change the flow conditions which, of course, is to be avoided.

The temperature can be measured by taking an excitation spectrum of NO by scanning the dye laser wavelength (226 nm), also known as LIF thermometry [11]. This spectrum (compare Fig. 2.8) has a unique structure for NO. At a different temperature, the position of the peaks is exactly the same, but the relative intensities are different because these reflect the (temperature-dependent) lower level populations. A simulation program like LIFBASE [12] can predict such an excitation spectrum as a function of temperature. The measured spectrum can be compared to spectra simulated at different temperatures and on the basis of this comparison an estimate of the temperature can be made.

2.4.2 Results

A typical APART setup is employed to measure the temperature. The excimer laser is used to create NO in the focus and a short time later the dye laser is triggered. By scanning the dye laser over a short wavelength range (λ = 225.45–225.75 nm) and recording the fluorescence in the focus an excitation spectrum of NO (A←X) is created at one time delay.

Figure 2.8 shows such an excitation spectrum of NO. The other plots included in this figure are simulations performed using the program LIFBASE [12] at three different temperatures. As can be seen, due to different populations in the lower states, the relative intensities change with temperature.

When several excitation spectra are simulated for different temperatures a correlation with the measurement at one delay time between reading and writing will result in a temperature. The same procedure was performed at different delay times, the result of which can be seen in Fig. 2.9. From this figure we can conclude that the temperature immediately after focusing the excimer laser beam does not exceed the ambient temperature by more than 250 K. Within several microseconds this temperature has also stabilized to ambient. The error bars are chosen to be ± 50 K, since this was the maximum resolvable spacing between temperature simulations. The differences between spectra at smaller steps were not distinct enough to be able to distinguish within experiments.

There are, however, several remarks to be made on the accuracy of these measurements. From Fig. 2.8 it can be seen that the agreement between measurement and simulation is not perfect. This may be an indication that 50 ns after the excimer laser pulse the NO formed up to then is not completely thermalized. Note that the NO formation under these conditions continues up to at least 1 μs delay, see Chapter 3. Furthermore, the NO fluorescence that is measured as a function of excitation wavelength is an accumulation of the signal of NO molecules in a chosen region of interest in a typical APART image. To get the temperature exactly in the focus and only in the focus, this region of interest should be as small as possible. On the other hand, this region can not be too small because of the signal-to-noise ratio. Our measurements have been performed using a region of interest of 150 μm×150 μm. Possibly, a measurement using a smaller region of interest would result in a higher temperature. A measurement (at 50 ns delay) using a region of interest of 30 μm×30 μm resulted in a spectrum at 900 K rather than one at 550 K, which was reproducible within 100 K. It could still be debated whether it is possible to speak about a temperature here, especially at short time delays. Very locally a plasma with a large temperature gradient over a very small volume may be created, but how long this plasma remains and what its effect is on the flow dynamics is unknown.

2.4.3 Conclusion

Estimates of the local temperature rise induced by the write laser strongly depend on the detailed spectral structure of the laser radiation and the beam profile of the laser. These parameters being largely unknown, the initial estimates based on measurements of absorption of laser beam intensity along the line varied between about 20–500 K [14]. The measured temperature rise of 200±50 K does not exceed this range. Initially, the temperature rise is expected to be confined to the region illuminated by the write laser.
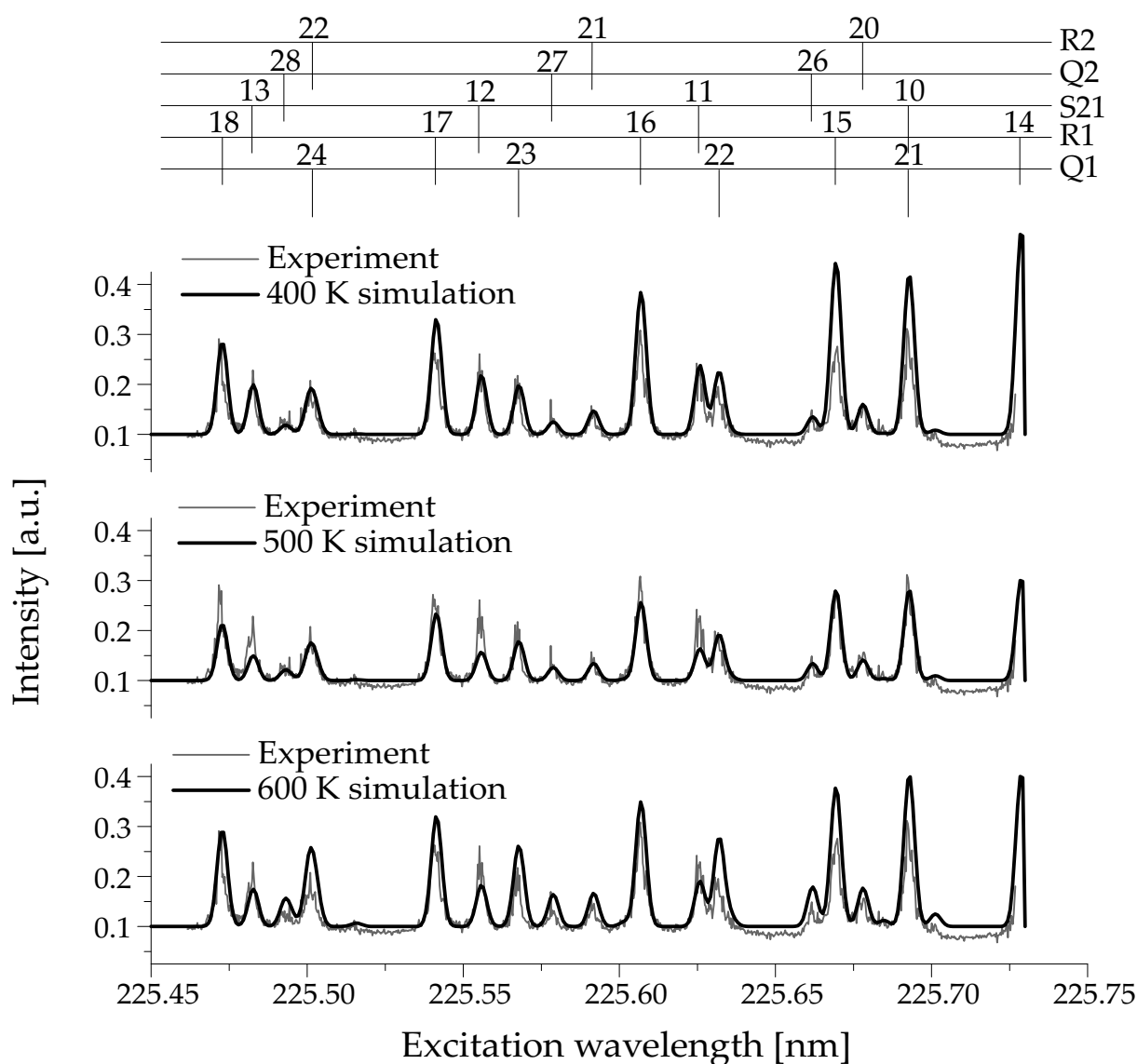
Figure 2.8: *Measured excitation spectrum of NO (corrected for laser intensity and background) and LIFBASE simulations for 400 K, 500 K and 600 K. Although none of the simulations exactly fit the measurements, the relative intensities of the maxima mostly correspond to the simulation at 500 K. The strong deviations are caused by the fact that this scan is taken over a longer time, where shot-to-shot laser pulse fluctuations strongly influence the intensities in this spectrum. At the top a rotational assignment of this $v' = 0$ to $v'' = 0$ transition is included.*
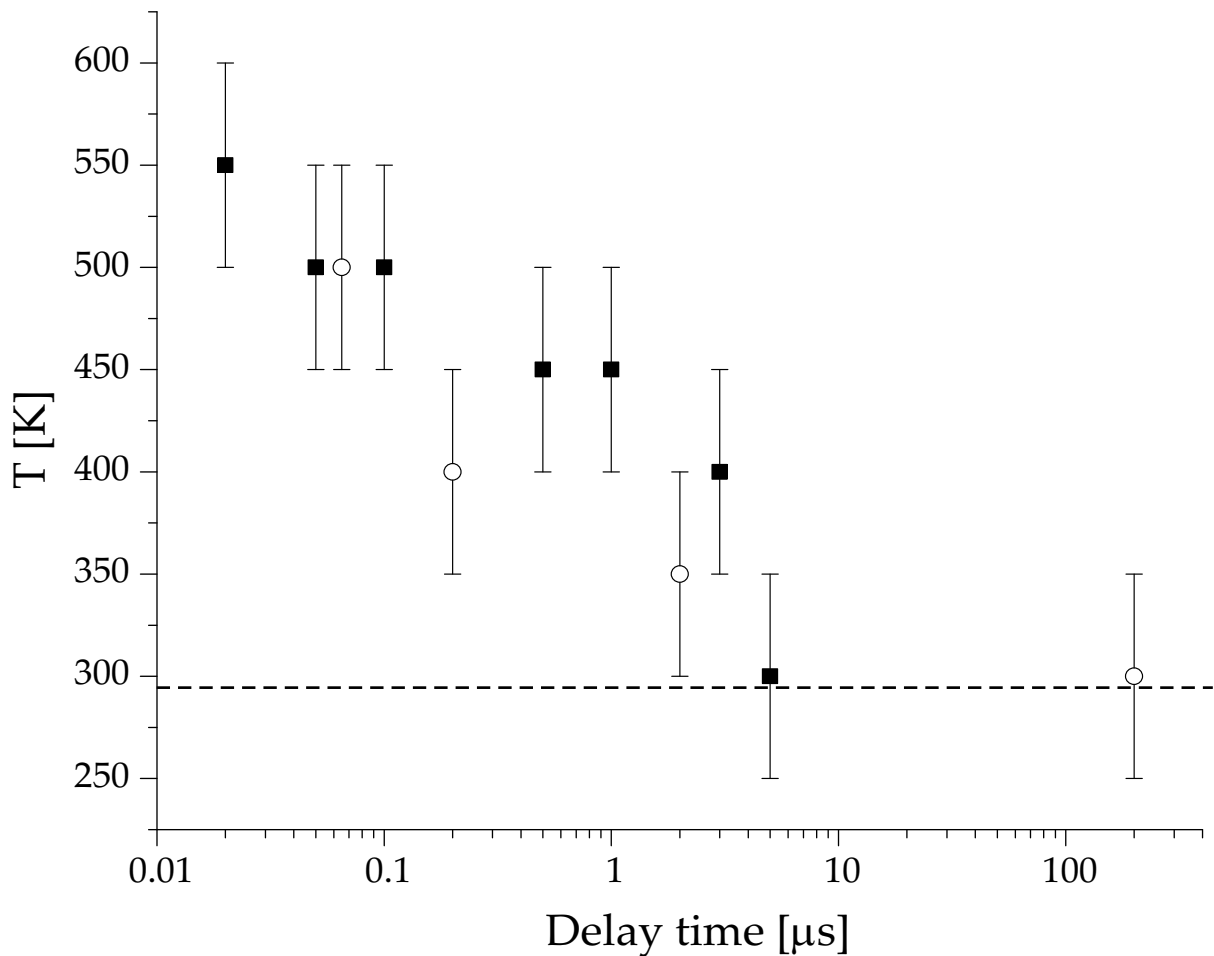
Figure 2.9: *The measured temperature profile as a function of delay time. The open circles (from [13]) represent measurements performed in different conditions compared to the closed squares. The difference lies in the chosen region of interest for accumulation, which is larger for the open circles. The resolution of the comparison between the simulations and experiments only permitted a step size of 50 K. The error bars, therefore, have a size of 50 K.*

Thermal diffusion will subsequently lead to quick thermalization. Indeed, measurements have resulted in room temperature spectra after a delay of $2 \, \mu$s.

2.5   Concentration estimation

In order to obtain more quantitative information about the NO formation by the excimer laser beam focused in air, we tried to determine the quantity of NO created under the conditions used for APART by an absorption technique called Cavity Ring Down Spectroscopy (CRDS).

2.5.1 CRDS principle

Cavity Ring Down spectroscopy [15] is a very sensitive absorption technique, based on the decay time of an optical cavity formed by two high reflectivity mirrors. A pulse of light is injected into the optical cavity and makes a large number of round-trips in the cavity. The intensity of the signal transmitted is collected after each round-trip by a detector placed behind the second mirror. The lifetime of the light pulse in the cavity is a function of losses due to the mirrors and due to the absorption and scattering of the medium between the mirrors. The signal analysis permits to obtain minor species concentrations.

The temporal evolution of the signal can be described by an exponential decay:

$$I(t) = I_0 exp(-t/\tau) \tag{2.8}$$

with I_0 the intensity of the signal at time $t(0)$ and τ the lifetime of the pulse in the cavity.

When the cavity is empty, $\tau = \tau_0$, with

$$\tau_0 = \frac{d}{c(1-R)} \quad , \tag{2.9}$$

with d the distance between the mirrors or path length and R the reflectivity coefficient of the mirrors. When the cavity contains absorbing species

$$\tau = \frac{d}{c(1-R) + k(\lambda)L} \quad , \tag{2.10}$$

with $k(\lambda)$ the absorption coefficient of the studied species and L the absorption path length.

The measurement of τ_0 and τ permits to obtain $k(\lambda)L$ representing the losses per pass due to absorbing species. This determination is independent of the incident intensity due to energy fluctuations of the laser source. By inducing an electronic transition of this species the total population of a species can be obtained from the decay time measurement. For that, we record the evolution of the decay time as a function of the laser wavelength in order to calculate the losses per pass as a function of the wavelength. The integrated absorptivity A (in m^{-1}) of a peak corresponding to a specific rovibronic transition $e', v', J' \leftarrow e'', v'', J''$, where e stands for the electroncic state and v and J are the vibrational and rotational quantum numbers, respectively, is directly proportional to the population density $N_{J''}$ on the rovibronic level probed [16]:

$$N_{J''} = 8\pi c \frac{A}{L} \frac{g_{J''}}{g_{J'}} \frac{\omega^2_{J''J'}}{A_{J''J'}} \tag{2.11}$$

with g_J the degeneracy factor $(2J+1)$, $A_{J''J'}$ the Einstein emission coefficient and $\omega_{J''J'}$ the excitation energy (in m^{-1}).

From this value, the total population N_T of the species can be derived using the Boltzmann factor F_B:

$$N_T = \frac{N_{J''}}{F_B} \tag{2.12}$$
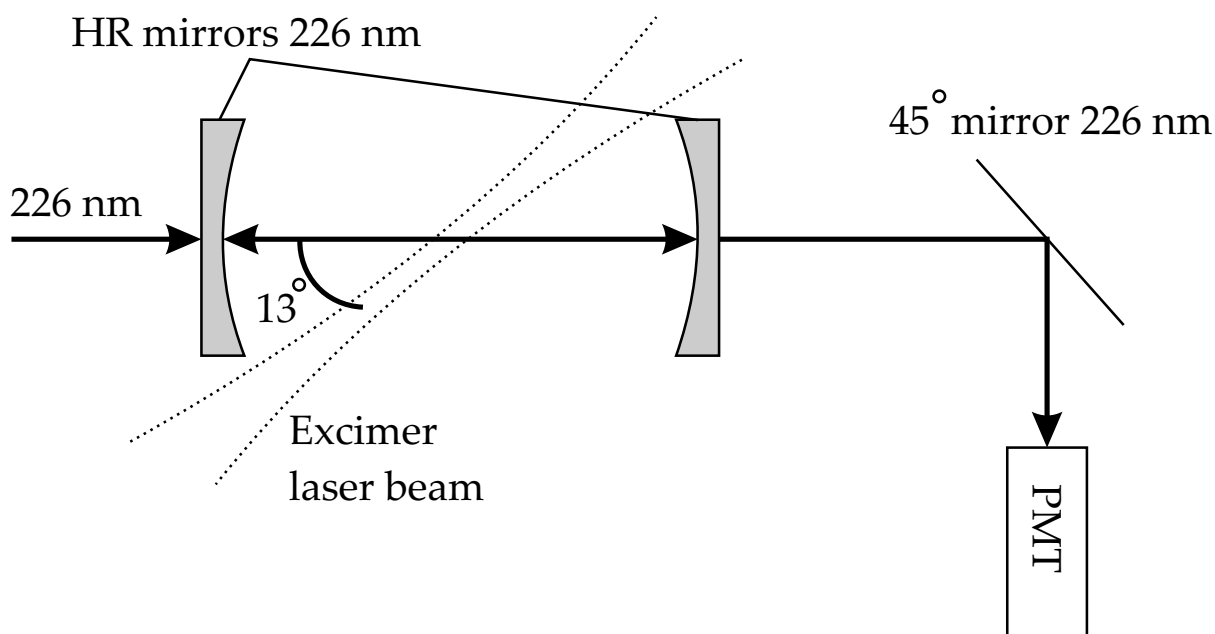
Figure 2.10: *Schematic setup of cavity ringdown experiment. To obtain a maximum overlap an angle of 13° was made between the excimer laser and the dye laser beams. The resulting signal is measured with a photomultiplier tube (PMT).*

with

$$F_B = \frac{2J'' + 1}{Q_e Q_v Q_r} exp(-\frac{hc}{kT} [T_e(e'') + G(v'') + F(J'')])$$ (2.13)

with Q_e, Q_v and Q_r the electronic, vibrational and rotational partition functions and $T_e(e'')$, $G(v'')$ and $F(J'')$ the electronic, vibrational and rotational energy, respectively.

2.5.2   Experimental setup

An optical cavity was set up using high reflectivity mirrors (R>99%) at 226 nm (radius of curvature 250 mm, distance between the mirrors 400 mm). The excimer laser beam was focused in the center of the cavity and propagated into the cavity at a 13° angle with the cavity axis as shown in Fig. 2.10. The probe laser used was a frequency-doubled dye laser (coumarin 47) with an energy of 0.1 mJ/pulse at 226 nm. Because of absorption by ozone in this wavelength range, also created by the excimer laser beam, we had to use a ventilation system in order to remove the created ozone between two pulses and to limit the signal fluctuations due to ozone circulation in the cavity. The detector is a photomultiplier tube connected to a digital oscilloscope (LeCroy 9361).
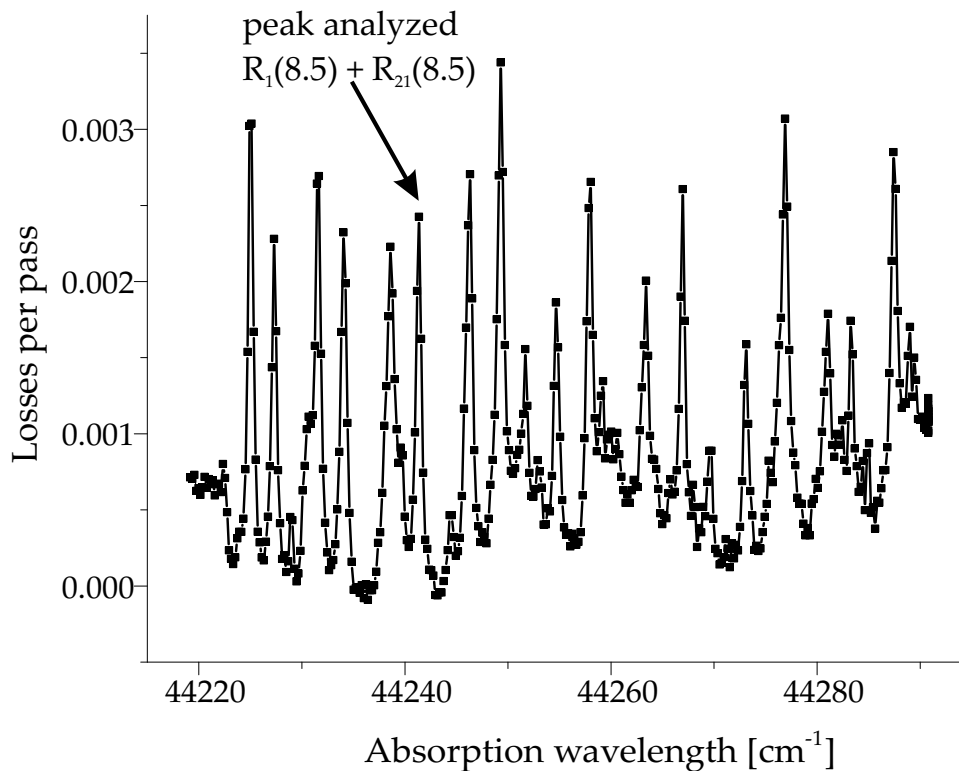
Figure 2.11: *Experimental absorption spectrum of NO 2 μs after creation by a focused ArF excimer laser beam.*

2.5.3   Results

The pulse decay time was recorded as a function of the wavelength in the range 225.7–226.05 nm. The NO absorption spectrum is shown in Fig. 2.11 in terms of the absorption coefficient or losses per pass.

For the determination of the NO density the area of the peak R1(8.5)+R21(8.5) was chosen, which is well isolated. The diameter of the excimer laser beam in the center of the cavity (estimated by calculation to 100 μm) is small compared to the diameter of the dye laser beam (estimated experimentally to 1 mm) and the excimer laser beam is considered to be cylindrical and the intensity uniform where the laser beams overlap. From that, we calculated the absorption path length and obtained $N_{J''}$ from Eq. 2.11. From a comparison of the absorption spectrum with simulated spectra (LIFBASE [12]), the temperature was estimated to be about 300 K. From Eq. 2.12, a value of 5 ppm was obtained at about 50 mJ/pulse of the write laser beam.
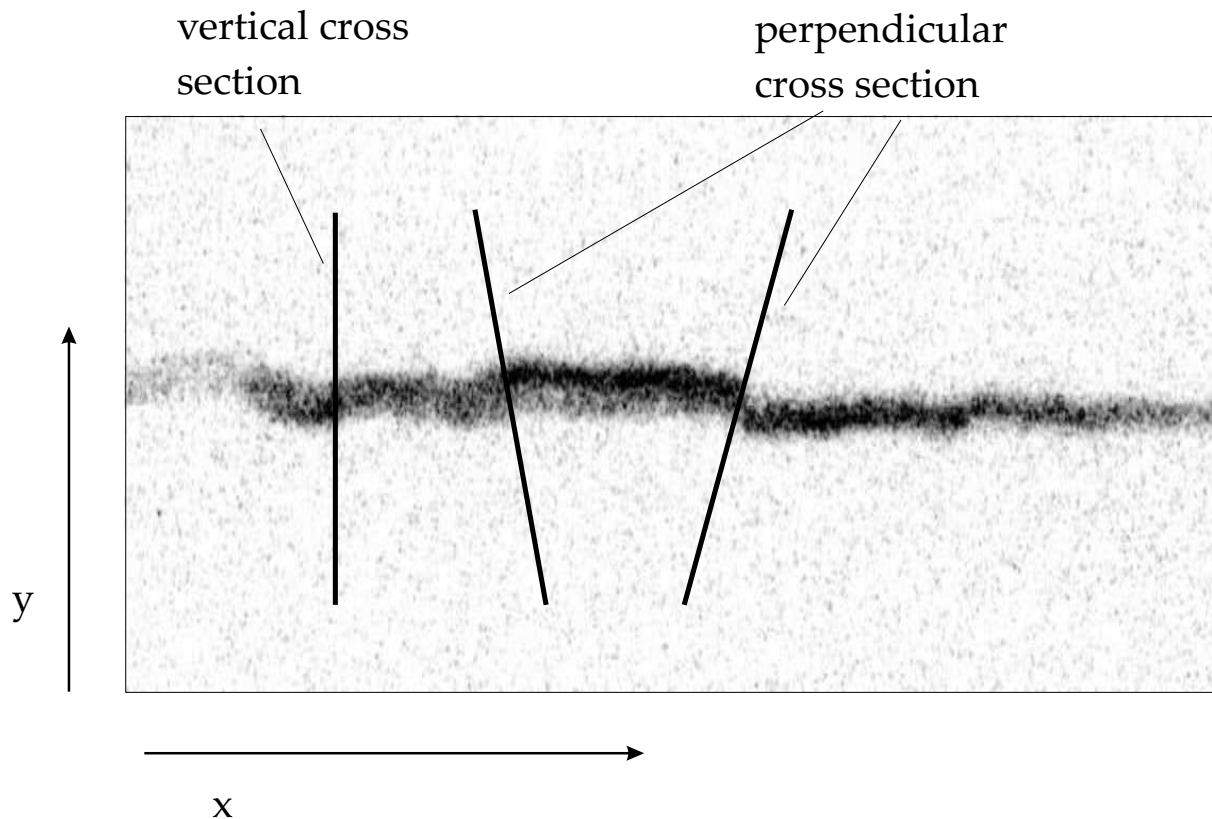
Figure 2.12: *A typical APART image with vertical and perpendicular cross sections used in image analysis. Each vertical column of pixels in the y-direction has an x-coordinate and crosses the written NO line resulting in a Gaussian intensity along the line of the cross section. The perpendicular cross section requires information on the slope of the written line.*

2.6 Data evaluation

2.6.1 Vertical cross sections

In the application of the APART technique we have developed a data analysis technique that may also be interesting for other MTV techniques. In order to extract velocity information from the written lines, the line center has to be determined with a high accuracy. Fitting the data with a profile that matches the distribution can yield sub-pixel accuracy [17]. To this aim, the intensity profile of the line cross section (see Fig. 2.12) was represented by a Gaussian profile whose height, width, and center were adjustable parameters. Since the focal point of the tagging beam lies in the center of the image, the beam diverges toward both sides of the field of view and decreases in intensity. Especially because the NO formation is a non-linear process, this results in a lower signal-to-noise ratio at the image edges. For this reason, fitting is always started in the image center, and is moved toward the edges, while keeping each fit result as starting values for the next

fit. This way, the first line profile has the highest signal-to-noise ratio, and the following ones will start with already fairly accurate initial values. Let us now discuss the algorithm used. If x is the horizontal coordinate and y the vertical coordinate in an image, the Gaussian profile to be fit for each vertical cross-section at x_i is:

$$\bar{I}_i(x_i, y) = a(x_i) + b(x_i)e^{(y-y_c(x_i))^2/\sigma^2(x_i)} \tag{2.14}$$

For lines that are only slightly deformed by turbulence, our results indicate that a line center can be determined with an accuracy of 0.1 pixel. The Gaussian distribution matches the NO profile well.

2.6.2 Perpendicular cross sections

Fits over a vertical cross section only allow for accurate parameter determination if the written line is nearly horizontal. For longer times between tagging and probing line bending can become quite significant and another method of line center determination that is always perpendicular to the local line orientation can be advantageous. The fit data extracted from the vertical cross sections are then used to determine the local slope of the line. The new cross-sections are extracted normal to this slope and the same Gauss fit procedure is applied to these normal cross sections.

2.6.3 Snakes

When the written line wrinkles and folds strongly, vertical cross sections will not work correctly to determine the slope of the written line. Instead of this procedure another fit can be used. This more complicated algorithm is based on a medical imaging technique called "active contour models" or "snakes" [18, 19]. A snake is defined as an energy-minimizing spline. The snake's energy is composed of an external and an internal energy. The internal energy serves as a smoothness constraint to prevent the line from getting big jumps and sharp bends. The external energy is derived from the image. The closer the snake is to the written APART line, the smaller this energy should be. To create this external energy a gradient vector field is calculated from the image [18], where all the vectors should point to high image intensity. To make sure that vectors are placed everywhere in the image, the gradient vectors have to be diffused [20], which means that the vectors spread over the entire image. In this way the capture range of the snake is extended to locations in the image where no gradients exist. An initial horizontal snake is placed in the image and an energy is assigned to it based on its position and shape. The best fit then is the curve with the lowest energy. The minimizaton procedure is performed using Euler-Lagrange equations, as commonly used in analytical mechanics [21].

Chapter 3

APART under Pressure

3.1   Introduction

Measurements of NO creation in high-pressure environments are usually performed in combination with combustion, such as gas turbines and high-pressure flames [22, 23]. Numerical studies on NO at high pressure generally focus on high pressure flames [24, 25]. In 2004 Hällsten *et al.* [26] studied chemical reactions between oxygen and nitrogen at high pressures by irradiation with a proton beam. He studied the optical emission of several NO bands and the oxygen atom to determine reaction characteristics. In other studies the ratio between oxygen and nitrogen concentration was central in determining nitric oxide creation processes in induced discharges [27] and natural discharges [28].

Next to chemical and spectroscopic studies under high pressures it is also important to study flow behavior, since this gives information on the mixing of different species. Turbulence, in particular, is a complex phenomenon to examine even in atmospheric conditions. Also for more fundamental studies, high pressures can aid turbulence studies because pressure, through density, can be used to tune the Reynolds number. This Reynolds number [29] (Re) is a dimensionless quantity, given by

$$Re = \frac{UL}{\nu} \tag{3.1}$$

where ν is the kinematic viscosity and U a scale of the variation of velocity in a length scale L. The kinematic viscosity is dependent on the density and by increasing the pressure of an environment, the Reynolds number will increase via the kinematic viscosity. This way, the inertial range will be stretched, such that interesting phenomena take place in a larger range of scales. The inertial range, is a range of sizes between the integral length scale (the size of the experiment) and the smallest scales at which the energy is dissipated. Increasing the pressure, therefore, may be interesting for studies on the clustering of particles and the spreading of clouds of particles in time.

Non-intrusive optical methods have not extensively been tried in turbulent flows at high pressures, but apart from the larger acceleration of the light-scattering particles, they should work equally well as at ambient pressure. We believe there is no fundamental limitation for the use of APART under high pressures. The applicability of APART at different pressures and gas compositions, was investigated in a high pressure cell, placed
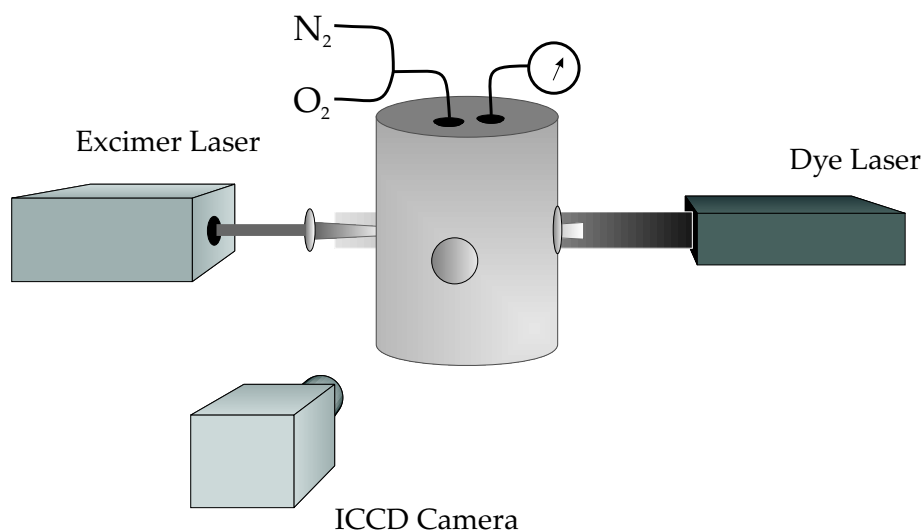
Figure 3.1: *Typical APART setup with high pressure cell in the focus of the write laser. Another window at the back side of the cell allows optical access for a spectrograph (not shown).*

in the focus of the excimer laser beam. For every condition lines of NO were created of which the evolution with respect to intensity and line width was followed in time.

3.2 Experiment

A high pressure cell with four quartz windows is placed in a typical APART setup as shown in Fig. 3.1. The laser beams are directed through two of the windows opposite to each other. The remaining two windows are used to image radiation perpendicular to the laser beams. Two separate sets of experiments have been performed under similar conditions. In the first set, only one ICCD camera imaged the NO line with a filter at 226 nm, where in the second set an ICCD camera images the Rayleigh scattered light from the excimer laser beam, while an ICCD camera mounted on a grating spectrograph monitors the NO fluorescence and the Rayleigh scattering (which can not be separated from the resonant NO LIF at 226 nm) from the dye laser beam simultaneously.

In the first set of experiments the diffusive widening of the written NO line was studied. Experimental complications caused significant intensity fluctuations in both laser beams (as well as wavelength fluctuations due to inconstant locking efficiency of the excimer laser), so it was difficult to compare intensities in different runs. We did, however, monitor the widening of the written NO line in still air with time. For various compositions and pressures from Fig. 3.2 (upper plot) ten images were taken for different delay times.

In the second set of experiments the laser intensities could be maintained at a constant level and monitored precisely. By filling the cell with oxygen and nitrogen from gas bottles (quality: Oxygen 2.5, Nitrogen 2.8) experiments were performed on various gas
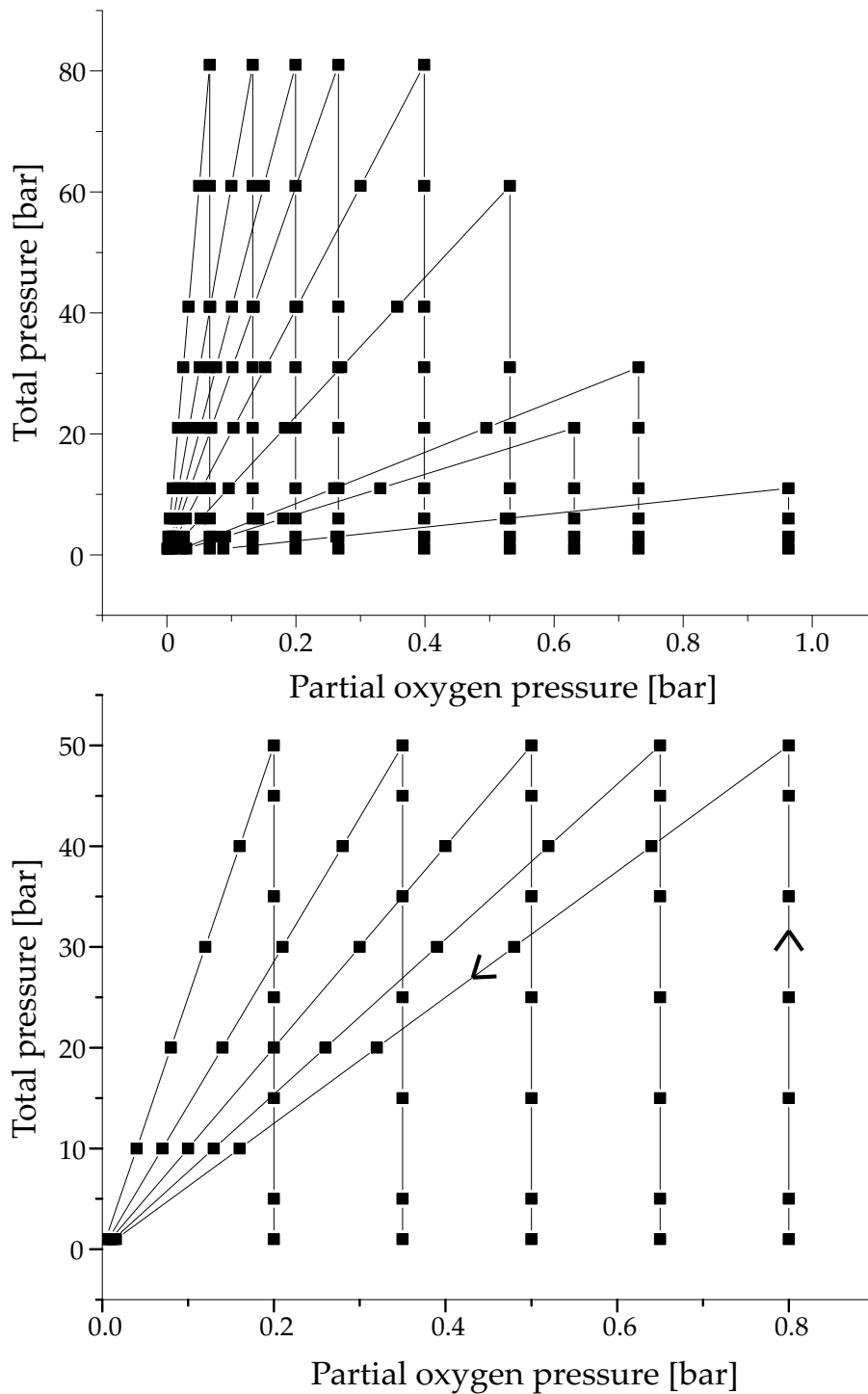
Figure 3.2: *Upper graph: all conditions of total pressure and partial oxygen pressure considered in the first set of this experiment. Lower graph: all conditions of total pressure and partial oxygen pressure considered in the second set of this experiment.*

compositions under many different pressures as given in Fig. 3.2 (lower plot). The difference with the upper plot is that a more uniform distribution of datapoints was taken. Following the arrows in this figure each series of measurements started with the injection of a certain amount of O_2 in the cell after which N_2 was added to reach the desired pressure. After having filled the cell to the maximum pressure, we decreased the pressure by shortly opening a valve to ambient surroundings. For each of the combinations indicated by dots in Fig. 3.2 the NO fluorescence intensity was measured as a function of delay time after creation, ranging from $1\,\mu$s to a maximum of $40\,$ms. The excimer laser beam was focused through a $13\,$cm lens and tuned to a resonance of NO. The dye laser beam was unfocused with a diameter of approximately $5\,$mm and its intensity was kept constant at $7\,$mJ/pulse. One ICCD camera monitored the stability of the excimer laser intensity shot-to-shot during the measurements, while an ICCD camera mounted on a spectrograph monitored the dye laser intensity at $226\,$nm and the NO fluorescence at $237\,$nm and $248\,$nm by accumulating 500 spectra integrated over the written NO line. At every composition and pressure a background image was taken without the excimer laser to check build-up of NO in the cell. This background was subtracted from the data before analysis.

As can be seen from Fig. 3.2 we have only used low absolute oxygen pressures, since previous measurements indicated that at higher partial pressures breakdown can occur, which has to be avoided.

3.3   Results

First set: diffusion

Of the first set of measurements only a few images could be used for analysis. The width of each line was determined as described in Chapter 2, for which a minimum signal-to-noise ratio is necessary. Significant results were obtained by summing the measured ten images, which partially masks fluctuations in the data. In Fig. 3.4 the diffusion rate (D) is presented, calculated from the line width increase

$$\Delta^2(t) = \Delta^2(0) + 4Dt \tag{3.2}$$

against the inverse pressure. The same trend is seen for lines written in environments with different amounts of oxygen. The plot contains both data measured at 0.24% O_2 and 0.49% O_2 in a pure N_2 environment. As expected from kinetic theory estimations [14], there is a linear relation between diffusion and the inverse pressure. From Fig. 3.4 we find a pressure dependency of the diffusion rate of

$$D = 0.37(\pm 0.04) \times 10^{-5} + 2.04(\pm 0.11) \times 10^{-5} p^{-1} \quad \text{m}^2/\text{s} \tag{3.3}$$

with p in bar. This result for the diffusion rate has the same order of magnitude as the value of the NO diffusion rate in plain air which is predicted to be $D_{\text{NO,air}} = 1.8 \times 10^{-5} p^{-1}$ by Elenbaas [14]. However, most striking is the nonzero offset. Probably this offset is caused by an initial increase in temperature with the creation of NO. As can be seen in Fig. 3.5 this effect increases with increasing pressure. This temperature increase is also
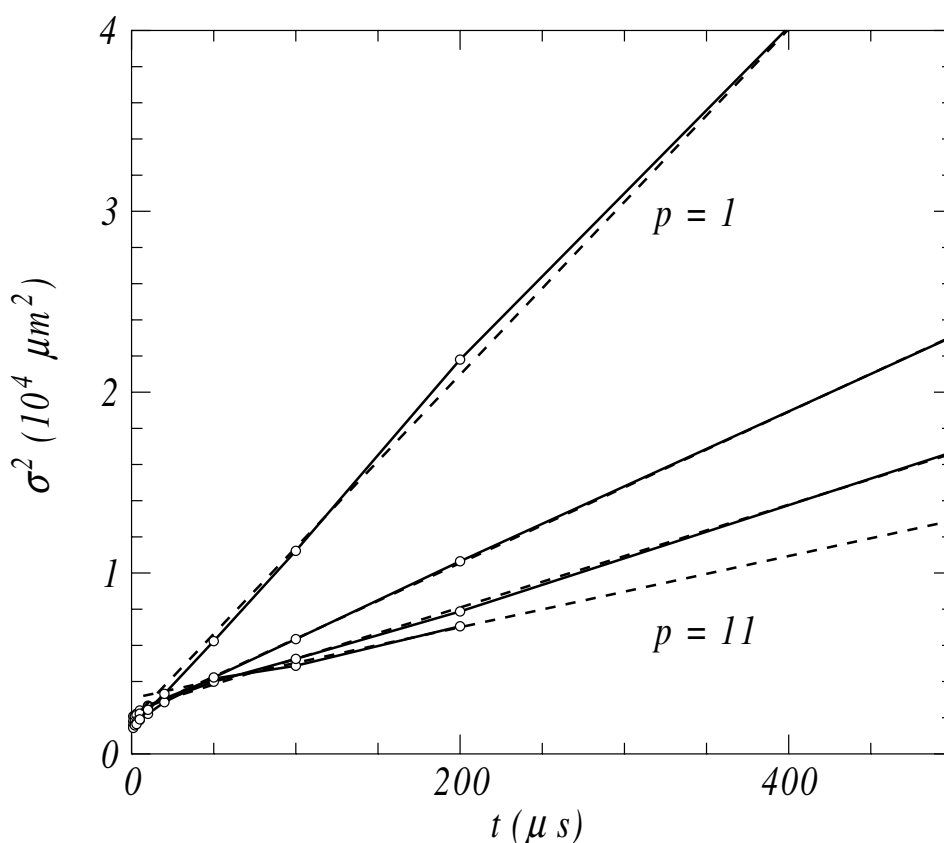
Figure 3.3: *The increase of the width $\sigma^2(t)$ of lines written in a gas mixture with reduced oxygen content at various pressures: from top to bottom, p = 1, 3, 6, and 11 bar, respectively. At the highest pressure (p = 11 bar) the spreading rate is smallest, and σ^2 is clearly nonlinear. The dashed lines are best linear fits $\sigma^2(t) = A + 4Dt$ (see Eq. 3.2), from which the diffusion coefficient D shown in Fig. 3.4 is derived.*

described in Chapter 2.6. The 193 nm write laser beam is very efficiently absorbed by oxygen, which produces oxygen atoms, and converts about 20 % of the absorbed energy into heat. This process is expected to be more significant than the heat production by the creation of vibrationally excited products in the NO formation process.

Second set: Intensity

From the second set of measurements a plot of the NO fluorescence intensity versus delay time for the selected compositions and total pressures is given in Fig. 3.6. The dye laser intensity was kept constant throughout all the measurements. The measured signal was linearly scaled to the excimer laser intensity. A gradual decrease of NO over time is observed, caused by diffusion and convection of NO to lower intensity regions of the dye laser beam and by destruction of NO by radicals. Since the displacement in the typical time frame is only expected to be of the order of several hundreds of microseconds, the diffusion is not expected to play a major role.
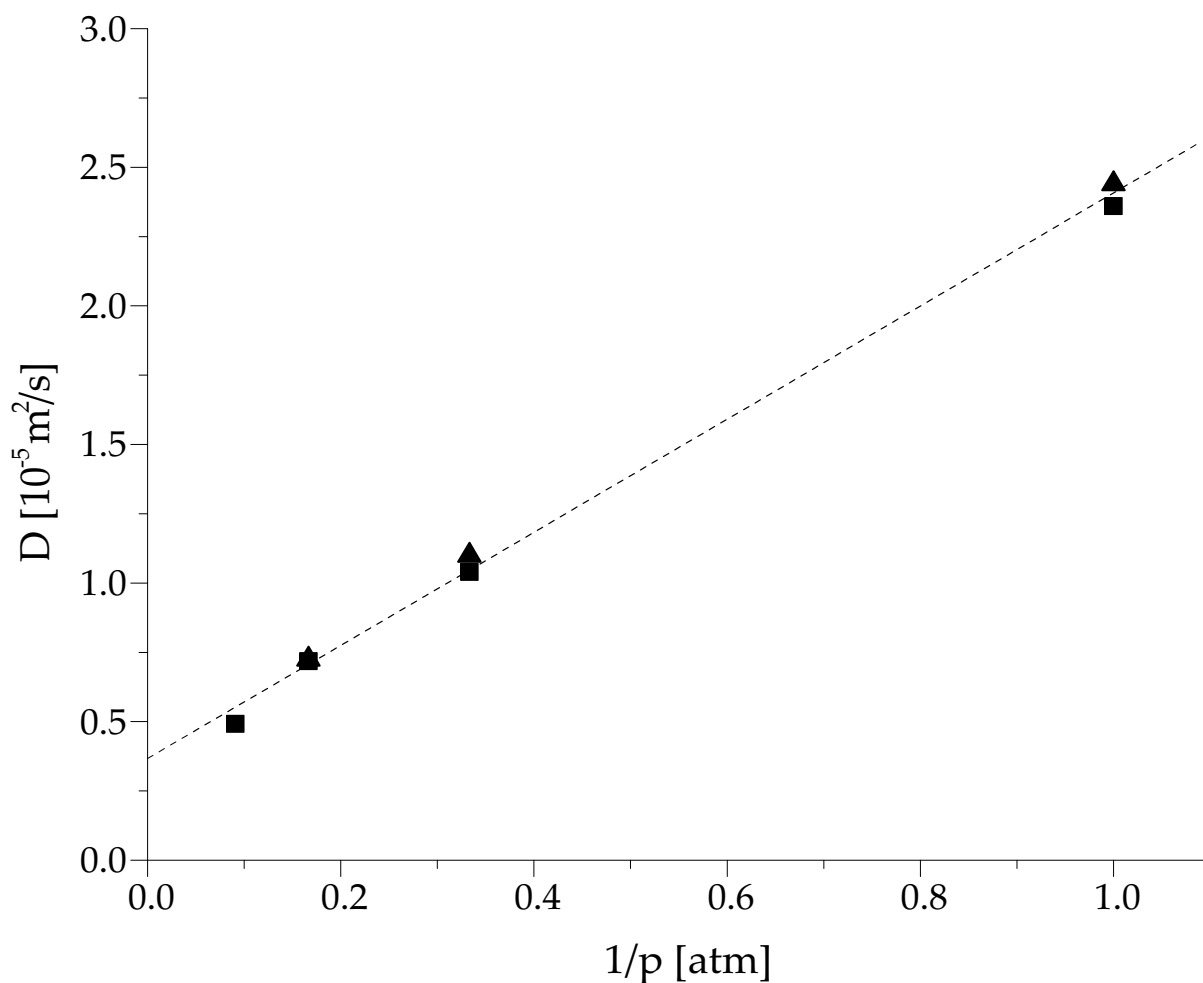
Figure 3.4: *The diffusion rate as a function of inverse pressure. (for both 0.24% O_2 (■) and 0.49% O_2 (▲)). A linear relation is found, as shown by the dashed line. The data are taken with the upper scheme in Fig. 3.2. Only the data that resulted in a signal-to-noise ratio that was high enough to determine the diffusion rate is included in this figure.*

Using the equation for the line widening as a function of delay time (Eq. 3.2) and an initial width $\Delta_0 \approx 100\,\mu$m the time it takes for the created NO line to become thicker than the width of the dye laser beam ($\Delta(t) \approx 5$ mm) can be estimated. This results in a delay time of approximately 300 ms before the NO moves out of the dye laser beam. Since the times used in these experiments never exceeded more than several milliseconds, we can safely assume that no NO has diffused out of the beam. The beam profile, however, was not completely uniform, which might result in lower NO fluorescence intensities when the NO moves to regions with lower laser intensity. Another cause for decreasing NO fluorescence in time is the destruction of NO by created radicals or molecules, such as oxygen and nitrogen atoms and ozone. Nitric oxide is well-known for the destruction of
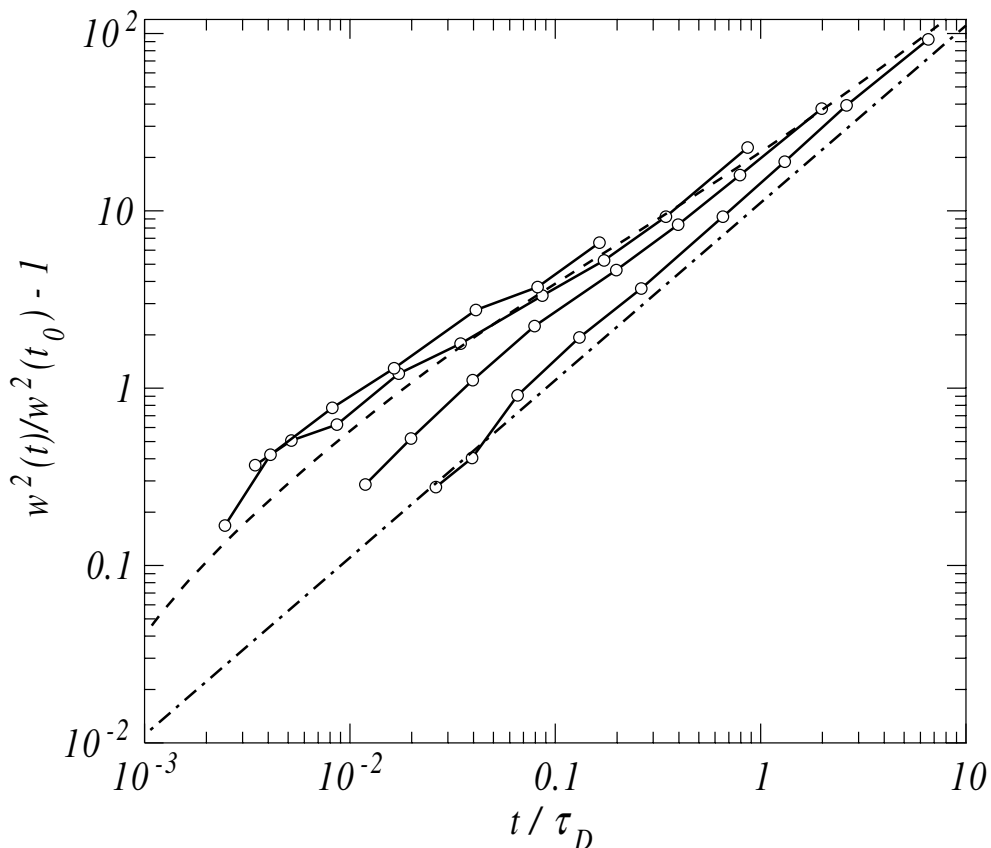
Figure 3.5: *The data of Fig. 3.3, but now plotted in dimensionless units. Dots connected by lines: measured spreading rates of written lines at pressures p = 1, 3, 6, and 11 bar, respectively. The pressure is increasing from the lowest to the highest curve. The experiments were done in an oxygen-poor environment (a mixture of 99.76% N_2 and 0.24% O_2). The time axis is scaled with $\tau_D = p\sigma^2(t_0)/D$. Dashed line: prediction from the model described in [13] for an initial temperature rise $\Delta T = 300$ K. Dash-dotted line: ordinary molecular diffusion, $w^2(t)/w^2(t_0) - 1 = 16\ln 2 t/\tau_D$, where a factor $4\ln 2$ accounts for the ratio between half width w^2 and Gaussian width σ^2.*

ozone via [30, 31]

$$NO + O_3 \rightarrow NO_2 + O_2 \quad . \tag{3.4}$$

This process is partly responsible for the destruction of the ozone layer [32]. Furthermore, we [13] have shown that convection plays a role in the disappearance of NO out of the focus.

Fitting the curves

Almost all the plots resemble a mirrored S-curve. In order to organize the data we fitted an equation of the form

$$I = B + \frac{A}{1 + \exp(C(\Delta t - \tau))} \tag{3.5}$$

35
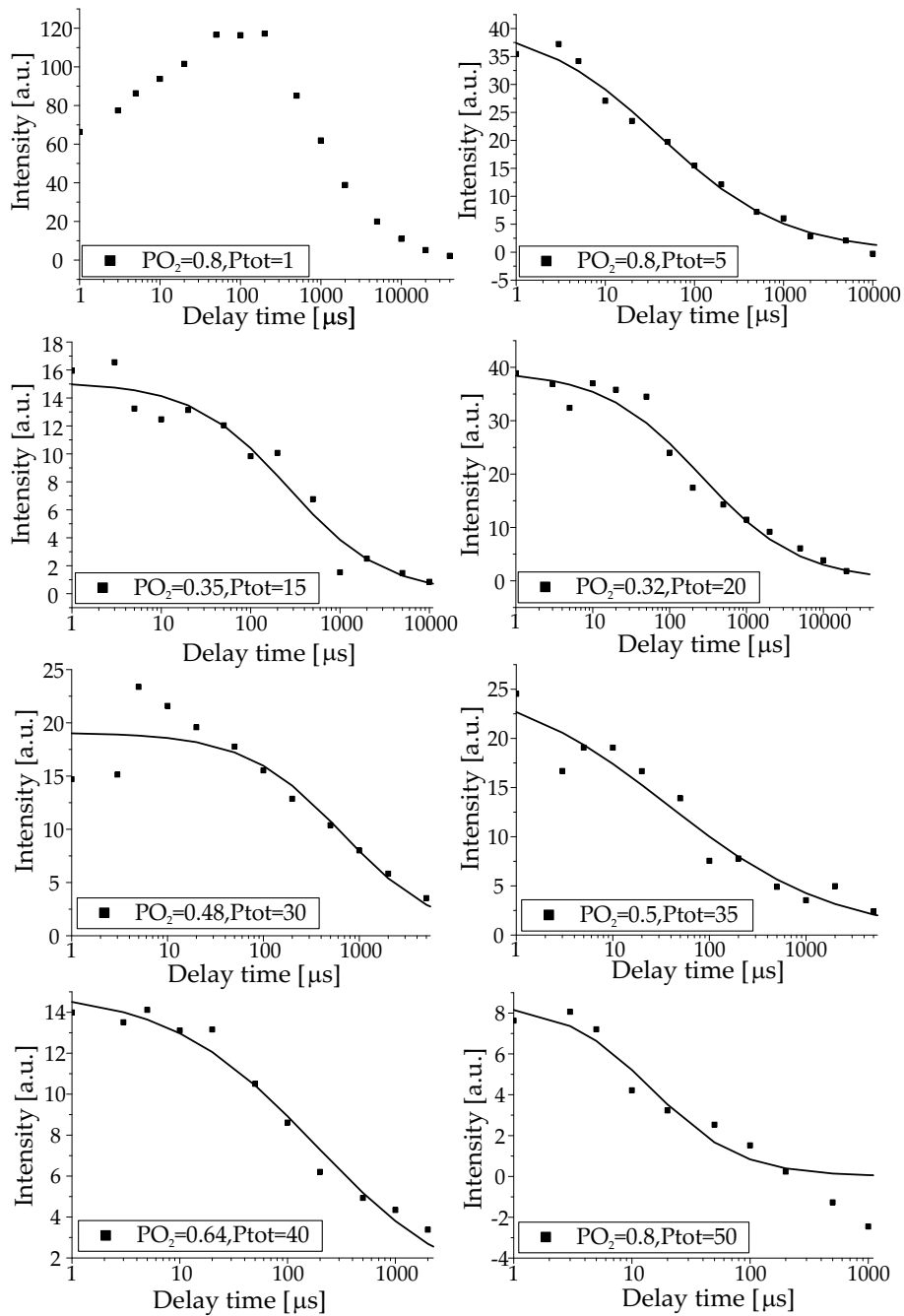
Figure 3.6: *A selection of plots of NO fluorescence intensity as a function of write-read delay time for several gas compositions and total pressures. All graphs have been corrected for background signal, which explains negative values. The solid lines are fits to S-curves (Eq. 3.5). The upper left graph is representative for all graphs at 1 bar where the points increase to a maximum before gradually decreasing. It is impossible to fit an S-curve to these plots.*

to all plots. In this equation, I is the NO fluorescence intensity, Δt the write-read delay time and A, B, C and τ are the fitting parameters. The variable B, which is the intensity at infinite delay time, was set equal to zero, because there should be no NO left at that time. Some of these graphs with fits included can be seen in Fig. 3.6. In a few cases Eq. 3.5 could not fit the data, because there was no unique fit, or the datapoints became negative at longer times. Those plots were not considered in further analysis.

A striking observation are the results for 1 bar. These graphs all have a tendency to rise before decreasing to lower values as can be seen in the first graph in Fig. 3.6. This indicates that the NO formation proceeds for a while after the write laser pulse, possibly driven by diffusion of photochemically synthesized reactive intermediates. It cannot be excluded that at higher pressures this initial increase is also present, but before 1 μs, the shortest delay time in the measurements. At low pressures (≈ 1 bar) the creation of NO is slow enough to be seen in our data. This creation process becomes faster at higher pressures, causing the maximum NO concentration being reached before 1 μs. At longer times a convolution of diffusion, and convection, and possibly the destruction of NO by ozone, oxygen radicals, and other species result in a decrease of the NO signal.

In Fig. 3.7 the half-life parameter τ and the slope parameter C (proportional to the slope at $\Delta t = \tau$) are plotted as a function of total pressure, oxygen pressure and oxygen percentage. The error bars in these graphs are taken from the least-squares curve fit of the S-curve.

Since the data is not evenly spread over the range of the oxygen percentages and there are only a few measurements at high oxygen percentage, we can not give very well supported conclusions on these percentage plots. On most of the plots we have included a linear fit, but it is clear that the spread around the line is relatively large.

With increasing pressure, the destruction of NO is expected not to change, since the reaction rate is proportional to the product of density and diffusion rate ($\sim \rho D$). We have shown before (Eq. 3.3) that $D \sim p^{-1}$ and since the density is proportional to the pressure for an ideal gas ($\rho \sim p$), this means that the reaction rate should be constant. The data, however, show a very small increase of the slope parameter (Fig. 3.7: Panel 1) and a very small decrease of the half-life parameter (Fig. 3.7: Panel 4). These slopes are small, but not insignificant.

With increasing partial oxygen pressure, we expect the energy uptake to be larger and therefore the diffusion to increase. When oxygen absorbs more laser light, more oxygen atoms and ozone molecules are created, which may decrease the amount of NO. However, not much is known about the NO reaction mechanism, which means that it is difficult to draw definite conclusions. Again, there is no clear trend in the data for the slope parameter (Fig. 3.7: Panel 2), which might indicate a balance between production availability and diffusion. The decrease in the half-life parameter with partial oxygen pressure (Fig. 3.7: Panel 5) agrees with our prediction.

When comparing the slope parameter C and the half-life parameter τ, we would expect to find a correlation between the two. This is because when the half-life parameter decreases, this also would mean that the NO concentration goes down faster and the slope parameter is larger. With constant half-life parameter the S-curve will be close to a straight line at a small slope parameter, while the curve will resemble an S-curve for larger slope parameters. Figure 3.8 shows a plot of these two parameters. There appears
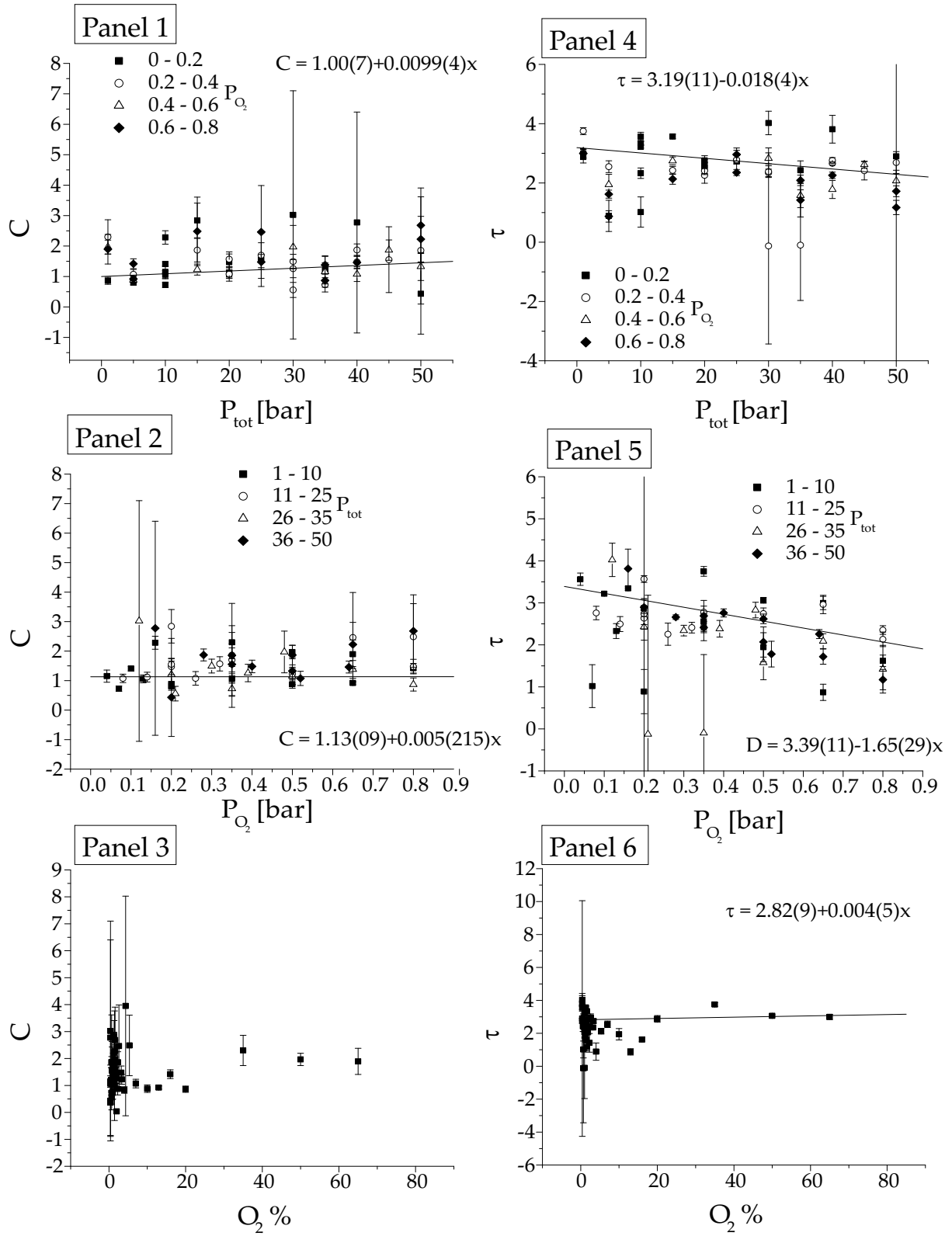
Figure 3.7: *Plots of different relations in the high pressure data. The solid lines are linear weighted fits through all data points. The symbol x stands for the partial oxygen pressure, total pressure, or oxygen percentage. The fit data of the linear fits drawn in each graph are given with an accuracy in parentheses given in final digits (3.39(11) = 3.39 ± 0.11). There is no obvious structure in the positions of partial oxygen pressures or total pressures in these graphs. Panel 1: A plot of the fitted slope parameter of the S-curve (C) as a function of total pressure. Panel 2: A plot of the fitted slope parameter of the S-curve (C) as a function of oxygen pressure. Panel 3: A plot of the fitted slope parameter of the S-curve (C) as a function of oxygen percentage. Panel 4: A plot of the fitted half-life parameter of the S-curve (τ) as a function of total pressure. Panel 5: A plot of the fitted half-life parameter of the S-curve (τ) as a function of oxygen pressure. Panel 6: A plot of the fitted half-life parameter of the S-curve (τ) as a function of oxygen percentage.*
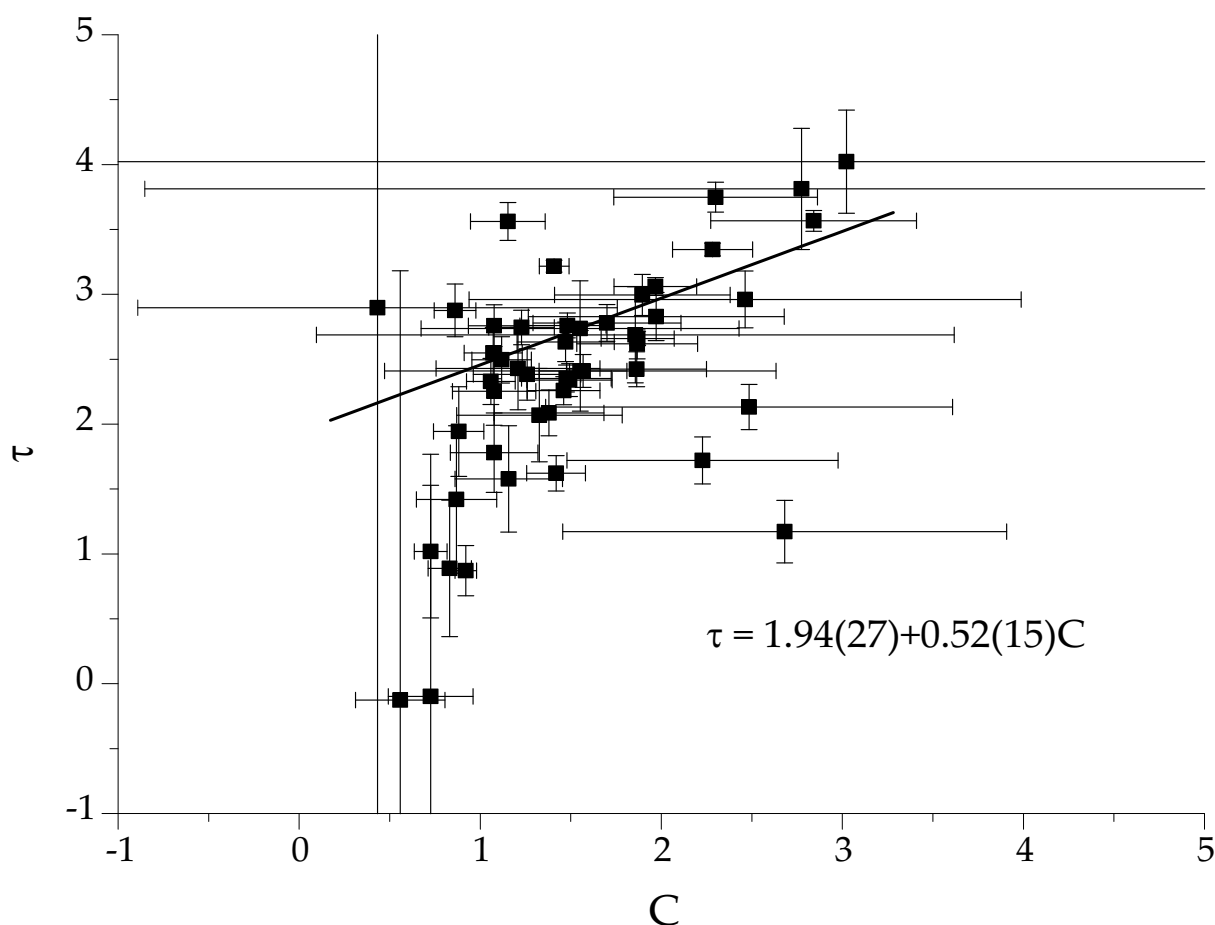
Figure 3.8: *A plot of the fitted half-life parameter of the S-curve (τ) as a function of the fitted slope parameter of the S-curve (C). The solid line is a weighted linear fit through all data points with fit results and accuracy given.*

to be only a weak correlation between the two, since there is a large variation from the weighted linear fit. Probably this is caused by the averaging of the large amount of data.

3.4 Conclusion

We have shown that the diffusion rate increases linearly with inverse pressure. However, the diffusion does not go to zero for infinite pressure, which is probably caused by a laser-induced temperature jump at the moment of writing the NO line.

Interestingly, although the experiment was set up in such a way that diffusion of created NO out of the probe volume should be insignificant, the integrated NO LIF yield was found to decrease with write-read delay time. Other experimental parameters being constant, this decrease in fluorescence yield indicates a decreasing total amount of NO with time, most probably due to reactions. Although NO should, in pure air (only oxygen and nitrogen), be stable on the time scales of the present experiment, the APART process inherently also produces O_3, which can scavenge NO. For practical reasons, the experiments reported in this chapter had to be performed in a closed cell, the contents of which were completely refreshed only once per O_2 concentration cycle (Fig. 3.2).

At short time delays the NO creation process is dominant over the destruction and combined diffusion and convection of NO. This effect is visible in our experiments only at low pressures. At higher pressures the balance between NO creation and removal or destruction is reached sooner in the process. Since our experiments have shown that the expected decrease in diffusion with increasing pressure does not occur, we believe that the destruction process should play the more important role.

In the present data, the most significant effect on the decrease of fluorescence intensity was found in the half-life parameter versus relative oxygen pressure (Fig. 3.7: Panel 5). Here the increase with increasing oxygen pressure is probably caused by convection.

Finally, for practical purposes it can be concluded that writing lines of nitric oxide is feasible up to pressures of at least 50 bar, but that the O_2 concentrations should be reduced relative to those in ambient air, if the total pressure is increased. A next step in the feasibility study would be to measure velocities under high pressures, which should give no fundamental problems.

Chapter 4

APART on Fire

4.1   Introduction

Despite of numerous experimental and theoretical studies, the phenomenon of combustion is still not completely understood, especially if turbulent combustion is concerned. This is mostly due to the combination of complex chemistry, turbulent flow and large temperature and composition gradients. Also in present gas turbine combustion chambers and spark ignition engines there is a very strong interaction between turbulence and chemistry [33]. Due to increasingly stringent emission regulations there is a strong need for cleaner combustion which necessitates fundamental research into turbulent flames. Detailed studies on many types of flames including the flame wrinkling and local heat release and on NO formation in a flame have been reported (see for instance [34–36]). These experiments are mainly used to (in)validate chemical models and fluid flow simulations. The complex nature of these turbulent flames makes it practically impossible to simulate the complete flame from first principles, and filters and approximations are necessary [37].

The main types of flow models used in simulating flames are Large Eddy Simulations (LES) [38, 39] and the more detailed Direct Numerical Simulation (DNS) [40], where the latter takes the most computing power. However, with the increasingly powerful computers nowadays, the use of DNS will become more widespread [41]. An interesting overview of modelling in turbulent combustion is given by Peters [42].

Experimentally many techniques are used. Where it is relatively easy to apply LDA [43] and hotwire [44] techniques when no combustion is present, the seeding of a burning flow needs careful consideration and hotwire does not work in combustion at all. Small Al_2O_3 spheres are the particles most used in present PIV [35, 45] and LDA [46] setups, but oil drops [47] are also possible, albeit without combustion. Besides measuring turbulence characteristics it is also important to get parameters on the chemical process such as species concentrations and temperature. Several molecules can be detected simultaneously with the flow velocity such as OH [48], CH [47] and NO [34]. Other optical techniques include Coherent Anti-Stokes Raman Spectroscopy (CARS) [49], spontaneous Raman scattering and Rayleigh scattering [50].

Combustion requires mixing of fuel and oxidizers. Mixing is enhanced by turbulence, and this establishes the connection between chemistry and the small flow scales. It is,

therefore, of interest to investigate the applicability of APART to turbulent flames. In principle, since APART requires only N_2 and O_2 for tracer NO creation, no limitations are expected in fuel-air mixtures. On the other hand, the energy input associated with the write process might locally affect the flame. In the burned and burning gas, furthermore, the O_2 is depleted, so any laser-induced NO formation might be expected to follow a different pathway through, for instance, CO_2 [51]. (But, of course, the burned gas is less interesting from the point of view of flame chemistry.)

The experiments described in this chapter were performed on a premixed turbulent flame burner from the Institut de Combustion, Aérothermique, Réactivité et Environnement of the Université d'Orléans, the flow field of which has previously been characterized by Laser Doppler Anemometry (LDA) [43,52].

4.2   Setup

A pilot measurement was first performed in a premixed laminar flame burner (Fig. 2.5), where we measured the velocity of the gas at 13 mm above the burner exit, in the burned gas. The gas flow was set at 24 cm/s and a line of NO was written and detected at several delay times. Subsequently, we strongly increased the gas flow to apply APART in the burning part.

A second series of measurements was performed, using a different, turbulent flame burner (see Fig. 2.6). The turbulent flame was operated at a stoichiometry of 0.7; methane was set at a flow of 0.2 l/min and air at a flow of 2.8 l/min for the pilot flame and for the main flame methane was set at a flow of 4.6 l/min and air at a flow of 63 l/min. This gives a very light blue flame with a height of 8 to 10 cm. The pilot flame front is a horizontal ring a few millimeters above the base of the burner and it ignites and stabilizes the main flame. The average initial velocity of the flame is 2.3 m/s [43]. The grid that was used for turbulence generation in the main flow has hole diameters of 2.5 mm. Mass flow controllers (Bronkhorst HI-TEC) were used to control the amount of air and fuel through the burner.

Measurements of the second series were taken in three different sessions. In the first session we applied APART at three different heights in the flow:

- 5 mm above the burner exit,

- 40 mm above the burner exit, in the burning, blue-colored part of the flame and

- 75 mm above the burner exit,

all centered above the burner exit. In the second session we measured approximately 5 mm above the burner exit, but a lens was used with a longer focal distance to increase line lengths. In the final session qualitative measurements were performed on the correlation between line length and flame structure by simultaneously imaging the created NO LIF and the natural emission of the flame (for optical equipment used in this experiment see Chapter 2).

It was difficult to determine the exact position of combustion, because of the strong fluctuations of the balloon-shaped flame front, inside of which no combustion is present,
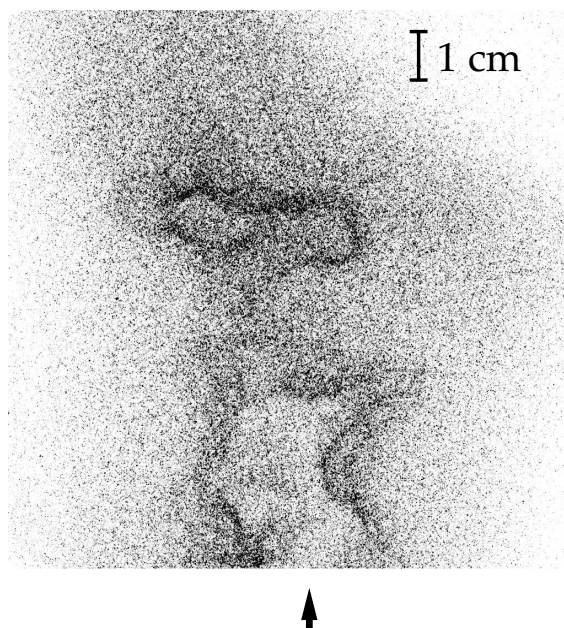
Figure 4.1: *Typical OH natural emission picture of the turbulent flame, showing the "balloon" shape of the flame front. The arrow indicates the position of the burner exit.*

as shown in Fig. 4.1. The experiments from which we extracted average and *rms* velocities did not suffer from these fluctuations since we did not measure close enough to the flame front, but completely inside the "balloon".

4.3 Results

4.3.1 The flat flame burner

Figure 4.2 shows pictures taken in the laminar stoichiometric, premixed flame. The images at a delay time of 1 and $10\,\mu$s are accumulations of 10 shots, while the other two are accumulations of 50 shots. The line position increases in height with time as does the line width. Gaussian fits were applied through line profiles perpendicular to the written NO line and from the fit parameters a vertical position was deduced. Figure 4.3 displays the line center positions and the applied linear fit. From this fit the average velocity was calculated to be $2.886 \pm 0.033\,$m/s. Note that, even though the flame produces NO by itself, the written line is well distinguishable. As compared to measurements in ambient air, however, the signal-to-noise ratio in the post-combustion gas is lower (by a factor of ≈ 15).

By changing the gas flow we could produce a flame with a jagged flame front, stabilized on only a few points at the burner surface. Thus, the write laser beam could be directed to pass through both burned and unburned gas, crossing the flame front within
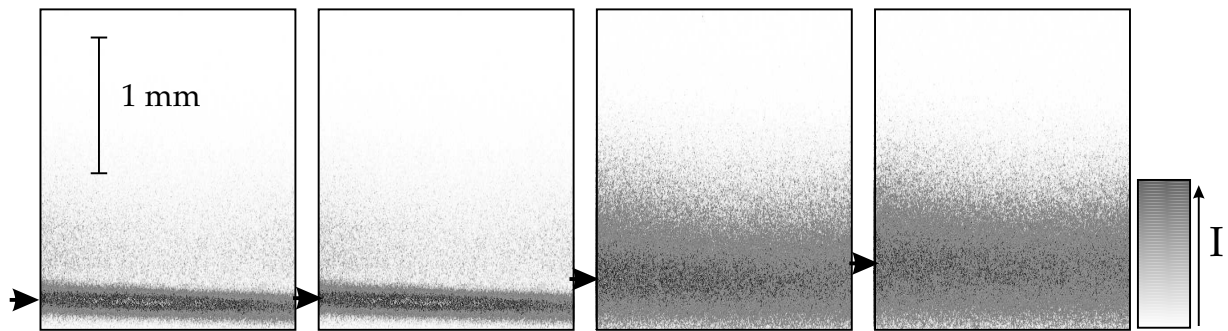
Figure 4.2: *Consecutive images of APART above the laminar flame burner at delay times of 1 μs, 10 μs, 50 μs and 100 μs (from left to right). The arrows indicate the centers of the NO fluorescence signal and the gray scale is a linear measure for the fluorescence intensity (I). The images at a delay time of 1 and 10 μs are accumulations of 10 shots, while the other two are accumulations of 50 shots, which explains the strong difference in width.*

the field of view. Figure 4.4 shows that the flame front puts limits on the imaging of NO. Apparently, whereas NO is created both in burned and unburned gas, the process is so much more efficient in the latter, that it is difficult to visualize both simultaneously. The conditions under which the images of Fig. 4.4 were recorded were, unfortunately, set such that the energy input in the unburned gas was high enough to locally ignite the flame, producing a roughly spherical propagating flame front. In practice, this (undesired) side effect can be avoided by reducing the write laser power. No velocities were extracted from Fig. 4.4.

4.3.2 The turbulent flame burner

Figures 4.5, 4.6 and 4.7 show histograms of all measured velocities in the turbulent flame for the probe heights of 5 mm, 40 mm and 75 mm above the burner exit, respectively, and at each height for all set delays. The measured lines were analyzed by acquiring the position of every point on the written APART line and extracting a velocity by comparing to

Table 4.1: *Measured average velocities ($\langle U \rangle$) and velocity fluctuations (u_{rms}) for different positions in the flame. The average velocities are calculated from histograms of velocities for each delay after which the average for all delays was taken. The rms velocities are calculated from the deviation of every point on every line in all images from the average velocities. The given values and inaccuracies are still correlated, since the data from every point on the line was used.*

height [mm]	$\langle U \rangle$ [m/s] $\pm$ SD	u_{rms} [m/s] $\pm$ SD
5	2.83 $\pm$ 0.13	0.21 $\pm$ 0.04
40	3.03 $\pm$ 0.14	0.20 $\pm$ 0.04
75	3.55 $\pm$ 0.29	0.42 $\pm$ 0.16
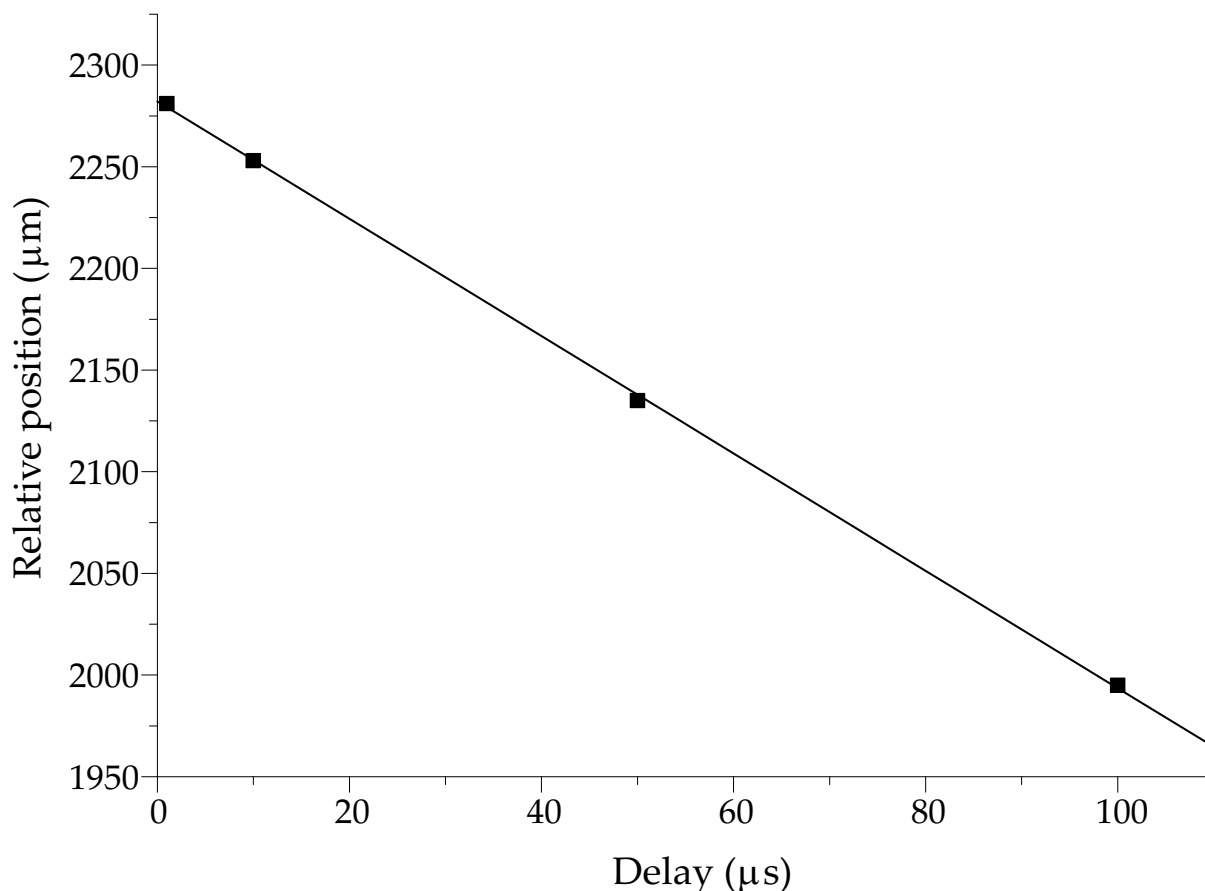
Figure 4.3: *Fit line centers for each time delay. The linear fit results in a velocity of 2.886±0.033 m/s.*

the line at zero delay. Then every velocity on each of the 270 points in the APART line for all the 1000 images taken was put in a histogram. This resulted in a histogram consisting of 270,000 data points per histogram. The resulting average velocities and *rms* velocities are given in Table 4.1. It is clear that there are large discrepancies between histograms at one height but with different delay times. The difference in intensity is easily explained by the instability of the laser over time and varying settings of the flow controllers, which had to be reset manually several times during experiments. The fluctuating intensity is not critical in determining velocities. The differences in width and peak position are probably due to low signal-to-noise ratios, resulting in different accuracies for different measurement settings. The measured low velocities correspond to small displacements in the image causing relatively large uncertainties in determining exact line centers. At a time delay of $700\,\mu s$, for instance, the displacement of the line corresponds to a shift of 40 pixels, where the line width is approximately 10 pixels. The *rms* velocity is even determined from deviations in the order of 4 pixels.

Figure 4.8 shows a comparison between LDA measurements performed on this burner [43] and the present APART measurements. Unfortunately, the two measurements can
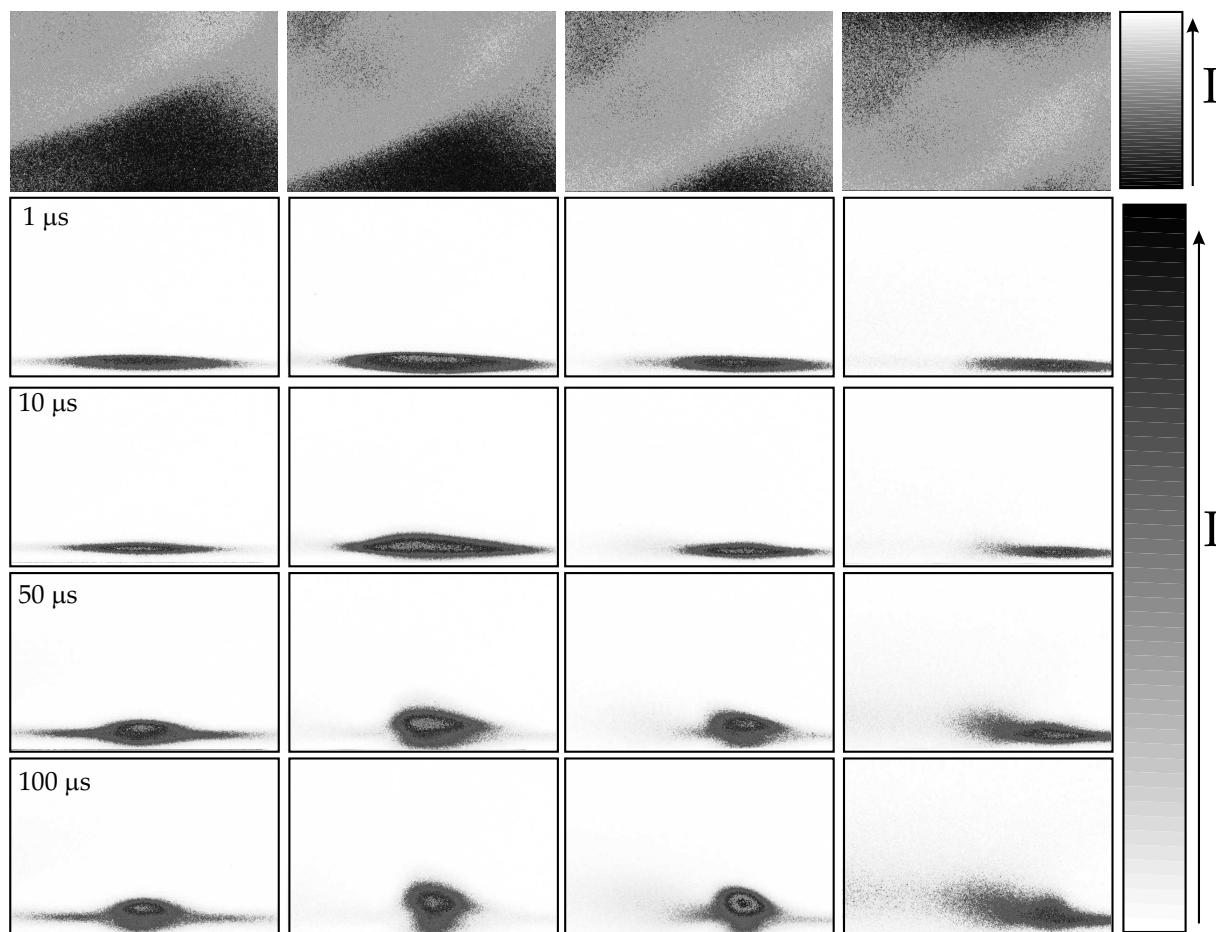
Figure 4.4: *APART pictures in the burning part of the flame at several delay times and gas flows. The four upper pictures show the natural emission from the flame where a lighter part represents the burning gas. The pictures at 1 and 10 µs were an accumulation of ten laser shots and at 50 and 100 µs an accumulation of fifty shots. From left to right, the flow was decreased such that the flame became more stable and APART was applied more in the flame front. From the pictures on the right it can be seen that it is difficult to image NO in the flame front. The "blobs" at longer delay times indicate the local ignition of the flame by the excimer laser. The widening in the middle of the line at shorter time delays is a typical feature of APART, possibly caused by local heating. The gray scales are a linear indication for the fluorescence intensities (I). To increase the contrast for the upper pictures, the scale is reversed.*

Figure 4.5: *Velocity probability density functions at 5 mm height above the burner exit for various delays between writing and reading the NO line. The histograms are composed of 1000 images per delay with approximately 270 velocities per image, the number of vertical strips per image containing NO fluorescence from the created line. The inset shows a typical single-shot APART image in a flame. The encompassing flame front lies outside this image.*

only be compared qualitatively, because of uncertainties in the mass flow controller calibration and the use of different flow controllers. Shortly after calibration, a mass flow controller will start to shift significantly from its calibration. The experiments were performed some time after the calibration and at the moment this was discovered, too much time had past since the measurements to perform a calibration to compare. Both measurements, however, show the same trend of increasing velocity with axial distance. The APART velocities, however, increase significantly more with height, which may be explained by the use of different equipment. Another explanation may be that the ventilation suspended above the burner was extracting air at such velocities that it interfered with the flame characteristics.

By using a lens with a larger focal distance we recorded results of velocities at 5 mm
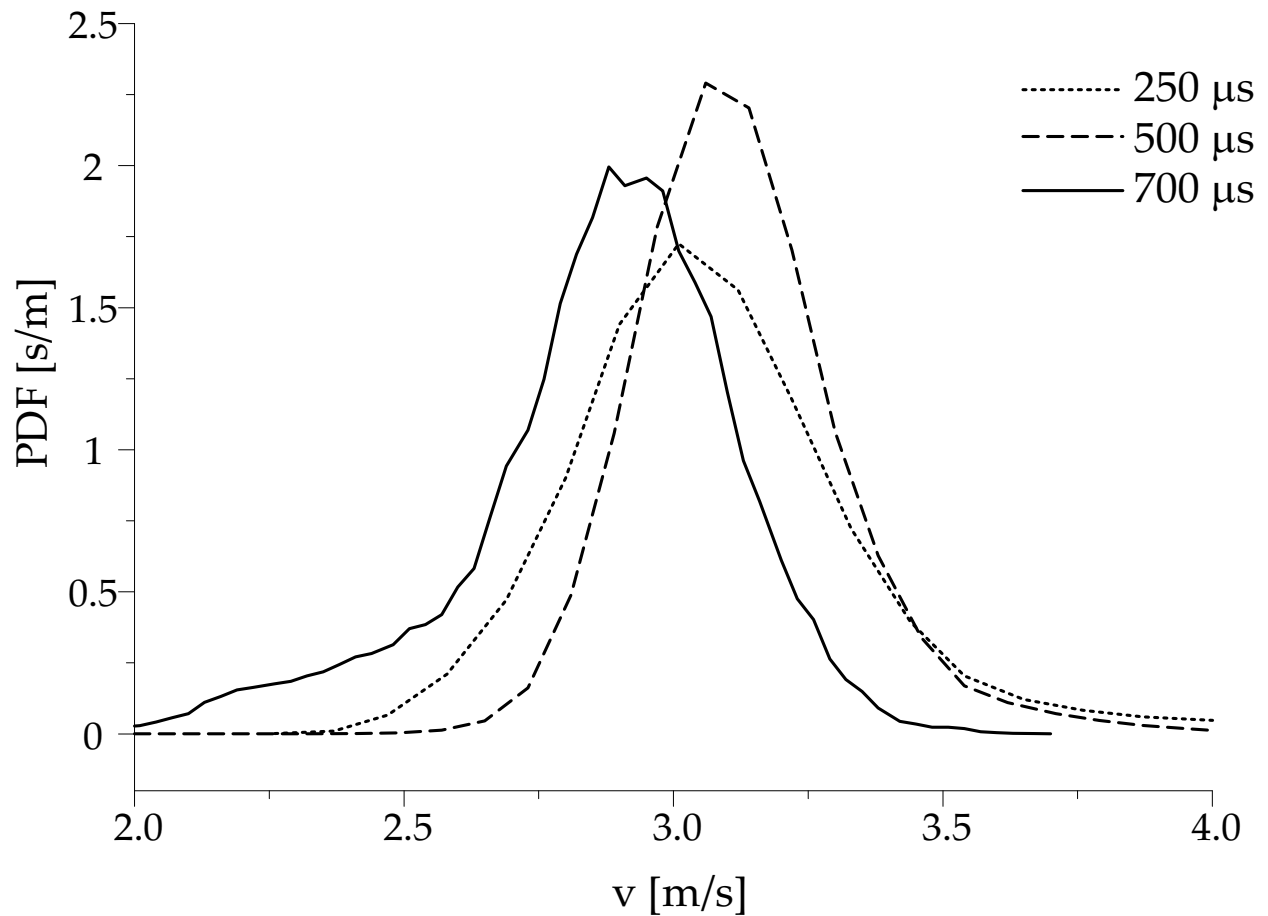
Figure 4.6: *Velocity probability density functions at 40 mm height above the burner exit for all delays between writing and reading the NO line. The histograms are composed of 1000 images per delay with approximately 270 velocities per image, the number of vertical strips per image containing NO fluorescence from the created line.*

above the burner exit along a line that spans a larger part of the flow. Figure 4.9 shows the measured mean and *rms* velocities for different delay times. The mean velocities do not differ for different delay times. At 400 μs, however, the global line lies lower, possibly due to a different flow setting or a velocity gradient in the examined region. The displacement of the written NO lines at 400 μs corresponds to 25 pixels on the detector. This amount increases with increasing delay time, thereby increasing the effective resolution. This resolution can be increased by zooming in on the lines. The intention in these measurements, however, was to image longer lines. The relative displacements (between the line written at 0 μs and the one visualized at a later time) depicted in Fig. 4.9 correspond to only 3 pixels at a delay time of 400 μs. This explains the large amount of noise in the lines.

When we assume that the intensity of the NO line as a function of position (x) is given
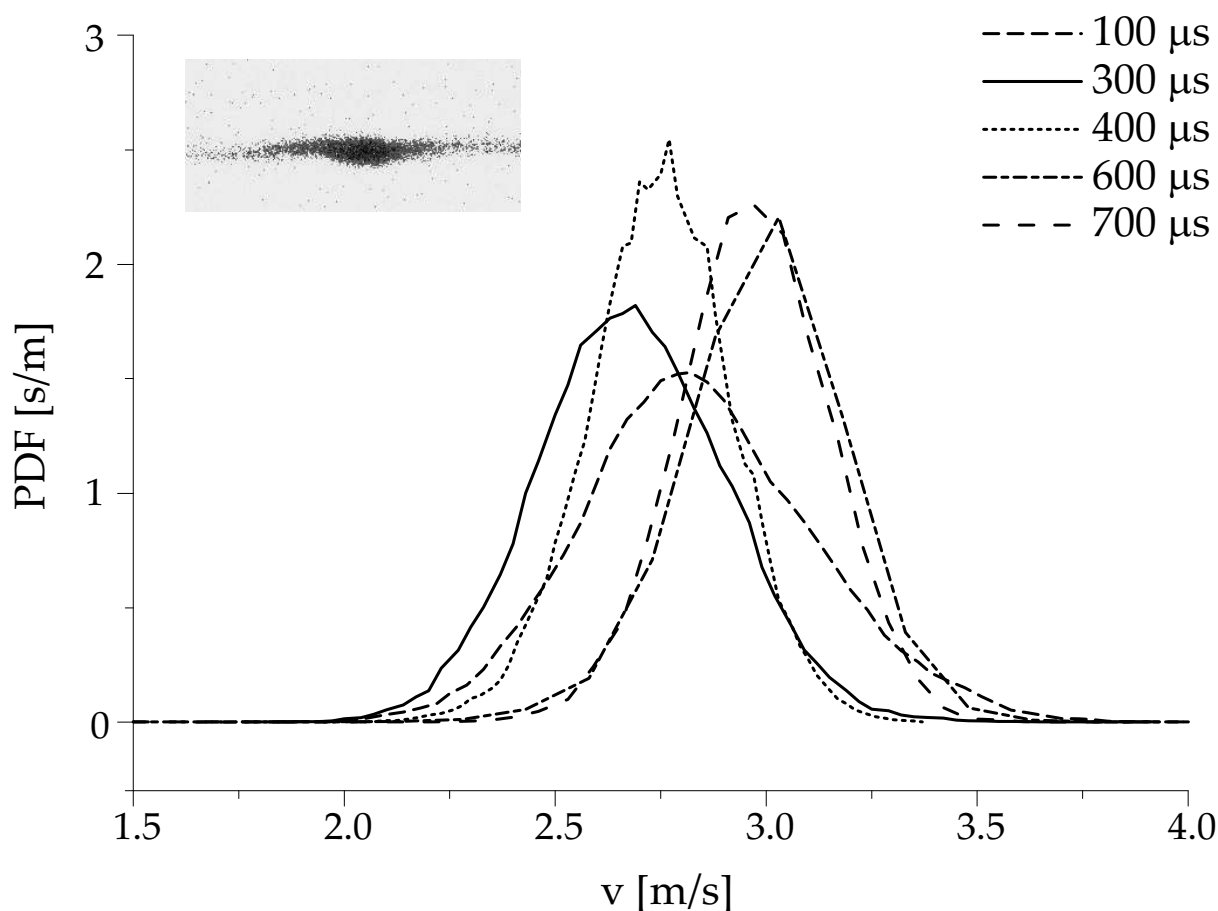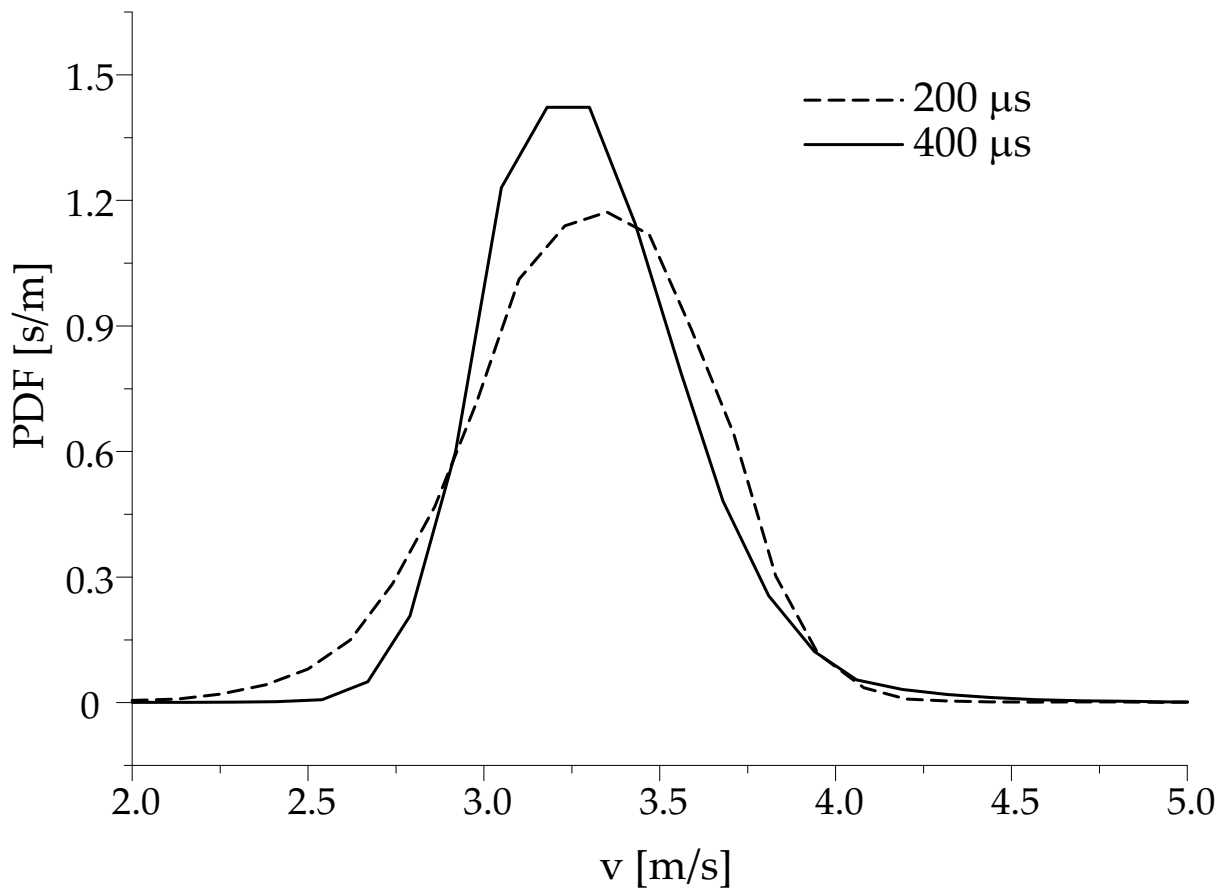
Figure 4.7: *Velocity probability density functions at 75 mm height above the burner exit for all delays between writing and reading the NO line. The histograms are composed of 1000 images per delay with approximately 270 velocities per image, the number of vertical strips per image containing NO fluorescence from the created line.*

by

$$I(t) \sim e^{-\frac{x^2}{\sigma^2(T)}} \tag{4.1}$$

where T is the delay time, $x=0$ corresponds to the center of the line and σ is the width of the line related to the diffusion constant D according to Eq. 3.2, the diffusion constant can be obtained by measuring the line width as a function of delay time. This plot is shown in Fig. 4.10, from which we extracted $D = 1.9 \pm 0.2 \cdot 10^{-5}\,\mathrm{m^2/s}$. This value is very close to the diffusion constant of air at room temperature (nominally $1.8 \cdot 10^{-5}\,\mathrm{m^2/s}$), which indicates that we have indeed not measured in the burned gas itself, but most likely in the pre-combustion area, as in the case of the laminar flame (Fig. 4.4). There is hardly any influence of a larger amount of methane compared to normal air, since the diffusion constant of methane in air is $1.96 \cdot 10^{-5}\,\mathrm{m^2/s}$ [53]. The diffusion constant depends mainly on temperature and pressure.

APART measurements were also performed in the upper part of the flame (approx-
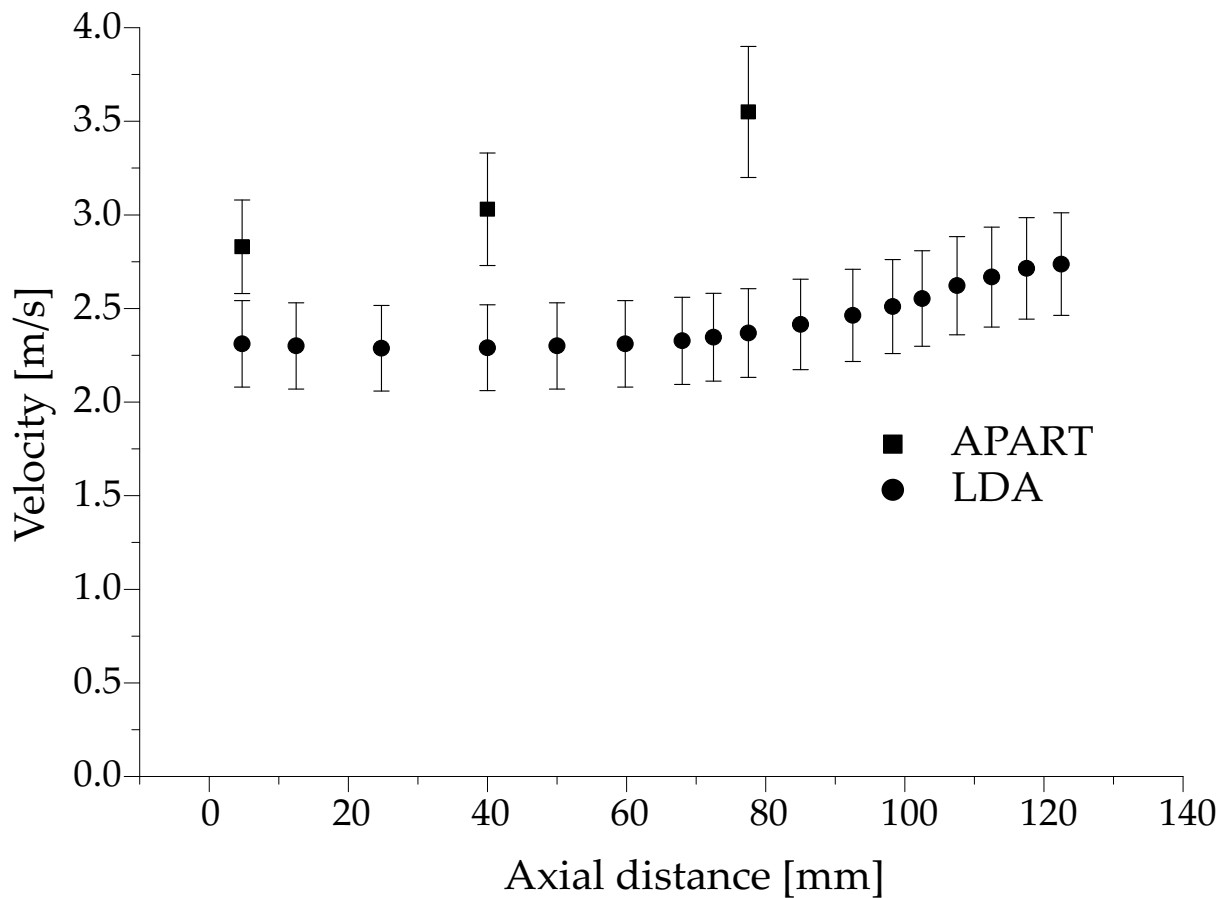
Figure 4.8: *Comparison between LDA and APART measurements performed on the flame at 5 mm above the burner using different flow controllers.*

imately 10 cm above the burner exit). It turned out that it was extremely difficult to write uniform NO lines. The NO intensity fluctuated from left to right, as can be seen in Fig. 4.11. This seems to be correlated to fluctuations of the flame front. Wavelength-resolved measurements at 308 nm showed that the emitted radiation is due to excited OH radicals, the fluorescence of which approximately indicates the position of the flame front. This flame front seems to act as a natural boundary for the laser-induced creation of NO, where the NO can only be created in the inner part of the flame, where the methane/air mixture is not burning. Outside of this flame front there is probably not enough oxygen present to induce NO creation. The images show that due to the turbulent character of the flame front, creation and imaging of NO does not result in line lengths that are reproducible so that averaging for improved signal-to-noise ratio is not possible as well as single-shot analysis.
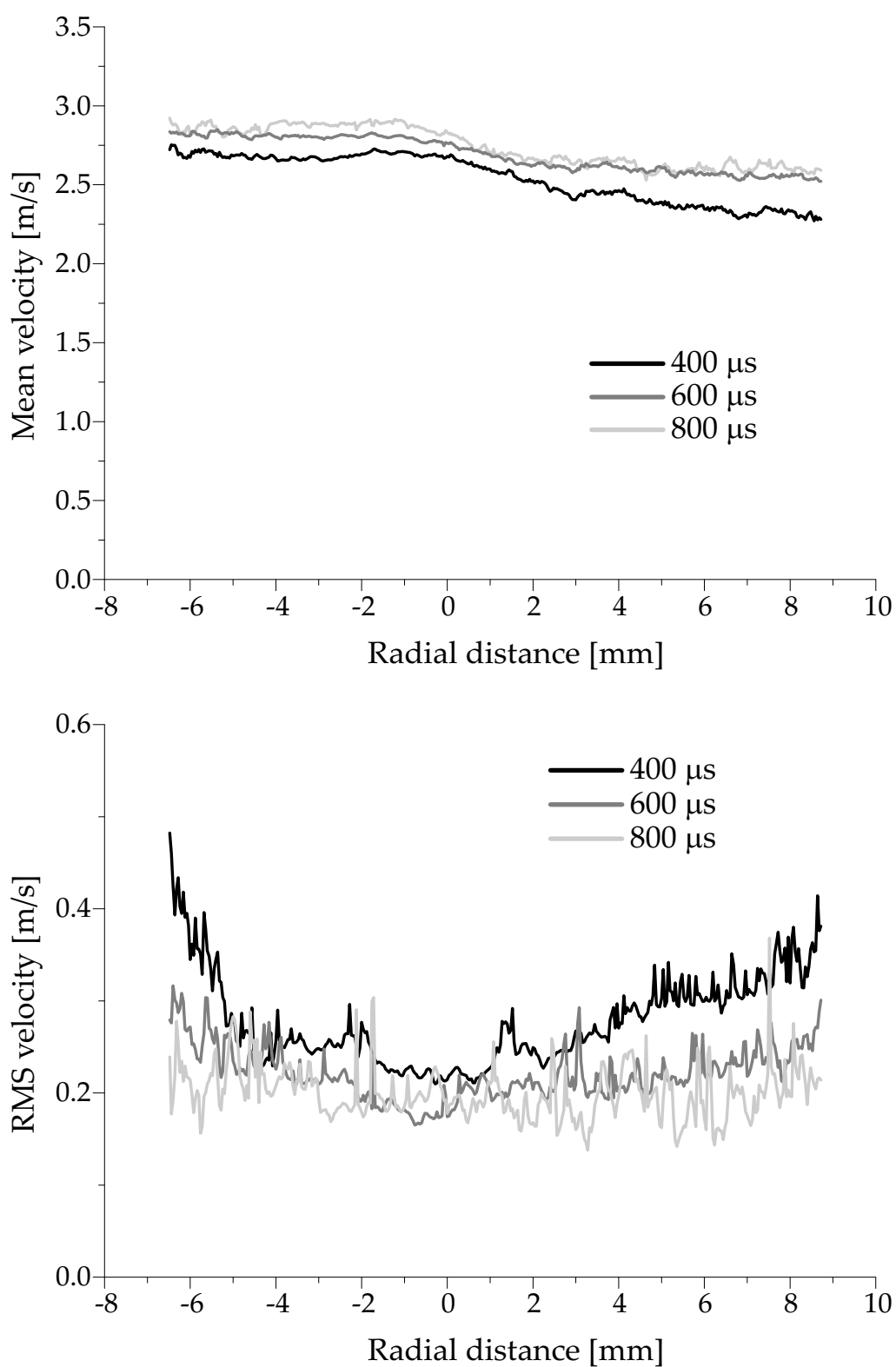
Figure 4.9: *Mean (top graph) and rms velocities (bottom graph) in the turbulent flame over a total width of 15 mm.*
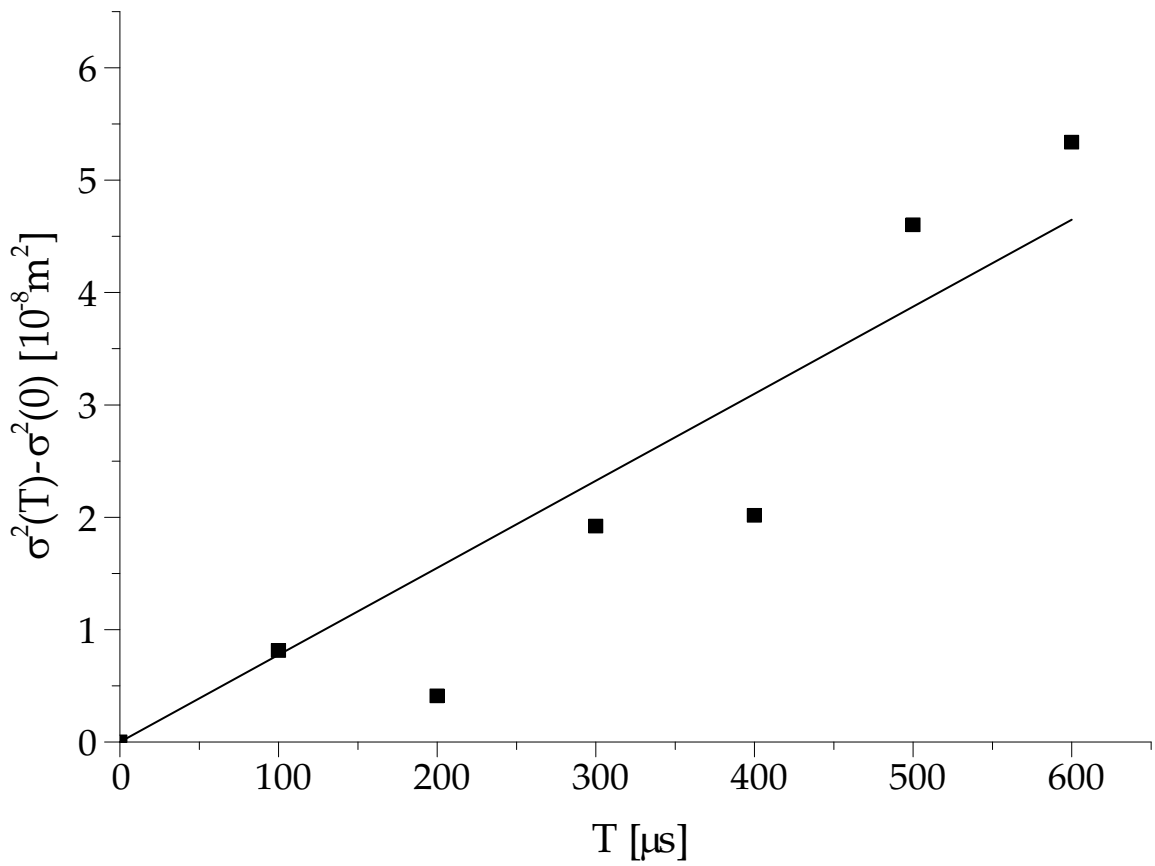
Figure 4.10: *Squared width (corrected for width at $t = 0\,\mu s$) as a function of delay time. A linear fit was applied to the data points resulting in a diffusion constant of $D = 1.9 \pm 0.2$ $\cdot10^{-5}\,m^2/s$.*

4.4   Conclusion

We have shown that it is possible to perform velocity measurements in at least the unburned part of a premixed methane/air flame. Although NO is photosynthesized by the write laser in the post-combustion gas as well, this process appears to be considerably less efficient than that in the unburned mixture. It was found that the flame front (as visualized by spontaneous OH fluorescence) forms a practical boundary for the extent of the NO line written by APART. Outside the flame front there is not enough oxygen available to form NO. No experiments have been performed in a lean combustion environment.

Many studies reported in literature concern numerical simulations of various types of combustion. Most of the experimental studies aim at the simultaneous detection of many different parameters, like temperature, chemical composition, velocity and turbulence characteristics. To measure temperature and composition, spectroscopic techniques such as LIF, Raman and Rayleigh imaging are used. Unfortunately, the inclusion of APART in measuring flame velocities has proven to be difficult.
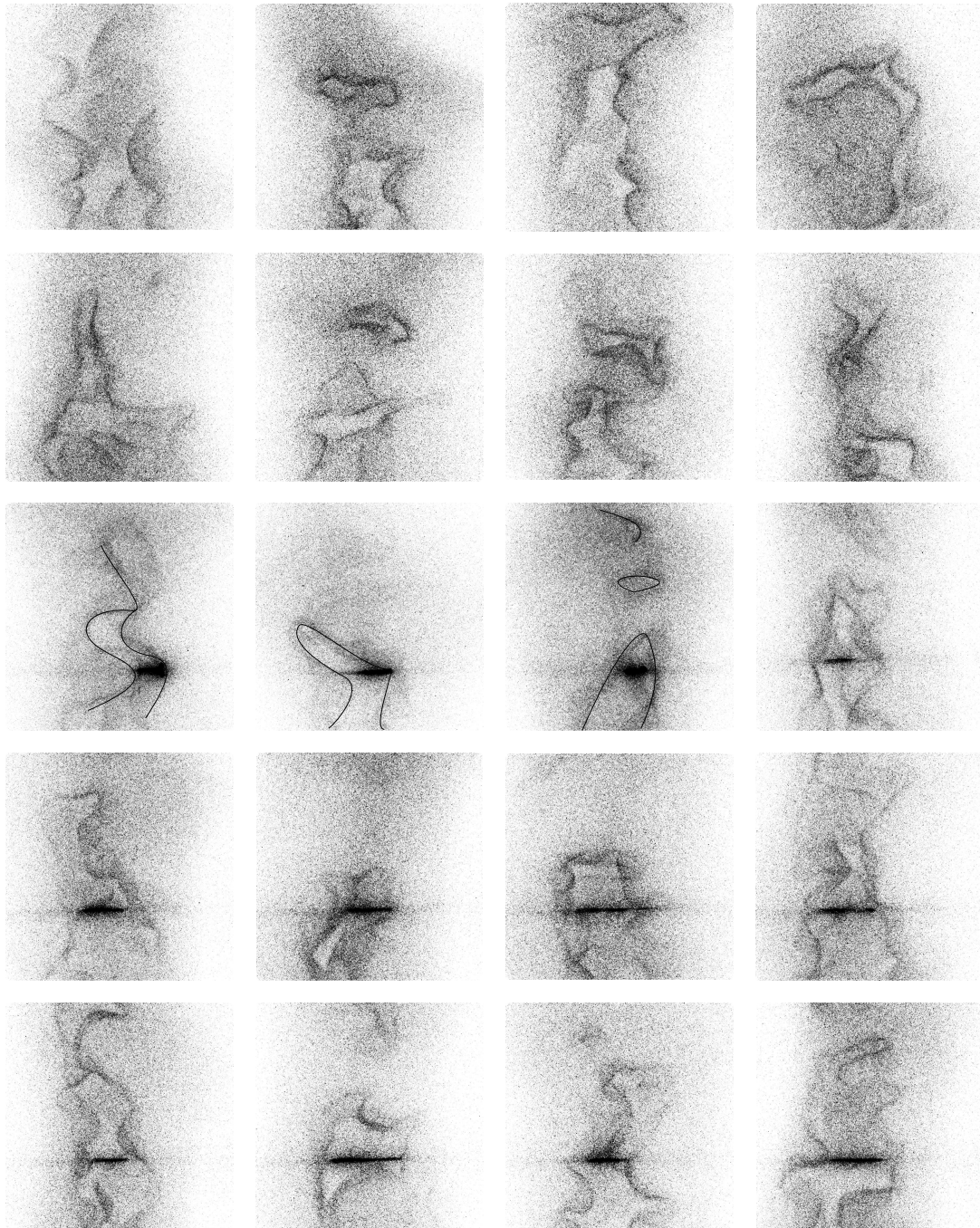
Figure 4.11: *Compilation of typical single-shot measurements of the natural emission of the flame, combined with NO fluorescence lines (lower three rows). In the middle row, the resolution of the flame front was lower, such that a black line was included to indicate the position of the flame front. The colors of the images have been scaled such that the flame front OH emission signal was enhanced. The grey background is noise.*

Chapter 5

The 2+1 REMPI spectrum of molecular nitrogen

Based on "(2+1) REMPI on molecular nitrogen through the $^1\Sigma_g^+$ (II)-state", J. Bominaar, C. Schoemaecker, N. Dam, J.J. ter Meulen and G.C. Groenenboom, Chemical Physics Letters, volume 435 (2007) pages 242 - 246 [54].

5.1   Introduction

Under ambient conditions, molecular nitrogen is transparent in the whole spectral range above $\lambda \approx 101\,\mathrm{nm}$ [55], but it has an extended absorption spectrum, containing many lines, in the extreme UV. The numerous Rydberg states causing this spectrum are the subject of several interesting studies. Many of these Rydberg states were discovered in the 1930's and 1940's by Hopfield [56], Worley and Jenkins [57, 58] and Tanaka and Takamine [59]; they converge to the ground state or first excited states of the ion. In recent decades, several studies have been dedicated to the absorption characteristics of molecular nitrogen in the extreme UV. Berg *et al.* [60] measured the nitrogen spectrum in the range from 400 to 600 Å and assigned many spectral features to Rydberg states. Between 550 and 650 Å, however, no significant signal was reported, apart from a few weak structures, which were assigned to Rydberg states converging to the $N_2^+\ D^2\Pi_g$ state. Other authors used synchrotron radiation [61, 62] or extreme ultraviolet laser radiation [63] to investigate the nitrogen absorption spectrum between 650 Å and 1000 Å, whereas McCormack *et al.* [64] applied double-resonance spectroscopy to study Rydberg states converging to the ionic ground state of N_2^+. Spectral structure found in the region of 960 Å was assigned to the $b'^1\Sigma_u^+$-state, which is forbidden for two-photon transitions from the ground state.

   In 1967 Dressler *et al.* [65] reported a singlet electronic state which was denoted with the symbol a'' as the lowest excited $^1\Sigma_g^+$ state of N_2. Within a few years, however, Michels [66] found an even lower lying $^1\Sigma_g^+$-state in his *ab initio* calculations at larger N–N distance. This state has an avoided crossing with the a''$^1\Sigma_g^+$ state, but it is much broader. More extensive calculations on this new state were performed by Ermler *et al.* [67, 68], who reported first order spectroscopic constants and named it $^1\Sigma_g^+$ (II). Good spectra involving the a''$^1\Sigma_g^+$-state have been reported by Hanisco *et al.* [69], but the $^1\Sigma_g^+$ (II)-state

has not been seen experimentally up to now.

The spectroscopy of molecular nitrogen is also of interest from an application-oriented point of view. Many technologically important processes involve air flows (e.g. aerodynamics, combustion). Nitrogen, of course, is an interesting, but notoriously uncooperative candidate for optical, non-invasive diagnostics of such processes. The molecule, for instance, plays a crucial role in a technique that we recently developed to accurately measure flow velocities by all-optical means. This technique, dubbed APART (Air Photolysis And Recombination Tracking), involves locally creating a line of nitric oxide molecules out of ambient nitrogen and oxygen, using a weakly focused excimer laser beam at 193 nm [8]. In a previous paper [70], it was shown that the NO production yield scales linearly with the intensity of N_2^+ fluorescence ($\lambda = 391$ nm, $B\,^2\Sigma_u^+ \rightarrow X^2\Sigma_g^+(0,0)$) that also originates from the laser focus [71,72]. Thus, optimization of the N_2^+ fluorescence might be expected to optimize the NO production as well.

In this chapter we report on the excitation spectrum of N_2 to the $B\,^2\Sigma_u^+$-state of the ion, using a spectrograph in front of an intensified CCD camera to spectrally disperse the fluorescence emitted from the excimer laser focus. We focus on the emission and excitation spectra of nitrogen in a pure nitrogen environment, the latter of which is measured by collecting fluorescence in the Hopfield bands ($B^2\Sigma_u^+ \rightarrow X^2\Sigma_g^+$ of N_2^+) while scanning the excimer laser around 193 nm (51,600–51,800 cm^{-1}). Neutral molecular nitrogen in the vibronic ground state can be excited to the B-state of the ion by absorbing three of these photons (Fig. 5.1). The effective excitation energies, therefore, lie in the range of 154,800 to 155,400 cm^{-1}. We report a remarkably regular excitation spectrum in this energy region, that is tentatively assigned to rotational structure in the $^1\Sigma_g^+$(II) state at the two-photon level.

5.2   Experimental

A closed glass cylinder with quartz Brewster windows on either side and one quartz window in the middle, is filled with pure nitrogen ($^{14}N_2$) at atmospheric pressure. A laser beam (ArF tunable excimer laser, Lambda Physik, EMG 150 MSCT, 80 mJ/pulse, 51,600–51,800 cm^{-1}) at 193 nm is focused into this cell by an $f = 150$ mm UV lens. When necessary, the lens is slightly tilted to avoid optical breakdown. The focus, which has an approximate FWHM of 60 μm, is examined using an intensified CCD camera (Princeton Instruments, ICCD-512-T) mounted on the exit port of a grating spectrograph (Acton Research Company, SpectraPro 300i, 1200 grooves/mm). Some experiments were performed under ambient pressure on a laminar N_2 flow, emanating from a laminar flow generator. Otherwise the setup was similar to that described in Chapter 2.

For recording the excitation spectrum the fluorescence at $\lambda \approx 391$ nm from the $B^2\Sigma_u^+(v = 0)$-state to the $X^2\Sigma_g^+(v = 0)$-state of the ion (see Fig. 5.2) is monitored as a function of excimer laser wavelength. At the same time the second-order Rayleigh scattering signal, that is visible around 387 nm, is used to monitor the laser intensity. The grating of the oscillator of the excimer laser is tuned using a stepper motor. It is calibrated off-line by comparing an NO excitation spectrum in a flame [73] with LIFBASE simulations [12]. We expect the distance between neighboring lines to be accurate within 1 cm^{-1}.
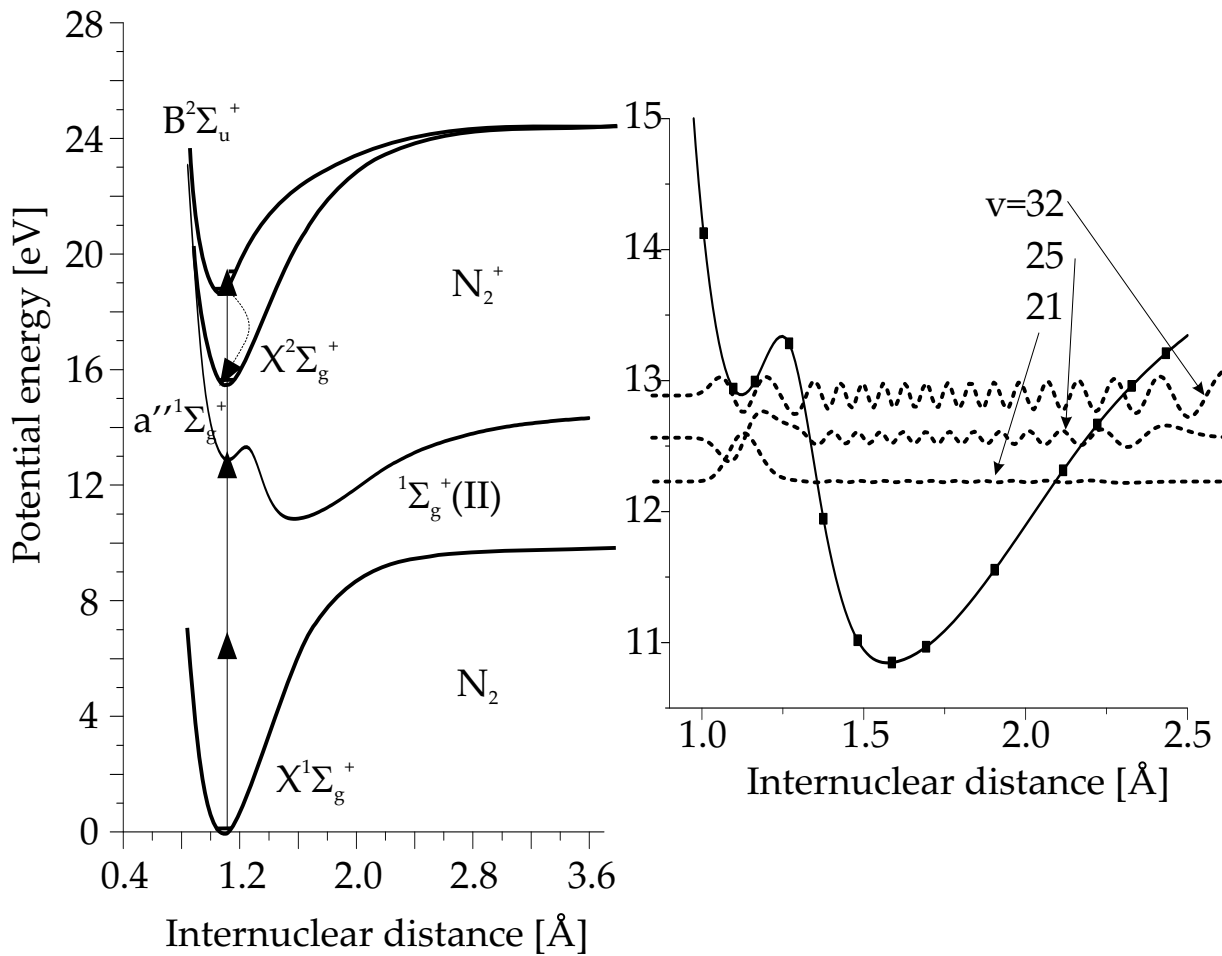
Figure 5.1: *Potential energy curves of N_2 involved in three-photon excitation and fluorescence from the B state to the ground state of the ion. On the right we included an enlarged view of the proposed double well with calculated wavefunctions of the $v = 21$, 25 and 32 states of the $^1\Sigma_g^+$ well respectively. The points in the graph are taken from Ermler et al. [68], the solid line is a spline fitted through them.*

5.3 Results and discussion

5.3.1 Emission spectrum

Figure 5.2 shows the entire emission spectrum emanating from the excimer laser focus. In the 'empty' wavelength range between ~220 and 300 nm there was no emission present or it was too weak to be detected. All transitions could be assigned to the second positive system of N_2 ($C^3\Pi_u \rightarrow B^3\Pi_g$) and the second negative system of N_2^+ ($B^2\Sigma_u^+ \rightarrow X^2\Sigma_g^+$) [2] (see Fig. 5.3).

Considering the amount of energy per photon that is put into the nitrogen molecule (193 nm $\approx$ 51800 cm^{-1}), it follows that the B-state of N_2^+ can be reached using three pho-
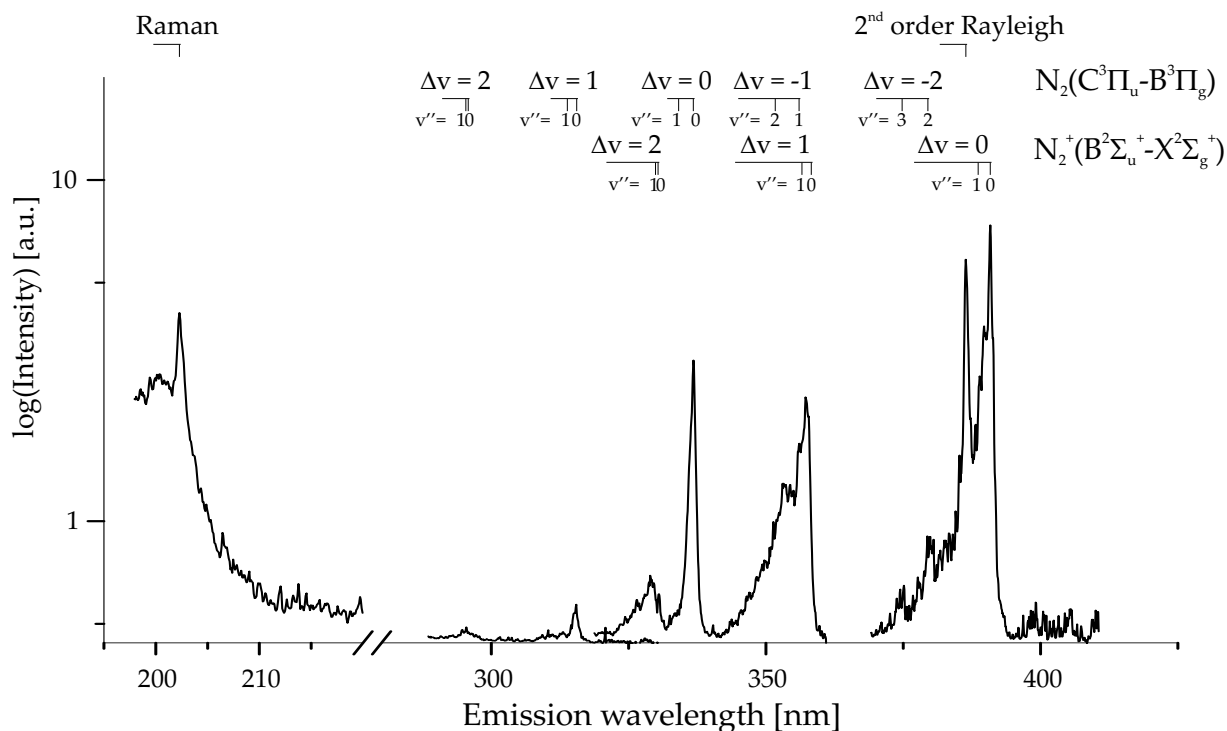
Figure 5.2: *Total measured emission spectrum of pure nitrogen with assignments included* $(\Delta v = v' - v'')$.

Table 5.1: *Vibrational energies of the N_2^+ (B) state calculated from constants taken from Huber and Herzberg [74].*

v	Energy [cm^{-1}]
0	151233.5
1	153608.7
2	155942.4
3	158237.7

tons, where the $v' = 2$ state is an absolute maximum (see Table 5.1).

In 2003 Ekey *et al.* [75] reported the afterglow emission spectrum of nitrogen in a discharge source. Although there are some dissimilarities, their spectrum corresponds strongly to our emission spectrum. The most prominent differences are the less distinctive features resulting from a lower wavelength resolution in our spectrum and a higher intensity of the B-X transitions compared to the C-B transitions. The latter might be due to a more efficient pumping of the B-state of the ion using the excimer laser. Another feature in our spectrum is the difference in line widths between the $B^2\Sigma_u^+$- and the $C^3\Pi_u$-state. Where the C-B transitions have narrow peaks, the B-X transitions show a larger spread in rotational population. Probably the excited state of the ion is longer lived than
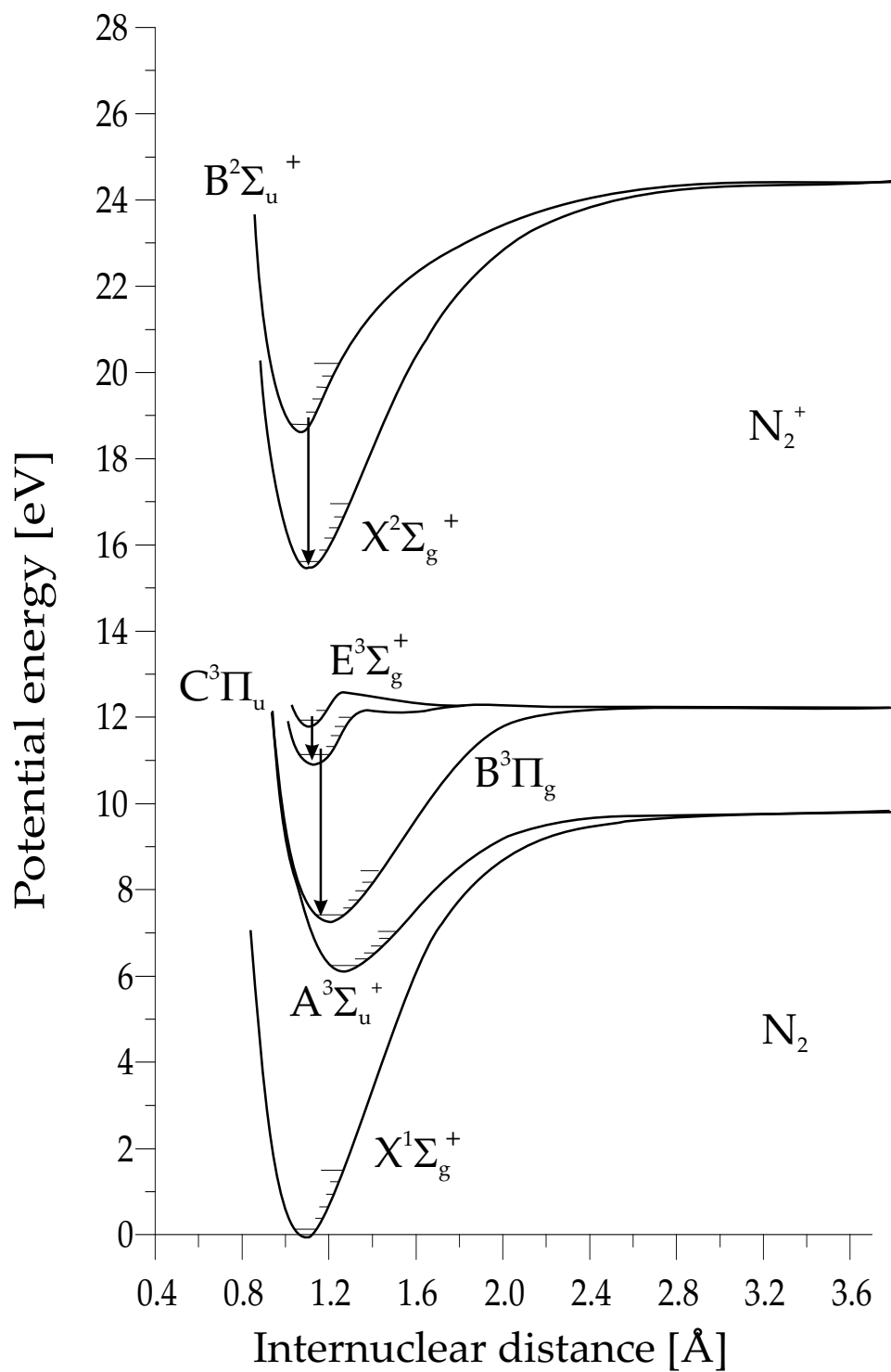
Figure 5.3: *Potential energy diagram of nitrogen with all electronic states involved in the emission spectrum included.*

Table 5.2: *Measured two-photon transition frequencies with corresponding rotational assignment. The spacing between the frequencies has an estimated accuracy of $1\,\mathrm{cm}^{-1}$.*

$\nu\ [\mathrm{cm}^{-1}]$	$Q(J)$
103549	7
103532	8
103513	9
103490	10
103464	11
103439	12
103410	13
103379	14
103345	15
103311	16
103274	17
103237	18

the excited state of the neutral, resulting in more rotational redistribution.

According to Ekey *et al.* [75] the C-state of N_2 is reached via a metastable intermediate state ($E^3\Sigma_g^+$). The lifetime of this E-state is approximately $300\,\mu$s. If this pathway is followed, this should implicate that the C-B emissions should also be visible when measuring several tens of microseconds after the laser pulse. There was no indication of this long-lived effect, but possibly this state is quenched by other energetic species of nitrogen. This E-state has been seen mostly in electron transmission and electron impact studies [76, 77] and it seems that it can most easily be reached in electron bombardment of the nitrogen molecule. Since a local plasma is created in the laser focus, there are many free electrons, which makes it plausible that the E-state will be reached. From there it populates the C-state through collisions. Another possibility to reach the C-state is recombination of the N_2^+(B)-state. A free electron goes into the $1\pi_g$ orbital of the nitrogen ion to form the C-state. Recombination with the ionic ground state is not possible on the basis of single electron transitions [78].

Sharpe *et al.* [79] also suggest this E-state to be responsible for the population of the B-state of the ion through a Rydberg state. In the next section we will point to a more likely candidate as an intermediate state in the transition from the ground state of the neutral to the B-state of the ion.

5.3.2 Excitation spectrum

Figure 5.4 shows a typical $^{14}N_2$ excitation spectrum (transition frequencies in Table 5.2). The spectrum is seen to consist of a regular progression, truncated at both ends by, probably, the limited tuning range of the excimer laser. Three possible assignments have been pursued, in which the spectral structure was attributed to either an electronic (Rydberg) progression or a rotational progression. When the experiment was repeated with $^{15}N_2$ only the excitation wavelength-independent background of $^{15}N_2^+$ B-X fluorescence was
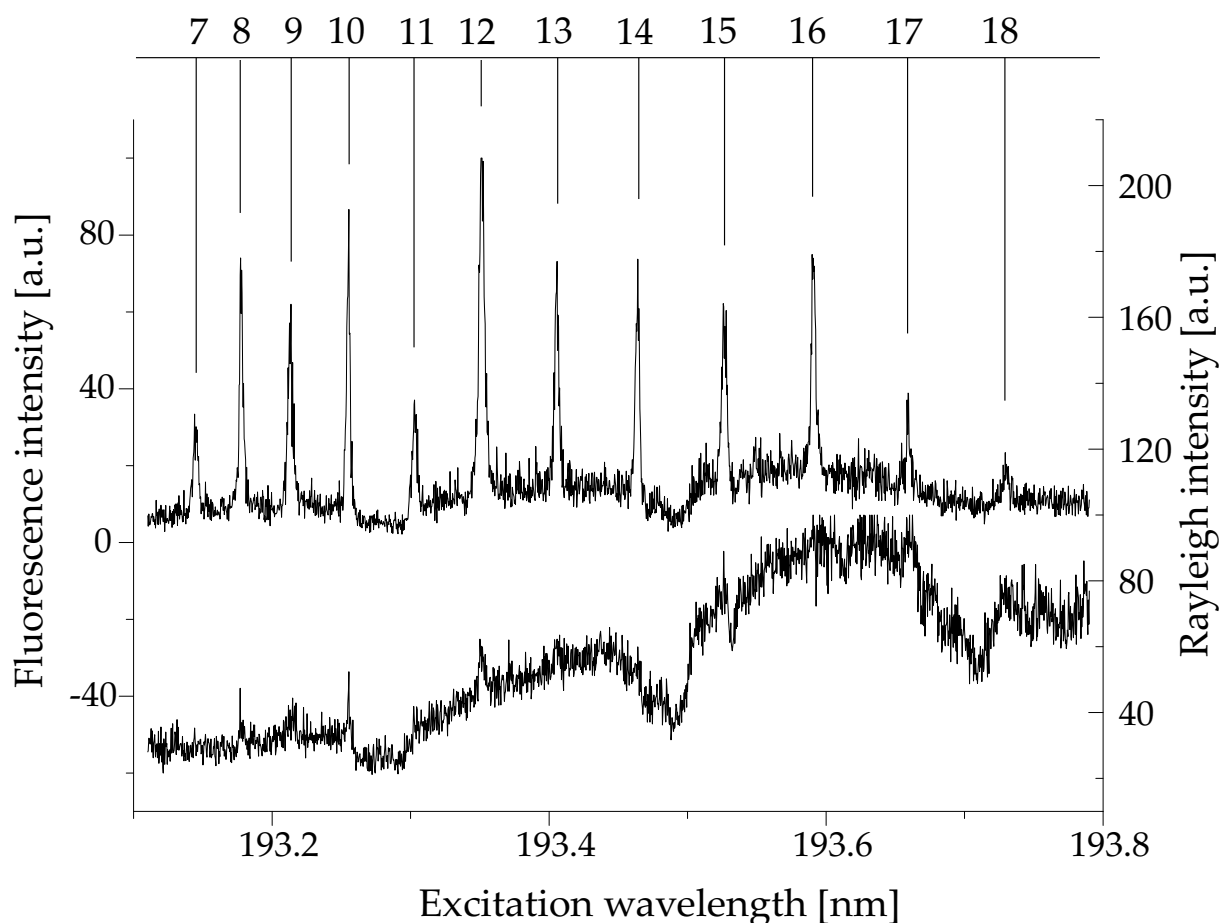
Figure 5.4: *Upper curve: Measured N$_2$ spectrum with assignments; lower curve: Rayleigh scattering intensity as a measure for laser intensity. The abscissa gives vacuum wavelengths. The upper spectrum has been corrected for laser intensity by dividing by the lower curve.*

found.

The a$^1\Pi_\text{g}$(v = 26) state

Rotational spectral structure could arise from an intermediate resonance at the 2-photon level (2 + 1) REMPI; the Vegard-Kaplan bands at the 1-photon level are very weak and would produce a more irregular spectrum due to the singlet-triplet transition. As a possible candidate for the intermediate resonance we consider the $v = 26$ level of the a$^1\Pi_g$-state [80]. The spacing between the peaks fits well for either the P-branch, or the Q-branch, or the R-branch separately, but according to the selection rules for this transition [81] all three branches should be visible in the same spectral region, and not just one of them. Furthermore, the fitted band origin does not correspond to the literature value [74], and the Franck-Condon factor is probably very small. This makes the assign-

ment unlikely, and we do not consider it further.

Rydberg levels in the three-photon range

As an alternative we considered assigning the spectrum to one or more Rydberg series, employing the standard Rydberg formula for the upper level energies:

$$E_{n_j} = IP_j - \frac{R_{N2}}{(n_j - \delta_j)^2} \ . \tag{5.1}$$

In this equation, IP_j is the ionization limit, n_j the principal quantum number (integer) and δ_j is the quantum defect; the index j labels individual Rydberg series. R_{N2} is the Rydberg constant for the N_2 molecule; it can be calculated from

$$R_{N2} = \frac{\mu}{m_e} R_\infty = 109,733 \ \text{cm}^{-1} \tag{5.2}$$

in which R_∞ is the Rydberg constant proper, m_e is the electron rest mass, and μ is the reduced mass of an electron in an N_2 molecule.

It turns out that Eq. (5.1) fits the peak positions (at the 3-photon level) very well, if the spectrum is attributed to three alternating Rydberg series. All series converge to the same limit: $IP = 155,891(5) \ \text{cm}^{-1}$ (uncertainty in units of the last digit), which is close to, but significantly lower than the ionization limit of the $B^2\Sigma_u^+(v' = 2)$-state (155,934.0(3) cm^{-1} [74, 82]). This assignment, however, was also discarded because of several reasons. i) There is no indication of a rotational structure, which would be expected at room temperature; ii) Autoionization lifetimes of states in Rydberg series converging to the N_2^+ B-state have been estimated as about 0.03 ps [83]. This would result in linewidths of about 150 cm^{-1}, two orders of magnitude larger than observed (Fig. 5.4); iii) Assuming such a three-photon process to involve only a single electron, the creation of N_2^+ in the B-state would imply removal of a $2\sigma_u$-electron from the neutral ground state molecule [78]. In this case, only two Rydberg series (p and f) would be expected, rather than three.

The $^1\Sigma_g^+$(II) state

When fitting a single branch of a rotational spectrum in the two-photon range, we find a rotational constant of the upper state of $B' = 0.95 \ \text{cm}^{-1}$ and a vibronic energy offset of approximately 103,600 cm^{-1}. This value of B' corresponds to an internuclear separation of approximately 1.6 Å, much larger than that of the ground electronic state of N_2. Ermler *et al.* [68] reported a double potential energy well, comprising the $a''^1\Sigma_g^+$ and $^1\Sigma_g^+$(II) states (see Fig. 5.1), the latter of which has a large internuclear separation (calculated $r_e = 1.58$ Å). Two 193 nm photons would excite the N_2 molecule close to the top of the barrier separating the two wells. There is a large Franck-Condon overlap with the part of the well at smaller internuclear separation ($a''^1\Sigma_g^+$ in Fig. 5.1). The transition intensity can therefore be taken from the $a''^1\Sigma_g^+$ well, while more time is spent in the $^1\Sigma_g^+$(II) well, resulting in a small rotational constant.

In order to calculate molecular constants for the double-well state we extrapolated the data provided by Ermler *et al.*, who used configuration interaction calculations to derive

Table 5.3: *Calculated vibrational energy levels, rotational constants and Franck-Condon factors relative to the $X^1\Sigma_g^+$ (v = 0) ground state for the $^1\Sigma_g^+$(II) well. The data that were used to calculate these values were taken from Ermler et al. [68]; from their table we estimate a systematic uncertainty to be approximately 0.5 eV in T_e and 1–5 % in ω_e and $\omega_e x_e$. Notation: 7.98(-1) = 7.98·10^{-1}.*

v	$E(v)$ [cm^{-1}]	$B(v)$ [cm^{-1}]	Franck-Condon factors
21	98841	1.893	7.98(-1) [a]
22	99239	0.712	1.06(-3)
23	99839	0.708	9.56(-4)
24	100405	0.733	4.43(-3)
25	100827	1.442	1.05(-1) [b]
26	101022	0.996	4.68(-2)
27	101497	0.746	7.35(-3)
28	101965	0.777	5.90(-3)
29	102382	0.875	7.61(-3)
30	102748	0.920	7.63(-3)
31	103115	0.834	4.66(-3)
32	103497	0.761	2.60(-3)
33	103876	0.731	1.69(-3)
34	104241	0.718	1.24(-3)

[a] v = 0 from a″
[b] v = 1 from a″

the energy of the $^1\Sigma_g^+$(II) state as a function of internuclear separation (up to 4.0 bohr = 2.12 Å). This state dissociates into two ^{2}D atoms at a dissociation limit of 14.2 eV [84]. Using this limit and an extrapolation of the form

$$E = D - Ce^{A(r-Z)} \tag{5.3}$$

(with E the potential energy, r the internuclear distance, D = 14.2 eV the dissociation limit and $A = -1.61$ Å^{-1}, $Z = 2.12$ Å and $C = 2.23$ eV), we could construct the graph as seen in Fig. 5.1.

The parameterization of this curve was used to calculate the molecular constants of the double well. Using the method "sinc-function DVR" [85,86], with a grid of 300 points from 1.6 to 7 bohr, the rotational constants are computed as expectation values: the vibrational wave functions are computed for J = 0 in both ground and excited states. Franck-Condon factors are also calculated, for transitions between v'' = 0 and vibrationally excited states (see Table 5.3). The vibronic energy level v' = 32 in this table lies closest to the level required by the rotational fit mentioned above (103,600 cm^{-1}).

We used the rotational constant corresponding to this vibrational level to fit the energy equation for the Q-branch to the experiment:

$$\begin{aligned}
E_{\text{total}} = T_e + E(v') \quad &+ \quad B_v' J(J+1) - D_v' \left(J(J+1)\right)^2 \\
&- \quad B_v'' J(J+1) + D_v'' \left(J(J+1)\right)^2
\end{aligned} \tag{5.4}$$
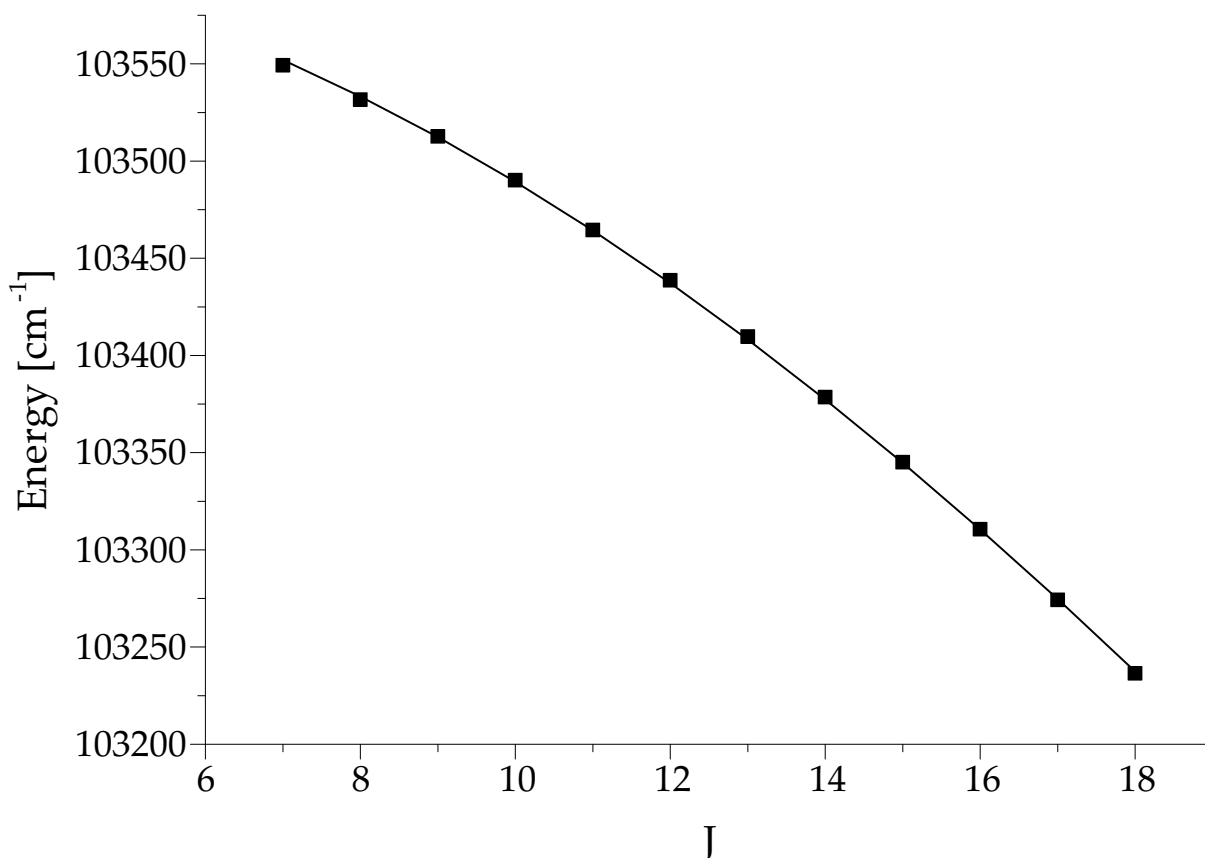
Figure 5.5: *A fit through the data using Eq. 5.4 with $B_v'' = 1.989581\,cm^{-1}$, $D_v'' = 5.76 \cdot 10^{-6}\,cm^{-1}$ and $B_v' = 0.761\,cm^{-1}$, resulting in $T_e + E(v') = 103,621\,cm^{-1}$ and $D_v' = -3.2 \pm 0.1 \cdot 10^{-4}\,cm^{-1}$.*

Here $B_v' = 0.761$ cm^{-1}, $B_v'' = 1.989581$ cm^{-1}, $D_v' = -3.2 \pm 0.1 \cdot 10^{-4}$ cm^{-1} and $D_v'' = 5.76 \cdot 10^{-6}$ cm^{-1} [78]. The fit resulted in a vibronic energy ($T_e + E(v')$) of 103,621 cm^{-1} and rotational levels from $J = 7$ to $J = 18$ as can be seen in Fig. 5.5. This transition does not require a condensation of multiple branches (as was the case with the a$^1\Pi_g$ state, discussed above), since $\Sigma - \Sigma$ transitions usually have a strong Q-branch and weak well-separated O- and S-branches. In the two-photon spectrum, the P and R branches are also absent. The intensities of the lines appear to follow an alternating trend. This is consistent with the spin statistics of the nitrogen molecule where even rotational levels have a population twice as high as odd levels.

Because of the limited tuning range of an ArF excimer laser, the above assignment necessarily bears a tentative nature. It would be of interest to record the MPI spectrum outside the range of Fig. 5.4, in particular at the blue side, but we have not been able to generate such radiation with sufficient intensity.

5.4 Conclusions

We have assigned a nitrogen excitation spectrum in the tuning range of an ArF excimer laser (51,600 to 51,800 cm^{-1}) to rotational structure in a 2+1 REMPI process involving the coupled a$''^1\Sigma_g^+$ and $^1\Sigma_g^+$ (II) states, the latter of which has not been observed experimentally before. The a$''^1\Sigma_g^+$ component of the well closely resembles the ground state of the N$_2$ molecule. We believe that the probability of the transition to the $^1\Sigma_g^+$ (II) state is enhanced due to the overlap of the a$''^1\Sigma_g^+$ state with the ground state. Close to the crossing of the two wells, the intensity borrowing by the $^1\Sigma_g^+$ (II) state from the a$''^1\Sigma_g^+$ state is relatively efficient. The limited tuning range of an ArF excimer laser does not allow a complete recording of the spectrum, causing the assignment to remain tentative.

This study was initiated by a desire to understand the photodynamics of molecular nitrogen in air rather than in pure nitrogen. Interestingly, when we add a small amount of oxygen ($> 1\%$) the observed excitation spectrum changes completely and becomes exactly the same as what would be observed in pure oxygen (which can be observed via O$_2^+$-fluorescence). This phenomenon will be discussed further in Chapter 7.

Chapter 6

APART in Oxygen

6.1 Introduction

In 1935 W.C. Price and G. Collins published a paper on the absorption spectrum of molecular oxygen in the ultraviolet [87]. Many lines in the spectrum that they photographed correspond to transitions within the ion, especially the Hopfield [88] bands, later assigned as $c^4\Sigma_u^-$-$b^4\Sigma_g^-$. They were also one of the first to assign part of their spectrum to Rydberg states converging to bound electronic states in the oxygen ion. These assignments were indicated with lettering schemes $HIJ\cdots$, $MNO\cdots$ and $PQR\cdots$ each denoting different groups. In an extensive publication Dehmer *et al.* [89] continued on these assignments and more recent work using the same lettering schemes. They assigned most of the lines to different Rydberg states converging to known electronic states in the oxygen ion. Nishitani [90] mentions the difficulty in assigning states in the ultraviolet region due to many perturbations from the different states. Further studies, which mostly consisted of photo-electron spectroscopy unveiled more electronic [91, 92] and Rydberg states [93–95].

In the present study the processes taking place in the focus of an ArF excimer laser beam were examined, where only molecular oxygen is involved. The use of the ArF excimer laser at 193 nm to excite oxygen has resulted in some unsolved problems [96–98], which will also be discussed in this chapter. One single photon excites ground state oxygen to the $B^3\Sigma_u^-$-state. This transition is well known from atmospheric studies, where solar UV radiation is absorbed strongly by molecular oxygen in these bands. By focusing the laser multi-photon processes should be expected. Results of X-ray experiments at twice (96.5 nm) and three times (64.3 nm) the energy of 193 nm photons can be comparable to our multiphoton experiments, although different selection rules hold for two and single-photon excitation. Around 96 nm both Dehmer *et al.* [89] and Wu [99] assign structure to Rydberg states. The same authors also measured in the range of 64 nm, where they assigned weak structures to Rydberg states converging to the $B^2\Sigma_g^-$ state in O_2^+. The selection rules for single-photon transitions also apply to three-photon transitions, but an important difference is that no intermediate resonances can be reached with a single-photon transition.

The experimental setup is exactly the same as described in Chapter 5. Instead of a closed cell, however, in some cases we needed to utilize a laminar flow of pure oxygen. Alternatively, for measurements at low pressures a small flow was maintained through
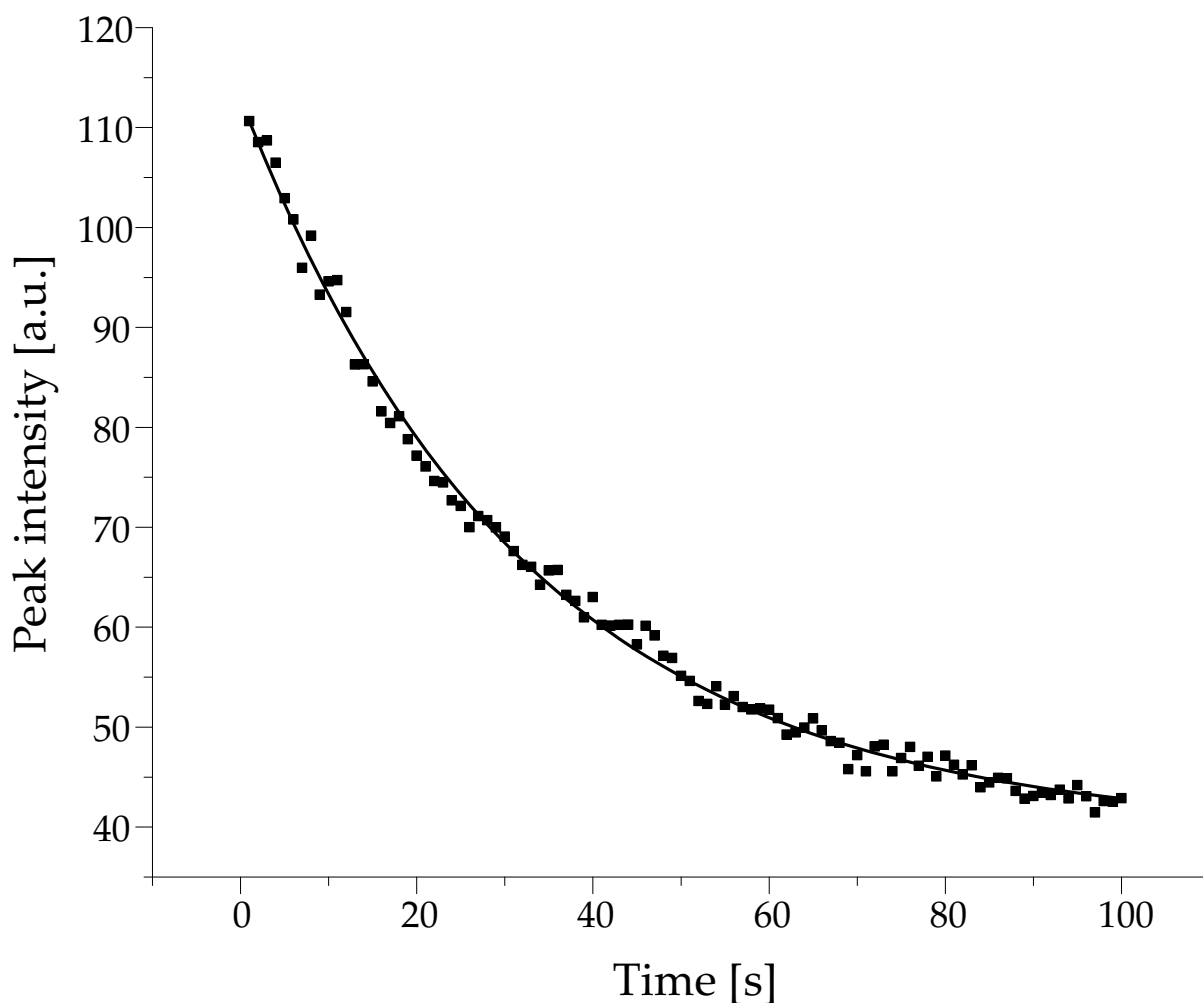
Figure 6.1: *A typical decrease of the intensity of an emission band at 202 nm as a function of time in a closed cell. An exponential function (Eq. 6.1) was fit to each emission structure decrease. The fit parameters for this measurement are y_0 = 39.7 ± 0.5, A = 73.3 ± 0.5 and τ = 32.2 ± 0.7 s.*

the absorption cell, so as to avoid build-up of photochemical byproducts, notably ozone.

6.2 Results

6.2.1 Ozone excitation

When performing an oxygen emission experiment in a closed cell (used for isotope measurements), instead of in a flow of pure oxygen, we noticed that the intensity of some of the emission bands around 240 nm in the oxygen emission spectrum decreased significantly with time. Therefore, the intensity decrease of several bands was followed as a
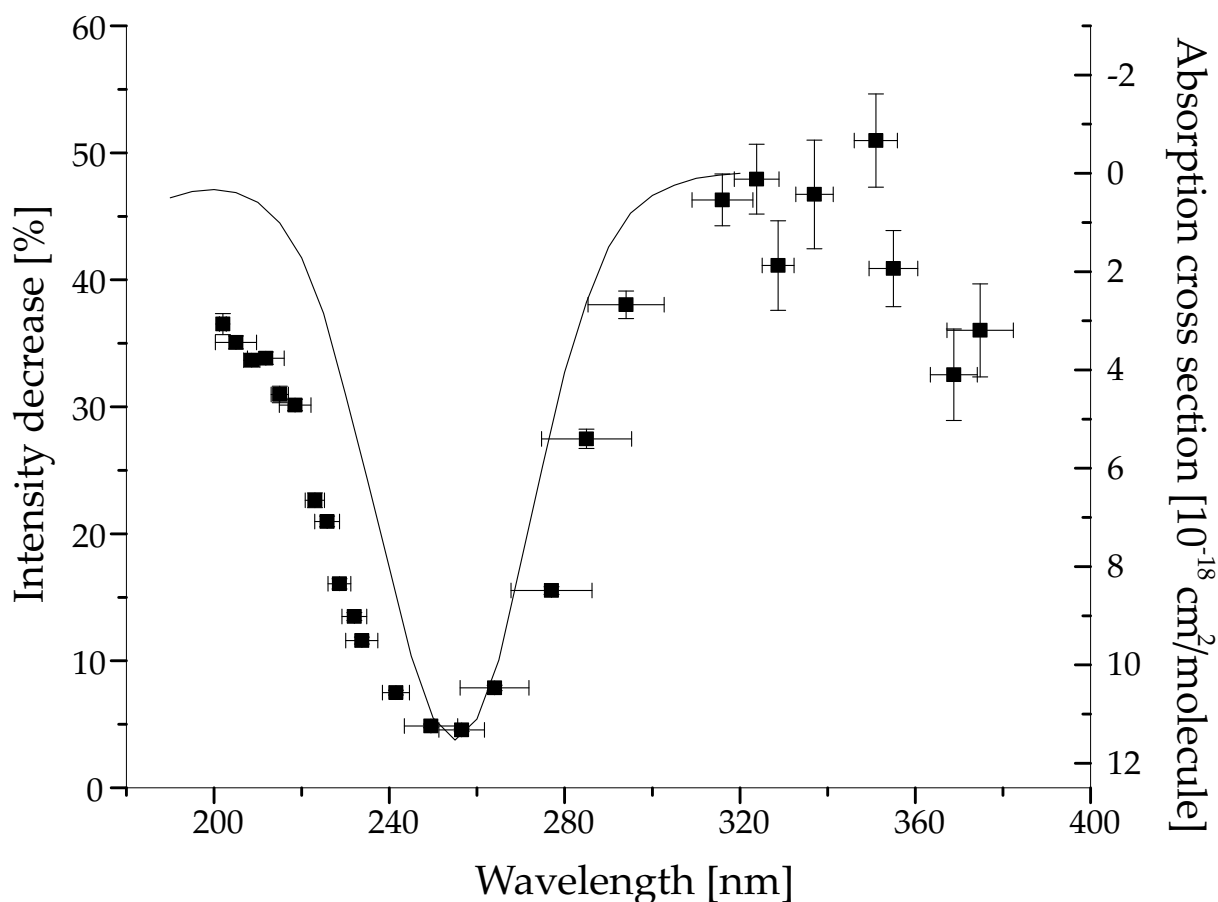
Figure 6.2: *Ozone absorption of oxygen emission lines with an irradiation time of 100 s. The data points represent the percental intensity decrease of every emission structure as a function of emission wavelength. The x-error bars are a measure for the width of the emission bands and the y-error bars are the least-squares fit errors. The solid line is the absorption spectrum of ozone measured by Takahashi et al. in an absorption cell [100]. Due to our resolution, no additional structure is visible.*

function of time after a fresh oxygen fill of the cell under steady illumination by the excimer laser at 10 Hz. A typical decrease is shown in Fig. 6.1. Each trace was fitted to an exponential decay:

$$I = y_0 + Ae^{-t/\tau} \quad , \tag{6.1}$$

where $y_0 + A$ is the initial band intensity which decreases to y_0 with a $1/e$-decay time of τ.

For every emission band the parameter $y_0/(y_0 + A) \cdot 100\%$ is plotted as a function of center wavelength of the band. Figure 6.2 shows this plot, where the x- and y-error bars are indicators for the band widths and fit uncertainties, respectively. Ozone absorption data measured by Takahashi *et al.* [100] were included in the graph to compare with our measured decrease. Obviously, the 193 nm laser radiation converts part of the oxygen in the cell into ozone, and it does so at a sufficiently fast rate to significantly affect our fluo-

rescence measurements. To estimate the conversion rate of O_2 to O_3 in our measurement cell, its volume (V_c = 138 ml) is used to calculate the initial amount of O_2 molecules

$$n_{O_2} = \frac{N_A V_c}{V_M} \tag{6.2}$$

where N_A = $6.0 \cdot 10^{23}$ is Avogadro's number and V_M is the molar volume of the gas (we used the value of the ideal gas, 22.4 ℓ/mol). This amounts to n_{O_2} = $3.7 \cdot 10^{21}$ molecules.

The ozone creation goes via the reaction

$$3O_2 + h\nu_{193\,\text{nm}} \rightarrow 2O + 2O_2 \rightarrow 2O_3 \tag{6.3}$$
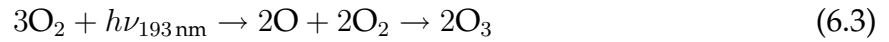
which means that only one photon is needed to convert three oxygen molecules. The amount of photons per laser pulse $n_{\text{photons/pulse}}$ is calculated via

$$n_{\text{photons/pulse}} = \frac{E_{/\text{pulse}}}{E_{/\text{photon}}} = \frac{E_{/\text{pulse}}}{hc\tilde{\nu}} \tag{6.4}$$

where $E_{/\text{pulse}}$ is the amount of energy per pulse (50 mJ) and $E_{/\text{photon}}$ = 51813 cm^{-1}= $1.03 \cdot 10^{-18}$ J/photon the amount of energy per photon. This results in an input of $n_{\text{photons/pulse}}$ = $4.9 \cdot 10^{16}$ photons/pulse.

The absorption path length l of oxygen in air, defined by:

$$I = I_0 \exp(-x/\ell) \quad , \tag{6.5}$$

with I the intensity of the laser and x the distance, was measured by determining the decrease in beam intensity as a function of distance along the beam path. From this ℓ = 5 m in air was calculated, which corresponds to 1 m in pure oxygen. Since the length of the cell is approximately 20 cm the absorption probability is 20%. Thus from each pulse 20% of $4.9 \cdot 10^{16}$ photons are absorbed, destroying $3.0 \cdot 10^{16}$ oxygen molecules. To completely empty the cell of its $3.7 \cdot 10^{21}$ oxygen molecules, $1.3 \cdot 10^5$ pulses or 3.6 hours would be needed. This estimation falls short in that the absorption path length will increase with a decreasing concentration of oxygen, which will even increase the time needed. The time scales of this experiment are too short to reach this saturation.

The created ozone will, however, absorb radiation emitted from the oxygen molecules still present. As can be seen from Fig. 6.2, the wavelength dependence of the O_2 fluorescence intensity decrease nicely follows the O_3 absorption spectrum. The difference in width of the two spectra is most likely due to the higher temperature at which our experiment was performed. For the present purpose, it suffices to conclude that for spectroscopical measurements a small flow must be maintained, in order to avoid O_3 accumulation.

6.2.2 Excitation spectrum

Figure 6.3 shows three spectra, recorded by monitoring the fluorescence intensity at a specific wavelength (which is different for all three spectra) while scanning the excimer laser wavelength. In all cases the excimer laser beam is focused (conditions for APART). The spectra represent:
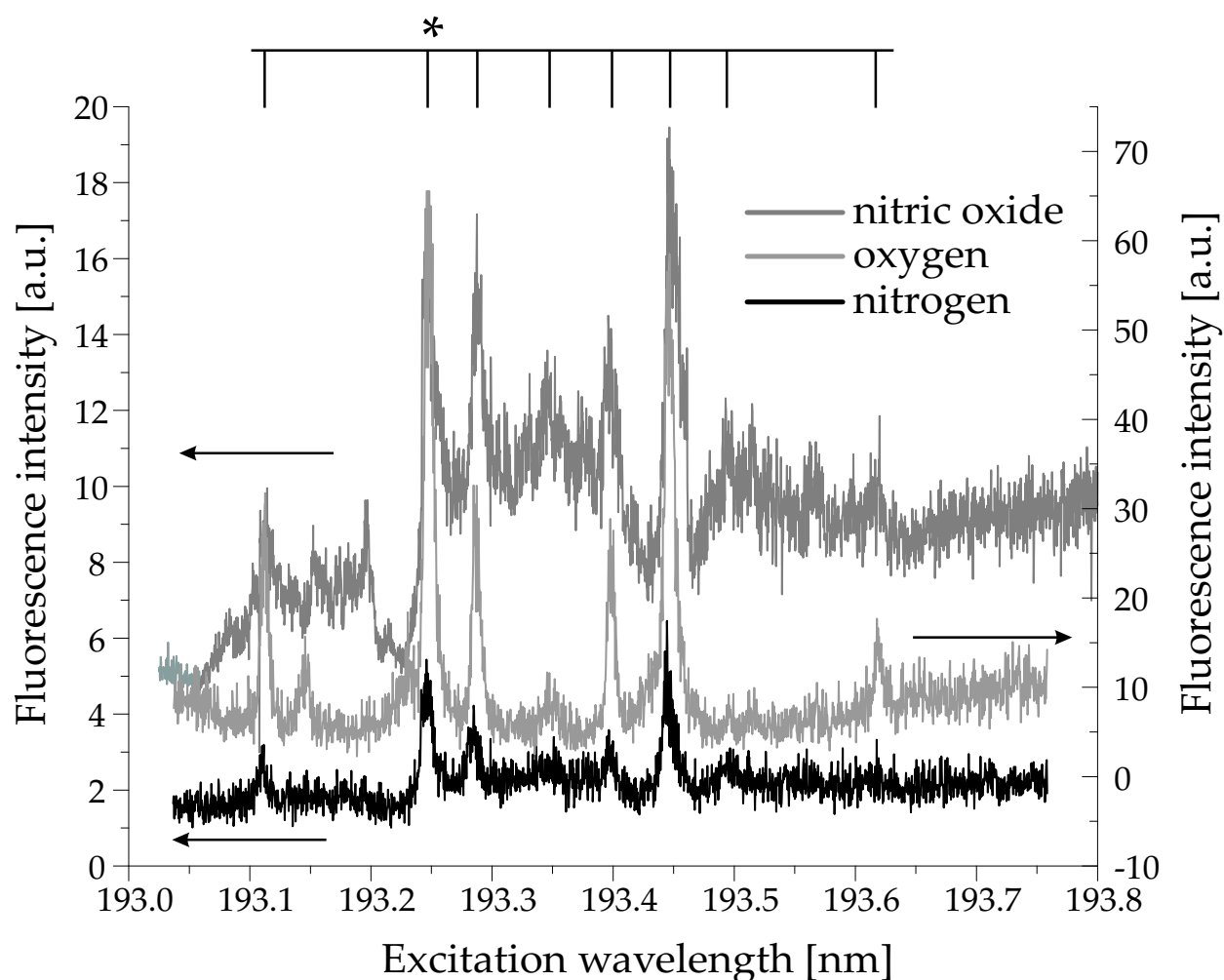
Figure 6.3: *Creation spectrum of NO (upper plot), the excitation spectrum of oxygen (in a flow of pure oxygen: middle plot) and the excitation spectrum of nitrogen in air (lower plot). The assignment corresponds to the energies given in Table 6.1 and the asterisk is the resonant wavelength used in emission experiments.*

Table 6.1: *Excitation wavelengths (indicated in Fig. 6.3) and energies for the structure in the oxygen excitation spectrum for single-photon and two-photon transitions.*

λ [nm]	$1h\nu$ [cm^{-1}]	$2h\nu$ [cm^{-1}]
193.11	51784	103567
193.25	51748	103496
193.28	51737	103475
193.35	51719	103439
193.40	51707	103414
193.44	51695	103389
193.50	51680	103361
193.62	51648	103296
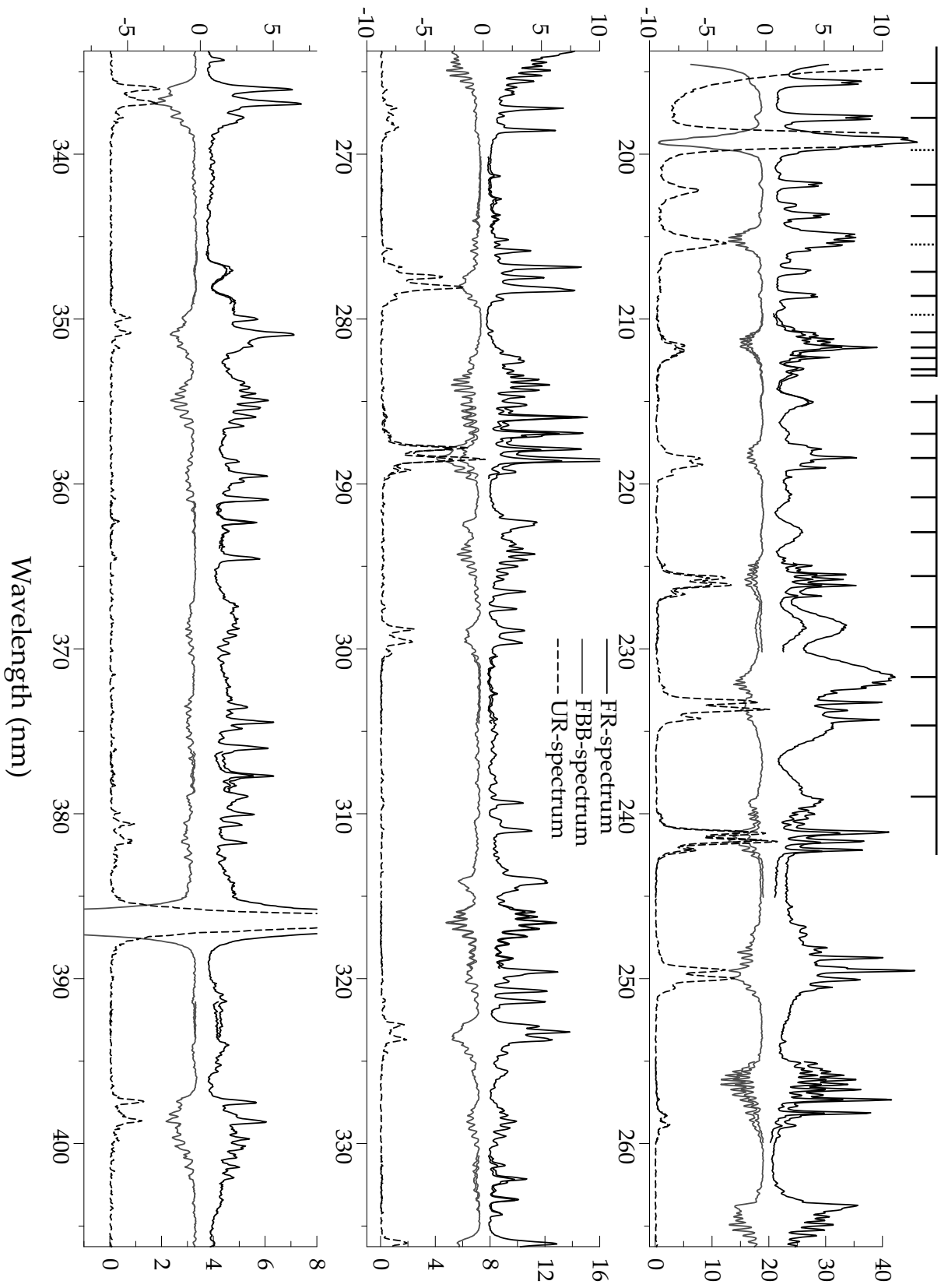
Figure 6.4: *Emission spectra of a pure oxygen flow irradiated by the ArF excimer laser. The spectral range from 195–405 nm is split over three panels. Three plots are drawn in every panel depicting the emission spectrum resulting from (1) a focused laser with the wavelength set to a resonant (193.25 nm) excitation wavelength (FR-spectrum, upper plot), (2) the unfocused laser at the same wavelength (UR-spectrum, lower plot), and (3) the focused laser set in broadband mode (FBB-spectrum, inverted, middle plot). Ordinates are in arbitrary units, at the right for the UR-spectrum and at the left for the other two. The spectrum is a concatenation of fourteen emission spectra each covering approximately 20 nm with a resolution of 0.04 nm/pixel. The gain settings for part of the spectra were individually adjusted to utilize the dynamic range of the detection system as efficiently as possible. (This is the reason why intensities usually do not match in overlap regions.)*

  i a creation spectrum of NO in air; the dye-laser induced fluorescence of NO is monitored in the *gamma*-bands,

 ii an excitation spectrum of O_2 in pure oxygen flow; the fluorescence of characteristic O_2-bands (discussed below) around 210 nm is monitored,

iii a creation spectrum of N_2^+(B) in air; the fluorescence in the 0-0 band of the first negative system of N_2^+ is monitored.

The spectra are clearly very similar, and we conclude that the spectral structure must, in all cases, have the same origin. Several more conclusions can be drawn:

1. The spectral structure must be due to O_2, since this is the only species present in case ii (and present with 20 % in air).

2. The spectral structure is not observed when the excimer laser beam is not focused. It must be due to a multiphoton process.

3. The individual lines are relatively narrow, so the upper state must be long-lived.

4. In air, a mechanism exists that transfers the O_2 excitation to NO and N_2^+ (will be discussed in the next chapter).

6.2.3 Emission spectra of pure O_2

Atmospheric pressure

A flow of pure oxygen was irradiated by an excimer laser in three ways; focusing the beam and tuning the wavelength to a resonance (indicated in Fig. 6.3) of the excitation spectrum (FR-spectrum), not focusing the beam but using the same wavelength (UR-spectrum) and a broadband, focused beam (FBB-spectrum). All three resulting emission spectra are depicted in Fig. 6.4. The unfocused spectrum gives a regular progression of bands that can all be assigned to the single-photon transition from the $B^3\Sigma_u^-(v' = 4)$-state of molecular oxygen down to the ground electronic state $X^3\Sigma_g^-(v'')$. This B($v' = 4$) state is reached by exciting the vibronic ground state of oxygen with one 193 nm photon. This

Figure 6.5: *Part of the total emission spectrum in pure oxygen as a function of pressure. The pressure goes from 1 bar (panel a) through 80 mbar (panel b) to approximately 50 mbar (panel c). Experimental details as in Fig. 6.4.*

same progression, but with more structure in the individual vibronic emission bands, is also apparent in the two emission spectra resulting from excitation by a focused excimer laser beam. In these cases, however, there are several more progressions to be distinguished, which will be discussed in the next sections. Two of these progressions, that are characteristic for the FR-spectrum, are marked in Fig. 6.4.

Low pressure

The relatively long duration of excimer laser pulses (≈ 20 ns) may give rise to spectral complications at ambient pressures. Under conditions of STP molecular collision rates are in the order of $1\,\text{ns}^{-1}$, so that the laser pulse provides sufficient time for multiple photon absorptions separated by collision-induced population redistribution. For instance, in Chapter 2 it was shown that APART measurements locally increase the air temperature by a few hundred degrees. Such an increase would imply a significant increase in the population of the vibrationally excited state(s). For the first few vibrationally excited states the Franck-Condon factors for absorption of 193 nm radiation increase by about one order of magnitude for each unit increase in vibrational quantum number [101]. Thus, it is conceivable that a temperature increase during the first part of the laser pulse gives rise to additional absorption (and subsequent emission) during the second half.

The contribution of such collision-related structures to Fig. 6.4 can be assessed by experiments under reduced pressure. Decreasing the pressure will affect emission spectra (recorded under otherwise identical conditions) in different ways. The density decreases linearly with pressure, and this reduces both the number of excited molecules and the collision rate. Therefore, fluorescence quenching and collisional line broadening also decrease. The former typically increases the fluorescence yield, but the latter may work both ways, depending on whether excitation is resonant or not. In molecular oxygen, there is an additional complication caused by predissociation of the B-state. Anyhow, in general it can be expected that the intensity of spectral features related to collision-induced population redistribution decreases faster with pressure than "direct" features.

Emission spectra of pure O_2 in a small flow cell with valves on entrance and exit were recorded. A small flow was maintained in order to prevent ozone build-up, and the pressure was set by manual "tuning" of both valves. Figure 6.5 shows part of the emission spectrum at three different pressures, recorded with a focused, resonant laser beam. Panel a) corresponds to the FR-spectrum of Fig. 6.4. It turns out that only the two progressions labelled in Fig. 6.4 "survive" the pressure reduction by about two orders of magnitude. We will focus on these structures in the following. The spectral features at $\lambda \geq 240$ nm in Fig. 6.4 are apparently due to collision-induced population transfer, and can probably all be assigned to the Schumann-Runge system. Moreover, it can be observed in Fig. 6.4 that they all occur on broadband excitation (FBB-spectrum) as well. Apparently they are not involved in the resonances of Fig. 6.3, that play a role in the NO formation.
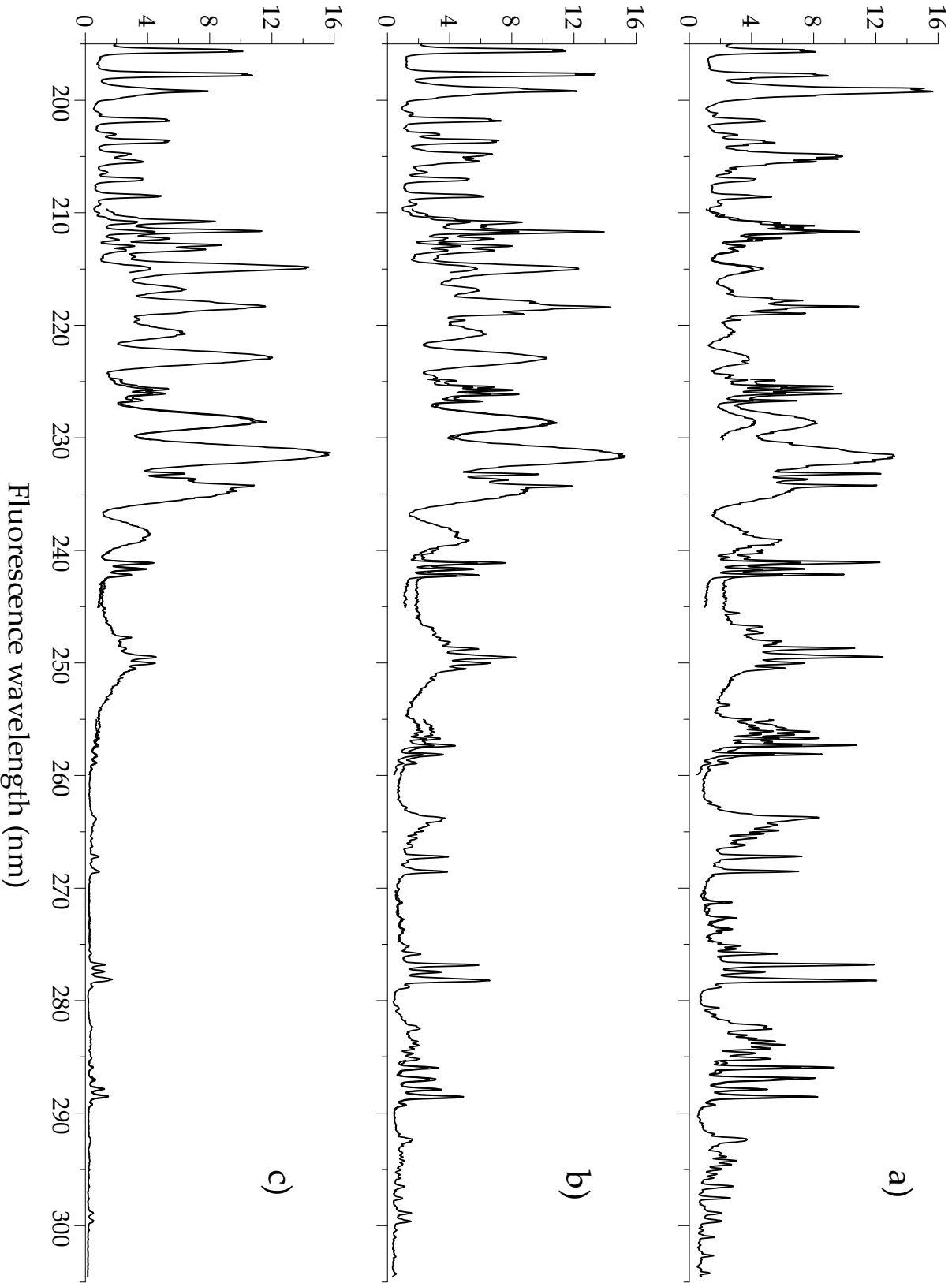
6.3 Discussion

The excitation and fluorescence spectra of molecular oxygen that were reported in Figs. 6.3-6.5 have been observed before, but they have remained enigmatic. To our knowledge, the first observation of the fluorescence features was reported by Laufer *et al.* [96]. They used a broad-band ArF laser, so they could not observe the excitation spectrum, and tentatively attributed the fluorescence to the doublet system of the O_2-ion. The excitation spectrum was first reported in 1992 in the PhD-thesis of Versluis [102], in LIF and later DFWM [103]. Versluis speculated that the transition might belong to the quartet system of O_2^+, that might be reached by 2+1 REMPI with an intermediate resonance involving Rydberg states converging to the ionic ground state [98].

   Although the O_2^+-ion indeed shows many transitions in the wavelength range that is of interest here, the observed emission spectrum can not, in fact, be matched to any particular system. Below, an alternative assignment is presented, in which the excitation is a two-photon step to (one of) the Rydberg states that converge(s) to the $O_2^+ A^1\Pi_u$-state, and the observed fluorescence is due to radiative decay of this Rydberg state back to the $B^3\Sigma_u^-$ state of O_2 (the predissociated upper state of the Schumann-Runge bands) as well as to a repulsive state with the same dissociation limit.

6.3.1 Emission spectrum

Figure 6.6 shows two progressions assigned in the blue part of the emission spectrum from Fig. 6.5. Progression I is characterized by relatively narrow features that come close together at longer wavelengths. Progression II seamlessly connects to progression I, but contains broader features that move apart with increasing wavelength. This can be interpreted as a combination of bound-bound emission followed by a bound-continuum emission, similar to what has been observed for the NaK dimer [104]. In the next sections we will discuss these progressions separately.

Progression I: The bound-bound emission

The highest-energy progression is shown in more detail in Fig. 6.7. This regular progression (sometimes with a hint of doublet structure) becomes increasingly dense towards lower energies, as would be expected from a vibrational progression out of a single excited state that converges towards the dissociation limit of the lower electronic state.

Assignment of the lower state

When fitting this progression to a formula suitable for a vibrational progression without rotational structure,

$$
\begin{aligned}
\Delta E \;=\; & E_0 - \omega_e\left(v+\frac{1}{2}\right) + \omega_e x_e\left(v+\frac{1}{2}\right)^2 \\
& -\omega_e y_e\left(v+\frac{1}{2}\right)^3 - \omega_e z_e\left(v+\frac{1}{2}\right)^4 - \omega_e a_e\left(v+\frac{1}{2}\right)^5 \quad,
\end{aligned}
\tag{6.6}
$$
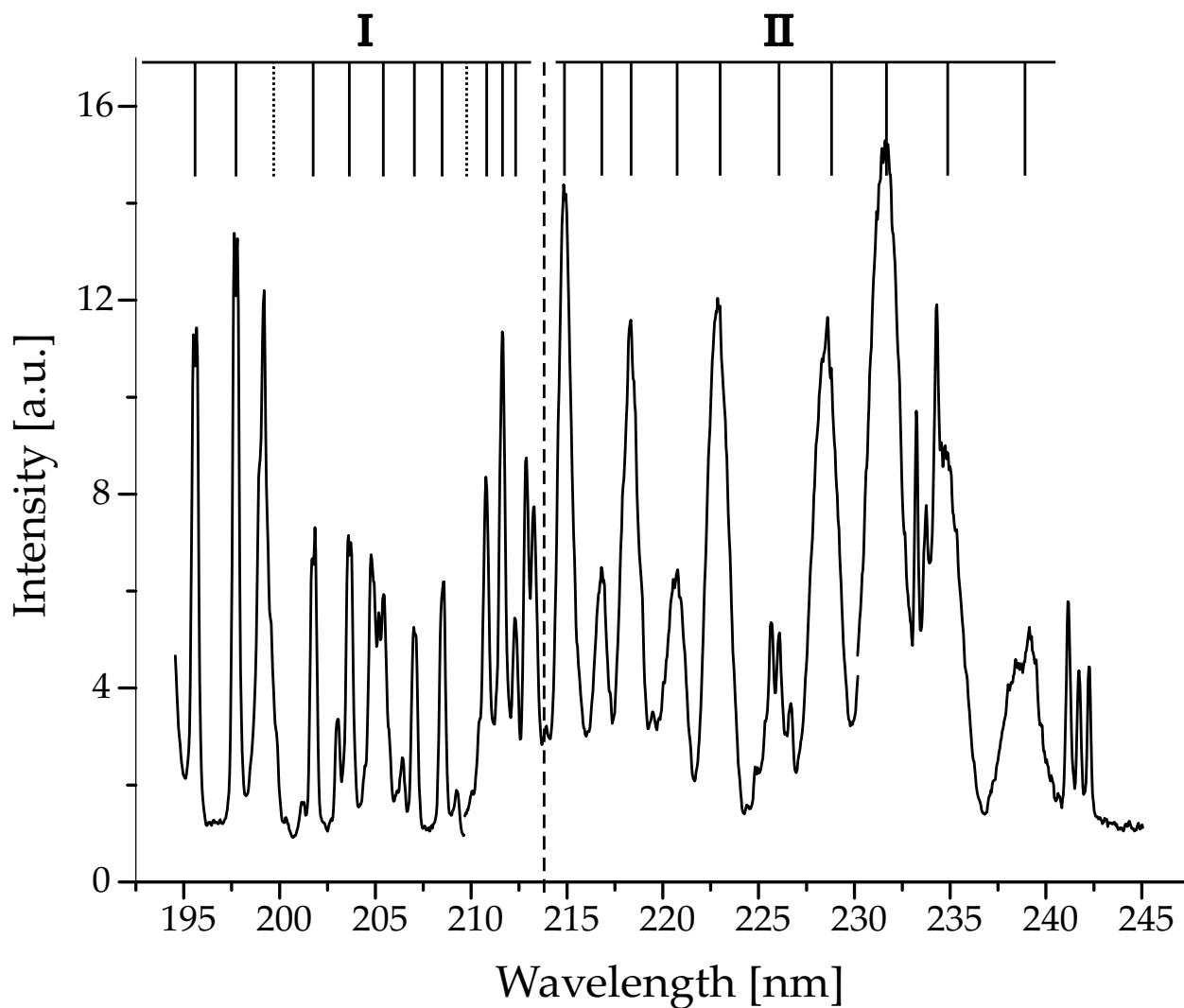
Figure 6.6: *Part of the emission spectrum at ~50 mbar with two progressions of bands indicated. At the shorter wavelength side we see a progression of relatively narrow structure, with a small pile-up arising close to 214 nm. Beyond this wavelength a progression of bands was measured, appearing to be wider and moving further apart with increasing wavelength.*
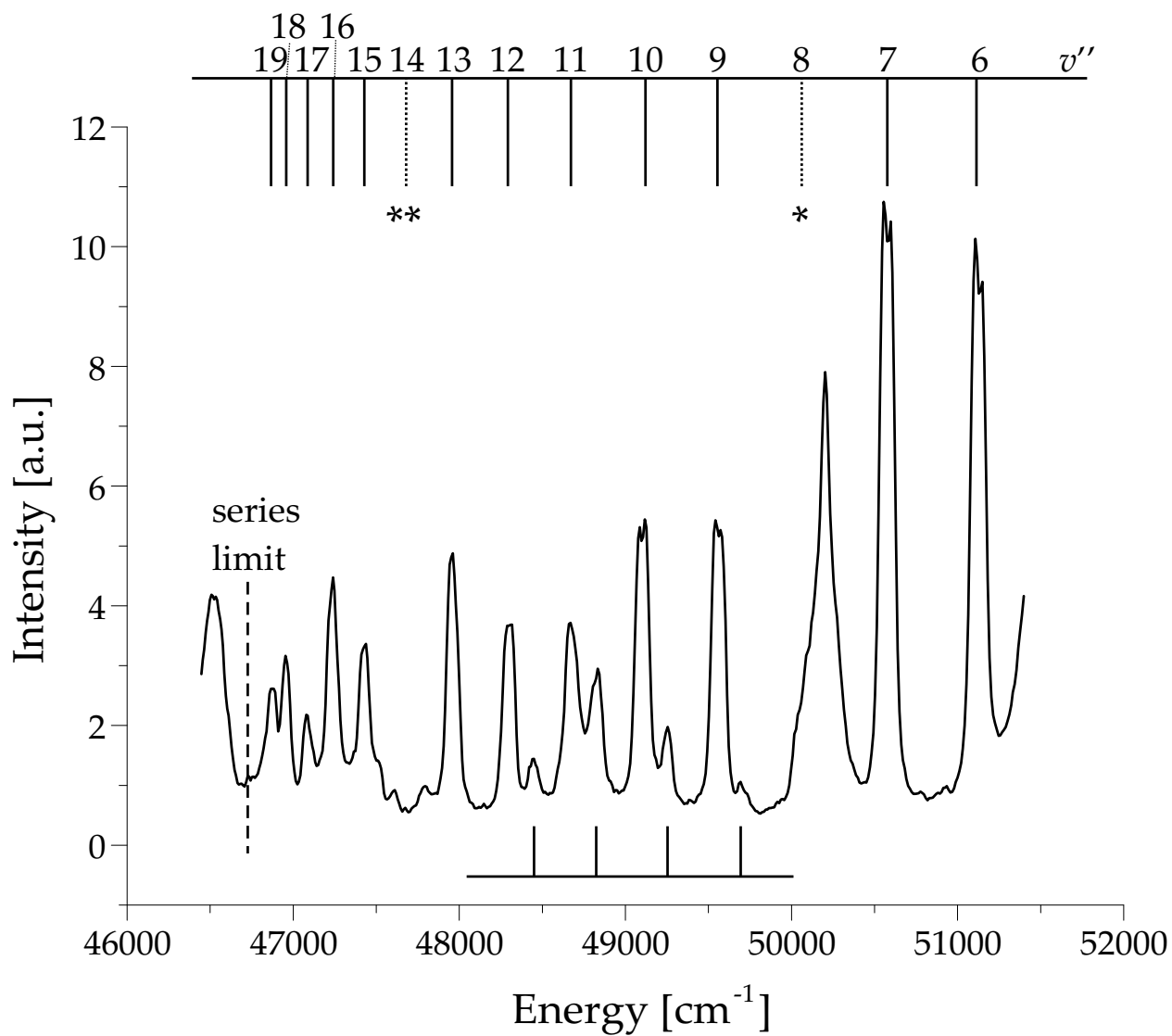
Figure 6.7: *Part of the emission spectrum at ~50 mbar with a progression of bands indicated. Dotted lines in the assignment rake at the top indicate uncertain band positions due to overlap with a Raman line (*) or insufficient intensity (**). Around 49000 cm^{-1} a weak additional structure arises (indicated below the spectrum) which might be caused by a perturbation.*
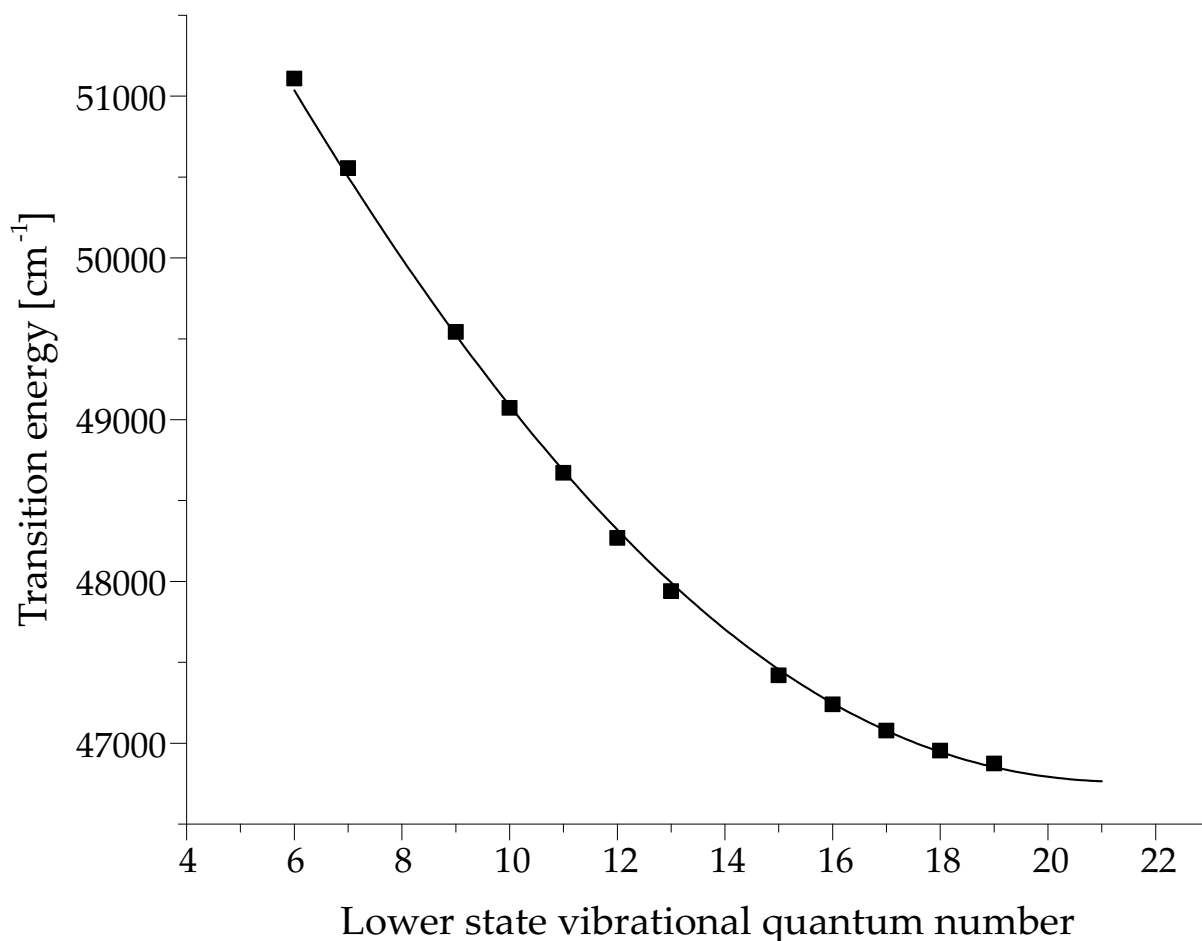
Figure 6.8: *A fit of the vibrational energy function Eq. 6.6 to the structure indicated in Fig. 6.7. The parameters of the $B^3\Sigma_u^-$-state (ω_e = 709.56 cm^{-1}, $\omega_e x_e$ = 10.92 cm^{-1}, $\omega_e y_e$ = -0.0176 cm^{-1}, $\omega_e z_e = -0.0180$ cm^{-1}, $\omega_e a_e$ = 0.00048(1) cm^{-1} [105]) are used for the fit. The fifth order term ($\omega_e a_e$) was altered to improve the fit. The fitted energy difference between the radiating state and the minimum of the $B^3\Sigma_u^-$-state potential energy curve is E_0 = 55155 $\pm$ 16 cm^{-1}. The fit was extrapolated to v = 21, which is the last vibrational state in this well. The energy at this extrapolation is 46765 cm^{-1} and lies only 300 cm^{-1} from the calculated dissociation energy.*

Table 6.2: *The quantum defects belonging to different vibrational states of the Rydberg state (n=3) converging to the $a^4\Pi_u$-state lying close to the calculated energy value of 104160 cm^{-1}.*

v'	δ	v'	δ	v'	δ	v'	δ	v'	δ
0	0.949	5	1.117	9	1.216	13	1.293	17	1.354
1	0.988	6	1.144	10	1.237	14	1.310	18	1.368
2	1.024	7	1.170	11	1.257	15	1.325	19	1.380
3	1.057	8	1.193	12	1.275	16	1.340	20	1.392
4	1.088								

we find that the known parameters for the B-state of the neutral oxygen molecule fit the spectrum very well as can be seen in Fig. 6.8. Molecular parameters ((ω_e = 709.56 cm^{-1}, $\omega_e x_e$ = 10.92 cm^{-1}, $\omega_e y_e$ = −0.0176 cm^{-1}, $\omega_e z_e$ = −0.0180 cm^{-1}, $\omega_e a_e$ = 0.00029 cm^{-1}) for the $B^3\Sigma_u^-$-state were derived by Cheung *et al.* [105]. The fifth order term, however, had to be changed significantly, from 0.00029 cm^{-1} to 0.00048(1) cm^{-1}, to improve the fit. The one free parameter in the fit, E_0 = 55155 ± 16 cm^{-1}, gives the energy difference between the radiating upper state and the minimum of the potential of the lower state ($B^3\Sigma_u^-$).

Assignment of the upper state

Rydberg series

The energy difference between v = 0 of the rotationless ground state of oxygen and the minimum of the well of the B-state is 49005 ± 1 cm^{-1} [105]. Adding this number to E_0 = 55155 cm^{-1} gives the energy difference between the excited state and the v = 0 state of the ground state: E_{total} = 104160 ± 16 cm^{-1}. The two-photon energy of the laser at 193.25 nm lies at approximately 103500 cm^{-1}, which is relatively close to the calculated level. The difference remaining may be explained by a calibration error in the monochromator. This value also lies above the lowest ionization potential of oxygen. To still be able to record fluorescence from this state its valence needs to be equal to that of the lower state. Therefore, the fluorescing state is expected to be a Rydberg state converging on the $a^4\Pi_u$-state [106] or a high vibrational state of a high-lying Rydberg state converging to the ionic ground state. The proposed transition is shown in the potential energy diagram in Fig. 6.9. This two-photon excitation goes through the B-state, which undoubtedly also contributes to the transition strength.

Which v'

To calculate the position of the Rydberg state converging to this a-state the Rydberg formula given in Chapter 5 (Eq. 5.1) was used. The ionization potential, defined as the energy between the rovibronic ground states of the neutral molecule and the ion, is IP = 97284 cm^{-1} [107]. Using the molecular constants of the a-state of O_2^+, the vibrational energy levels of the Rydberg state converging to the a-state are calculated. With a Rydberg constant of 109735.5 cm^{-1} [107], the (lowest) n = 3 Rydberg state converging to the v' = 0
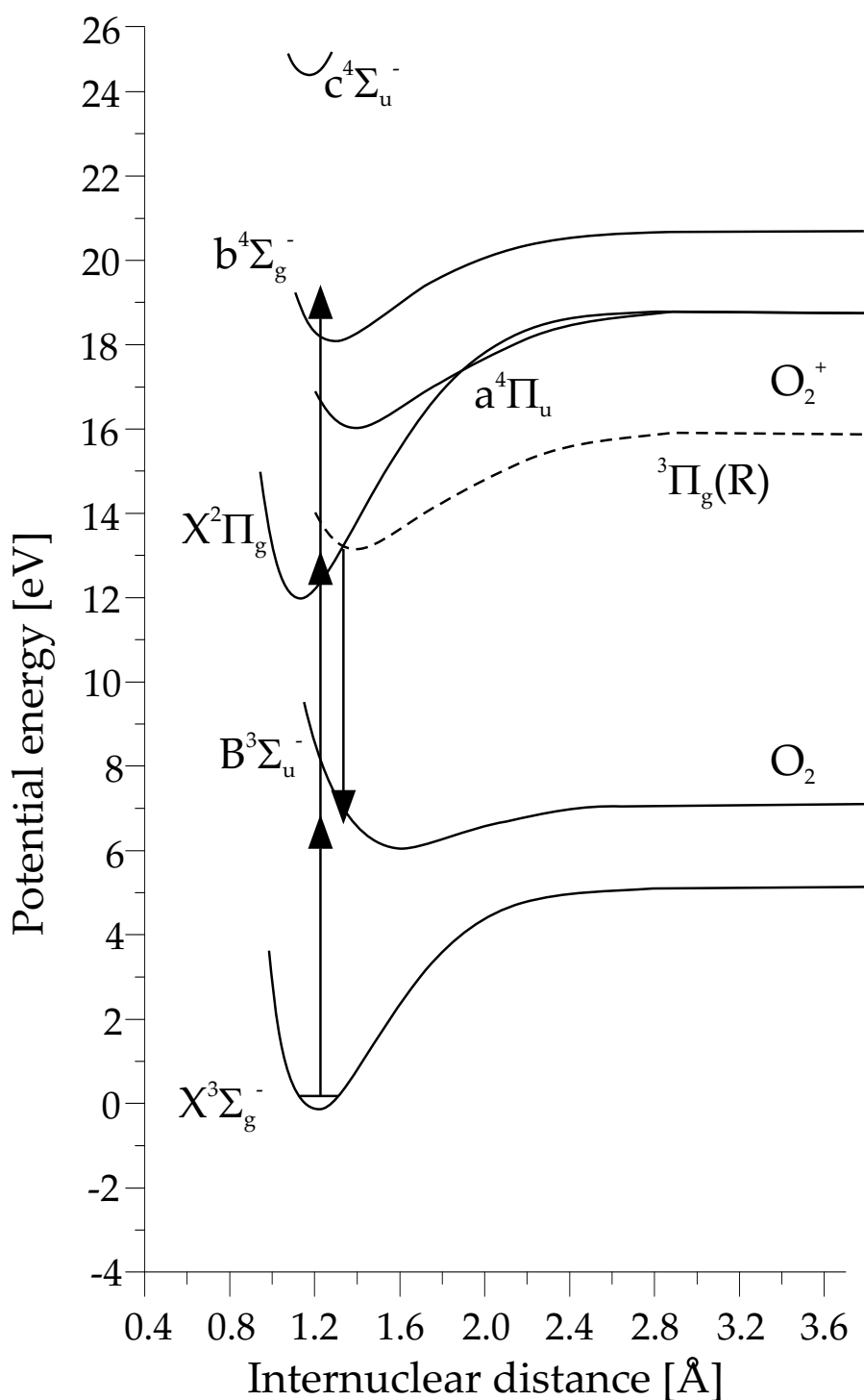
Figure 6.9: *A schematic picture of the potential energy curves involved in this assignment. The $^3\Pi_g(R)$ state is the Rydberg state converging to the $a^4\Pi_u$-state. A two-photon transition takes place from the molecular ground state to this Rydberg state. This state lives long enough to radiate back to the $B^3\Sigma_u^-$-state of the molecule.*
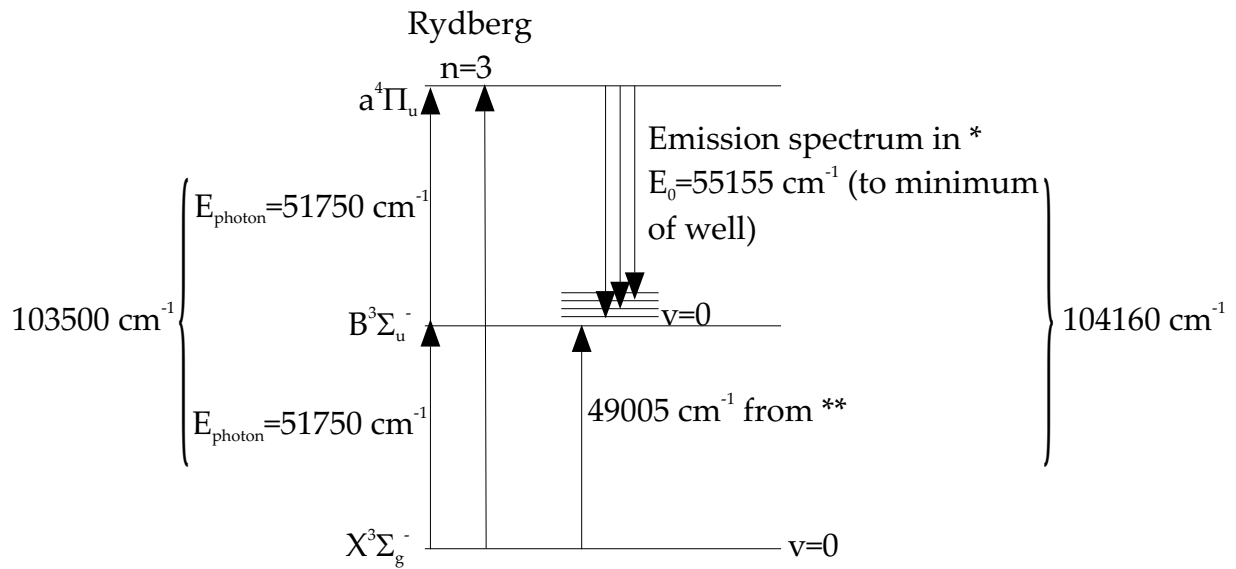
Figure 6.10: *A schematic overview of the energies and levels involved in the proposed two-photon excitation of oxygen. * = Fig. 6.7, ** = [105]*

level of the a-state was found, using a quantum defect of δ = 0.949 (Fig. 6.10). The calculated level lies closest to the fitted energy. This level and other vibrational levels together with the corresponding quantum defect are given in Table 6.2. An overview of the energies involved is given in Fig. 6.10. The difference between the photon energy level and the measured level is probably caused by an inaccuracy in the calculation of the Rydberg level, which has a low principal quantum number. The Rydberg equation is less accurate at low quantum numbers.

Since many vibrational levels are possible Franck-Condon factors were calculated for some low vibrational levels. By using a formula for approximate Franck-Condon factors derived by Nicholls [108] it was possible to plot relative intensities and compare them to the present experimental results. The general formula for the Franck-Condon factor $q(v', v'')$ is given by [108].

$$q(v', v'') = \frac{u^{v''-v'}e^{-u}}{v'!v''!}[(u - v'')^{v'} - \mathbf{H}(v' - 2)v''(v'(u - v'') + 2)^{v'-2}]^2, \qquad (6.7)$$

for $0 \leq v' \leq 3$, and $v'' \geq v'$, with $\mathbf{H}$ the Heaviside function and $u = S^2/2$, using

$$S = \Delta r_e \frac{\sqrt{c\mu_A\tilde{\omega}_e}}{\hbar} \qquad (6.8)$$

and

$$\tilde{\omega}_e = \frac{\sqrt{\omega_e'\omega_e''}}{\sqrt{\omega_e'} + \sqrt{\omega_e''}} \qquad . \qquad (6.9)$$

Figure 6.11 displays the calculated Franck-Condon factors for the vibrational states v' = 1, 2 and 3. The measured band intensities of the emission spectrum are included and
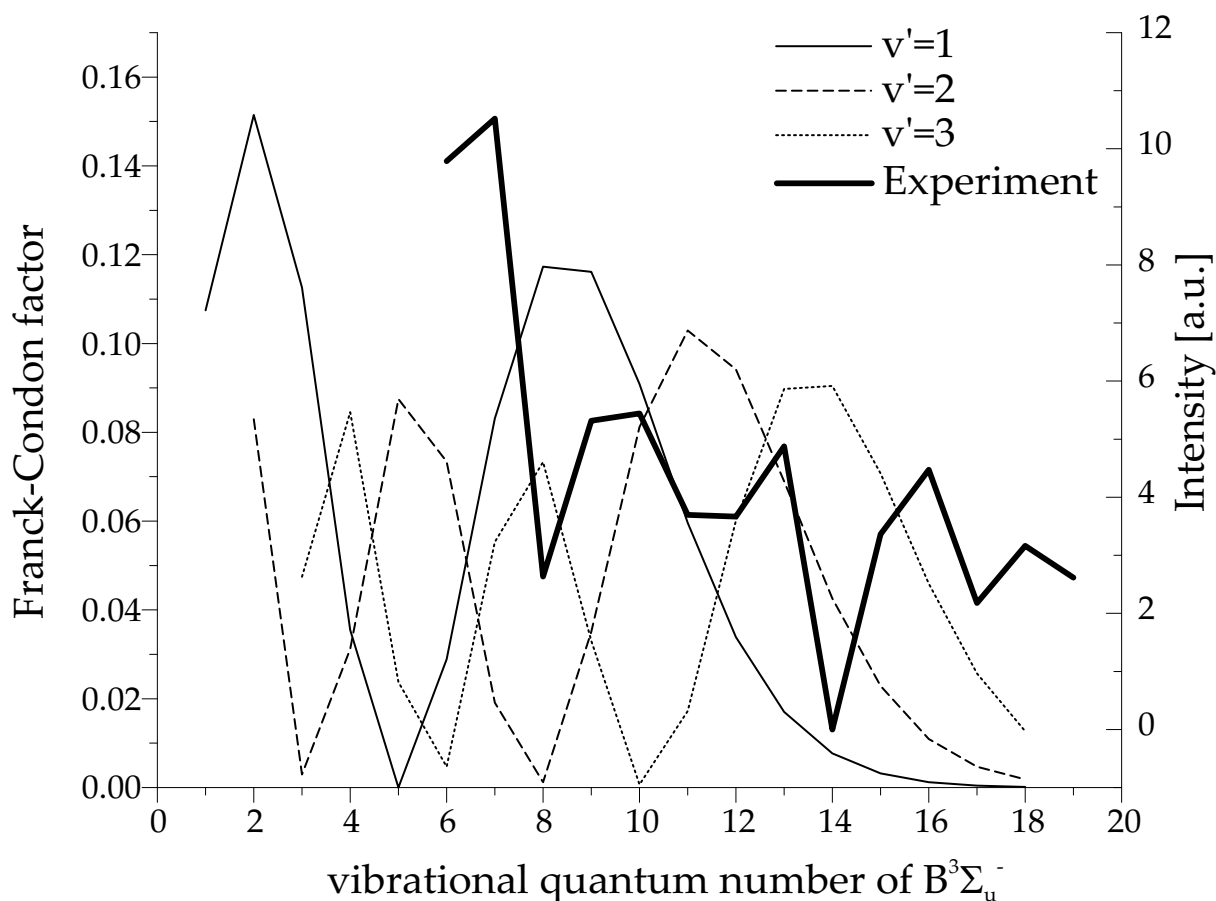
Figure 6.11: *A plot with calculated Franck-Condon factors for transitions from different vibrational levels of the $a^4\Pi_u$-state of O_2^+ to the B-state of O_2. The thick black line is a plot of the intensities of the bands appearing in the emission spectrum as a function of the assigned vibrational quantum numbers. The dips in the experimental intensities correspond to a band that coincides with the oxygen Raman line around 199 nm in Fig. 6.7 and a missing band around 210 nm in Fig. 6.7. The intensities of these bands have been estimated. Since the spectrum is composed of many accumulations, the intensities are assumed to be reproducible. There is no coincidence of the experiment and the calculations, which seems to indicate that a higher v' is involved.*

Table 6.3: *Electron configurations for different electronic states of the oxygen molecule and ion (taken from Krupenie [101]).*

	$(1\sigma_g)$	$(1\sigma_u)$	$(2\sigma_g)$	$(2\sigma_u)$	$(3\sigma_g)$	$(1\pi_u)$	$(1\pi_g)$	States
	2	2	2	2	1	4	2	$B^2\Sigma_g^-$, $C^2\Delta_g$, $b^4\Sigma_g^-$
O_2^+	2	2	2	2	2	3	2	$A^2\Pi_u$, $a^4\Pi_u$
	2	2	2	2	2	4	1	$X^2\Pi_g$
O_2	2	2	2	2	2	3	3	$B^3\Sigma_u^-$
	2	2	2	2	2	4	2	$X^3\Sigma_g^-$

it seems that the variations in band intensity with v'' in the experimental data is faster than that of the simulations. With increasing vibrational quantum number, the variation decreases, which is an indication that a higher vibrational Rydberg state is reached. Unfortunately, Nicholls' formulas are intended only for low vibrational states in at least one of the electronic states.

From the electron configurations of the involved states (see Table 6.3) it follows that excitation from the ground state of molecular oxygen to the proposed Rydberg state consists of exciting one $(1\pi_u)$-electron into a Rydberg orbit. For fluorescence to take place this Rydberg electron has to relax back to the $(1\pi_g)$-orbital corresponding to the configuration of the B-state. This overview also shows that autoionization to the $X^2\Pi_g$ of the ion involves a two-electron de-excitation process, which makes it less probable. The $A^2\Pi_u$ state does not have a Rydberg state in the desired region.

The calculated value for the quantum defect, however, results in an assignment of a Rydberg state which seems to be in conflict with a selection rule. According to Wu *et al.* [99] the quantum defect of oxygen Rydberg states is $\delta \leq 0.1$ for nd electrons, between 0.3 and 0.5 for np and between 0.9 and 1.2 for ns electrons. This means that the derived quantum defect of 0.95 for $v' = 0$ up to 1.39 for $v' = 20$ would correspond to an s-Rydberg electron. The parity of the orbitals of s- and d-electrons is *gerade*, while the parity of orbitals of p- and f-electrons is *ungerade* [109]. Together with the overall *ungerade* parity of the a-state the total parity gives an *ungerade* Rydberg state in case of an s-Rydberg electron. Coming from the *gerade* ground state, this two-photon transition is not allowed. The $n = 3$ Rydberg state, however, is the lowest possible Rydberg state, which raises the question whether the quantum defects obtained by Wu *et al.* are generally valid. Lewis *et al.* found that the quantum defect for $3p$ states lies between 0.6 and 0.8. This argument points in favor of the assignment of a p-Rydberg electron making the two-photon transition possible.

Progression II: The bound-continuum emission

The second progression that remains at low pressures can be seen in closer detail in Fig. 6.12. The band spacing is not completely regular, but generally is seen to increase with wavelength. As compared to the bound-state progression discussed above, the greater width of the individual bands is a distinct feature of progression II. Also, these widths show a regular trend (see Fig. 6.13). At 238 nm the progression is apparently
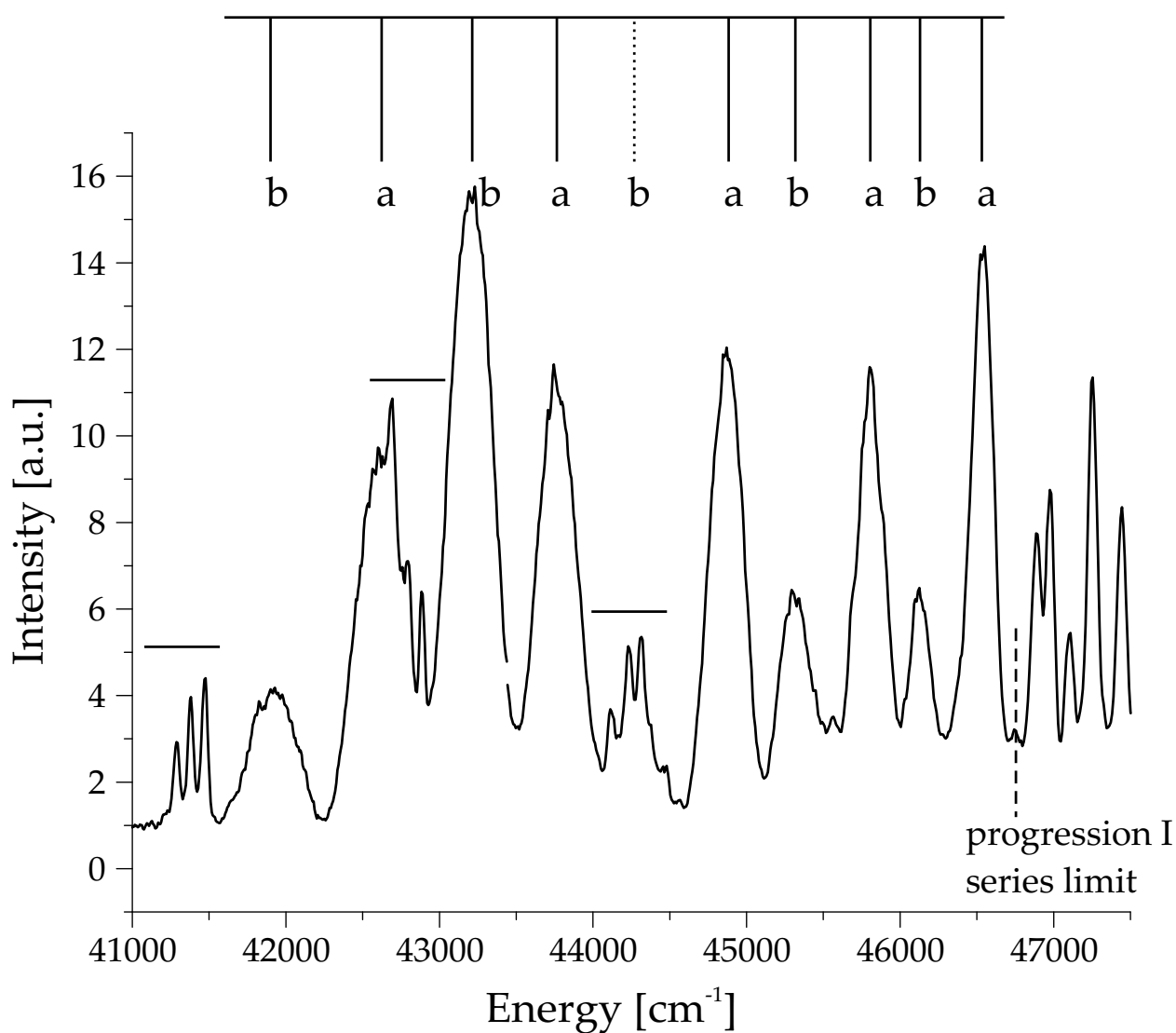
Figure 6.12: *Part of the emission spectrum at very low pressure with a progression of bands indicated. Horizontal bars indicate remaining structure from the Schumann-Runge band, that is not yet completely eliminated at the lowest pressure obtainable in our experiments (limited by practical constraints). Besides assigning all structure to the same progression, it is also possible to split this structure in two progressions: a and b.*
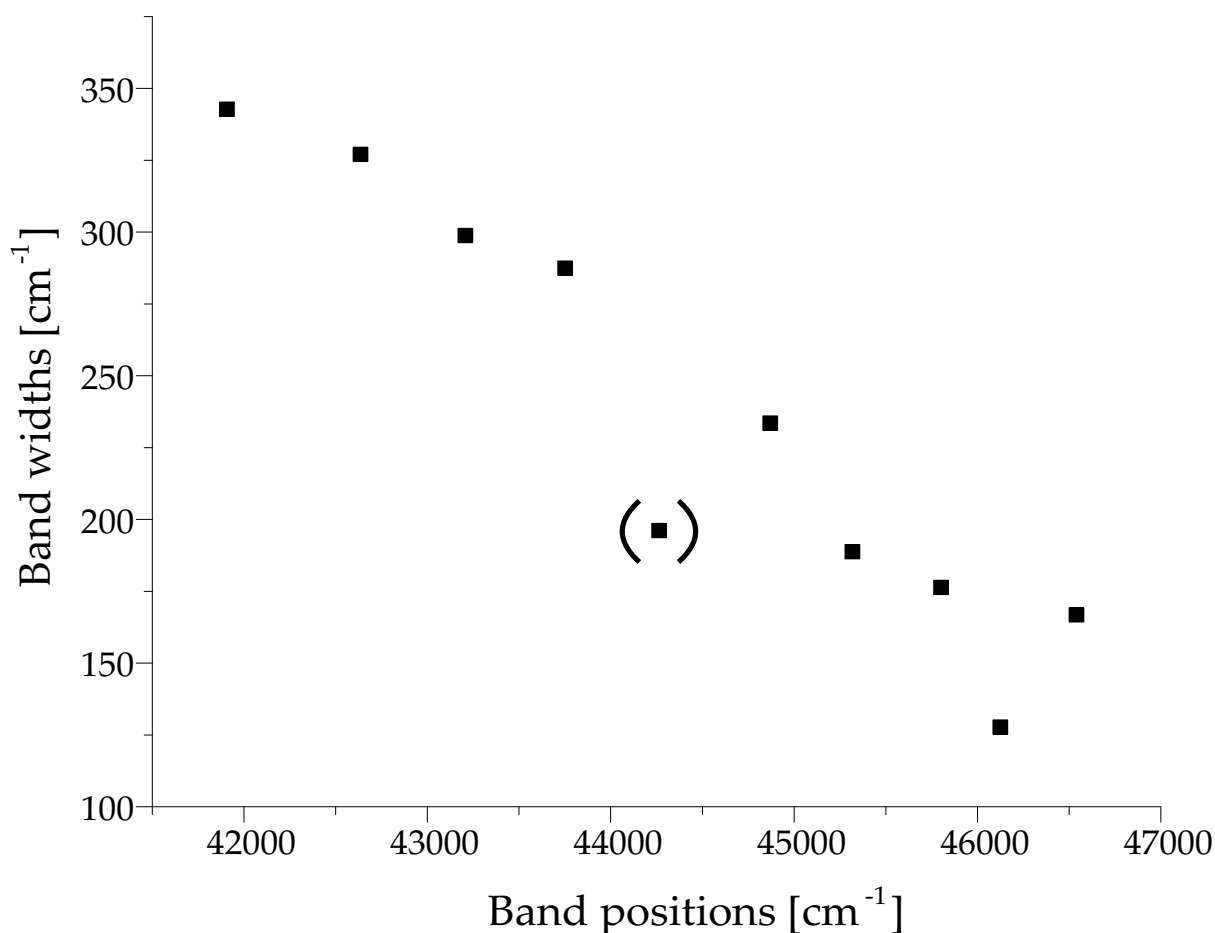
Figure 6.13: *Widths of the band structure in Fig. 6.12 (FWHM) as a function of band position. The width of the band at 44264 cm^{-1} is hard to determine due to the structure on top of it.*

truncated by a relatively weak and broad band (see also the spectrum of Fig. 6.5c). The assignment gives rise to some interesting complications.

Each consecutive structure in the spectrum is given a vibrational index number. Figure 6.14 shows a plot of the band energies. When fitted to the vibrational energy equation (6.6) it can immediately be seen that the energy differences between the bands increase with increasing wavelength. This trend does not correspond to normal potential energy wells, where the vibrational level spacing tends to decrease higher up in the well.

There is, in fact, another potential contradiction that the assignment needs to take care of, and that involves the large difference in widths of the bands in both progressions I and II. The structure in the excitation spectrum always gives rise to both emission progressions simultaneously. Thus, both the narrow structures of what was called the bound-bound emission as well as the broad structure of progression II must apparently arise from the same upper state. Since also the spectral structure in the excitation spectrum (Fig. 6.3) is narrow, the upper state cannot be predissociated (at least not as extensive
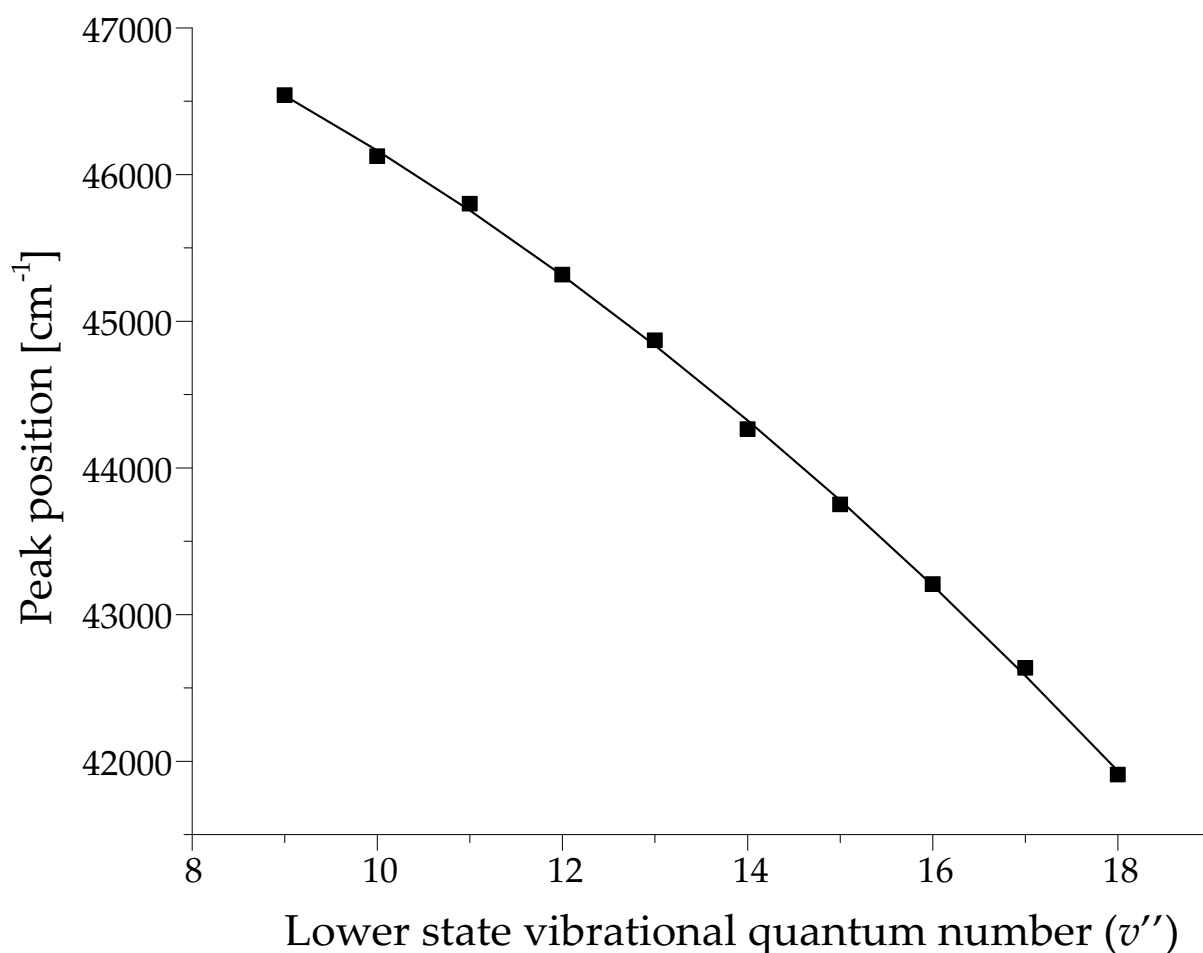
Figure 6.14: *A fit of the vibrational energy function to the bands indicated in Fig. 6.12, assuming all structure in progression II to belong to a single progression. The distance between the bands is seen to increase with v'', which can not be the case for a realistic potential.*

as, for instance, the B(v' = 4)-state, which gives rise to the broad dips in the ArF excimer laser gain profile). Nevertheless, there also does not appear to be much rotational redistribution in the emitting state, because the bound state progression is narrow as well. This speaks in favor of a Rydberg state, in which the electronic excitation is decoupled from the rigid body rotation of the heavy part of the molecule. This, however, also implies that the width of the bands in progression II must have a different origin. In fact, the width must arise from the lower state, that is, progression II is likely to be the result of emission out of a long-lived upper state to the repulsive well of an unbound lower state.

Interestingly, what stands out in our spectrum is that the two different progressions are concatenated. Where the assigned bound-state emission band stops, the emission band with broader structure starts as can be seen in Fig. 6.6.

The phenomenon of structure in the transition from a bound state to a repulsive state
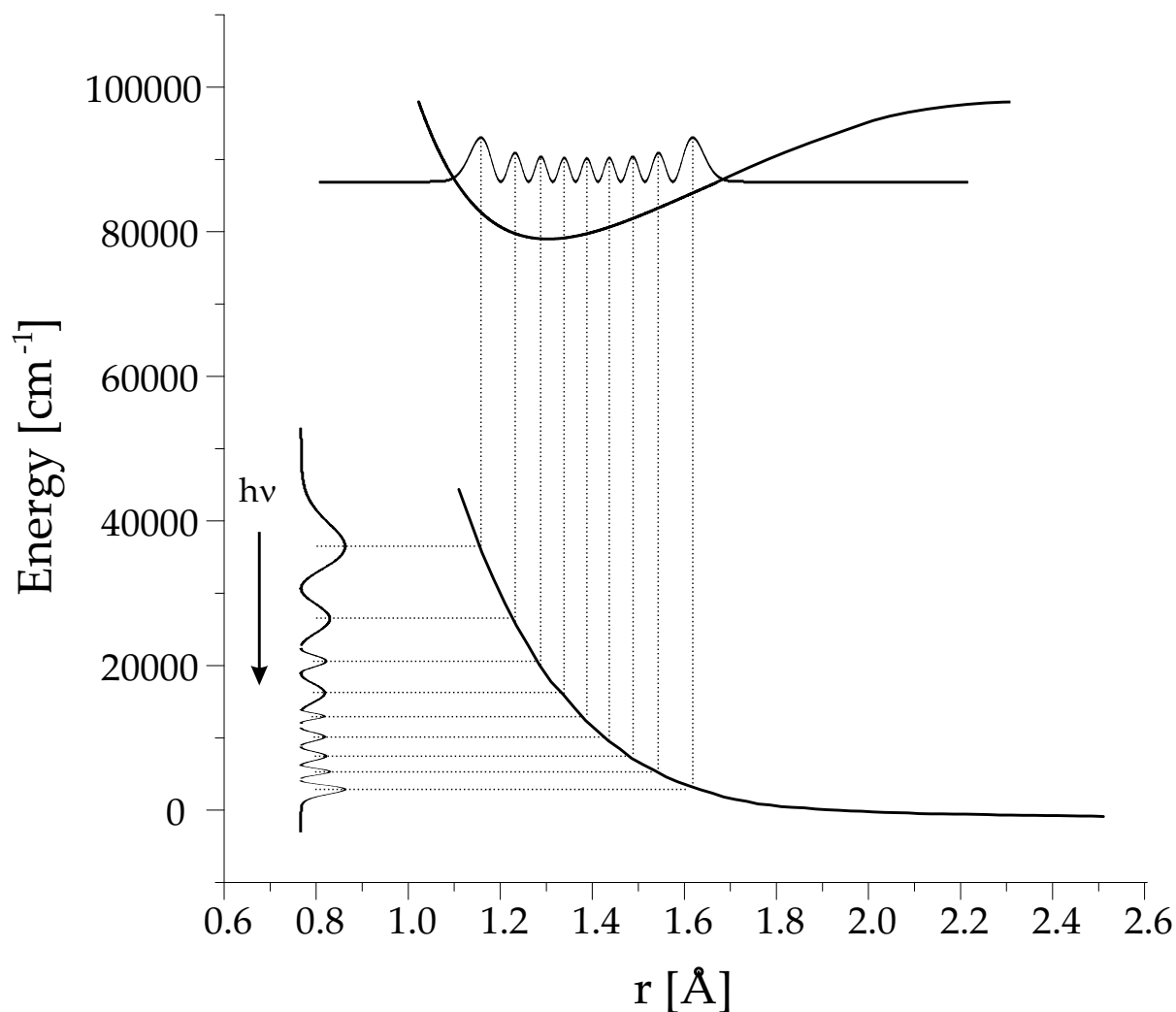
Figure 6.15: *Schematic representation of a transition between a higher-lying bound state and a lower-lying repulsive state or a bound state with a repulsive branch. Since the relaxation occurs into the continuum, no vibrational structure will be visible in the fluorescence. We will, however, detect the wavefunction of the upper state, where each maximum in the probability distribution will create a maximum in the fluorescence intensity. The energy position of the structure is determined by the difference in energy between the radiating state and the position of the repulsive curve. Note that the energy scale of the resulting spectrum is in the opposite direction of the y-scale of the graph. The exact shape and width of the resulting structure will be determined by the Franck-Condon factors and wavefunctions of the lower states.*

Table 6.4: *Calculated dissociation limits using the transition point between the two spectra at 214 nm for multiple (n) photon transitions at 193.2 nm (51750 cm^{-1}). More than three photons do not result in possible dissociation limits.*

n	Dissociation limit [cm^{-1}]	Dissociation limit [eV]	Products	Literature value [eV]
2	56800	7.04	O(^{3}P) + O(^{1}D)	7.08
3	108550	13.46	O(^{1}S) + O(^{1}S)	13.50
4	160300	19.87	-	-
5	212050	26.29	-	-
6	263800	32.71	-	-

has already been seen in the 1920s [110]. Since such a transition occurs from one vibrational bound state to the continuum of the lower state, the typical fluorescence structure consisting of vibrational bands will not be detected. What we will see, however, is the probability distribution of the wavefunction in the upper bound state. Figure 6.15 shows an example of a transition from a bound upper state to a repulsive lower state. The wavefunction of the lower state is now essentially a free particle wavefunction, with increased amplitude near the classical turning point. In zeroth approximation, and as a direct manifestation of the Condon principle [111], the Franck-Condon factors now sample the vibrational wavefunction of the upper state, and therefore we will now detect a representation of the probability distribution of the wavefunction in the upper state. The maxima of this distribution will become maxima in the emission spectrum. The spectral positions of these maxima are not directly determined by the internuclear separation, but indirectly by the energy difference between the radiating state and the repulsive curve at that internuclear separation. Experiments showing this phenomenon have been performed previously on molecular iodine, I$_2$ [112], and on the NaK dimer [113,114]. In the latter case also a mapping method was created to determine the shapes of the upper and lower potential curves.

In the present case the tentatively assigned bound-state spectrum (progression I) and the spectrum with broad structure (repulsive-state spectrum) lie next to each other, which indicates that both progressions have the same dissociation limit as illustrated in Fig. 6.16. The repulsive curve included in this figure was extracted from calculations by Michels [115]. Typical fluorescence structure due to a vibrational progression up to the dissociation energy was detected, and above that the repulsive-state spectrum is observed. The energy at the separation between the two spectra thus must represent the energy difference between the excited state and the dissociation energy. When comparing this energy to different dissociation energies, it turns out that the B$^3\Sigma_u^-$ state is by far the most likely candidate. The limit of 214.0±0.2 nm corresponds to an energy of 46700±40 cm^{-1}. Subtracting this from the two-photon excitation frequency of 103500 cm^{-1} an energy of the dissociation limit E = 56800±40 cm^{-1} is obtained. Using the dissociation energy of the B-state, D_e = 8121 cm^{-1} and adding the energy of the B-state with respect to the v = 0 of the ground state T = 49005 cm^{-1}, we arrive at an energy of E = 57126 cm^{-1} (see Fig. 6.17) which is in reasonably good agreement, when the previously mentioned monochromator
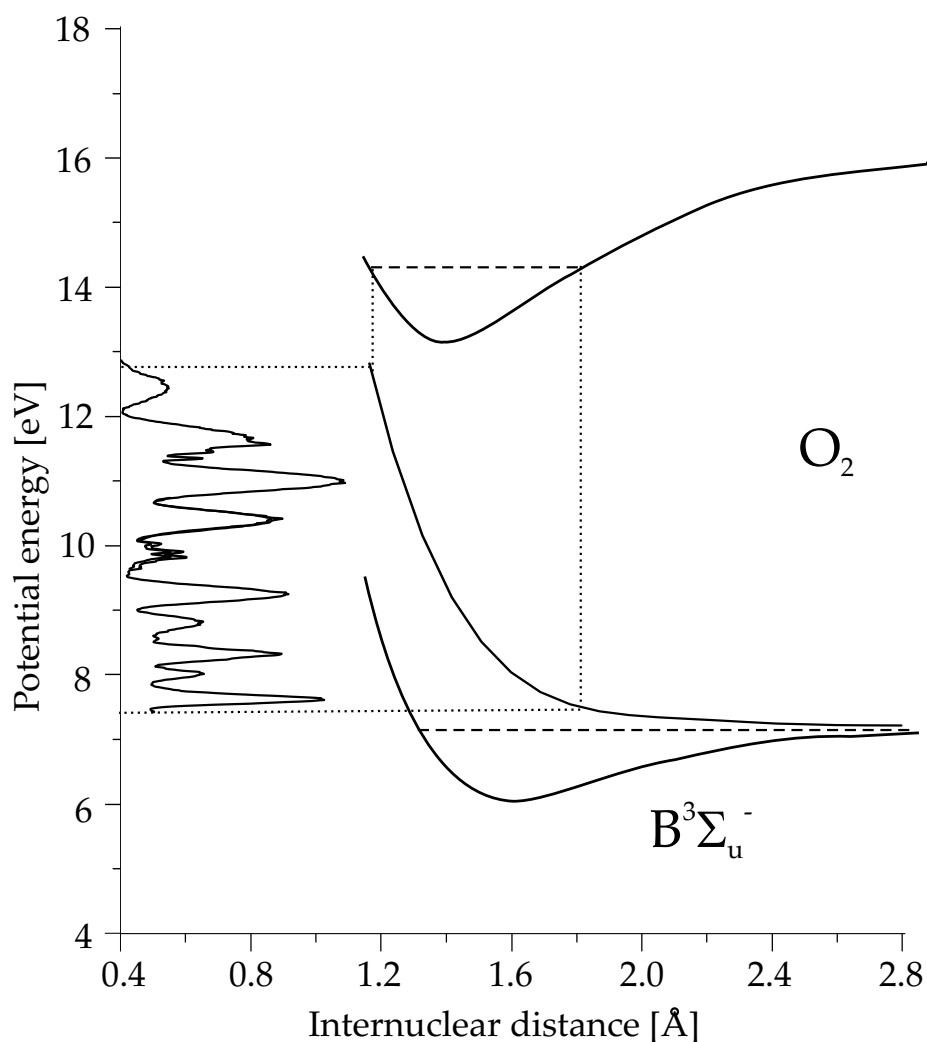
Figure 6.16: *The measured spectrum included in the transition down from the assigned Rydberg state to the B-state or to a repulsive $^3\Sigma_u^-$-state that has the same dissociation limit as the B-state. This repulsive potential well was determined by Michels [115]. This mapped wavefunction can be compared to the modelled one in Fig. 6.15. Note that if all experimentally observed structure is due to the emission from one single vibrational state, the emitting state would have $v' = 9$.*
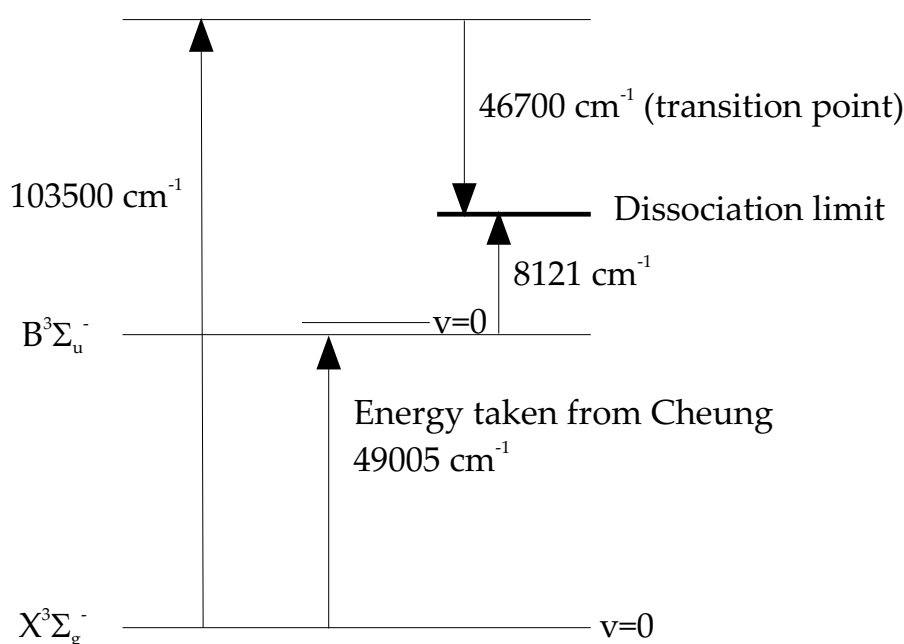
Figure 6.17: *A schematic overview of the energies and levels involved in the proposed two-photon excitation of oxygen, followed by a bound-continuum emission.*

error is taken into account.

As shown in Table 6.4 the limit for three-photon excitation would correspond to the dissociation into two ^{1}S oxygen atoms, which is unlikely, since the excitation spectrum is still very sharp. Moreover, there is no bound state with the same dissociation limit and sufficient well depth to accommodate all bands for progression I.

On the assumption that the emitting state is a Rydberg state in a progression that converges to the a$^4\Pi_u$-state in O$_2^+$, the energy axis of the spectrum can be mapped onto the internuclear distance. As can be seen in Fig. 6.15 there is a 1:1-relation between wavelength (λ) and internuclear distance (r). Using this figure, the measured spectrum can be projected onto the radiating state, resulting in the squared wavefunction of this state. In order to complete this mapping, the shape of the unbound potential has to be known.

Lower state: B$^3\Sigma_u^-$

In a first attempt we have assumed that the repulsive part of the B$^3\Sigma_u^-$-state is the relevant lower potential curve, and approximated this potential energy curve by a Morse potential [116]

$$V(r) = D\left(1 - e^{-a(r-r_e)}\right)^2 \tag{6.10}$$

Figure 6.18: *When mapping the energy axis of the emission bands on the Morse potential of the $B^3\Sigma_u^-$-state of oxygen, a spectrum as a function of internuclear separation is obtained, representing the square of the wavefunction ($|\psi|^2$) of the radiating part of the potential curve. The complete width of this state here is less than 0.05 Å, which is way too small for any realistic potential.*

with $D = \omega_e x_e S^2$, $a = \frac{1}{Sr_e}\sqrt{\frac{D_e}{B_e}}$ and $S = \frac{\omega_e}{2\omega_e x_e}$; the spectroscopic constants were taken from Cheung *et al.* [105]. Using the inverse of the Morse potential of the B-state

$$r = r_e - \frac{\ln\left(1 - \sqrt{\frac{E}{D}}\right)}{a} \qquad (6.11)$$

and shifting the turning point of the spectrum at 214 nm to the dissociation energy of this B-state, the spectrum can be mapped on the internuclear distance. The result can be seen in Fig. 6.18, which indicates that the assignment to the B-state is unlikely. Due to the steepness of the repulsive flank of the B-state, the whole spectrum would have to arise from vibrational structure in a range of less than 0.05 Å. This range is much too small for

a typical potential energy well, especially when considering that the amount of maxima in the probability distribution is at least one more than the vibrational quantum number, i.e. $v \geq 9$, where the well is relatively broad. Therefore, another potential energy curve, with the same dissociation energy as that of the B-state is more likely.

Lower state: $^3\Sigma_u^-$

In a second attempt, we considered as possible lower state the unbound $^3\Sigma_u^-$ state with the same symmetry as the B-state as calculated by Michels [115]. An exponentially decaying curve was fitted to the data from his paper:

$$E = E_0 + A_1 \exp(-r/t_1) \tag{6.12}$$

with $E_0 = 57126$ cm^{-1}, $A_1 = 3.22 \cdot 10^7$ cm^{-1} and $t_1 = 0.21$ Å. Inversion of this function gives

$$r = -t_1 \ln\left(\frac{E - E_0}{A_1}\right) \quad . \tag{6.13}$$

Again shifting the turning point to E_0 a mapping is obtained as shown in Fig. 6.19. This mapping shows a much broader and more realistic curve, but the internuclear distance is shifted to larger distances as compared to the a$^4\Pi_u$-state, making the assignment nevertheless unlikely.

Upper state

It is also possible to start with the wavefunction of a vibrational level in the a$^4\Pi_u$ state in order to determine the shape of the repulsive curve. Assuming that the maxima in the measured spectrum represent the maxima in this wavefunction, values of the internuclear distance can be assigned to a potential energy value (classical turning points; compare Fig. 6.15). These energy values are obtained by subtracting the photon energies of the emission spectrum maxima from the two-photon energy level (the radiating state).

Assuming the entire structure, consisting of ten maxima, to belong to the same progression, so that the entire wavefunction is mapped, the $v' = 9$ state is the lowest possible vibrational state. For higher vibrational states the left part of the probability distribution is probably not measured. The probability distribution of the wavefunction in this state is simulated by using Hermite polynomials $H_v(y)$ [117]

$$\psi_v(x) = N_v H_v(y) e^{-y^2/2} \qquad y = \frac{x}{\alpha} \qquad \alpha = \left(\frac{\hbar^2}{\mu k}\right)^{1/4} \tag{6.14}$$

where N_v is a normalization factor

$$N_v = \left(\frac{1}{\alpha\sqrt{\pi}2^v v!}\right)^{1/2} \quad , \tag{6.15}$$

μ is the reduced mass of the oxygen molecule and k is the spring force constant

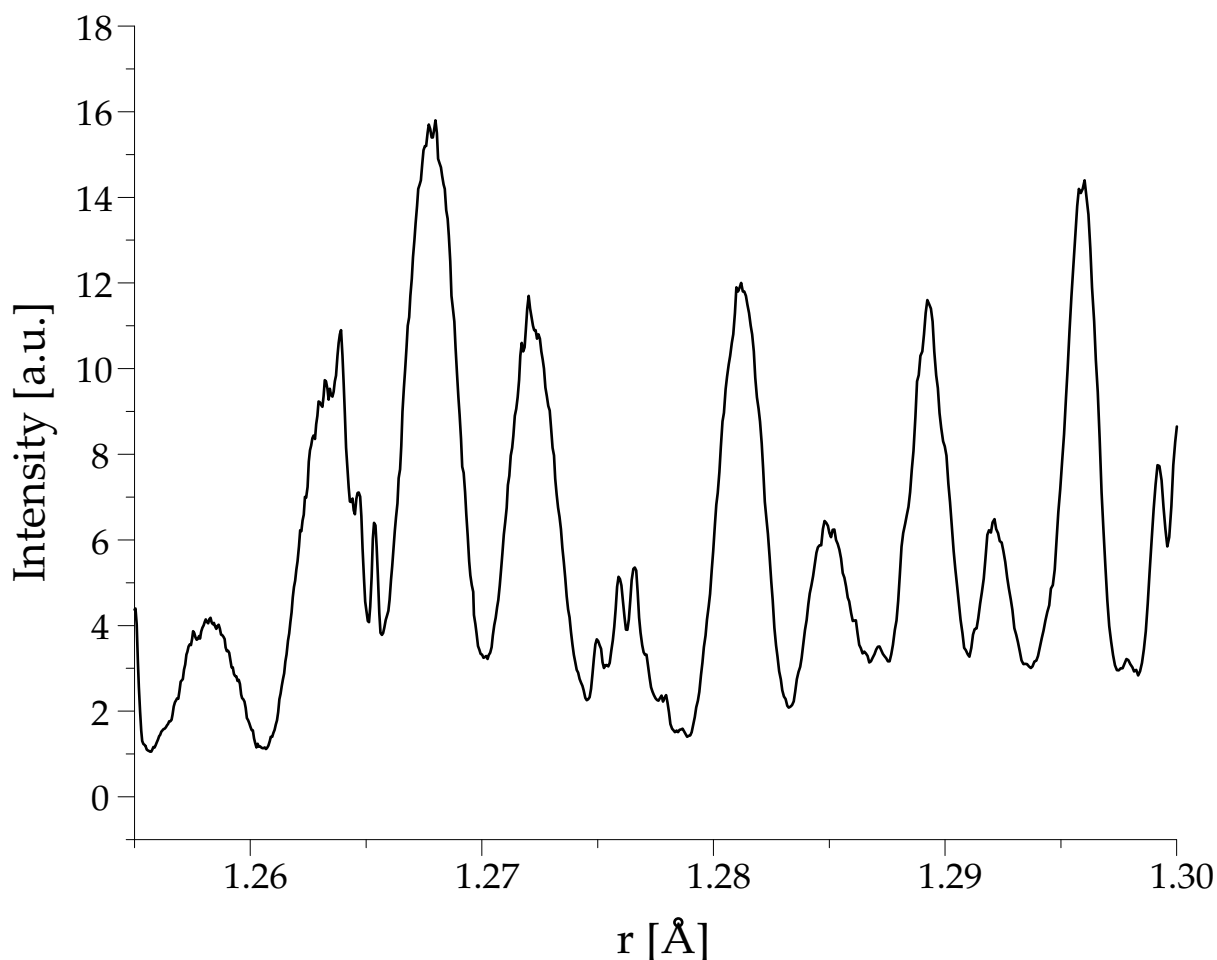$$k = \mu\omega_e^2 \quad . \tag{6.16}$$
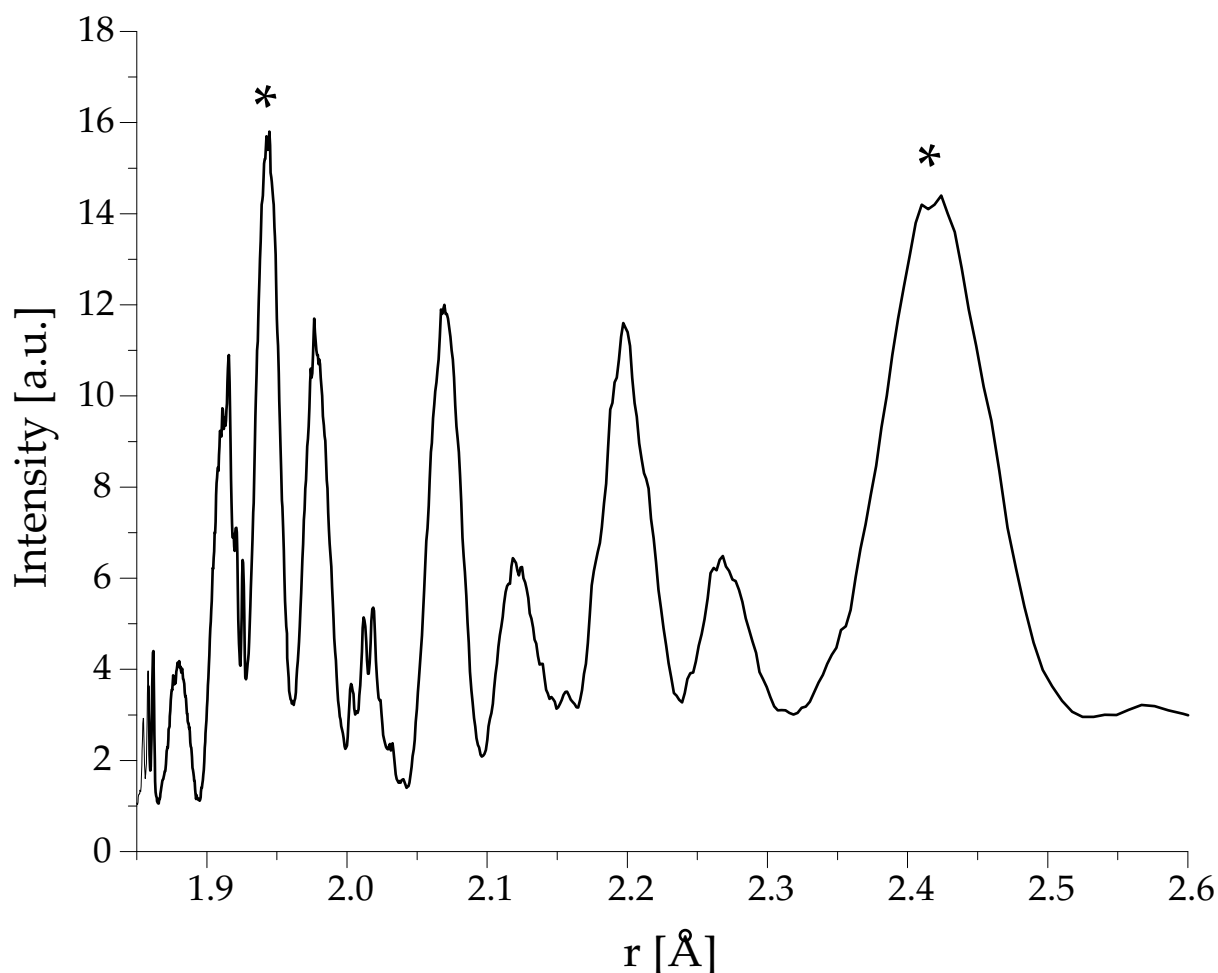
Figure 6.19: *When mapping the energy axis of the emission bands on the Morse potential of the unbound $^3\Sigma_u^-$-state of oxygen [115] a spectrum is obtained as a function of internuclear separation, representing the width of the radiating part of the potential curve. The complete width is large enough to represent a potential energy curve. The intensities of some of the bands break the regularity in the progression (*), since the intensities are higher than expected from surrounding bands. These might originate from an overlap with the B-state continuum.*
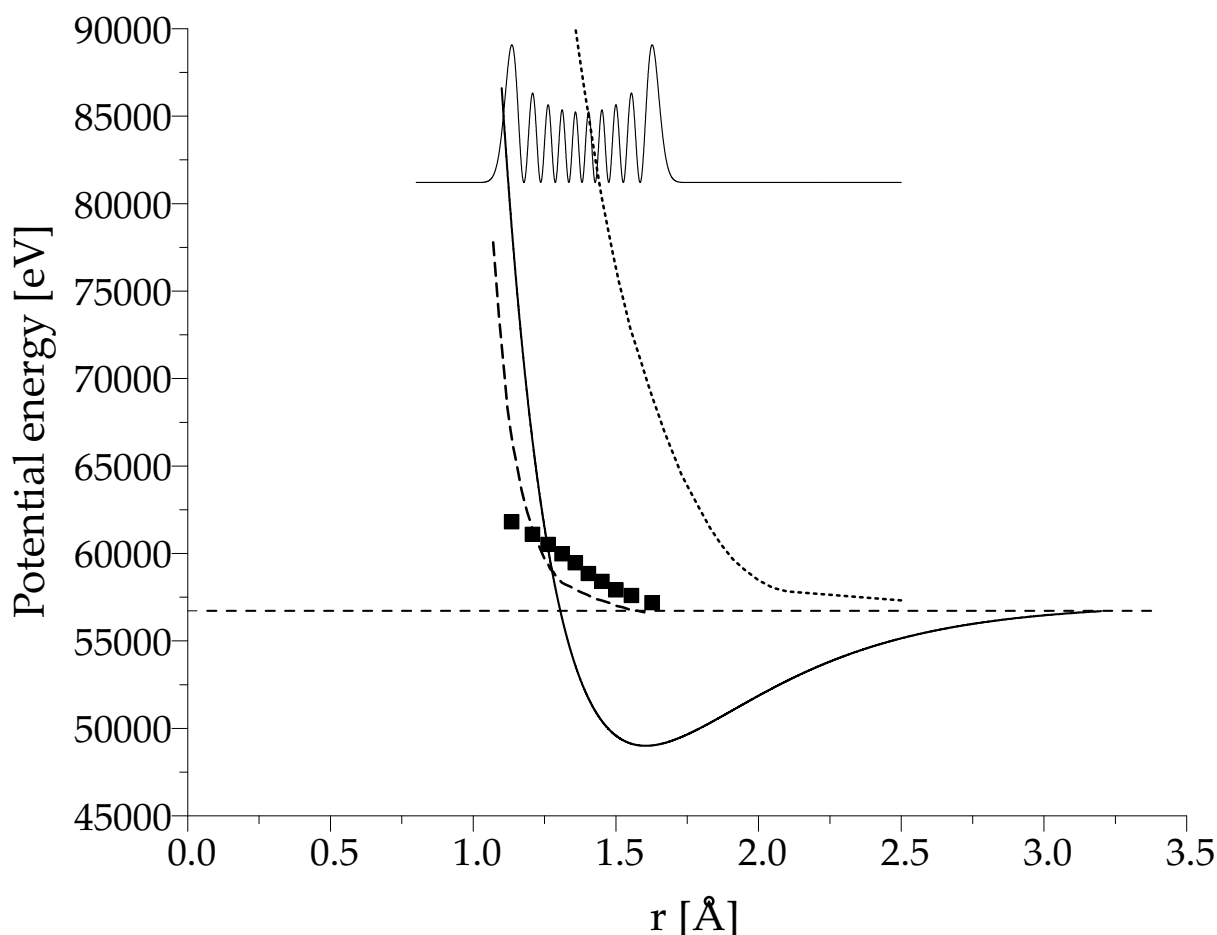
Figure 6.20: *Repulsive curve calculated from all maxima in the emission band starting at the lowest wavelength, together with the Morse potential of the $B^3\Sigma_u^-$ state. The position of the squared wavefunction is based on the internuclear distance of the a-state. Progression II is assumed to consist of only one progression. The dotted line is a $^3\Pi_u$ state, which is the allowed state (single photon emission form the emitting state) that lies closest to the created curve. The dashed line is a forbidden $^3\Pi_g$ state. Both curves are taken from Michels [115].*

Figure 6.20 shows the resulting points of the lower repulsive curve.

As an alternative, the emission structure is split up in two parts, the a and b designations from Fig. 6.12, based on the intensities of the bands. Figure 6.21 shows the repulsive curves resulting from, respectively, the a and b bands, when assuming that the $v' = 4$ state is the upper state. As expected the slopes of the repulsive curves in Fig. 6.20 and Fig. 6.21 strongly differ from the slope of the repulsive branch of the B-state. From literature no repulsive states are known with one of these two shapes. The figures also include curves calculated by Michels [115], that converge to the same limit of the $B^3\Sigma_u^-$ curve. Several allowed $^3\Sigma_u^-$ and $^3\Pi_u$ states have been described, but none resembles the calculated curve. Another forbidden $^3\Pi_g$ state also included in the figures lies relatively close, although the
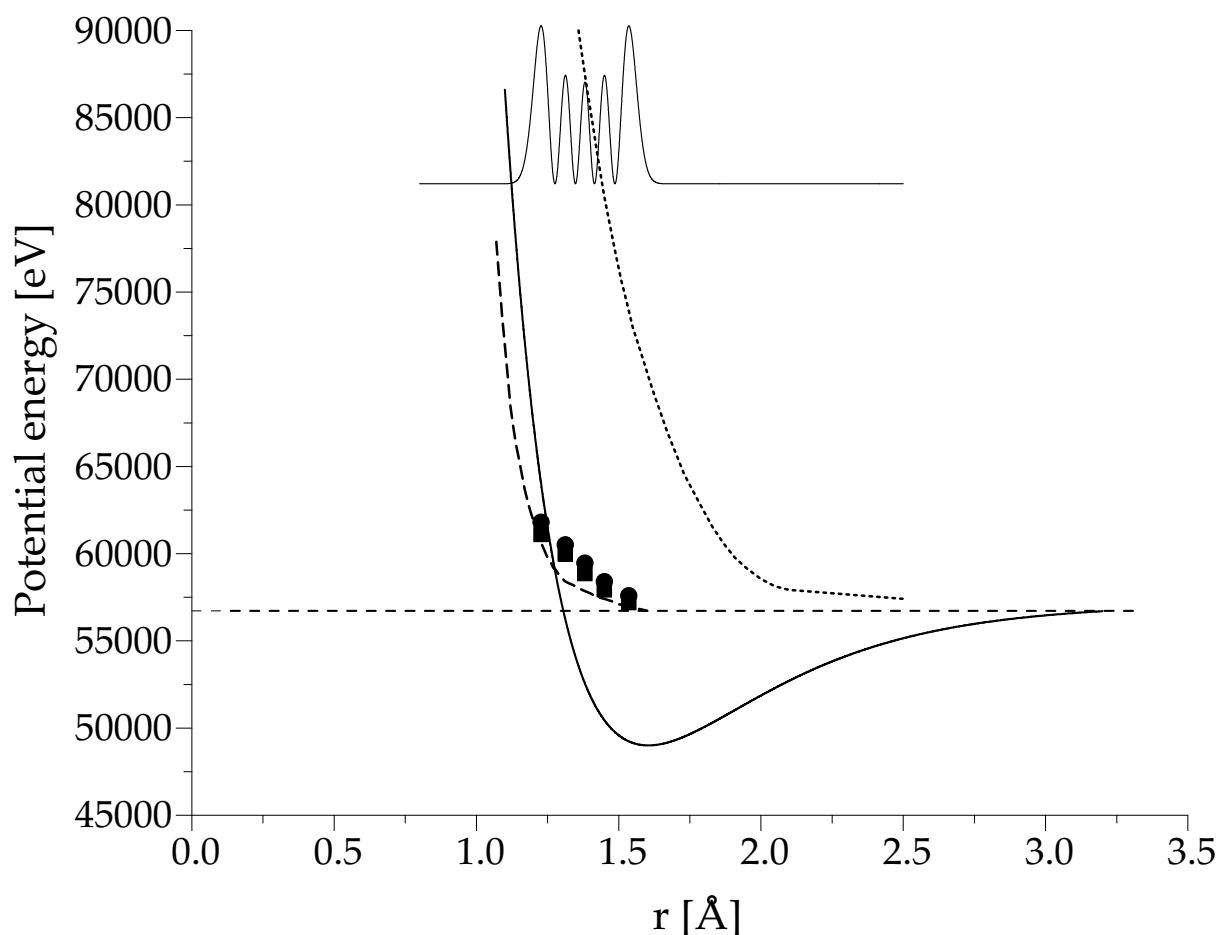
Figure 6.21: *Repulsive curve calculated from the b (dots) and a (squares) maxima (from Fig. 6.12) in the emission band starting at the lowest wavelength, together with the Morse potential of the $B^3\Sigma_u^-$ state. The dotted line is a $^3\Pi_u$ state, which is the allowed state (single photon emission form the emitting state) that lies closest to the created curve. The dashed line is a forbidden $^3\Pi_g$ state. Both curves are taken from Michels [115].*

difference is still too large to assign our curve to the $^3\Pi_g$ curve, within the accuracy of the calculations presented above. The calculations of Michels, however, do not place any accuracy on the values. This still leads to the conclusion that the present measurements point in the direction of a thus far unknown repulsive potential energy curve.

6.3.2 Excitation spectrum

The assignment for the excitation spectrum (see Fig. 6.3) has not been completed. Two possibilities are a rotational or a Rydberg structure. The sharp lines indicate that the upper state is stable, no autoionization or predissociation is taking place. The structure also remains at low pressures. Complete information on the emission spectrum should

provide the solution to the excitation spectrum of oxygen.

6.4   Conclusion

Multi-photon excitation of gas phase molecular oxygen shows sparse but sharp spectral structure in the tuning range of the ArF excimer laser (51,600–51,800 cm^{-1}). This structure is thought to arise from bound states at the two-photon level, but the paucity of the spectrum and the limited tunability of the ArF laser preclude definite assignment. The emission spectrum that is induced by focused ArF laser radiation is highly structured (195–405 nm range). Most of the structure is ascribed to the Schumann-Runge system, resulting from sequential absorption of multiple photons during the relatively long (20 ns) excimer laser pulses. Between 195–240 nm, spectral features were found at which the excitation spectrum of oxygen showed distinct structures. This emission is assigned to arise from a $n = 3$ Rydberg state converging on the a$^4\Pi_u$ state of O$_2^+$. The emission spectrum consists of two different bands radiating from this a-state in the ion. The first band originates from relaxation back to vibrational states in the B$^3\Sigma_u^-$-state. The second band is caused by bound-continuum transitions onto a repulsive potential converging to the same dissociation limit as the B$^3\Sigma_u^-$-state. The measured emission spectrum consists of a projection of the vibrational wavefunction of the radiating state onto the radiation energy axis. We have not found in the literature any repulsive potential energy curve that resembles the derived curve.

Progression I has led to an assignment of $v' = 0$, which does not correspond to progression II, which resulted in $v' > 9$ (or > 4). This can be caused by different Franck-Condon factors between the two lower-lying states.

The structure of multiple bands in the excitation spectrum is not in disagreement with the assignment of the emission spectrum. Possibly it is a concatenation of rotational bands from both progression I and progression II, although no assignment could be made to fit that hypothesis.

Chapter 7

APART in Air

7.1 Introduction

The goal of this spectroscopic study was to examine the origin and creation of nitric oxide in the APART process. In the previous chapters the two important molecules involved in this process, oxygen and nitrogen, were discussed separately. In this chapter some experiments where those molecules were present together will be described, and their respective influences and interaction are investigated.

The study of the interaction between oxygen and nitrogen has many implications on atmospheric issues [118–120]. Under the influence of solar UV-radiation oxygen molecules, nitrogen molecules and many species involving their excited, ionized or dissociated states together form a very complex system. The formation of NO is a phenomenon that is also important in combustion processes where it is a major cause for pollution in industrial and urban areas.

In Chapter 6 it was shown that the processes in the focus of the ArF excimer laser closely resemble those occurring in plasmas and afterglows. In the literature a lot of information can be found on plasmas of nitrogen and oxygen [121,122], where the excited species play major roles. Afterglows are closely related to plasmas since they are the result of relaxing species after the driving force of the plasma has disappeared. The assignment of the nitrogen emission spectrum was aided by this knowledge, but, unfortunately, it did not give any help in the understanding of the oxygen emission spectrum.

Chemical NO creation pathways are also abundant in literature. Details of the environments and concentrations of oxygen and nitrogen influence branching ratios and excited-state species and atom formation to create NO and NO^+ [123–127]. Mixtures of oxygen and nitrogen will also effect their respective molecular spectra. Additions of small amounts of oxygen to nitrogen will quench certain transitions [128], and several rare gases [129] and other impurities [130] are known to alter intensities and sometimes even change spectral appearances of nitrogen. The interaction between the different molecules present in atmospheric conditions, including the impurities, appears to be very complex.

In this Chapter experiments are described which have been performed on determining the relation between the fluorescence intensities of different species (N_2^+, O_2 and NO) and the excimer laser intensity. The influence of the addition of oxygen to pure nitrogen on the typical nitrogen spectrum is studied and the creation mechanism of NO is discussed,

using available information from literature and experiments.

7.2 Fluorescence intensities versus laser power

7.2.1 Introduction

In APART nitric oxide is created photochemically out of molecular nitrogen and oxygen. Even if one neglects reaction barriers, the reaction

$$N_2 + O_2 \rightarrow 2NO \tag{7.1}$$

is endothermic by 1.9 eV [131, 132]. The dissociation energies (D_0) of N_2 and O_2 are 9.8 eV and 5.2 eV, respectively. If this is compared to the energy in one write laser photon, $h\nu \equiv 6.4$ eV, then only dissociation of oxygen and recombination with nitrogen can result in NO creation. The ArF laser, however, needs to be focused to create NO, which indicates that the NO creation must be a multiphoton process. Such processes generally show a non-linear dependence on the intensity of the inducing laser radiation. In this section we therefore study the intensity relations between several light scattering phenomena that are related to APART.

7.2.2 Experiment

This experiment was performed as described in Chapter 5 in a laminar flow. Two cameras, of which one was mounted on a spectrograph, as described in Chapter 2, were used to simultaneously measure laser power and fluorescence signals from different species. Because it was not possible to measure all relevant fluorescence intensities simultaneously, several series of experiments were performed.

In the first series of experiments the Rayleigh scattering signal from the ArF excimer laser beam was measured as a function of the excimer laser power measured with a power meter. Then, as a function of the intensity of the same excimer laser, the intensities of Rayleigh scattering, the N_2^+ fluorescence at 391 nm and the dye laser induced NO fluorescence 3 μs after creation were measured. The power of the excimer laser was varied in these experiments by changing the high voltage that drives the laser. The signals were accumulated for ten shots, resulting in averages and not single shot measurements.

In the second series we tried to employ the variations in shot-to-shot pulse energy to investigate the N_2^+, O_2 and NO fluorescence as a function of Rayleigh signal at 193 nm. By recording 9000 single-shot images per measurement of the combined signals, the variations in laser power permitted us to study the fluorescence dependence on laser power. The N_2^+ fluorescence signal was monitored by tuning the grating of the spectrograph to 390 nm, where both the fluorescence at 391 nm and the second order reflections of the Rayleigh signal could be recorded simultaneously. For the oxygen fluorescence the grating was tuned to 210 nm, where emission bands between 206 and 230 nm (including Schumann-Runge transitions and structure assigned at the two-photon level) were measured simultaneously with the Rayleigh signal at 193 nm. Because a band rejection filter for 193 nm was placed in front of the camera, the intensities of Rayleigh scattering
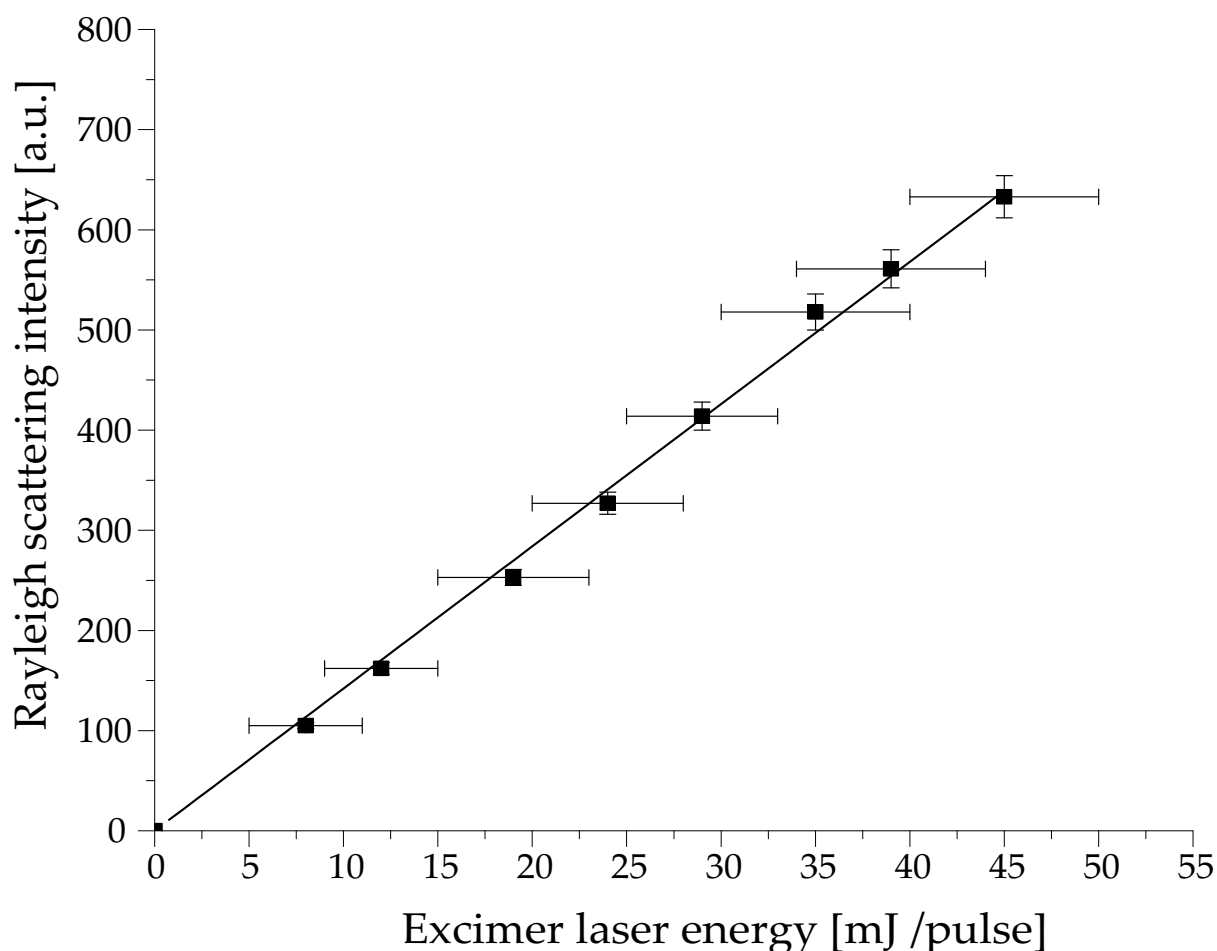
Figure 7.1: *Rayleigh intensity at 193 nm as a function of laser pulse energy in mJ/pulse. The solid line is a fit to Eq. 7.2 with a = 0 and c = 1.*

and fluorescence were comparable, but the emission between 193 nm and 206 nm was too weak to be taken into account. Two cameras had to be used to record the excimer intensity and the NO fluorescence occurring $3\,\mu$s later for every shot of the excimer laser. The spectrograph was tuned to 240 nm to record NO fluorescence at 236 nm, 247 nm and 258 nm and the dye laser Rayleigh signal at 226 nm simultaneously. Before comparing fluorescence with excimer Rayleigh signal imaged with a second ICCD camera, the NO signal was scaled linearly to dye laser intensity.

7.2.3 Results

Averaged

The results are plotted in Figures 7.1, 7.2 and 7.3. The first graph shows the linear dependence of the Rayleigh scattering intensity (integrated over approximately 5 cm over the
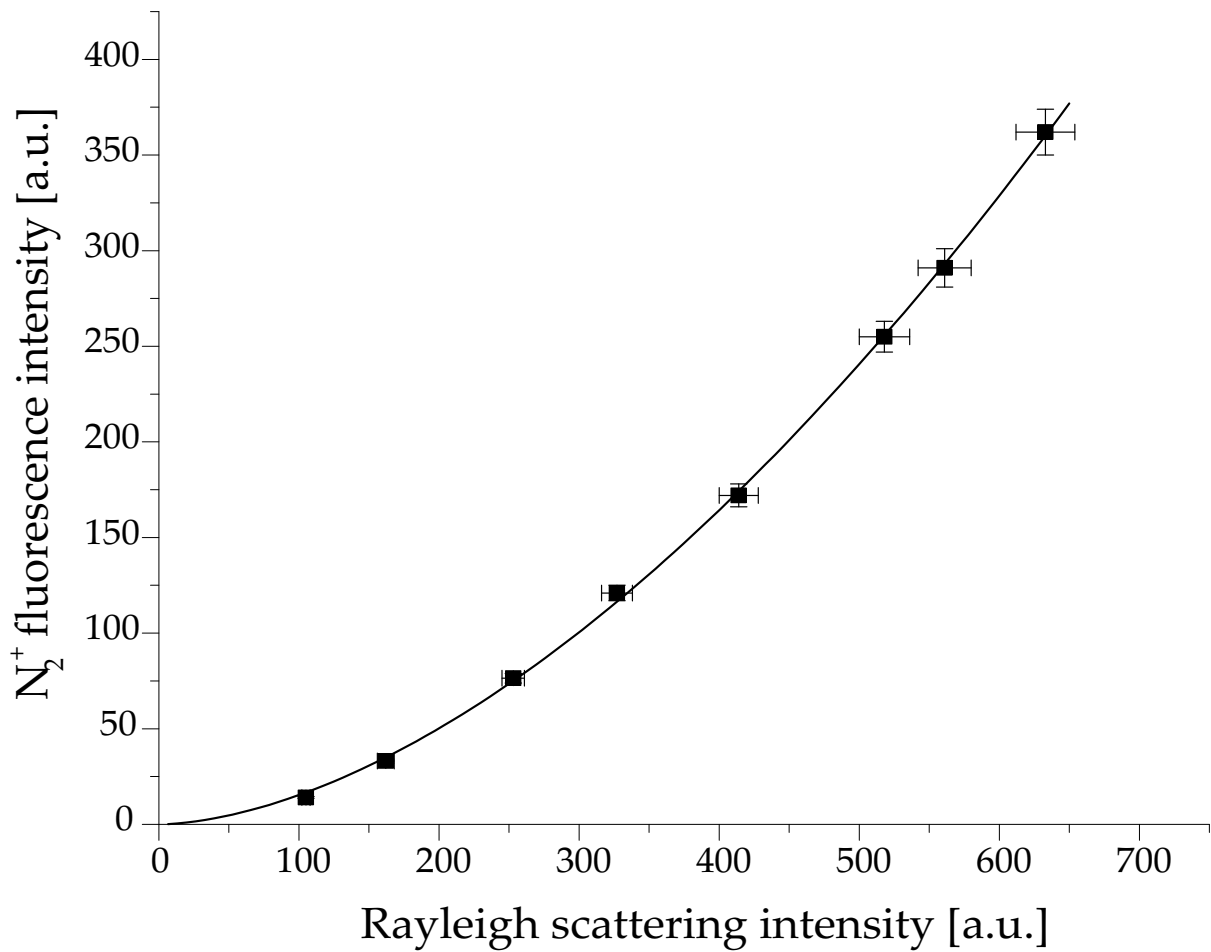
Figure 7.2: *N_2^+ fluorescence at 391 nm as a function of second order Rayleigh intensity at 386 nm. A power law (Eq. 7.2) has been fitted, from which the exponent was estimated to be c = 1.70 ± 0.02 and the offset a = 0.*

beam) measured by the spectrograph and camera on the average laser power measured with a power meter. Figure 7.2 shows the fluorescence intensity of N_2^+ in air (induced by the excitation line at 193.25 nm) at 391 nm integrated over all fluorescence along the laser beam as a function of Rayleigh scattering intensity around 386 nm. Figure 7.3 shows the dependence of NO fluorescence intensity as a function of separately measured Rayleigh intensity. To the data in Figures 7.1-7.3 a fit has been applied:

$$f(x) = a + bx^c \tag{7.2}$$

Here a indicates the offset from the x-axis and c gives the sought-after information on the intensity dependence. The parameter b is merely a scale factor, which mostly depends on alignment and other conditions and therefore contains no information we will use. The N_2^+ fluorescence data results in $a = 0$, and $c = 1.70 \pm 0.02$, and the NO fluorescence data (Fig. 7.3) results in $a = 160 \pm 30$, and $c = 2.0 \pm 0.2$. It seems that the creation of N_2^+
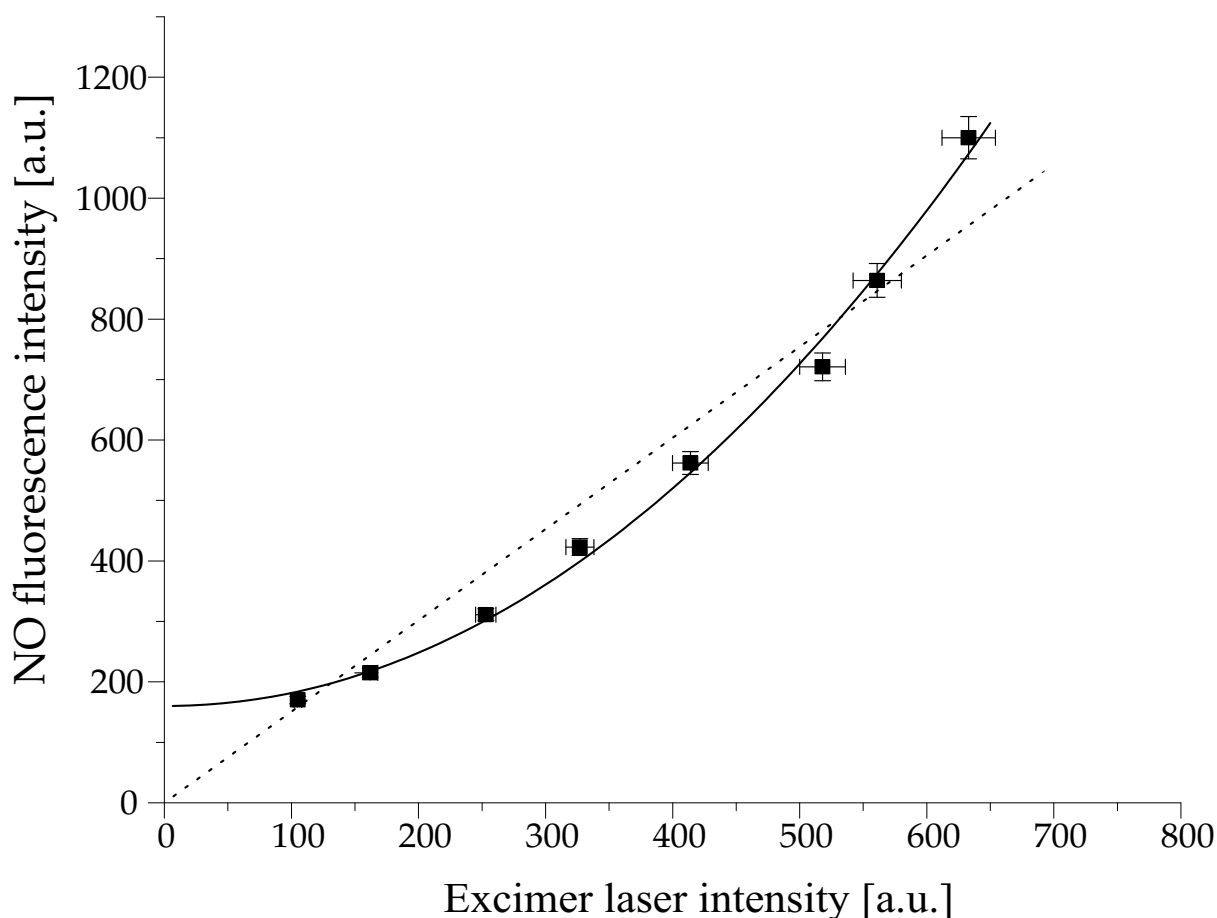
Figure 7.3: *NO fluorescence at 236 nm, 247 nm and 258 nm as a function of Rayleigh intensity at 193 nm. A power law (Eq. 7.2) has been fitted, from which the exponent was estimated to be c = 2.0 ± 0.2 and the offset to a = 160 ± 29 (see text). The dotted line indicates a linear fit which does not apply well.*

has an almost quadratic dependence on excimer laser pulse energy, whereas the NO creation shows an exact quadratic dependence (also shown in Fig. 7.4). There is, however, an offset in the graph in Fig. 7.3 which seems to indicate that no excimer laser power is needed to nevertheless create a small amount of NO. This can be explained by an increased amount of NO in the focus of the excimer laser, due to insufficient ventilation. Since background measurements were performed before the experiment, this NO would not disappear with background corrections. The large error on the offset value is an indication that this amount did not stay constant in time.

Single-shot

The single-shot measurements did not work out as expected. The relative spread in fluorescence intensities of oxygen, nitrogen and nitric oxide was too large to extract any
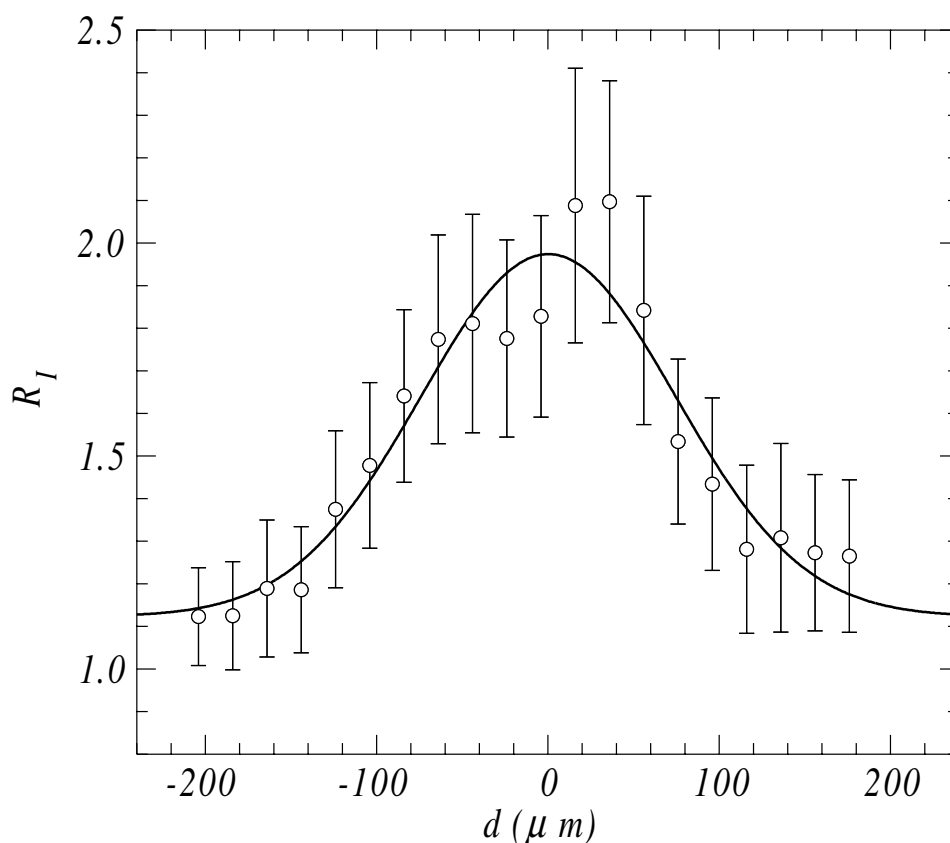
Figure 7.4: *Measuring the nonlinearity of the writing process by moving two writing beams trough their intersection point. Open circles: ratio $R_I = I_s/(I_1 + I_2)$ for 100 laser shots each, the size of the error bars indicates the rms fluctuation; full line: Gaussian fit $R_I(d) \sim exp(-(d/\sigma_s)^2)$, with $\sigma_s = 100\,\mu m$. This data was taken from [13] and confirms the data given in Fig. 7.3.*

useful information as shown for example in Fig. 7.5. This might be due to extremely low signals, where photon counting comes into play, resulting in discrete jumps in intensity. It is also possible that the locking efficiency of the laser varies from shot-to-shot, causing the wavelength of the laser to change from narrow-band to broad-band. This problem did not have a noticeable effect when performing excitation-emission experiments from Chapters 5 and 6, where averages where acquired, instead of single-shot measurements.

Accumulated single-shot

Since the single-shot measurements resulted in a widely scattered distribution of data points, the evaluation was altered such that the data was ordered with increasing Rayleigh intensity and then it was summed over 100 points. This gave us data points for altogether 90 bins of the Rayleigh intensity value; see Fig. 7.6.

The picture that emerges is that of a very intensity-sensitive photochemical process, possibly involving multi-photon excitation of more than one molecule simultaneously.
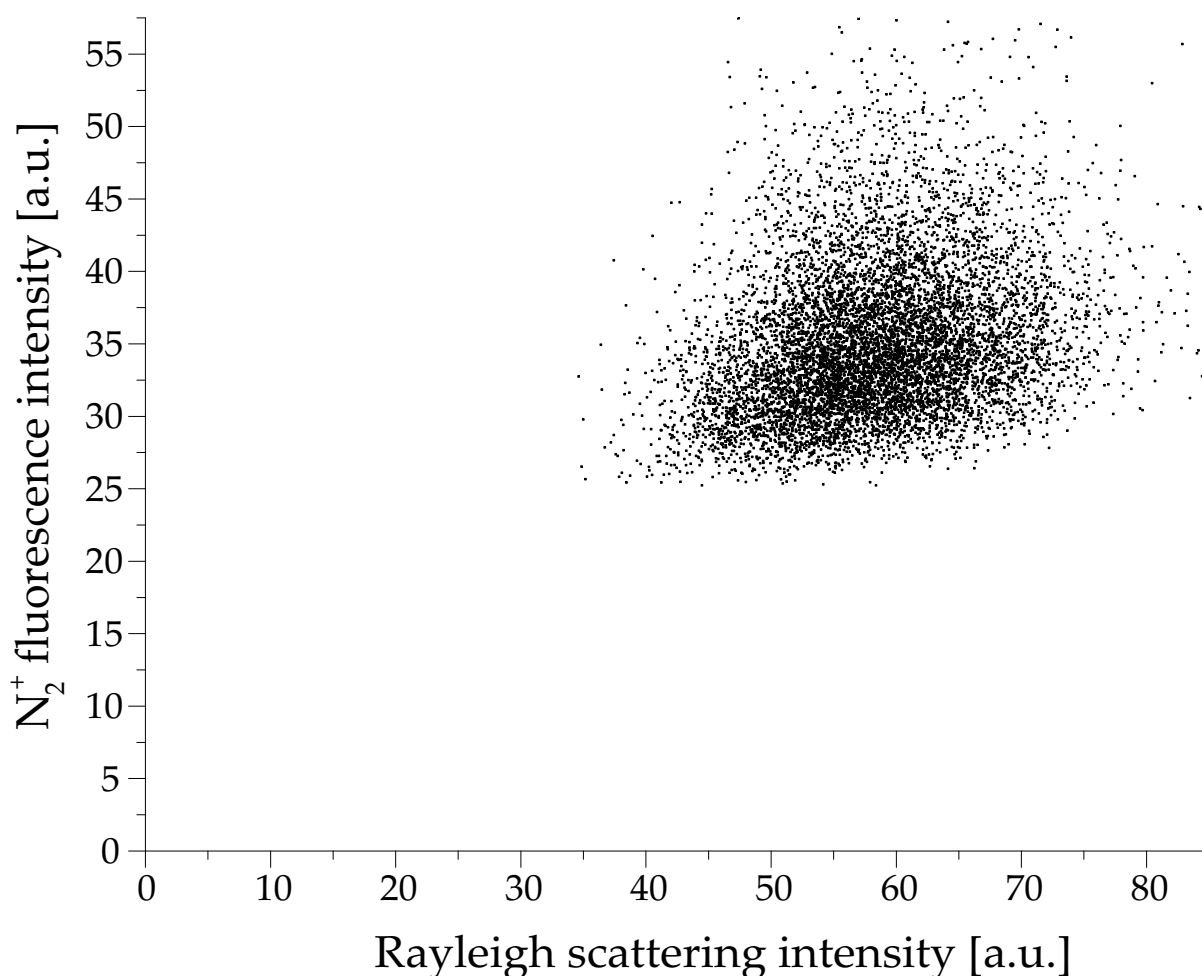
Figure 7.5: *Single-shot measurements of N_2^+ fluorescence in air on an oxygen resonance as a function of Rayleigh intensity. Similar graphs were found for O_2 and NO fluorescence (not shown).*

As shown in Chapters 5 and 6, the conditions of APART are such that both O_2 and N_2 can be multi-photon excited via resonances of the 2-$h\nu$ level. Reproducible excitation on such transitions requires a light source with a high degree of stability in both wavelength and intensity. The excimer laser available for this study (Lambda-Physik EMG 150 MSCT) consists of two discharge tubes, with a grating-tuned oscillator and an amplifier with unstable resonator optics, both operated through a single klystron. Although the amplifier alone is sufficient in principle to produce useful amounts of NO, it is the oscillator that provides spectrally narrow intensity and peak power. The oscillator works close to threshold, and as a result its output fluctuates on a shot-to-shot basis in both bandwidth and intensity. Apparently, the output characteristics are insufficiently stable for intensity-sensitive measurements as attempted here. The ArF excimer laser, however, is the only high-power laser source in this wavelength region.
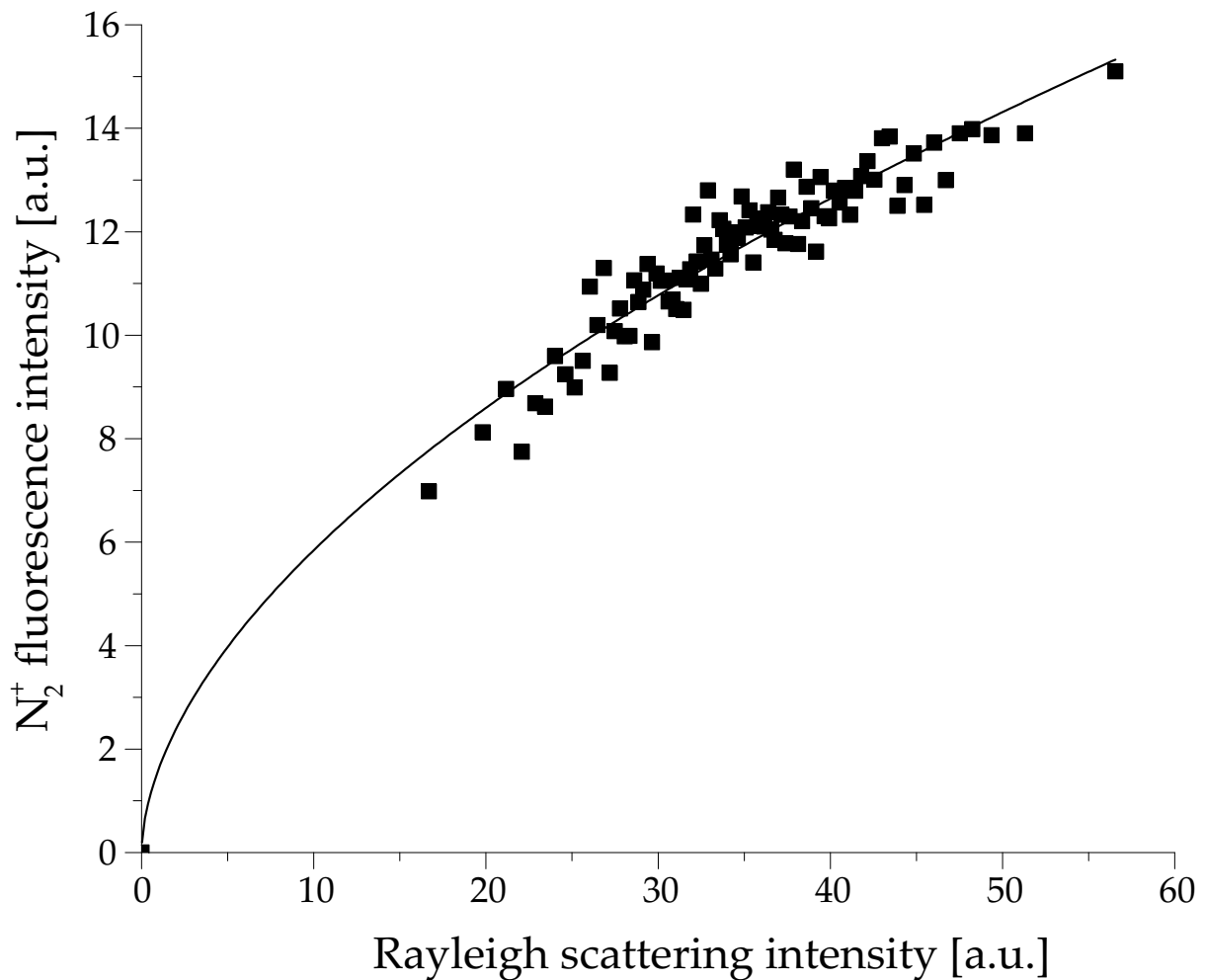
Figure 7.6: *Averaged single-shot measurement of N_2^+ fluorescence as a function of Rayleigh intensity, in pure nitrogen flow and tuned on a nitrogen resonance. The power law fit that was applied resulted in parameters $a = 0$ and $c = 0.56 \pm 0.02$.*

7.2.4 Conclusion

We have performed experiments where we measured the fluorescence intensities of nitrogen, oxygen and nitric oxide as a function of excimer laser intensity. All dependencies have been fit by a power function resulting in exponents for every species and condition. When looking at the different sets of averaged and single-shot measurements it is clear that there are differences between these different types of measurements, in that the fitted exponentials differ. Probably these inconsistencies can be attributed to variations of the laser wavelength and different ranges of the excimer laser power; when manually varying the laser power, a range between 10 mJ/pulse and 70 mJ/pulse was reached. By just looking at shot-to-shot fluctuations, the variations only spanned a range between 55 mJ/pulse and 65 mJ/pulse. Another influence could be the creation of effec-

tive quenchers of the studied fluorescence at different laser intensities. A variation in their creation could change the dependencies.

The measured quadratic dependencies in N_2^+ and NO fluorescence correspond to what would be expected from the calculated two-photon excitations. Since these were measured when averaging the data, no influence of varying laser power should be noticed. The value of $c = 1.7$ for N_2^+ in air, where a value of 2 is expected is probably caused by the tuning of the laser to the right wavelength and wavelength instabilities. This effect may have been less when measuring NO. Therefore, the conclusion follows that there is a (near) quadratic dependency between the Rayleigh intensity and the N_2^+ and NO fluorescence, respectively.

We have seen that, with the available equipment, it is not possible to perform single-shot measurements in order to extract accurate information on relations between species fluorescence and Rayleigh intensity. Better results may be expected with an excimer laser in which the discharge voltage of the amplifier can be regulated independently from that of the oscillator (so that locking efficiency can be maintained).

7.3 Energy transfer between N_2 and O_2

7.3.1 Introduction

As described in previous chapters the fluorescence excitation spectrum of nitrogen, measured by monitoring the emission in the first negative system of N_2^+, depends strongly on the amount of oxygen present (see Fig. 6.3). The excitation spectrum in air is completely different from that in pure nitrogen. To test how this transition between the two spectra evolves, we performed experiments in which we measured the excitation spectrum for several oxygen concentrations.

Starting with a pure nitrogen flow, a spectrum as discussed in the nitrogen chapter is obtained. By carefully mixing air into the flow, the change of the structure in the nitrogen excitation spectrum into that of the oxygen excitation spectrum is investigated.

7.3.2 Experiment

The experiment was conducted as described in Chapter 5. A premixed gas consisting of variable amounts of air with 19 % oxygen content and pure nitrogen was flushed through the flow device and the excimer laser was focused 5 mm above the exit. At every combination of air and nitrogen a scan over the excimer wavelength range was made, and the resulting emission at 391 nm (second negative emission lines of the nitrogen ion) was recorded using the spectrograph.

We started with a pure nitrogen flow and from there the air flow was increased to reach oxygen levels of 19 %.

7.3.3 Results

The excitation spectrum of nitrogen to the $B^2\Sigma_u^+$-state of the ion was measured six times with oxygen concentrations of 0 %, 3.6 %, 8 %, 10 %, 13 % and 19 %, respectively. These
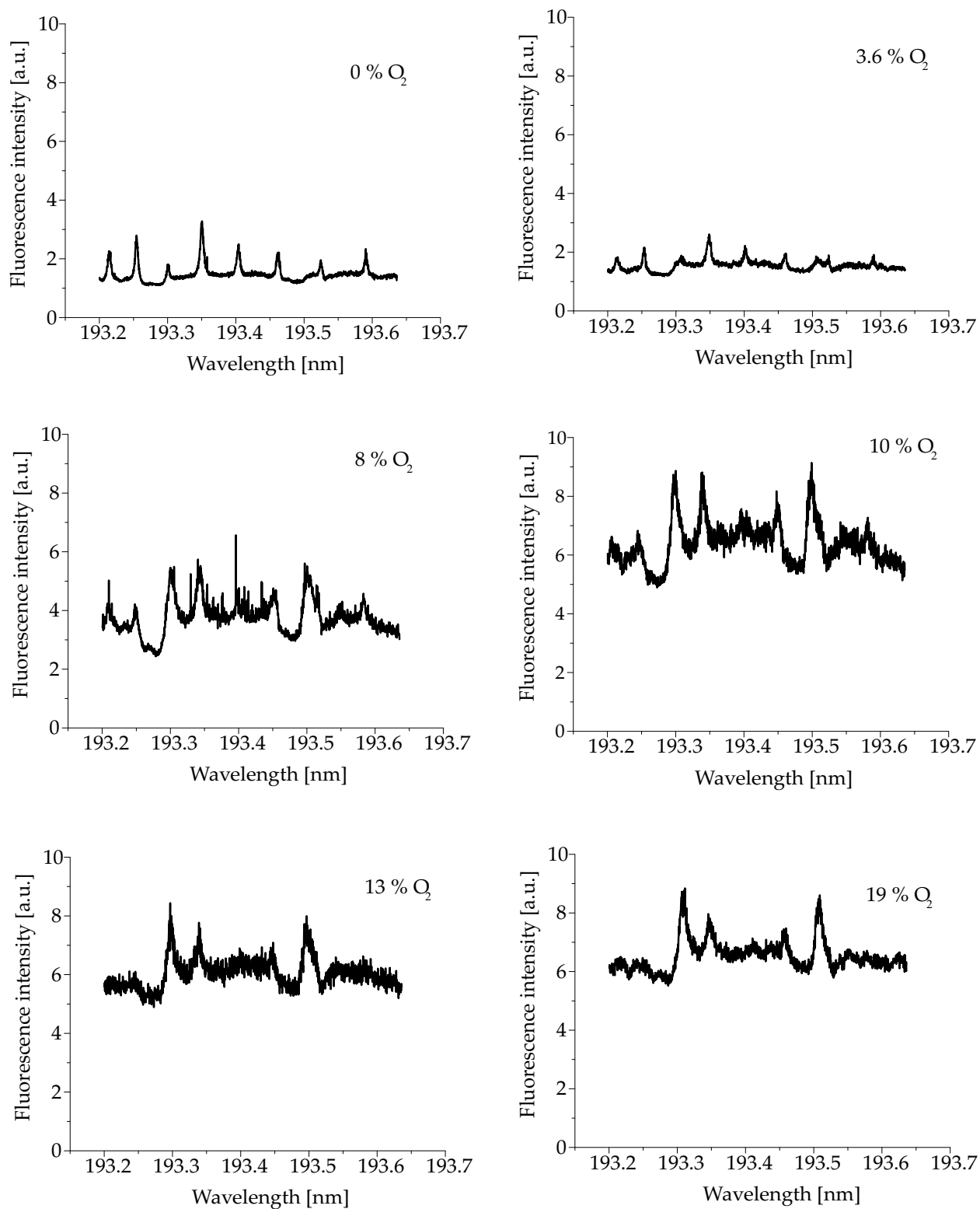
Figure 7.7: *Six excitation spectra of nitrogen to the B-state of the ion at increasing oxygen concentration. The data is presented such that the relative intensities can be studied.*
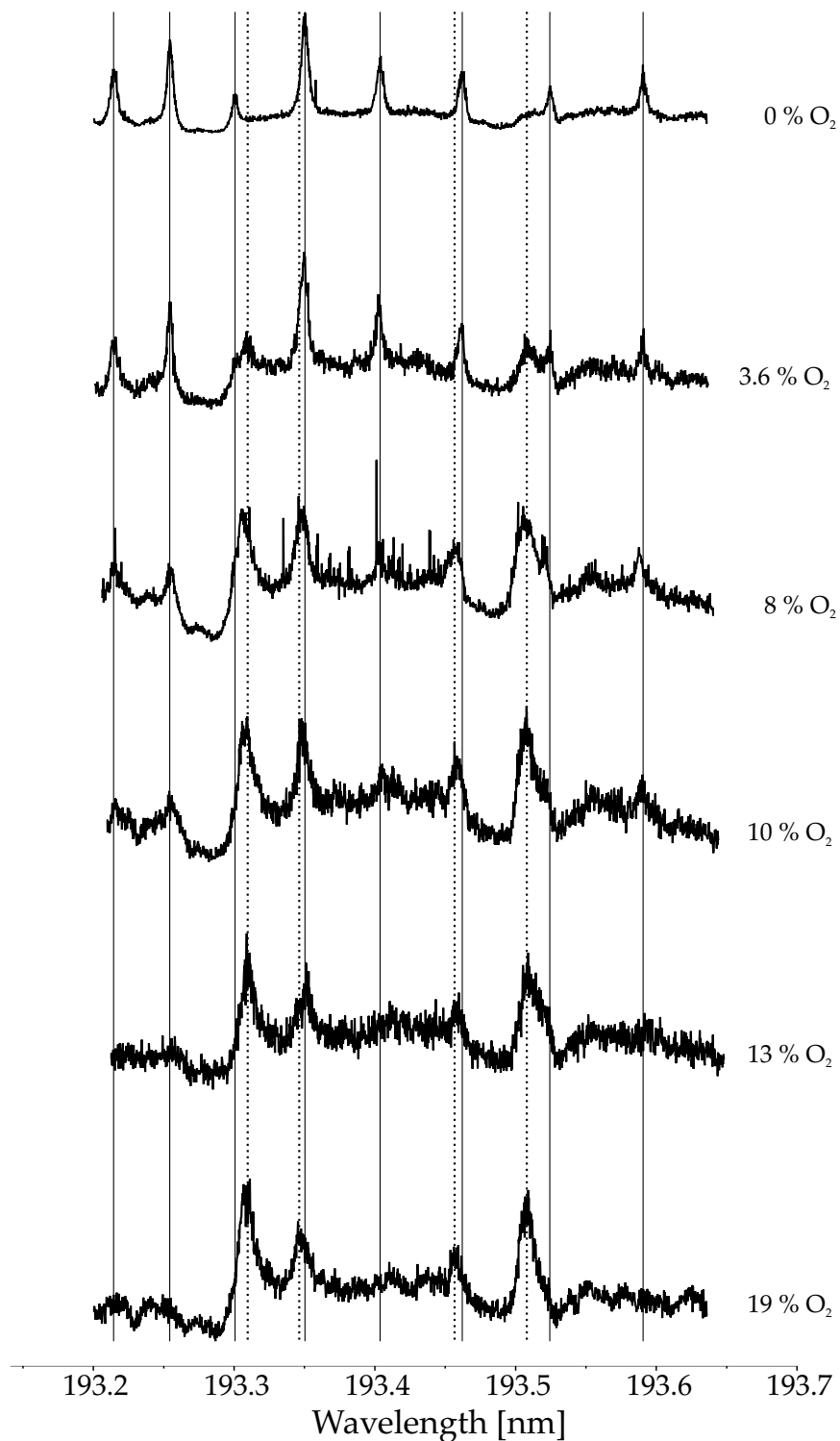
Figure 7.8: *Six excitation spectra of nitrogen to the B-state of the ion with increasing oxygen concentration. This is the same data as shown in Fig. 7.7 but now it is presented to compare the wavelength of the measured structure. The vertical solid lines indicate the positions of the prominent lines in the pure nitrogen spectrum (upper plot). The dotted lines indicate the positions of the prominent lines in the pure oxygen spectrum.*

spectra are presented in Fig. 7.7, in which the fluorescence intensity scales of all plots are the same. It is clear that for pure nitrogen the background level is much lower than when oxygen is added.

Figure 7.8 shows the six excitation spectra aligned above each other. From this figure the transition of the bands can clearly be seen. With increasing oxygen concentration, the structure of the regular nitrogen spectrum gradually decreases, while at the same time the spectrum induced by oxygen rises. Only the line around 193.35 nm appears to have been unchanged. This is probably a coincidental appearance of different excitation lines. Another clear feature in these graphs is the difference in linewidths between the upper and lower spectrum. The lines in the pure N_2 spectrum are distinctly narrower than those in the O_2 spectrum.

The spectrum induced by oxygen appears already at a few percent O_2 concentration. Above 8 % oxygen concentration, all spectral structure due to N_2 has essentially vanished.

7.3.4   Conclusion

The typical excitation spectrum that is observed in a pure N_2 flow, assigned in Chapter 5 to a (2+1)REMPI process in N_2 is suppressed by adding small amounts of O_2 to the flow. It is gradually replaced by a spectrum due to O_2 when the oxygen content is increased. 8 % of O_2 in N_2 is already sufficient to render the typical N_2 spectrum unobservable. It should be noted, however, that even in this case the excitation is monitored by recording fluorescence of N_2^+ ions. From this it can be concluded that the creation of N_2^+ molecules involves two dominant pathways. The first one is the (2+1)REMPI assigned pathway in N_2, which is apparently suppressed by oxygen. The second pathway must directly be linked to the excitation of oxygen, since the excitation spectrum matches the one found in oxygen.

7.4   The NO formation process

In this section we will try to speculate on the photophysical and photochemical processes that lead to NO formation out of air in the ArF excimer laser focus, and try to present a synthesis of all observations in this and previous chapters. Our model will have to explain the following observations:

1. Emission in the fundamental band of the first negative system of N_2^+ is always observed, whether pure nitrogen or air is used, and whether the ArF excimer laser is tuned to resonance or not, or is used in broad-band mode.

2. The excitation spectrum of N_2 disappears when adding oxygen.

3. There is a (nearly) quadratical dependency of [NO] and [N_2^+(B)] on laser power.

4. The excitation spectrum of O_2 is also seen for N_2 (resulting in N_2^+, Fig. 7.7) and for NO.
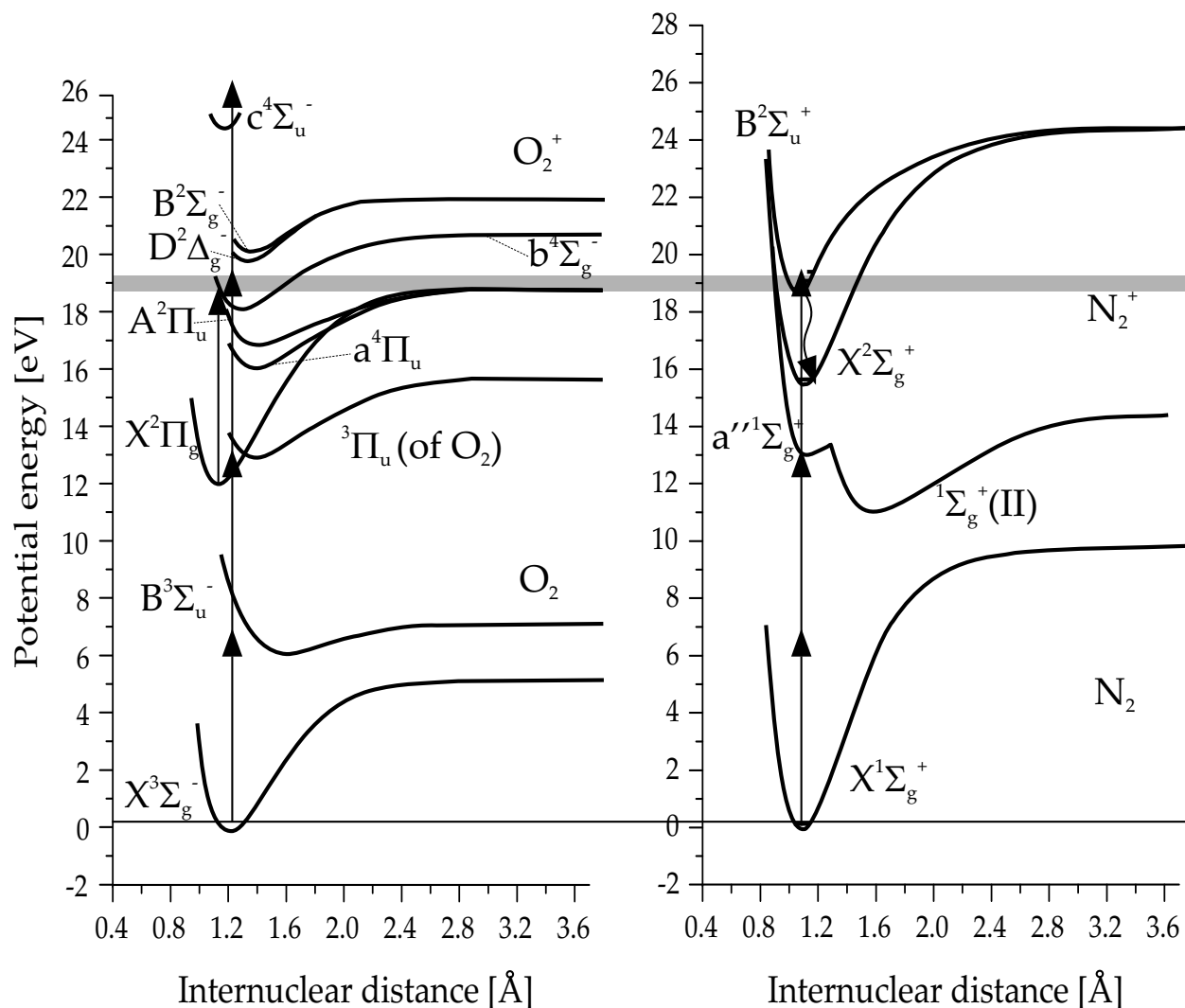
Figure 7.9: *Schematic representation of the potential energy diagrams of the oxygen and nitrogen molecules with (possibly) involved electronic states included. The diagrams are on the same scale, and positioned such that the vibronic ground states of both molecules coincide. The ground state of both molecules is at the horizontal line just above 0 eV. The grey horizontal bar is placed between the three-photon limit and vibrational ground state of the $B^2\Sigma_u^+$ state of the nitrogen ion and the $A^2\Pi_u$ state of the oxygen ion. The $^3\Pi_u$ designation of the Rydberg state is taken from the Ph.D. thesis of Van der Zande [106].*

These observations are discussed below using Fig. 7.9, and a model for the energy flow involved in the process is proposed. This model, dealing with the photophysical processes in N_2 and O_2, is schematically illustrated in Fig. 7.10. The chemistry leading to NO is discussed shortly at the end of the chapter.

1. Irrespective of whether the ArF excimer laser is focused in air or in pure nitrogen and at which wavelength the laser was used, fluorescence from the first negative system of N_2^+ is always detected. More specifically, most of the emission can be assigned to the B→X (0,0) band, with small (but non-zero) intensity also in the (1,1) band. However, the structure of the excitation spectrum strongly depends on the oxygen concentration. From this it can be concluded that at least three creation pathways for N_2^+ $B^2\Sigma_u^+$ ($v' = 0$) exist. One of these pathways does not depend on wavelength. When looking at Fig. 7.7 it can be seen that the background signal increases when adding oxygen (it levels off above about 10 % of O_2), but there is always a background present. Possibly the background is caused by the broadband component of the ArF laser radiation that is always present, or by nitrogen directly absorbing three photons in a bound-continuum transition. The increase of background on adding oxygen may be caused by a stronger non-resonant three-photon absorption by oxygen resulting in extra energy transfer to nitrogen forming nitrogen ions in the $B^2\Sigma_u^+$ state (see 4 below).

2. The "resonant" creation pathway of N_2^+ in the B-state that is described in Chapter 5 is suppressed by oxygen. The addition of oxygen apparently inhibits nitrogen from reaching the ionic B-state via the double-well pathway. We only see this effect in the fluorescence from the B- to the X-state of the nitrogen ion, that is, at the three-photon level (relative to $N_2(X)$). It is considered likely that the inhibiting step occurs at the level of the intermediate resonances, that is, at the two-photon level. Most probably the population of the double well in the two-photon resonance of nitrogen is efficiently removed by collisions with oxygen before it can absorb a third photon. Vibrational relaxation into lower levels of the $^1\Sigma_g^+$(II)-state is already sufficient to inhibit absorption of a third photon, because the B-state of the ion would be out of reach. As a second possibility quenching by oxygen may occur after the third photon-induced excitation of the N_2 molecule to an autoionizing Rydberg state. However, since autoionization generally is a fast process, it is not expected that the addition of a few percent of oxygen to be sufficient to completely quench this pathway.

3. The tentative assignment of the oxygen emission spectrum assumes a resonance at the two-photon level. This excitation is expected to show a quadratic dependency on laser power. Subsequent absorption of a third photon is expected to be highly efficient and non-resonant ($\sim$bound continuum), so that the energetic requirements of N_2^+(B) formation can be fulfilled by a (2+1)REMPI process. Apparently, the products resulting from the two-photon O_2 excitation play a significant role in the NO creation as well, since both the O_2 excitation spectrum as the quadratic laser power dependence of the fluorescence intensity are recorded when NO is monitored.

4. One of our most curious observations is that the O_2 excitation spectrum is perfectly reproduced when N_2^+ fluorescence rather than O_2 fluorescence is monitored. Energetically, the creation of $N_2^+(B)$ requires the absorption of (at best) three ArF laser photons (or their equivalent) by single N_2 molecules. And, of course, N_2^+ is charged. Apparently, then, the two-photon excitation of (neutral) O_2 must be followed by both ionization of and energy transfer to N_2, and the absorption of (at least) one additional photon somewhere along the way. The possibilities for energy and charge transfer between N_2 and O_2 at the two-, three-, and four-photon levels will be considered separately.

   (a) **Energy transfer at the two-photon level** For auto-ionization to take place, the Rydberg state needs to be embedded in the continuum associated with the final ionic state, which is not the case for the $a^4\Pi_u$-state. Auto-ionization into the $O_2^+(X)$ state would energetically be possible, but it would involve a two-electron transition, which is considered unlikely. Moreover, if energy transfer would take place at this level, nitrogen would have to be excited to the double well ($a''^1\Sigma_g^+/^1\Sigma_g^+(II)$) at high vibrational levels by an energy transfer with oxygen. This process would have to occur without quenching, which is unlikely.

   (b) **Energy transfer at three-photon level**

   Figure 7.9 displays schematic representations of the potential energy curves of oxygen and nitrogen. The horizontal grey band at the three-photon level in the ions of both molecules gives an indication of the region where N_2^+ creation may be induced by an excitation in collisions with $O_2^+(A^2\Pi_u)$. The stability of the two-photon excited state in O_2 (probably a Rydberg state converging to the a-state of O_2^+) permits the observed fluorescence to the $B^3\Sigma_u^-$ state of O_2 and might also permit excitation to higher states through absorption of another photon. The most probable state to excite to, based on energy differences, would then be the $b^4\Sigma_g^-$ or a Rydberg state converging to it. In the case of the $b^4\Sigma_g^-$ state the fluorescence back to the $a^4\Pi_u$-state [2] might have been observed, which was not the case. This might indicate that rather a Rydberg state converging to the $b^4\Sigma_g^-$ or to the $D(^2\Delta_g)$ or $B^2\Sigma_g^-$ [89, 99] states is reached, where autoionization is very slow compared to dissociation. In the presence of nitrogen, efficient charge transfer might take place, resulting in the production of $N_2^+(B)$ ions (the fluorescence of which is observed); for instance

$$N_2(X) + O_2^+(b) \rightarrow N_2^+(B) + O_2(X) \tag{7.3}$$
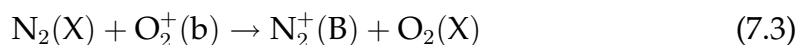
   Although we have not been able to find literature reports on this particular reaction, similar near-resonant energy transfer processes are known, like for instance the charge transfer between He^+ and the oxygen molecule [133, 134]:

$$He^+(2s) + O_2(X^3\Sigma) \rightarrow He(1s) + O_2^+(c^4\Sigma) \tag{7.4}$$
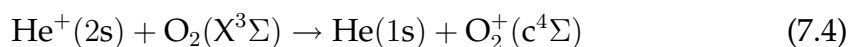
   where the $c^4\Sigma$ state lies at 24.6 eV above the ground state, resonant with the ground state of He II.
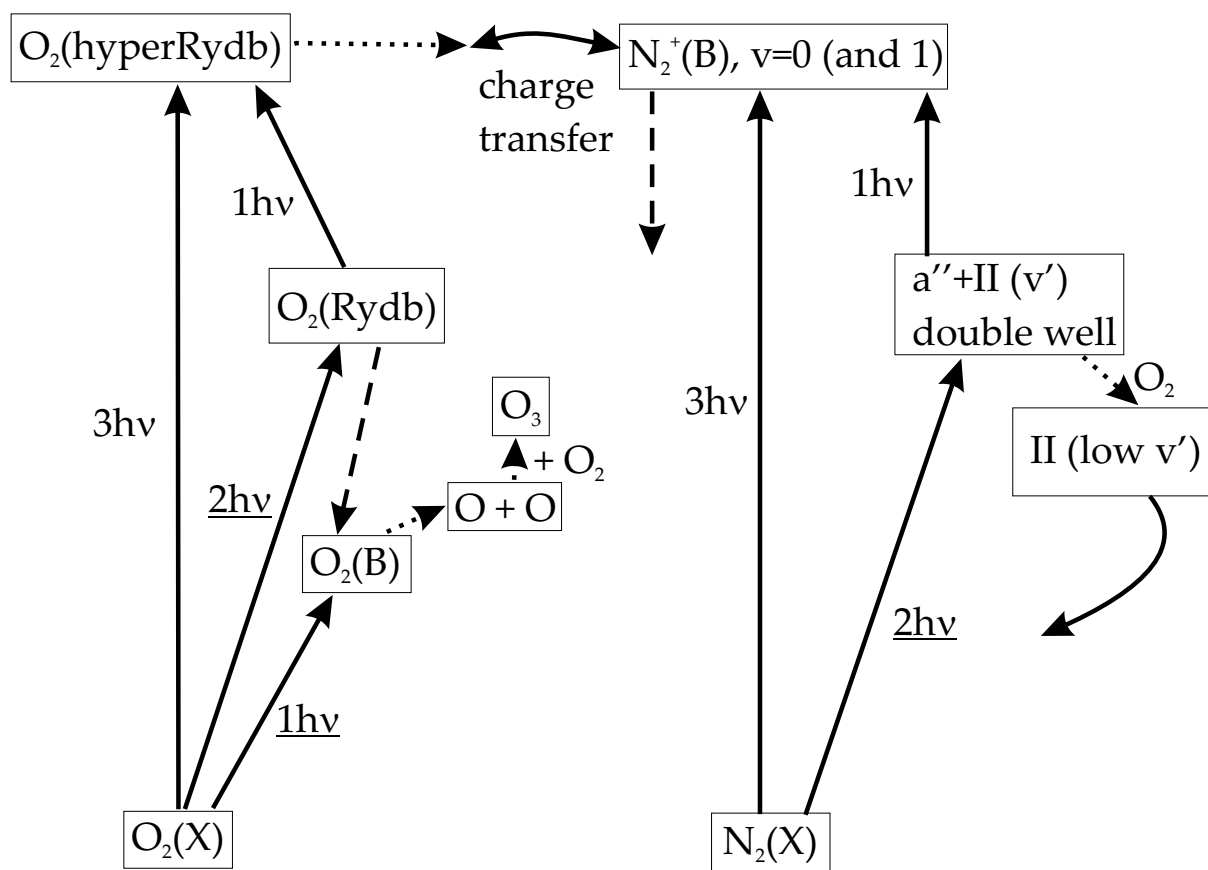
Figure 7.10: *A schematic representation of the possible pathways involved in the creation of different species in the focus of the excimer laser. The solid lines indicate excitations where electromagnetic radiation is involved, the dotted lines indicate transitions caused by collisions or dissociation and the dashed lines display relaxations resulting in measured fluorescence. The underlined photon number designations indicate that we have found spectral structure in that transition.*

(c) **Energy transfer at four-photon level**

Absorbing a fourth photon might bring oxygen in the $c^4\Sigma_u^-$-state. There was, however, also no indication of fluorescence corresponding to a transition from the $c^4\Sigma_u^-$ to the $b^4\Sigma_g^-$-state [135, 136]. The energy difference between these states is 6.39 eV [134] which is exactly the energy of one 193 nm photon, which makes excitation to this high-lying state, through an electric-dipole-allowed transition, not unlikely. It does, of course, require the $b^4\Sigma_g^-$ state to be populated. Energy transfer to the nitrogen ion will be less efficient than radiative decay. Of this high-lying c-state only the first two vibrational states have been recorded [135].

7.5 NO formation chemistry

There is a lot of information in literature on NO formation schemes. Many of these studies involve formation in reactive environments [126,137] in the atmosphere [123,127,131,138], or even photochemically induced [124,125].

When looking at the results of the APART experiments several conclusions can be extracted from the observations related to the NO formation. It is clear that in both nitrogen and oxygen, excited species are involved. Since the formation time is in the order of microseconds, it is assumed that no recombination of ions is involved in the NO creation. The relaxation of ions is considered to be faster than NO formation and only relatively stable species are considered for the NO reactions.

Figure 7.10 shows photo-induced processes involving nitrogen and oxygen, which may be responsible for the NO formation observed in APART. The left hand side shows the excitation processes of O_2, containing the proposed two-photon excitation scheme to a Rydberg state converging on a$^4\Pi_u$ of O_2^+ after which fluorescence takes place to the B-state of O_2. A third photon may be absorbed to a higher-lying Rydberg state, which might be reached non-resonantly as well. Oxygen in the B-state is also known to dissociate and consecutively form ozone.

The right hand side shows the excitation processes occurring for nitrogen. The proposed three-photon excitation through a double potential energy well is included, as well as a(n increased) relaxation to lower vibrational energies in this double well caused by interaction with oxygen. A charge transfer between nitrogen and oxygen takes place at the three-photon level. As discussed above, this sequence of events explains how the same excitation spectrum of O_2 is observed for N_2^+(B).

As discussed in the previous chapter, the excitation spectrum of the two-photon transition in O_2 is also recovered when NO LIF is used as a monitor (Fig. 6.3). This NO creation spectrum, like the others, shows a background with superposed spectral structure. Thus, there may be several chemical pathways that lead to NO formation in the excimer laser focus, but at least one of them involves species that are created via two-photon excitation of O_2. In the following we will speculate on the possible NO formation pathways, with an emphasis on the resonance-enhanced path. Although trivial, it should be remarked that we have no information on species possibly formed in non-luminescent states (like N_2^+(X) or N_2(A)).

This leaves us with several possibilities, where nitric oxide is created from one oxygen atom and an excited nitrogen molecule, or from one nitrogen atom and an (excited) oxygen molecule (see Table 7.1).

7.5.1 Processes involving oxygen atoms and nitrogen molecules

Assuming one oxygen atom is involved, the following reaction may take place (see Table 7.1 for references):

$$O(^3P, {}^1D) + N_2(A,B) \rightarrow NO(X) + N(^4S, {}^2D) \tag{7.5}$$
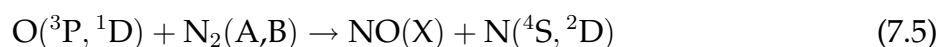
Both ^{1}D and ^{3}P oxygen atoms are formed when oxygen relaxes back from the Rydberg state to a repulsive curve converging to the dissociation limit of the B-state of oxygen,

which dissociates into $O(^1D) + O(^3P)$. We do not believe $O(^3P)$ atoms to play a significant role. These atoms are efficiently produced by one-photon excitation of O_2 in the Schumann-Runge bands, but the corresponding spectral structure is not reflected in the NO creation spectrum.

The reaction of $O(^3P, {}^1D)$ with $N_2(X)$ is not expected to be important, since multiphoton excitations are necessary and the creation of NO goes linear with N_2^+ creation as described in Chapter 2. The oxygen atoms $O(^3P, {}^1D)$ can already be made using one excimer laser photon. Furthermore, the quenching of $O(^1D)$ by ozone is very strong ($\sim$ 10^{-10} cm^{3}molecule^{-1}s^{-1} [139, 140]) and due to high concentrations of oxygen and nitrogen, the quenching by these molecules will also play a major role.

Probably $N_2(A)$ and $N_2(B)$ are formed via the C-state of N_2. Emission from N_2 (C→B) was observed in the experiments, and (B→A) emission is also known to exist, although this emission can not be observed with the equipment used in this thesis. Probably $N_2(C^3\Pi_u)$ is formed when nitrogen ions recombine with an electron. We have no information on the possible direct formation of $N_2(A$ or $B)$ in a similar recombination process. All these reaction are endothermic. Since the production of both $O(^1D)$ and N_2^+ (and thus N_2 (triplet system) through recombination) is enhanced by the two-photon resonance in O_2, the pathway 7.5 would explain the structure observed in the NO creation spectrum. Reactions (1) and (2) in Table 7.1 show that quenching of the excited A-state of nitrogen to the ground state is stronger than the formation of NO.

7.5.2 Processes involving nitrogen atoms and oxygen molecules

Reactions involving a nitrogen atom proceed as follows:

$$N(^4S, {}^2D) + O_2(X, B) \rightarrow NO(X) + O(^3P, {}^1D) \tag{7.6}$$
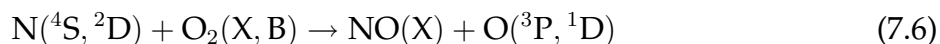
Nitrogen ions in the ground state are known to dissociate into two nitrogen atoms in reaction with an electron [124]. After excitation to the Rydberg state converging on the $a^4\Pi_u$ state of O_2^+ the oxygen molecule relaxes back to the B-state and can react with a nitrogen atom. Although this is a predissociated state, not all vibrational states are short-lived. All these reactions are endothermic, and therefore possible candidates in the APART NO formation process. Unfortunately, no reaction rate constants have been found involving the B-state of oxygen. Both reactions 7.5 and 7.6 can explain why the excitation spectrum of oxygen is also visible in the creation spectrum of NO.

7.5.3 Conclusion

Table 7.1 gives an overview of the rate constants of reactions that may be involved in the APART creation scheme of NO. Nitrogen in the A-state will form NO, but the quenching by oxygen atoms (^3P) into nitrogen in the ground state has an energy barrier that lies 3.3 eV lower [131]. In the reaction of an oxygen molecule with the nitrogen atom (^4S) a very small reaction rate constant around room temperature is found compared to the other reactions. The reaction with the $N(^2D)$ atom gives a reaction rate constant of $5.2 \cdot 10^{-12}$ cm^{3}molecule^{-1}s^{-1} (around 300 K). This nitrogen atom, however, also destroys nitric oxide resulting in ground state nitrogen with an order of magnitude higher reaction rate

Table 7.1: *Rate constant for reactions involved in the creation of nitric oxide when using APART.*

	Reaction	Rate constant [cm^{3}molecule^{-1}s^{-1}]	Reference
	reaction of N$_2$(A)		
(1)	O(^{3}P) + N$_2$(A) $\rightarrow$ NO(X) + N(^{2}D)	$7 \cdot 10^{-12}$	[141–143]
(2)	O(^{3}P) + N$_2$(A) $\rightarrow$ N$_2$(X) + O(^{1}S)	$2.1 \cdot 10^{-11}$	[143, 144]
	reaction of N(^{4}S)		
(3)	N(^{4}S) + O$_2$(X) $\rightarrow$ NO(X) + O(^{3}P)	$1.1 \cdot 10^{-14} \, T(K) \exp(-3150/T(K))$	[142, 143, 145]
(4)	N(^{4}S) + O$_2$($^1\Delta_g$) $\rightarrow$ NO + O	$2.7 \cdot 10^{-15}$	[146]
(5)	N(^{4}S) + O$_3$ $\rightarrow$ NO + O$_2$	$< 2 \cdot 10^{-16}$	[143]
	reaction of N(^{2}D)		
(6)	N(^{2}D) + O$_2$(X) $\rightarrow$ NO(X) + O(^{3}P, ^{1}D)	$9.7 \cdot 10^{-12} \exp(-185/T(K))$	[141, 147]
(7)	N(^{2}D) + NO $\rightarrow$ N$_2$(X) + O(^{3}P, ^{1}D, ^{1}S)	$6 \cdot 10^{-11}$	[147]
	reaction of N(^{2}P)		
(8)	N(^{2}P) + O$_2$(X) $\rightarrow$ NO(X) + O	$2.5 \cdot 10^{-12}$	[147]
(9)	N(^{2}P) + NO $\rightarrow$ Products	$2.9 \cdot 10^{-11}$	[147]
	reaction with ions		
(10)	O$_2^+$ + N(^{4}S) $\rightarrow$ NO$^+$ + O	$1.2 \cdot 10^{-10}$	[148]
(11)	N$_2^+$ + O $\rightarrow$ NO$^+$ + N(^{2}D)	$1.4 \cdot 10^{-10}$	[148]

constant. Singlet oxygen [149,150] will also react with the nitrogen atom, but the reaction rate constant is much smaller for this reaction [146] than for the other reactions in Table 7.1. Finally, the N(^{2}P) atom will also form NO in the reaction with O$_2$, but NO is also quenched by this atom at a higher rate [147].

The table also lists some reactions involving ionic states of nitrogen and oxygen, resulting in ionized nitric oxide. The reaction rate constants are larger than the ones not involving ions, but the recombination of NO with an electron is not included. This will decrease the rate constants, but by how much is not known. At room temperature all the reaction rate constants are similar (except reactions (3)–(5), which are much smaller), but in this study, evidence was found of increased temperatures. The reaction rate of N(^2D) with oxygen (reaction (6)) increases with temperature, but no temperature dependencies of the other reaction rate constants have been reported.

Campbell *et al.* [151] have developed a model describing NO creation processes from excited nitrogen in atmospheric environments. Large differences are present between this model and the situation in our lab with respect to pressure and temperature (both are lower in the higher atmosphere). These differences, however, do not change much in the reaction rates relative to each other. The concentration of O(^{3}P) and N atoms is more difficult to compare, since in the APART experiments they are formed efficiently by the excimer laser, but in the atmosphere solar radiation dissociates oxygen and nitrogen into O(^{3}P) and N atoms, respectively. Campbell *et al.*, unfortunately, do not give any information of the concentrations of oxygen and nitrogen atoms in their model. From the analysis of this model they conclude that the creation of NO from N$_2$(A) is more efficient than from N(^{2}D), N(^{2}P) or N(^{4}S) (by a factor of three). Based on these results it can be estimated that the reaction of N$_2$(A$^3\Sigma_u^+$) with an oxygen atom may play a major role in the creation of NO in the APART experiment, but it is not the only process that results in the nitric oxide molecules. It would be interesting to apply the model of Campbell *et al.* to the situations created in the APART experiments.

To test whether this set of reactions ((1) and (2) from Table 7.1) occurs in the NO formation process with an ArF excimer laser beam, it is necessary to follow the C→B and B→A emission from nitrogen, while monitoring the amount of N$_2^+$ ions in the ground state. At the same time the relation between this emission and the creation of nitric oxide should be studied. Since our measurements on the excitation-emission spectrum in air using the excimer laser showed that the emission of nitrogen is small compared to emission from processes of oxygen, and is completely overlapped by it, this experiment will be difficult.

Another possibility would be to monitor the creation of oxygen atoms as a function of NO formation. Velocity map imaging was used before to monitor the production of oxygen atoms in a two-step photodissociation of oxygen [152]. This experiment was repeated in our lab and the production of oxygen atoms in a multiphoton process was monitored as a function of excimer laser wavelength. No useful results were obtained, however, possibly because the intensity of the excimer laser beam was too low.

An application of the proposed experiments should give more conclusive results on the formation of NO, although the processes involved in the focus of a highly energetic ArF excimer laser beam are very complex and an accurate assignment is challenging.

Chapter 8

Outlook

In this thesis the exploration of the applicability of the APART technique in high pressure and high temperature regimes is described. The study on the NO formation has yielded information on the interaction between oxygen and nitrogen and a basic chemical description has led to a reaction that most likely is dominant in the formation of NO. After four years of work dedicated to applying and studying our measurement technique, the development and understanding are still not at an end. A lot of work can and should still be done to make APART a widely acknowledged technique. In the following paragraphs I will spend some time on describing ideas on what can still be done to improve APART as a technique and to understand how it works.

8.1 The APART technique

Where all the mentioned opto-mechanical velocimetry techniques are being used nowadays in wind tunnels and other setups, not one of the MTV techniques have gone past a proof-of-principle lay-out. This is, partly, due to the relative complexity of the technique and to the fact that MTV is a new type of technique that thus far can only be used in small scale applications.

We had some contacts with companies such as NLR (the Dutch Aerospace Institute), Philips, DNW (German Dutch windtunnels), NMi (Dutch Institute of Standards) and even ESA (European Space Agency). Some of these companies were interested in using the APRT technique. The problem here lies with the lack of equipment at the site of these companies and the impossibility of moving our equipment to their sites.

Although it is not the goal of our research department; in order to apply APART in a wider range of applications in cooperation with industry we need to search for equipment that is cheaper and easier in use, but that can still do the job, which is create NO from air, induce fluorescence and image this LIF. We have shown that larger working distances are possible, but the written NO line is still very small. It is not clear whether this 3 cm of NO line is long enough to be used in industrial applications.

The future of APART will not be to completely replace commercially available flow techniques. For most relatively simple applications, LDA, PIV, hotwire anemometry and other (opto-)mechanical measurement techniques still suffice. It is in the special cases that MTV or APART will fill in the gaps. Some examples of these are turbulent behavior at

very small scales, boundary layers along the wake of objects and outflow openings that are small enough to be clogged up by seeded particles. Fundamental research, but also investigations on satellite propulsion and airplane designs could make use of the APART technique.

The main disadvantages of the APART measurement technique are the following:

1. The write wavelength is strongly absorbed by oxygen molecules resulting in a temperature rise of the studied flow. This makes the technique less non-intrusive.

   When we completely understand the creation process of NO, we might be able to select a more suitable wavelength for the write process. This wavelength can be chosen such that oxygen absorption is minimal, thereby reducing the intrusiveness. Furthermore, an optimal oxygen concentration can be chosen in closed measurement systems. Probably this concentration is lower than that in air.

2. The read and write lasers are both large and complex, making it difficult to quickly build up a setup.

   The optimal choice of creation wavelength can also be directed towards easier laser systems, although in the regime used in this thesis, not many lasers exist. Solid-state laser design is also approaching blue and UV wavelength diode lasers. If we wait long enough a diode laser at the right wavelength and intensity is produced and we can use those devices.

3. The necessity for high powers in the write laser and the non-linear process of NO creation make it difficult to write grids of tracer molecules, because there is not enough energy in the laser beam to split it into many beams.

   This disadvantage could also be turned around to make it an advantage. The non-linearity of the NO creation process would not result in a grid of NO lines when using crossed beams, but it would result in dots. With these dots we can easily study separation behavior. Unfortunately, we have shown [13] that the quadratic dependence of NO creation on the laser power is not enough to create clear dots.

4. The high intensity of the write laser creates problems when measuring close to surfaces. Direct or indirect reflections of the laser from the surface may disturb the measurements or even damage imaging devices.

   To use APART near solid surfaces a very careful alignment is necessary, but we always remain limited to the thickness of the laser beam and its expansion. Wavelength and polarization filters can be used to remove reflections coming from walls and other surrounding equipment.

5. As was shown by Elenbaas [14] the NO molecules used in APART are affected too strongly by diffusion, resulting in wider lines that create large errors.

   The use of heavier molecules may reduce the diffusion effect and will cause the accuracy of the MTV technique to improve.

An attractive alternative to APART would be to employ phosphorescent molecules, since only one laser system is required. Already investigated phosphorescent molecules,

like biacetyl and acetone, have some serious drawbacks, already discussed in this thesis. A non-toxic molecule, of which the fluorescence is not quenched by either oxygen or nitrogen would be strongly preferable. We performed some pilot measurements on a phosphorescent molecule (terbium chelate), which unfortunately was not found to emit detectable radiation in the gas phase. An alternative would be glyoxal, which is, however, difficult to produce and maintain.

8.2 The NO creation

At the end of writing this thesis, the exact creation mechanism of NO has still not been elucidated. We have made some progress, partly resulting in even more mysteries surrounding the oxygen and nitrogen mechanisms in the focus of the excimer laser, but also giving more insight in the different species and quantum states involved.

In this study we have separated oxygen and nitrogen to discover that pure nitrogen differs strongly in excitation spectrum from nitrogen in air. The excitation spectrum of nitrogen in air, of oxygen in air and pure oxygen and the creation spectrum of nitric oxide (which are all equal) should give us the solution to the creation of nitric oxide. The problem remains, however, that due to the high energy density many different states and species are created.

To get closer to a complete understanding of the NO creation process several different treatments may be carried out.

Chemical treatment At the moment we have mainly looked at a quantum-mechanical description of this problem. In addition we have worked on the framework of a chemical model, which, however, was not followed yet by calculations. A quantitative chemical treatment might shed some light on the matter.

Scanning range The very short scanning range of the excimer laser limits our experimental window. If we could find a way to extend this tuning range, we could increase the amount of excitation information, thereby increasing our knowledge on the transitions occurring within the focus of the excimer laser. One possibility is using the Raman shift of the ArF excimer laser or a KrF excimer laser. This, however, will result in significantly lower laser powers. Another option is researching nonlinear crystals that can convert high power lasers to the right wavelength. Again, laser powers might be too low. By strongly focussing these weaker beams, however, we may still get the required information.

Excitation-emission spectrum Another aspect that was not worked out in this thesis is the excitation spectrum of oxygen measured at different emission wavelengths. The emission spectrum described in this thesis contains much structure, where we can extract an excitation spectrum at each maximum. We have seen many small differences between these different excitation spectra and a more detailed study on the emission wavelength dependence of the excitation spectrum of oxygen might give us new information necessary to solve the puzzle. Since the small differences between the excitation spectra consisted of different parts of the excitation structure appearing at different emission wavelengths, clusters of bands that belong to one

excitation can be extracted. The excitation spectrum could then be split up in several different excitations. This study was not finished due to the huge amount of data involved in the experiment and the lack of time remaining.

Pulse length In the light of examining chemical processes, it would be an option to vary the pulse length of the laser. At the moment it is in the order of 10-20 ns. By shortening it significantly we would exclude laser induced excitations that follow after a slower chemical processes. Of course we need to find the right laser to supply short laser pulses in the right wavelength and power regime.

Gas purity Since we have used oxygen of 0.995 % purity we could also look at oxygen flows, with even less contamination. This is to exclude any emission structure arising from trace gases, such as CO.

Gas composition The cell that was used for the high pressure measurements was only partially used to study the NO formation process as a function of air composition. A study on different ratios of nitrogen and oxygen using CRDS for quantitative measurements may aid in completing a chemical model.

Although my work on APART has come to an end, I hope the information gathered in this study will help in further evolving APART into a technique that is more widely used.

Appendix A

MTV techniques

A.1   Introduction

Many advances have been made towards accurate measurements of velocities in gas flows since the development of the first Molecular Tagging Velocimetry schemes. At first, this technique was applied in liquids, where photoluminescent chemicals or caged dyes were added to the flows (see reviews by Falco [153] and Koochesfahani [154–157]). In gas flows the phosphorescent molecule biacetyl was applied as one of the first gaseous molecules. Later other molecules were seeded to the flow, like *tert*-butyl nitrite, NO_2, or acetone and it also became possible to label molecules in unseeded flows.

The purpose of this Appendix is to describe the current state of Molecular Tagging Velocimetry (MTV) techniques in gas flows. We will introduce the basis of the technique and show a schematic overview of the different techniques with their specific tracers.

The basis of the MTV technique is the labelling of a certain distribution of molecules in a flow, which is visualized after being displaced and/or deformed by the flow, a set time delay later. It is crucial that the labelled molecules can be distinguished from the other molecules in the flow and that the lifetime of these tracers is longer than the typical timescales in the flow. The molecules are labelled by creating a new, unique molecule or by bringing existing ones to a previously unpopulated quantum state. The lifetime of the new molecule or the altered state determines the range of velocities for which the technique is suitable.

The application of MTV comes in many different forms, involving the type of tracers, the type of lasers and the number of lasers (Table A.1). Of course this all depends on the flow one plans to study. The parameters to consider are the environment, the typical timescales, the size and vulnerability of the setup, etc. Basically the types of tracers can be divided in two groups: the phosphorescent molecules and the fluorescent molecules. Since phosphorescence is long-lived (ranging from microseconds to seconds), only one laser needs to be used, to label the molecules. After being labelled, the molecules start radiating and keep on doing that for the timescale of the experiment. This phosphorescence can be imaged at any time during the radiation lifetime, thereby registering the tracer displacement. The radiation lifetime of fluorescing molecules is extremely short (typically several nanoseconds) and therefore two lasers are required. The first laser changes the molecules to a unique species and the second laser brings these tracers to a fluorescing

Table A.1: *Overview of published MTV schemes in air. HTV = Hydroxyl Tagging Velocimetry, LEI = Laser Enhanced Ionisation, OTV = Ozone Tagging Velocimetry, RELIEF = Raman Excitation and Laser Induced Electronic Excitation, LIF = Laser Induced Fluorescence, PDL = Pulsed Dye Laser, SRS = Stimulated Raman Scattering, fluo = fluorescence, phos = phosphorescence, mf = mole fraction, ppm = parts per million, * indicates electronic excitation.*

Name	Tracer	Precursor	Write	Read	Seeding	Width of written line [μm]
APART	NO	air	ArF excimer (193 nm)	LIF (226 nm)	no	50-80
HTV	OH	H_2O	ArF/KrF excimer (193 nm / 248 nm)	LIF (308 nm)	no	300
LEI	Na^+	Na	PDL (589+449 nm)	LIF (589 nm)	yes	$\simeq$ 500
OTV	O_3	O_2	ArF excimer (193 nm)	LIF (248 nm)	no	$\simeq$ 500
RELIEF	$O_2(v=1)$	$O_2(v=0)$	Nd:YAG + SRS (532+580 nm)	LIF (193 nm)	no	50-100
(6)	acetone*	acetone	Nd:YAG (266 nm)	phos	yes	$\simeq$ 200
(7)	biacetyl*	biacetyl	XeCl excimer (308 nm)	phos	5% mf	$\simeq$ 200
(8)	NO(A)	NO(X)	Dye (225 nm)	fluo	1% mf	200
(9)	NO	NO_2	XeCl excimer (308 nm)	LIF (226 nm)	600 ppm	750
(10)	NO	tBN	ArF/KrF excimer (193/248 nm)	LIF (226 nm)	1% mf	1000
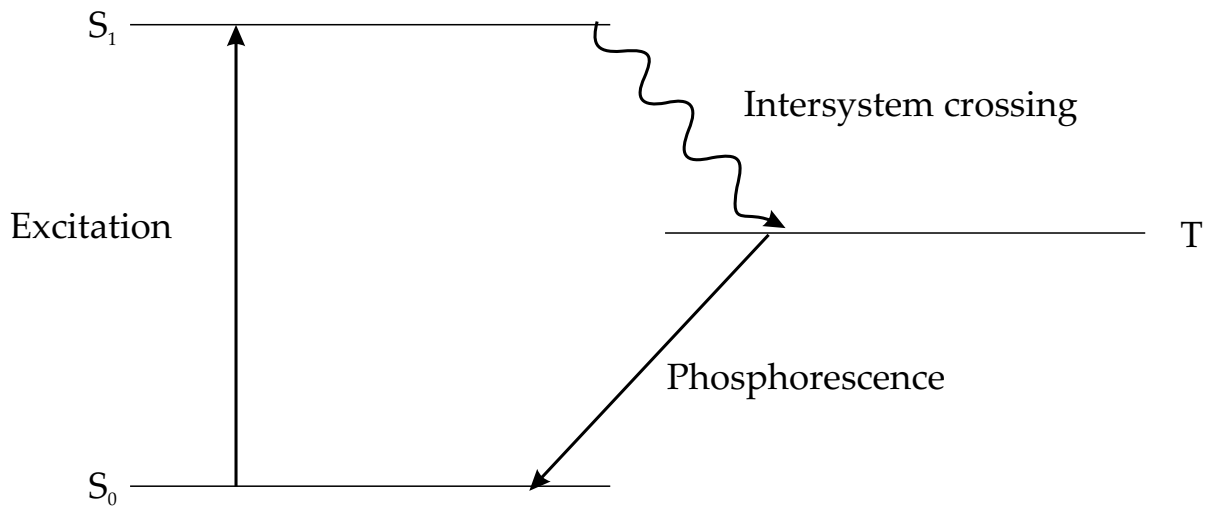
Figure A.1: *Schematic representation of phosphorescence, where a molecule is electronically excited from one singlet state (S_0) to another singlet state (S_1), after which an intersystem crossing to a triplet state occurs. Relaxation to the forbidden singlet ground state then results in phosphorescence.*

state. The imaging should then occur at exactly the same time as the firing of this second laser. To capture the right timing an Intensified CCD (ICCD) camera is often used. If properly selected, this camera is able to visualize ultraviolet radiation and can be gated at very short time intervals ($\sim 5\,\text{ns}$).

A.2 MTV-schemes in gas

In this section an overview is given of MTV schemes published to date (see Table A.1). The techniques will be briefly described, with some emphasis on the following points, that are particularly relevant to practical applications.

(a) **Equipment** Description of needed equipment.

(b) **Applicability** In what environments can the technique be used, what is the velocity range and what is the tracer lifetime.

(c) **Practicability** Any peculiarities about the tracers or the equipment.

(d) **Intrusiveness** Calculated heat release.

The final issue deserves some comment. Even though MTV is an all-optical technique, it is true that the creation of tags involves local heat input. Although this is difficult to quantify without experimental data, the possible pathways for heat input for all techniques will be indicated.

1. **Biacetyl:** The first gas velocimetry results were published by Hiller *et al.* [158] in 1984, who used a phosphorescent molecule called biacetyl. The feasibility of the technique was shown by measuring velocities between 5 cm/s and 6 m/s in a flow chamber. Biacetyl is an organic molecule that can be added to the flow by bubbling nitrogen through a mixing chamber containing liquid biacetyl. A laser with a wavelength around 280 nm or 420 nm electronically excites the molecule to a singlet state. An intersystem crossing takes place between the excited singlet state and a lower energy triplet state. Finally, relaxation to the singlet ground state takes place, which results in long lived radiation (phosphorescence) because the transition is forbidden (see Figure A.1).

   The most recent paper on MTV with biacetyl was published by Stier *et al.* who measured two components of the velocity field of the intake flow into a steady flow rig model of an internal combustion engine [159].

   The advantage of a phosphorescent molecule is that there is no need for a second visualization laser, resulting in a relatively easy setup.

   (a) To excite biacetyl the fourth harmonic of the Nd:YAG laser (266 nm), a frequency-tripled Nd:YAG laser pumping a stilbene dye laser (~433 nm) [158], a XeCL excimer laser (308 nm) [159], a N_2 laser pumped coumarin 120 dye laser (435 nm) [160], or the H_2-anti-Stokes-Raman shifted second harmonic of the Nd:YAG laser (435 nm) can be used. The emission of the phosphorescence is in the visible, which means that the detection device does not need to be optimized for UV detection. The tracers are easily created by bubbling nitrogen through liquid biacetyl (vapor pressure 5.3 kPa at room temperature) giving 5% molar seeding fraction [158]. Although radiation is quenched at higher laser powers (by other triplet molecules), the absolute phosphorescence yield is still enhanced, which means that higher laser powers are desirable.

   (b) The phosphorescence is strongly quenched by (small amounts of) oxygen. This makes it impossible to use biacetyl in ambient air. It has to be used in a closed system with for instance nitrogen as carrier gas. High temperatures will decrease the phosphorescence yield, but the strong temperature dependence of the vapor pressure makes elevated temperatures desirable [158]. Pressures between 1.3 kPa and 100 kPa have been applied.

   The phosphorescence lifetime of unquenched biacetyl is in the order of 10 ms, decreased by collisional quenching and annihilation reactions between triplet molecules, the probability of which increases with density and thus laser power [158].

   (c) Biacetyl can polymerize due to impurities and violent mixing and this can be avoided above temperatures of 60 °C [158]. It is also flammable, has a very strong smell, and contaminates all equipment long after use.

   (d) It is possible to write grids (more than 300 points have been reported by Stier *et al.* with not more than 1 mJ per beam), where two-dimensional velocity information can be extracted. The energy deposit in the flow, therefore, need not

be high. When using an optimal excitation wavelength, with highest absorption at 420 nm, the strongest phosphorescence wavelength is located at 525 nm, which indicates a heat input of 0.6 eV.

2. **Raman Excitation and Laser Induced Electronic Fluorescence (RELIEF):** The RELIEF technique was pioneered by Miles *et al.* [161]. It consists of vibrationally pumping ground state oxygen ($X^3\Sigma_g^-(v''=0)$) to a higher vibrational state ($X^3\Sigma_g^- (v'=1)$) by stimulated Raman excitation using two lasers differing 1555 cm^{-1} in energy. Another laser then excites the $v'=1$ molecules to a Schumann-Runge state $B^3\Sigma_u^-$ ($v'=7$) after which the oxygen fluoresces back to the ground state. The scheme of RELIEF is given by

$$O_2(X, v=0) + h\nu_{580\,nm} + h\nu_{532\,nm} \xrightarrow{\text{Stimulated Raman Excitation}} O_2(X, v=1) \quad (A.1)$$

as the write step, and

$$O_2(X, v''=1) + h\nu_{193\,nm} \longrightarrow O_2(B, v'=7) \longrightarrow O_2(X, v=\ldots) + \text{fluorescence} \quad (A.2)$$
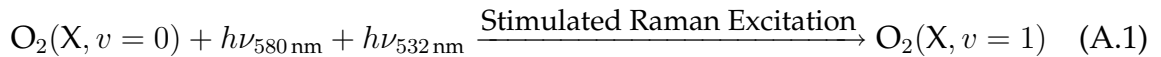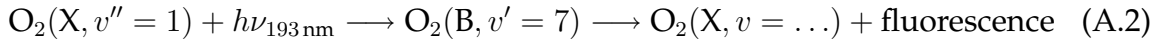
as the read step. Under ambient conditions, the $X(v''=1)$-state is hardly populated (1555 cm^{-1} $\equiv$ 2200 K), so all population visualized in the read-step can essentially be considered as induced by the write beam. Moreover, the $v''=1$ state is relatively long-lived, because relaxation back to the $v''=0$ state is electric-dipole forbidden.

The most recent results using RELIEF were also reported by Miles *et al.* [162], where its application in an engine testing wind tunnel and supersonic mixing of helium in air in coaxial jets were studied.

(a) Two lasers are required for the tagging process of stimulated Raman excitation. One of the tagging lasers is a frequency doubled Nd:YAG laser (532 nm) and the other one is a dye laser pumped by a fraction of the doubled Nd:YAG beam to get 580 nm [161]. The beams need to be combined collinearly and overlapped in time to get the stimulated Raman excitation. Later Lempert *et al.* proposed using a Raman shifting cell filled with oxygen to replace the dye laser [163]. This, however, gave a much lower power. Seeding the Raman cell with broad band Stokes radiation also worked and yielded an increase of a factor of three in signal [164]. For reading an ArF excimer laser at 193 nm and an ICCD camera are used.

(b) RELIEF can be applied in normal air. Since ground state population must not significantly exceed the $v=0$ state the technique is limited to temperatures below 750 K [162]. The minimum applied pressure is approximately 100 Torr [165]. The lifetime of the tracers is in the order of 30 ms in pure oxygen [161], which can be shortened by tri-atomic molecules, particularly water vapor [162] and CO$_2$. The presence of these molecules strongly increases the minimum velocity ($\Delta t > 100\,\mu$s in pure oxygen, $\Delta t < 10\,\mu$s with impurities) that can be measured [165]. There is no theoretical limit to the maximum velocity and measurements of supersonic velocities have been reported [166].

(c) The tagging laser system and setup are elaborate.

(d) The laser beams are focused in the measurement region [161], but the heat input is nevertheless minimal, since the Raman pumping process is expected to only produce the desired $X(v' = 1)$ molecules.

3. **Hydroxyl Tagging Velocimetry (HTV):** In 1989 Boedeker [167] showed that the dissociation of water into OH was an excellent way of tagging air flows. Naturally present water vapor in air is dissociated using a two-photon laser excitation. Part of the created OH ends up in a fluorescing excited state indicating the position of the initial tracer distribution. A laser beam with a wavelength of 308 nm can create the LIF for visualization. The creation and visualization of OH is shown schematically by [168]:

$$H_2O + h\nu_{248\,nm} \longrightarrow OH(X^2\Pi, v) \tag{A.3}$$

$$OH(X^2\Pi, v'' = 0) + h\nu_{308\,nm} \longrightarrow OH(A^2\Sigma, v' = 0) \longrightarrow OH(X^2\Pi, v'' = 0) + \text{fluorescence} \tag{A.4}$$
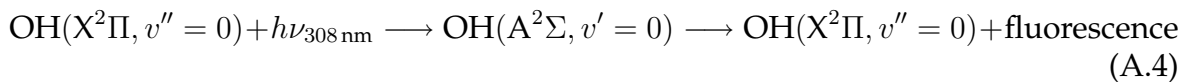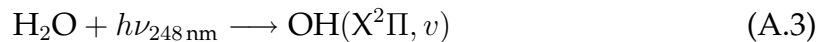
(a) The dissociation and visualization processes utilize a KrF excimer laser at 248 nm (two-photon) [167] or an ArF excimer laser at 193 nm (single photon) [169], and a dye laser pumped by a Nd:YAG laser at 308 nm [167] or at 282 nm [170], respectively. Because the fluorescence is in the UV an ICCD camera should be used for imaging.

(b) The technique can be applied at standard temperature and pressure [171] as well as in reacting flows, such as an H_2/air diffusion flame [169] or a cavity-piloted Mach 2 combustor [170]. The $(1/e)$ lifetime of the OH tracer in ambient air is approximately $150\,\mu s$ [172], which does not change dramatically in a lean flame. Rich flames, however, can strongly decrease the lifetime down to 200 ns [169]. Velocities ranging from 10 m/s [173] to up to 1800 m/s [167] have been measured, and high velocity combusting flows can be investigated because water is a natural constituent of advanced propulsion flows [167].

(c) KrF and ArF lasers are bulky and the suggested read lasers are complex systems.

(d) When the KrF laser is used for OH creation, the write process requires two photons. The heat input is caused by the energy excess after dissociation of water, which is approximately 5 eV. By using the ArF excimer laser the process involves a single photon and there will be no need for focusing (except for spectral resolution issues, of course). The energy deposit in the flow is caused by an efficient absorption of photons by oxygen. Grids have also been created by crossing 11×11 ArF laser beams [170], which is more elaborate when using the KrF laser.

4. **Ozone Tagging Velocimetry (OTV):** In 1996 Pitz et al. [174] developed a new MTV technique where ozone is created from oxygen molecules in the flow. The oxygen in the ground state is photodissociated using one 193 nm photon, after which the atoms form ozone in interactions with oxygen molecules. In the visualization step the ozone is dissociated into vibrationally excited oxygen, which is subsequently

excited to the B-state (both during the same laser pulse). This excitation results in fluorescence back to the ground state. In schematic form this is [174]

$$O_2 + h\nu_{193\,nm} \longrightarrow O + O \tag{A.5}$$

$$O + O_2 + M \longrightarrow O_3 + M \tag{A.6}$$

$$O_3 + h\nu_{248\,nm} \longrightarrow \left\{ \begin{array}{l} O(^3P) + O_2(X^3\Sigma_g^-, v'') \\ O(^1D) + O_2(a^1\Delta_g) \end{array} \right. \tag{A.7}$$

$$O_2(X^3\Sigma_g^-(v'' = 6, 7)) + h\nu_{248\,nm} \rightarrow O_2(B^3\Sigma_u^-(v' = 0, 2)) \longrightarrow O_2(X) + \text{fluorescence} \tag{A.8}$$
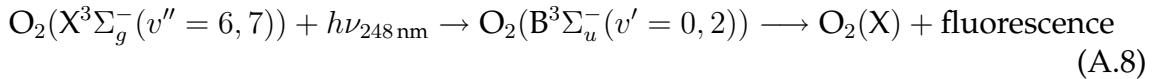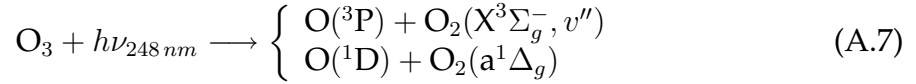
(a) One ArF excimer laser at 193 nm is used for the write step and one KrF excimer laser at 248 nm and an ICCD camera are needed for the visualization of the created NO.

(b) Ozone tagging velocimetry can be applied to dry and humid air environments. There can even be small pollutions of NO, but higher concentrations scavenge intermediate products of O_3 creation. In heavily polluted engine exhausts the NO levels decrease the typical O_3 concentrations by $\sim$20 %. It has been shown that at higher temperatures (T>600 K) the ozone molecule lifetime decreases to below 100 ms (at standard conditions the ozone molecule is stable) [175]. The combined use of OTV and HTV has been demonstrated by Pitz *et al.* [176].

(c) Two excimer lasers are needed.

(d) There is a slight temperature increase (approximately 30 K at 1% dissociation), but not due to focusing of the laser, which is not needed.

5. **APART:** A relatively new MTV technique was developed by Dam *et al.* [8] in 2001. From air present in the flow a new molecule (NO) is created by dissociation and recombination induced by laser radiation. NO is then visualized by LIF. This technique was baptized APART, Air Photolysis And Recombination Tracking [70]. The following equation describes the MTV scheme of APART

$$O_2 + N_2 + nh\nu_{193\,nm} \longrightarrow NO(X^2\Pi) \tag{A.9}$$

$$NO(X^2\Pi, v'' = 0) + h\nu_{226\,nm} \longrightarrow NO(A^2\Sigma, v' = 0) \longrightarrow NO(X^2\Pi, v'') + \text{fluorescence} \tag{A.10}$$
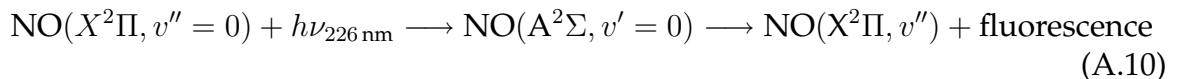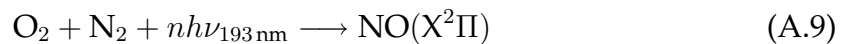
A more recent publication involves the application to base flow velocimetry behind a wedge in a supersonic wind tunnel [177]. Applications to turbulence have been described in the recent thesis by Elenbaas [14].

(a) The technique requires an ArF excimer laser at 193 nm to be focused in the flow and a Nd:YAG pumped dye laser at 226 nm to visualize the created NO. Since all radiation involved in APART experiments is below 300 nm all optics should be optimized for UV. For the same reason an ICCD camera is necessary.

(b) APART can be applied in practically any environment where oxygen and nitrogen are present. High temperatures and high pressures form no fundamental limitation. NO, furthermore, is a stable molecule and its fluorescence is not significantly quenched by oxygen.

(c) The technique requires relatively high powers of the Nd:YAG-pumped dye laser and the excimer laser.

(d) The tagging process is non-linear and the write laser needs to be focused to create NO. The energy deposit in the flow is caused by absorption of the laser light by oxygen in the Schumann-Runge system and subsequent dissociation, but the heating is much more local due to focussing than with the HTV technique.

6. **Tert-butyl nitrite:** By seeding the flow with a molecule that can be dissociated into nitric oxide, Krüger *et al.* [178] introduced tert-butyl nitrite as a tag precursor molecule. They also used a mirror system to perform stereoscopic detection of the velocity field in a laminar-free jet. Two arrays of 15 cylindrical lenses were used to write a two-dimensional grid, resulting in a measurement of the three-dimensional velocity field. The write and read processes of tert-butyl nitrite are given by

$$(CH_3)_3CONO + h\nu_{248\,nm} \longrightarrow NO + (CH_3)_3CO \tag{A.11}$$

$$NO(X^2\Pi, v'' = 0) + h\nu_{226\,nm} \longrightarrow NO(A^2\Sigma, v' = 0) \longrightarrow NO(X^2\Pi, v'') + \text{fluorescence} \tag{A.12}$$
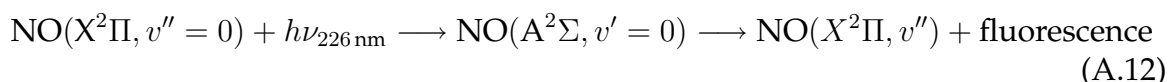
where the last step is identical to Eq. A.10.

(a) One ArF excimer laser at 193 nm [178] or a KrF excimer laser at 248 nm [179], a laser system to create 226 nm (H_2 Raman shifted KrF excimer laser or a frequency-doubled dye laser) and an ICCD camera are necessary for this MTV scheme. Although the photo-dissociation cross section at 248 nm is lower than at 193 nm, the higher powers and lower absorption losses of the former, make this laser the preferred write source.

(b) Tert-butyl nitrite has not been used in high temperature environments. NO is a stable molecule, which should not limit the velocity range theoretically.

(c) Tert-butyl nitrite (gaseous) has to be seeded into the flow. The photodissociation cross section of tert-butyl nitrite is ten times higher than that of NO_2 [178] (see scheme 9).

(d) To increase the out-of-plane resolution the write laser was focused and every 193 nm photon gave 4.9 eV excess energy, which gets lost quickly by molecular collisions [178]. The heat input for the KrF laser is much smaller.

7. **Acetone Tagging:** A negative form of Molecular Tagging Velocimetry is acetone tagging, which was developed by Finke and Grünefeld [180]. The molecule acetone is seeded into the flow after which it is photodissociated into methyl radicals and CO by 193 nm laser radiation. The visualization step is performed by another laser

which creates LIF in the remaining acetone. The line on the image will appear black because only at that position there is no acetone present.

In schematic form the write and read processes are given by

$$(CH_3)_2CO + h\nu_{193\,nm} \longrightarrow CH_3 + CO \tag{A.13}$$

$$(CH_3)_2CO + h\nu_{248\,nm} \longrightarrow (CH_3)_2CO + \text{fluorescence} \tag{A.14}$$
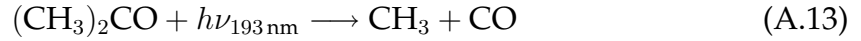
(a) The used lasers are an ArF excimer laser at 193 nm to dissociate NO and a KrF excimer laser at 248 nm or the third harmonic of a Nd:YAG laser [181]. An ICCD camera is required for imaging.

(b) The technique is not applicable in high temperature (> 800 K) zones of a flame, because acetone is combustible [180]. Under ambient conditions, acetone is a stable molecule and the dissociation products will not recombine. At low pressures (1 mbar) the fluorescence lifetime becomes 200 ns (to 50 ns at 24 mbar), probably because there is quenching to triplet states [181]. Similar to biacetyl, the fluorescence of acetone is strongly quenched by oxygen [182].

(c) Acetone needs to be seeded to the flow. The relatively short lifetime limits its use to high speed flows.

(d) The heat input is caused by photodissociation excess energy.

8. **Laser Enhanced Ionization(LEI):** Another, more exotic, negative tagging technique is the ionization of sodium (Na) [183] or strontium (Sr) atoms [184]. Sodium is seeded to the flow and a laser beam depletes a substantial fraction of the neutral species by exciting them to a high electronic state close to the ionization limit. Auto-ionization then follows due to collisions [185]. The use of strontium permits the visualization of the Sr ions themselves using laser radiation, instead of the unlabelled Na atoms.

The respective tagging schemes are as follows

$$Na + h\nu_{193\,nm} + \text{collisions} \longrightarrow Na^+ \tag{A.15}$$

$$Na + h\nu_{589\,nm} \longrightarrow Na + \text{fluorescence} \tag{A.16}$$

for sodium, and

$$Sr(^1S_0) + h\nu_{308\,nm} \longrightarrow Sr(^1P_1) \tag{A.17}$$

$$Sr(^1P_1) + h\nu_{461\,nm} \longrightarrow Sr^+ \tag{A.18}$$

$$Sr^+ + h\nu_{422\,nm} \longrightarrow Sr^+ + \text{fluorescence} \tag{A.19}$$
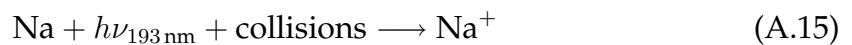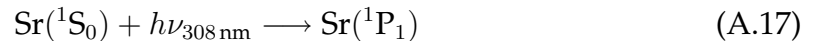
for strontium.

(a) For the ionization of sodium an ArF excimer laser at 193 nm or a dye laser at 450 nm combined with 589 nm (two-step ionization [183]) is utilized. Another dye laser giving laser radiation at 589 is used for the probing step of the neutral sodium. For strontium a XeCl excimer laser at 308 nm excites the molecules and this state is photoionized by a dye laser giving 461 nm. Another dye laser at 422 nm resonantly excites the ions resulting in fluorescence. Furthermore an ICCD camera should be used for detection.

(b) This technique can be applied in high temperatures (reactive environments have been tested [183]). The ionized molecules survive during several milliseconds, because recombination in a weakly ionized plasma is slow [183]. Furthermore, sodium has a relatively low ionization limit, is non-toxic and exists as impurity in many flow environments [186].

(c) Seeding of the atoms is required.

(d) A weakly ionized plasma is formed, locally raising the temperature.

9. **NO$_2$:** Another way of creating nitric oxide tracers is by dissociating NO$_2$ molecules. In 1999 Orlemann *et al.* published this technique [187]. It was applied in a small flow cell, where NO$_2$ was seeded uniformly and dissociated into NO by 308 nm radiation. The imaging was performed by a 226 nm laser beam. The schematic form of this technique is as follows

$$NO_2(X^2A_1) + h\nu_{308\,nm} \longrightarrow NO(X^2\Pi) + O(^3P) \tag{A.20}$$

initially, or

$$O(^3P) + NO_2(X^2A_1) \longrightarrow NO(X^2\Pi) + O_2(X^3\Sigma) \tag{A.21}$$
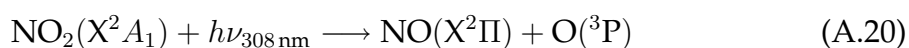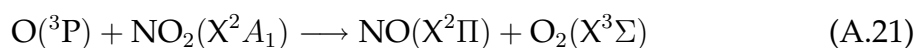
at high NO$_2$ concentrations. The subsequent imaging step is given by Eq. A.10.

(a) The NO$_2$ flow tagging technique require a XeCl excimer laser at 308 nm, a XeF excimer laser pumped frequency doubled dye laser and an ICCD camera.

(b) NO is a stable molecule and its lifetime should not be a limit to the technique.

(c) NO$_2$ is difficult to maintain due to condensation and formation of N$_2$O$_x$. Therefore it needs to be created on site and the required equipment should be available. The dissociation of NO$_2$ should be as close to saturation as possible, because NO fluorescence is efficiently quenched by NO$_2$. Too large concentrations of NO, however, will also attenuate laser and signal intensity. Therefore, an optimal NO$_2$ concentration needs to be found.

(d) The write laser needs to be focused to yield enough intensity to dissociate the NO$_2$.

10. **NO flow tagging:** Danehy *et al.* [188] developed a technique that does not require seeding, but where NO is naturally present by the shock-heating process during normal operation of a shock tunnel. Since velocities are very high, only one laser is needed to create LIF of NO, where fluorescence lifetimes are in the order of 200 ns. The MTV scheme is given by

$$N_2 + O_2 \xrightarrow{\text{shock wave}} NO \tag{A.22}$$

followed by the visualization step A.10.

(a) Only one laser (frequency-doubled excimer-pumped dye laser at 226 nm) is needed for application of the technique. An ICCD camera is necessary for visualization of the NO fluorescence.

(b) NO flow tagging should be applied in low collisional quenching flow environments to increase the fluorescence lifetime. Only high velocities can be measured, where the flow velocity is in the order of w/τ_{LIF} with w the laser sheet width and τ_{LIF} the fluorescence lifetime. NO is naturally present in the flow (created by the shock) and the mole fraction can be adjusted between 0 % and 8 % by varying the O_2/N_2 ratio. The maximum fluorescence lifetime in the absence of quenchers is 220 ns.

(c) Restricted to very high speed flows (appreciable displacement within the fluorescence lifetime).

(d) Extremely low pulse energies (1 mJ) are required, which means that there is almost no energy deposit.

11. **N_2^+ tagging:** By creating nitrogen ions from nitrogen present in air Ress *et al.* developed a tagging technique that requires an ion probe [71]. Since the fluorescence from excited nitrogen ions back to the ionic ground state can be imaged, this technique also has the potential for an all-optical technique.

(a) To ionize the nitrogen molecules the third harmonic of Nd:YAG laser is focused to reach six-photon excitation. An electrically biased probe is needed for detection.

(b) The technique can be used in reactive and non-reactive environment. The lifetime of the tracer in ambient conditions is at maximum 600 μs.

(c) The use of the probe is intrusive.

(d) When this experiment is performed in an oxygen-free environment, the energy excess should only be caused by the ionization energy excess, which is approximately 1.7 eV.

Appendix B

Vereenvoudigde beschrijving

Inleiding

Nadat ik dit proefschrift heb gevuld met tientallen pagina's aan interessante maar moeilijke natuurkunde, wilde ik ook iets te lezen bieden voor de geïnteresseerde leek. In het volgende hoofdstuk heb ik mijn best gedaan om mijn onderzoek zo begrijpelijk mogelijk uit te leggen. Om dit hoofdstuk te lezen is dus geen studie natuurkunde, maar wel wat tijd en concentratie nodig. Ik heb nog wat verwijzingen staan naar plaatjes en hoofdstukken uit de rest van het proefschrift, zodat je toch nog wat heen en weer kunt bladeren. Ik wens je dan ook veel plezier toe met het lezen van dit hoofdstuk. Hopelijk is het een beetje begrijpelijk en anders staat het natuurlijk vrij om mij persoonlijk nog vragen te stellen.

Het testen en onderzoeken van de meettechniek VLLAM (Verbreken van Lucht door Licht en het Achtervolgen van de Moleculen)

In dit proefschrift geef ik een beschrijving van een relatief nieuwe techniek die heel nauwkeurig snelheden van luchtstromingen kan meten. Er bestaan al veel methoden om snelheden te meten, maar onze techniek is uniek om een aantal redenen. Ik zal proberen uit te leggen waarom we geïnteresseerd zijn in het meten van snelheden en ik zal wat voorbeelden geven van meetmethoden. Dan zal ik uitleggen wat onze techniek precies inhoudt en wat ik eraan verbeterd en onderzocht heb.

B.1 Het meten van snelheden van luchtstromingen

B.1.1 Waarom?

Overal om ons heen bevinden zich verschillende soorten stromingen. Enkele voorbeelden hiervan zijn de wind die we buiten kunnen voelen en waterstromingen in een rivier. Het is erg interessant om die stromingen te onderzoeken, want er kan informatie worden
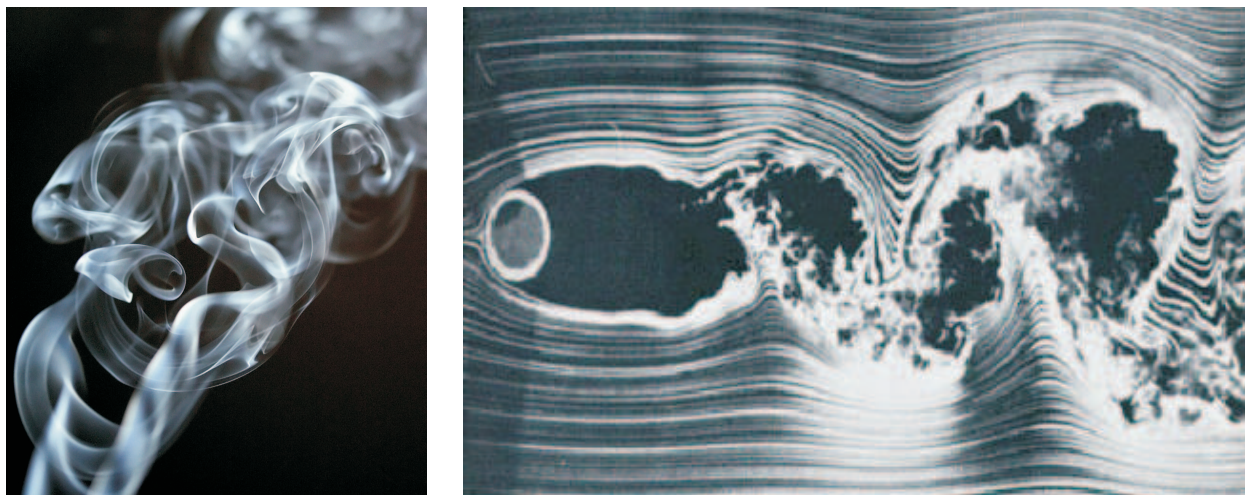
Figuur B.1: *Links: Een foto van omhoog kringelende sigarettenrook. Doordat de warme roetdeeltjes opstijgen en zich vermengen met de lucht, ontstaan er ingewikkelde patronen die moeilijk te beschrijven zijn. Deze turbulentiepatronen zijn erg interessant en treden ook op bij bijvoorbeeld vliegtuigen en auto's. Rechts: Een foto van turbulentie in een vloeistof die door een buis stroomt.*

gevonden over bijvoorbeeld het turbulentieprobleem, wat nog steeds niet helemaal uitgewerkt is (zie Figuur B.1). Verder is het nuttig om meer te weten over de verspreiding van giftige gassen in schoorstenen of auto-uitlaten, en het mengen van bestanddelen in een automotor of in generatoren van elektriciteitscentrales. Een vlam is hier een voorbeeld van op kleinere schaal en hierin worden zuurstof, roet en koolstofdioxide gemengd en vinden ook veel chemische reacties plaats. Om dit soort complexe processen optimaal te laten werken is het belangrijk om precies te weten wat er gebeurt.

Het meten van snelheden van luchtstromingen houdt niet alleen in dat je weet hoe lang de stroming erover doet om van het begin naar het eind te komen. De veranderingen van snelheid binnen die stroming zijn meestal veel interessanter. Tegenwoordig worden vaak computermodellen gebruikt om die informatie te krijgen, maar die moeten wel vergeleken worden met echte metingen om er zeker van te zijn dat ze kloppen met de werkelijkheid. Daarom is het belangrijk om meettechnieken te ontwikkelen en te gebruiken die gedetailleerde informatie geven over wat er gebeurt in een stromend gas.

In Figuur B.2 zien we een schematische voorstelling van snelheidsveranderingen op kleine schaal. Hierdoor is het heel belangrijk om niet alleen over het geheel te weten wat de stroming doet, maar ook in detail voor iedere plek in de stroming. Met dit soort informatie kunnen we meer leren over belangrijke fundamentele processen (waarbij je nieuwsgierigheid wordt bevredigd), maar ook toepassingsgerichte processen (waarbij gewerkt wordt aan iets waar direct gebruik van gemaakt kan worden door, bijvoorbeeld, bedrijven).
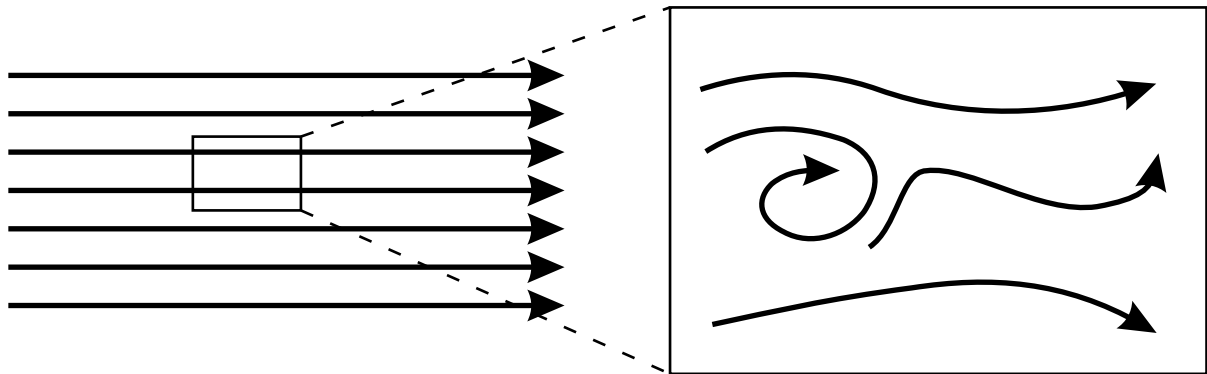
Figuur B.2: *Een luchtstroming van links naar rechts die overal hetzelfde lijkt. Als we een detail uit de stroming bekijken, zien we dat er veel snelheidsveranderingen kunnen plaatsvinden, terwijl de stroming over het algemeen naar rechts blijft stromen.*
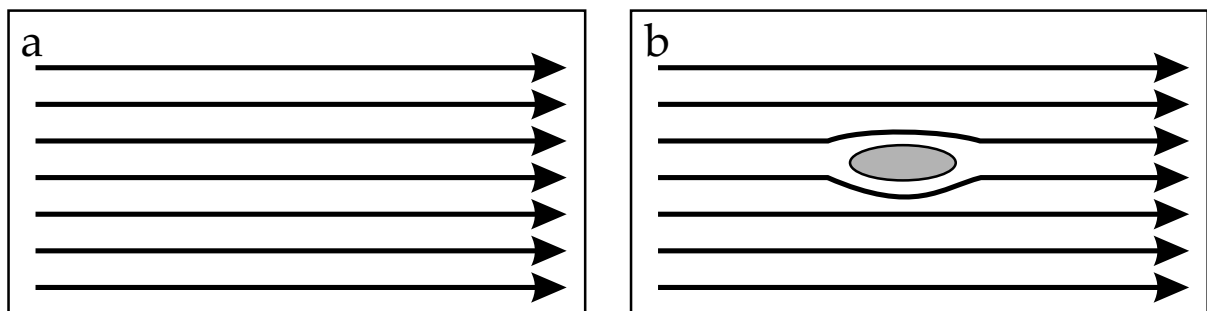
Figuur B.3: *Het plaatsen van een voorwerp in een stroming (a) beïnvloedt de stroming zelf, waardoor je verandert wat je wilt meten (b).*

B.1.2   Hoe wordt snelheid gemeten?

In Hoofdstuk 1.1 wordt in detail behandeld hoe stromingssnelheden kunnen worden gemeten. Hier zal ik een wat algemenere beschrijving geven.

Een apparaatje

Er zijn verschillende manieren om de snelheden in een stroming te meten. De makkelijkste manier is om een snelheidsmeter (een apparaatje) direct in de stroming te plaatsen en dan de snelheid af te lezen. Dit kan gedaan worden met een Pitot buis. Als de bewegende lucht door die buis heen stroomt, ontstaat in de buis een hogere druk door de stroming. Door deze druk te vergelijken met de druk van stilstaande lucht kan de snelheid gemakkelijk worden berekend.

Een ander meetinstrument is een "hotwire", of een "hete draad". Door een dun
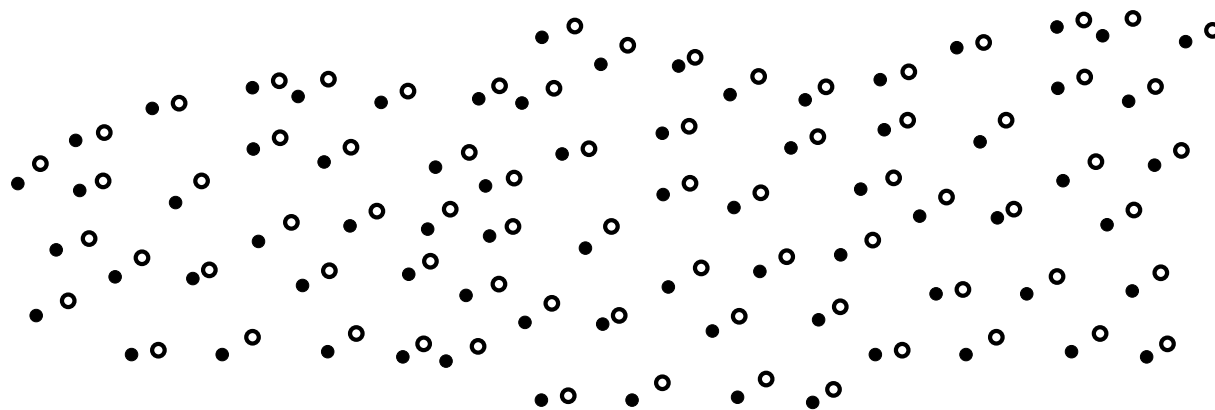
Figuur B.4: *Door een verzameling bewegende bolletjes twee keer te belichten en daar een foto van te maken kun je zien hoe ieder bolletje zich heeft verplaatst in de tijd tussen twee belichtingen. De zwarte bolletjes komen van de eerste belichting en de witte bolletjes van de tweede belichting. Natuurlijk zijn in het echt de witte en zwarte bolletjes niet te onderscheiden, maar met slimme berekeningen is het wel te achterhalen welke bolletjes van de eerste lichtflits komen en welke van de tweede.*

metaaldraadje dat in de stroming is geplaatst wordt een elektrische stroom gestuurd, waardoor die draad opwarmt, net als in een gloeilamp. Wanneer lucht langs de draad stroomt, zal deze lucht gedeeltelijk opwarmen, en de draad zal afkoelen. Hierdoor verandert de weerstand van de draad en dat is te meten. Hoe hoger de snelheid van de stroming, hoe meer de draad afkoelt. Zo kan met een berekening de snelheid worden bepaald.

Bolletjes

Omdat je bij deze methoden een voorwerp in de stroming brengt, zal dat de stroming zelf veranderen (zie Figuur B.3) en dat wil je natuurlijk vermijden. Daarom zijn er andere manieren bedacht om de snelheid te meten. Hierbij wordt niet een groot apparaat in de stroming gezet, maar worden er een heleboel kleine bolletjes in gespoten. Deze bolletjes hebben een diameter van ongeveer tien micrometer: tien keer zo klein als de dikte van een hoofdhaar. Ook al zijn deze bolletjes heel klein, ze weerkaatsen wel licht als je ze beschijnt met een lamp of een laser. Dit weerkaatste licht is op twee manieren te bekijken.

1. De eerste methode is een beetje vergelijkbaar met stofdeeltjes die je wel eens in het zonlicht ziet dansen. Door hun beweging kun je bepalen wat er in de lucht gebeurt: als je er bijvoorbeeld tegen blaast, zie je ze sneller en wilder bewegen. Bij deze techniek wordt een stroboscoop of knipperende lamp gebruikt. Omdat je de deeltjes kunt zien, kun je er twee foto's van maken en die over elkaar heen leggen. Dan zien ze er ongeveer uit als in Figuur B.4. Op die manier kan informatie over de snelheid worden verkregen op meerdere posities in de stroming.
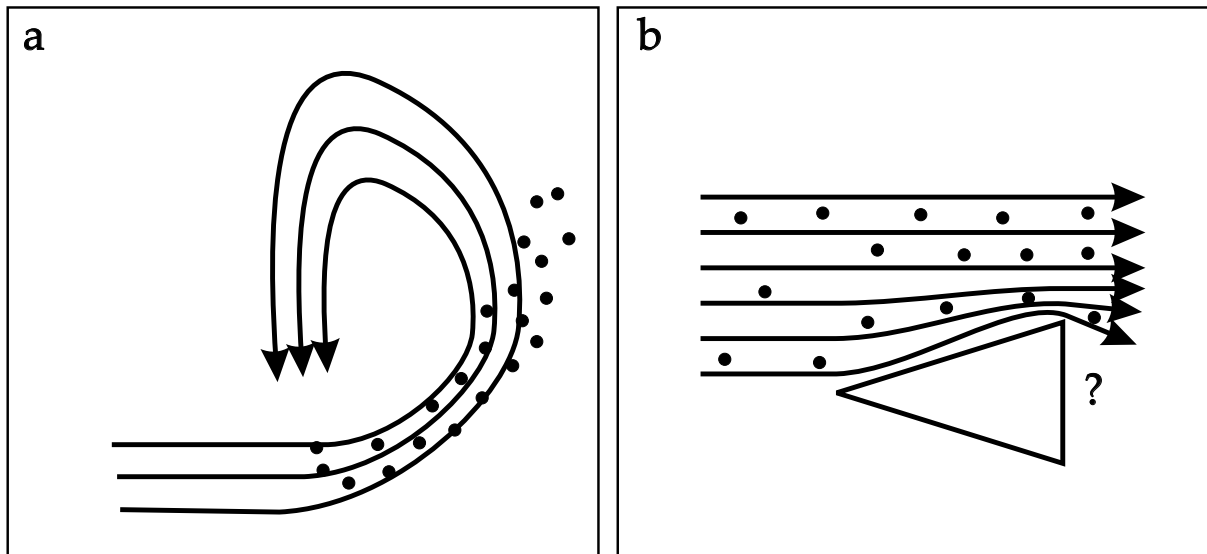
Figuur B.5: *a: Bij sterke veranderingen van snelheid op kleine schaal, zullen de ingebrachte deeltjes te zwaar zijn om precies het verloop van de stroming te volgen. Ze worden dan uit de bocht geslingerd. b: Informatie over de snelheid achter een object in de stroming is moeilijk te verkrijgen, omdat daar de lucht bijna stilstaat. Omdat de deeltjes met de stroming ingebracht moeten worden, komen ze bijna niet op die plaats en kan daar ook niets gemeten worden.*

2. Een andere methode is het meten van de Dopplerverschuiving van het weerkaatste licht. Het Dopplerprincipe is vooral bekend van geluidsgolven. Wanneer een ambulance met sirenes of een trein je voorbij rijdt, zal opeens het geluid veranderen: de toon wordt lager. Dit komt doordat het voertuig beweegt en de geluidsgolven als het ware platdrukt als hij naar je toe rijdt en uitrekt als hij van je afrijdt. Het platdrukken van geluidsgolven zorgt voor een hogere toon, terwijl het uitrekken een lagere toon teweegbrengt. Door het verschil in toon te meten, kan ook de snelheid worden bepaald. Datzelfde geldt ook voor lichtgolven die weerkaatsen op bewegende voorwerpen. Hoe groter de snelheid van dat bewegende voorwerp, hoe meer de kleur van het weerkaatste licht verandert. Dat verschil in kleur is te meten en om te rekenen naar een snelheid.

Deze methoden verstoren de stroming al een stuk minder, omdat er maar kleine voorwerpen ingebracht worden. Toch zijn ook hierbij nadelen aanwezig. Figuur B.5 toont de twee belangrijkste problemen, die te maken hebben met de traagheid en de dichtheid van de deeltjes. De techniek die wij ontwikkeld hebben, lost deze twee problemen grotendeels op.
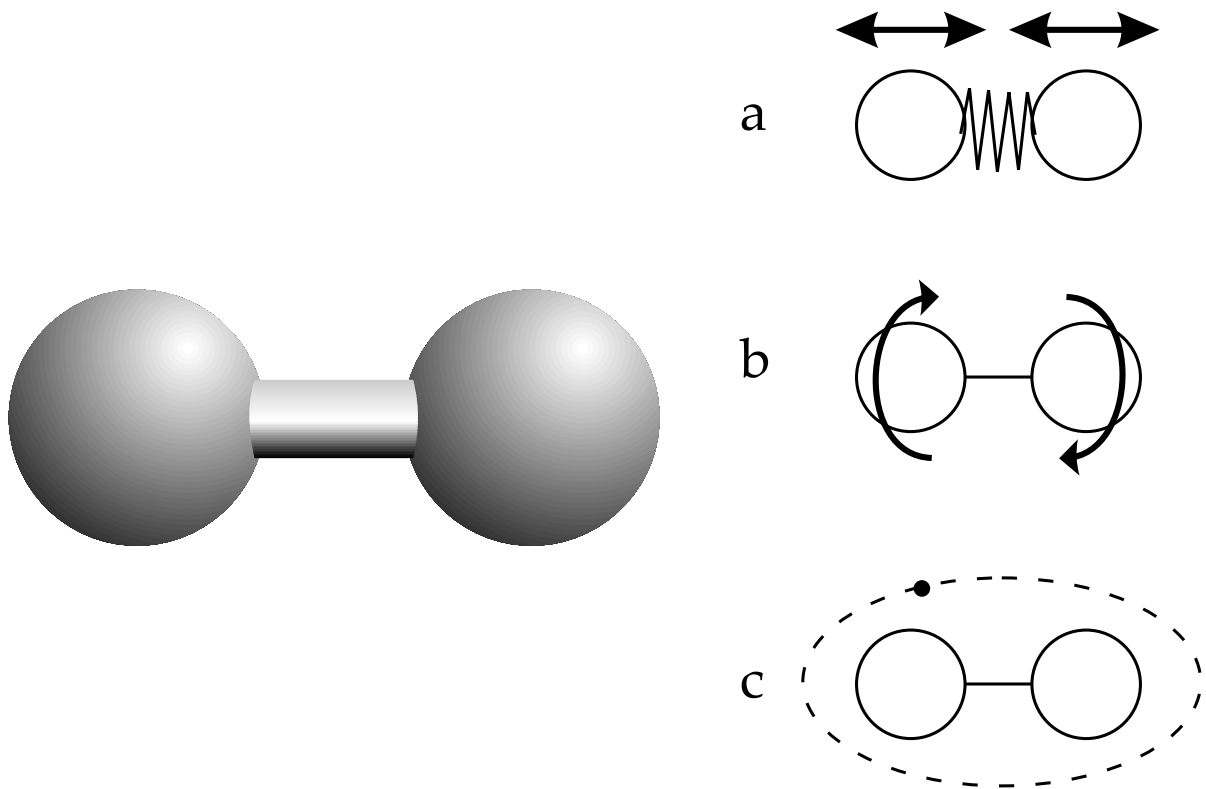
Figuur B.6: *Een schematische voorstelling van een zuurstof- of stikstofmolecuul; twee bolletjes die met elkaar verbonden zijn. Deze moleculen staan niet stil. Ze kunnen trillen alsof er een springveer tussen de bolletjes zit (a: vibratie), ze kunnen draaien ten opzichte van elkaar (b: rotatie) en een nog kleiner deeltje draait om het molecuul heen (c: elektron).*

B.2   Hoe werkt onze techniek?

B.2.1   Moleculen

In plaats van het toevoegen van kleine bolletjes gebruiken wij de kleinste deeltjes die aanwezig zijn rondom ons heen: moleculen. Om deze techniek en het verdere onderzoek te kunnen begrijpen is het belangrijk om iets over moleculen te weten. De lucht om ons heen bestaat grotendeels uit de moleculen zuurstof en stikstof. Deze moleculen zijn zo klein dat ze compleet onzichtbaar zijn voor ons oog. Om je te kunnen voorstellen hoeveel moleculen er zijn, moet je je een hoeveelheid lucht voorstellen, zo groot als een waterdruppel die aan een kraan hangt. Daarin bevinden zich ongeveer 1000.000.000.000.000.000 moleculen. Al deze moleculen bewegen rond ons heen en botsen tegen ons aan. Het botsen van die moleculen voelen we als luchtdruk en hoe sneller deze moleculen zich bewegen, hoe hoger de temperatuur.

Energie

Als we hier één molecuul uitlichten, zien we een deeltje zoals in Figuur B.6. Een stikstof-
of zuurstofmolecuul uit de lucht kun je je voorstellen als twee bolletjes met een springveer
ertussen. Die veer kan de bolletjes op en neer laten trillen en de bolletjes kunnen draaien
ten opzichte van elkaar, zodat het een beweeglijk geheel is. Moleculen hebben een eigen
energie, ook wel interne energie genoemd, en deze energie is opgeslagen in het molecuul.
Als zo'n molecuul harder gaat triller of sneller gaat draaien, betekent dit dat de interne
energie van het molecuul groter wordt. We spreken dan ook wel van vibratie(trillings)-
energie en rotatie(draaiings)-energie.

Een derde interne energie is de elektronische energie. Deze heeft niets met elektriciteit
in huis te maken, maar met elektronen. Dit zijn geladen deeltjes die nog veel kleiner zijn
dan moleculen (ongeveer 100.000 keer zo klein) en waarvan er 16 rondom het zuurstof-
molecuul vliegen, vergelijkbaar met de draaiing van de aarde om de zon. Als een elek-
tron meer energie krijgt, zal hij een grotere cirkel om dat molecuul heen maken. Je kunt
je dat voorstellen door een tennisbal aan een elastiek vast te maken en dan rondjes om je
eigen as te gaan maken, terwijl je het elastiek aan het uiteinde vasthoudt. Als je nu meer
energie toevoegt door sneller te gaan draaien, zal de elastiek zich verder uitrekken. Het-
zelfde gebeurt bij een elektron dat dan de interne energie van het molecuul groter maakt
door sneller om het molecuul heen te gaan draaien.

B.2.2 Licht

Voor de volgende paragraaf is het handig om ook wat basiskennis te hebben over licht.
Het licht dat we om ons heen zien heeft allerlei verschillende kleuren. Die kleuren zijn
bepaald door de golflengte van het licht, die weer gerelateerd is aan de energie van het
licht. Blauw licht bijvoorbeeld heeft een kortere golflengte en een hogere energie dan
rood licht. Voor dit onderzoek is het handig om licht te zien als kleine pakketjes energie,
die fotonen genoemd worden. Ieder foton heeft dan een energie die overeenkomt met
de kleur van het licht. Een rode lichtbundel bijvoorbeeld met een golflengte van 600 nm
(of 0,0006 mm), bestaat uit fotonen met een energie van 0,0000000000000000003 J of 2 eV
(waarbij eV, "elektronvolt", een andere eenheid van energie is die veel gebruikt wordt in
dit deel van de natuurkunde). Dat is heel weinig energie, maar iedere lichtbundel bestaat
weer uit heel veel fotonen.

B.2.3 Quantumfysica of stapjesnatuurkunde

De quantumfysica binnen de natuurkunde is een theorie die erg moeilijk te begrijpen is,
maar wel heel belangrijk is voor onze techniek. Om toch een idee te geven hoe deze
theorie in elkaar zit, zal ik een paar belangrijke begrippen bespreken en toelichten.

Ladders

De interne energie van moleculen, die we eerder besproken hebben, kan niet zomaar ver-
anderd worden in iedere willekeurige energie. Het is niet als met de tennisbal en het
elastiek, dat je een beetje sneller rondjes kunt draaien en dat de tennisbal dan een iets

Figuur B.7: *a: Het eerste kader toont een energieladder voor een molecuul. De laddertreden geven de verschillende mogelijke energietoestanden van dit molecuul aan. De balkjes 1 en 2 geven de energie weer van twee verschillende kleuren licht. Balkje 1 zal geen verandering veroorzaken, omdat deze niet precies past tussen twee laddertreden, terwijl balkje twee precies past. b: In het tweede kader zien we dezelfde ladder, maar nu geeft de omhooggaande pijl de stijging in energie aan, veroorzaakt door blauw licht met precies de juiste hoeveelheid energie. Het molecuul komt in een hogere energietoestand terecht en omdat het liever in de toestand zit met de laagste energie, valt het van de ladder omlaag. Dat kan naar verschillende laddertreden en daarbij zal het molecuul energie moeten kwijtraken in de vorm van licht. Als je dus blauw licht in zo'n molecuul stopt, geeft het blauw, groen en rood licht terug.*

grotere cirkel maakt. Die energieverandering kan alleen in stapjes, en vandaar de naam quantumfysica, of "stapjesnatuurkunde". De energie in een molecuul is te vergelijken met een ladder, waarbij de hoogte waarop je op de ladder staat aangeeft, hoeveel energie je hebt. Je kunt daarbij alleen op de treden staan. Het is niet mogelijk om tussen twee treden in te zweven. Datzelfde geldt ook voor de energie van moleculen, die daardoor niet met iedere frequentie kunnen trillen of draaien en waarbij het elektron zich niet in iedere baan kan bevinden.

Verder hebben alle gelijke moleculen (bijvoorbeeld twee zuurstofmoleculen) precies dezelfde ladder van energie. Als we dan naar verschillende moleculen kijken, bijvoorbeeld zuurstof en stikstof, dan hebben die compleet verschillende energieladders. Dit verschil geeft ons dus een manier om de verder voor het oog onzichtbare moleculen te onderscheiden. We kunnen ontdekken of we naar stikstof- of zuurstofmoleculen kijken, als we het verschil tussen die ladders kennen.

Energie en Licht

Er zijn verschillende manieren om moleculen een grotere energie te geven. Dit kan bijvoorbeeld door ze te verhitten of er een elektrische stroom doorheen te sturen. Een andere
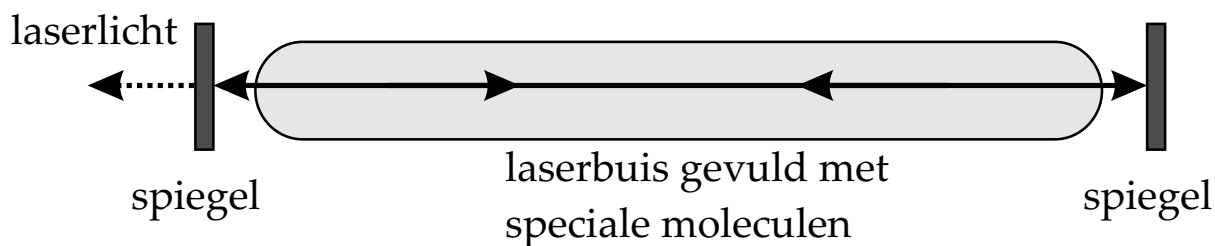
Figuur B.8: *Een schematische tekening van een laser. In de laserbuis bevinden zich speciale moleculen die in een hogere energietoestand worden gebracht door ze bijvoorbeeld onder een spanning van enkele tienduizenden Volt te zetten of met een speciale flitslamp te belichten. De moleculen vallen weer terug in de grondtoestand en zenden licht uit van één kleur. Dat licht weerkaatst tegen de spiegels die vrijwel niets doorlaten en zo stuitert het licht op en neer tussen de spiegels, waarbij zoveel mogelijk moleculen ook licht uitzenden. Op een gegeven moment zitten er zoveel fotonen tussen de spiegels dat er een klein beetje licht wordt doorgelaten en zo heb je laserlicht.*

manier is door er licht op te schijnen. Daarbij is het wel belangrijk dat de golflengte, oftewel de energie van dat licht goed gekozen wordt, want het is niet mogelijk om het molecuul halverwege een laddertrede te tillen: het moet precies op de volgende trede terechtkomen. In Figuur B.7 is zo een ladder te zien.

De meeste moleculen bevinden zich in de laagste energietoestand, oftewel de grondtoestand. Wanneer licht met precies de goede kleur op dit molecuul gericht wordt, zal het in een hogere energietoestand of "aangeslagen toestand" terechtkomen. Toch wil het zich in de laagst mogelijke energietoestand bevinden en valt het molecuul dus weer van de ladder omlaag. Dat kan door direct naar de grondtoestand te vallen of via verschillende laddertreden omlaag te gaan. Het overschot aan energie moet het kwijtraken en dat doet dat molecuul door licht uit te zenden. Als het niet direct naar de laagste laddertrede terugvalt, maar naar een iets hoger gelegen (zoals in Figuur B.7) zal het molecuul licht met minder energie uitzenden, bijvoorbeeld groen of rood licht. Als je naar één molecuul kijkt, zie je dus maar één kleur, maar omdat je altijd naar meerdere moleculen kijkt, zul je altijd veel meer kleuren te zien krijgen. Je krijgt een spectrum van kleuren en dit verschijnsel noemen we fluorescentie. Je kunt je hierbij voorstellen dat je met die informatie van de verschillende kleuren en wat rekenwerk kunt achterhalen hoe die ladder er precies uitziet en zo kun je dus de moleculen herkennen.

B.2.4 Lasers

In dit onderzoek hebben we die laddereigenschap van moleculen veel gebruikt. Nu is het natuurlijk niet alleen belangrijk om een goede kleur licht uit te kiezen; je moet hem ook kunnen maken. We pakken niet gewoon een gloeilamp en hangen er dan een groen papiertje voor om groen licht te maken. In de natuurkunde is een krachtig apparaat uitgevonden om verschillende kleuren licht met heel veel vermogen te maken: de laser.

De lasers die ik gebruikt heb (zie paragrafen 2.2.1 en 2.2.2), werken zelf volgens het ladderprincipe van de moleculen, waarbij een laserbuis gevuld met een bepaald molecuul onder een heel hoge spanning wordt gezet. De moleculen krijgen dan extra energie die ze weer kwijtraken door licht uit te zenden. Doordat een uitgezonden lichtdeeltje "botst" met een molecuul dat al een hogere energie heeft, maar nog geen licht heeft uitgezonden, wordt die opeens gedwongen om meteen een nieuw lichtdeeltje uit te zenden in dezelfde richting. Zo ontstaat een watervaleffect van lichtdeeltjes. Dit licht gaat op en neer kaatsen tussen twee spiegels (zie Figuur B.8) en zo wordt een heleboel energie opgebouwd.

Het typische aan een laser is dat hij maar één specifieke kleur uitzendt. Er komt geen andere kleur licht uit, ook al zenden de moleculen wel verschillende kleuren licht uit, zoals je eerder kon zien in Figuur B.7b. Die andere kleuren worden weggehaald door de afstand tussen de twee spiegels in Figuur B.8 precies af te stemmen op de gewenste kleur laserlicht. In zo'n laser kan zoveel vermogen zitten dat je er zelfs metaal mee kan snijden. Door de laserbuis te vullen met een ander soort gas of een bepaald soort kristal (dus andere moleculen) kan licht van allerlei kleuren (infrarood tot ultraviolet) gemaakt worden.

B.2.5 De techniek: VLLAM

Na deze uitgebreide voorbereiding komen we eindelijk bij de meettechniek zelf. Zoals we al eerder hebben besproken, zitten er een aantal nadelen aan het inspuiten en volgen van kleine bolletjes in een stroming. Met onze techniek gebruiken we geen bolletjes, maar volgen we de moleculen van de stroming zelf. Dat gebeurt in drie stappen:

1. We gebruiken voor de eerste stap een laser die onzichtbaar, ultraviolet licht uitzendt met een golflengte van 193 nm. Deze laserbundel schieten we door een lens waardoor hij in een heel dun lijntje wordt geperst, zoals te zien is in Figuur B.9. Omdat er erg veel energie zit in zo'n dun lijntje worden de luchtmoleculen (stikstof (N_2) en zuurstof (O_2)) in dit brandpunt als het ware stukgeschoten. Meteen vormen zich in een chemisch proces stikstofoxide-(NO)-moleculen. Dit zijn nieuwe moleculen die ook een andere ladderstructuur hebben dan de stikstof- en zuurstofmoleculen. Desondanks zijn deze moleculen met het oog niet te onderscheiden van de luchtmoleculen.

2. Omdat de nieuwe stikstofoxidemoleculen alleen in die dunne lijn van de laser zijn gemaakt, hebben we nu een dun lijntje van NO moleculen, omringd door luchtmoleculen. Deze lijn zal met een stroming meebewegen en iedere snelheidsverandering zal ook zijn effect hebben op de positie van die NO moleculen. Op sommige plekken in de stroming bewegen de moleculen sneller en op andere plekken langzamer, waardoor de lijn vervormt (zie Fig. B.9).

3. Een korte tijd later (gecontroleerd door de vertragingsgenerator in Figuur B.9) wordt een tweede laser gevuurd. Deze laser geeft ook ultraviolet licht af, maar dan met een golflengte van 226 nm. Deze kleur is zo gekozen dat hij precies tussen twee laddertreden van het NO molecuul past, maar helemaal niet past in de ladder van
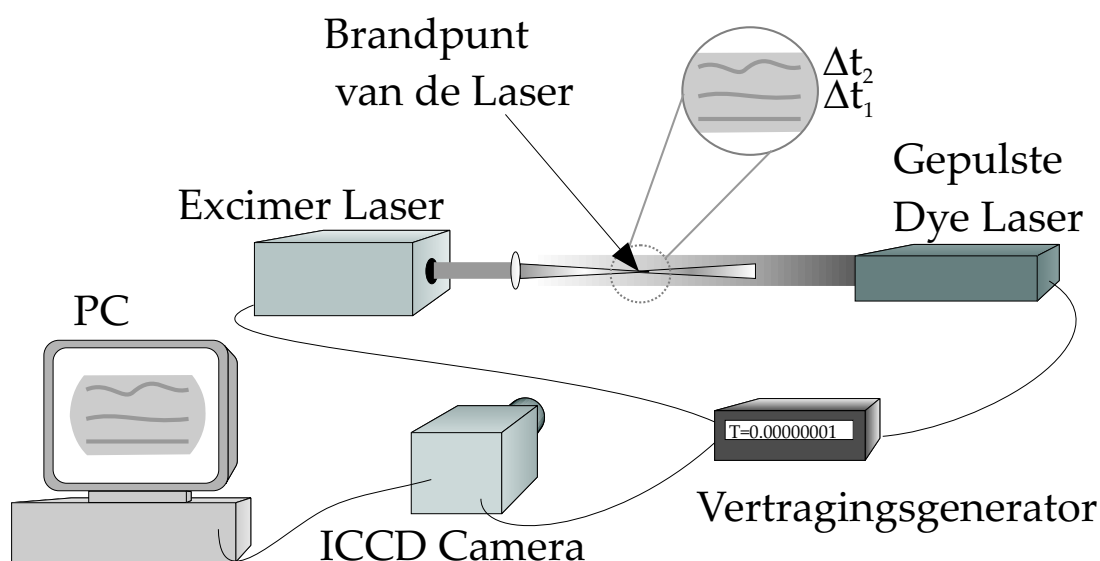
Figuur B.9: *De opstelling van VLLAM. De excimer-laser schrijft een lijn van stikstofoxide-moleculen die meebewegen met de stroming. Een dye-laser wordt een korte tijd daarna gevuurd om de verplaatste lijn van moleculen uit te lezen en hierdoor ontstaat een beeld op de camera. Zie ook Figuur 3.1.*

stikstof en zuurstof. Hierdoor zullen alleen de NO moleculen naar een hogere energietoestand worden gebracht en zullen we ook alleen licht zien terugkomen van die lijn van NO-moleculen. Een paar typische plaatjes kunnen worden bekeken in Figuur B.11. Een schematische voorstelling van het hele proces is te zien in Figuur B.10.

Verbeterde Techniek

De Engelse naam van deze techniek, APART, staat voor Air Photolysis And Recombination Tracking, wat zoveel betekent als het verbreken van lucht onder de invloed van licht en het volgen van de nieuw gecombineerde moleculen. Daarom heb ik als Nederlandse naam VLLAM gekozen, oftewel het Verbreken van Lucht met Licht en het Achtervolgen van de Moleculen. Er zijn meerdere technieken die lijken op deze VLLAM-techniek en die staan allemaal beschreven in Appendix A.

De twee genoemde problemen bij het meten met kleine bolletjes (zie Figuur B.5) hadden te maken met het uit de bocht vliegen van de bolletjes en dat er op sommige plekken in de stroming geen bolletjes terechtkomen. De moleculen in onze techniek zullen in principe alle veranderingen in stromingsrichting en snelheid moeten kunnen volgen, omdat de stroming is opgebouwd uit deze moleculen. Verder kunnen we gewoon overal stikstofoxide moleculen maken, als er maar lucht aanwezig is. Zo kunnen we onze laser, bijvoorbeeld, achter het object uit Figuur B.5 richten en maken we onze moleculen waar we eerder nog niet konden meten.
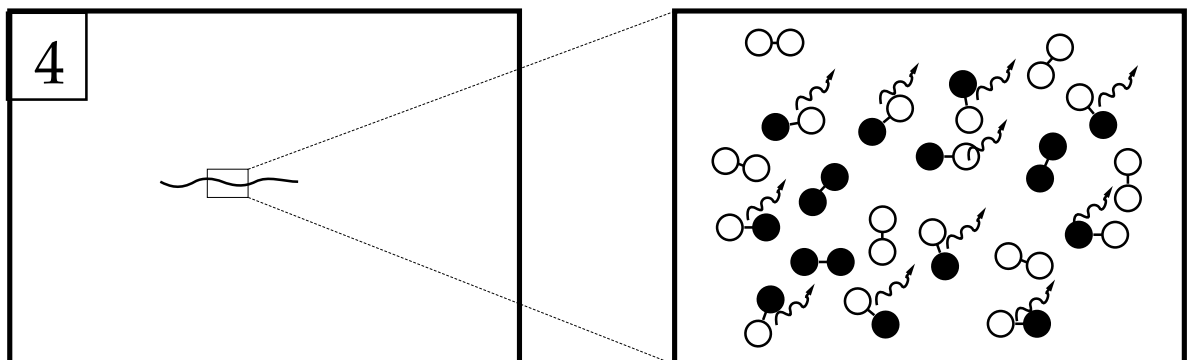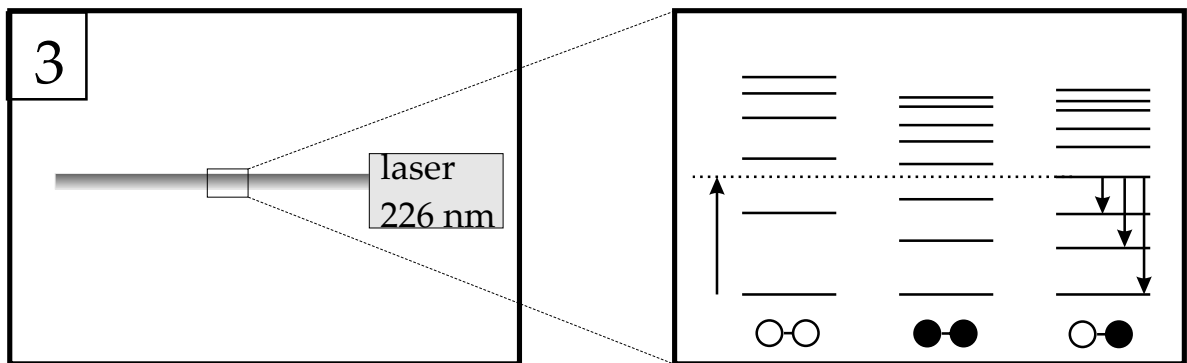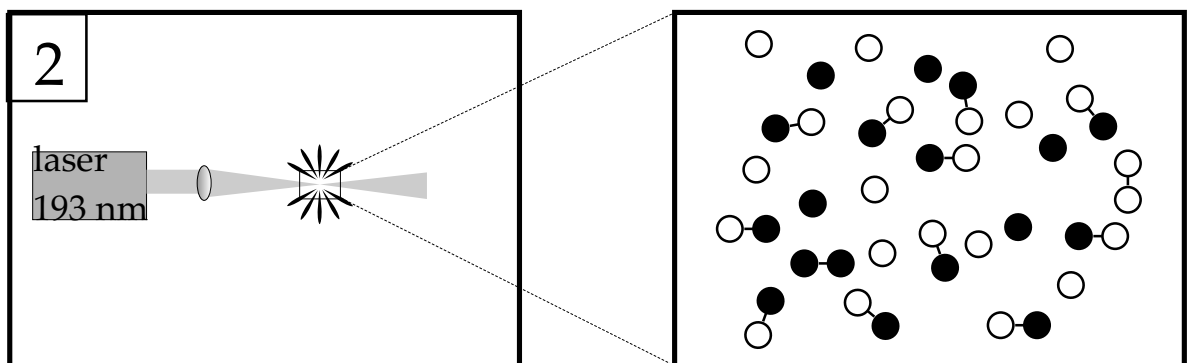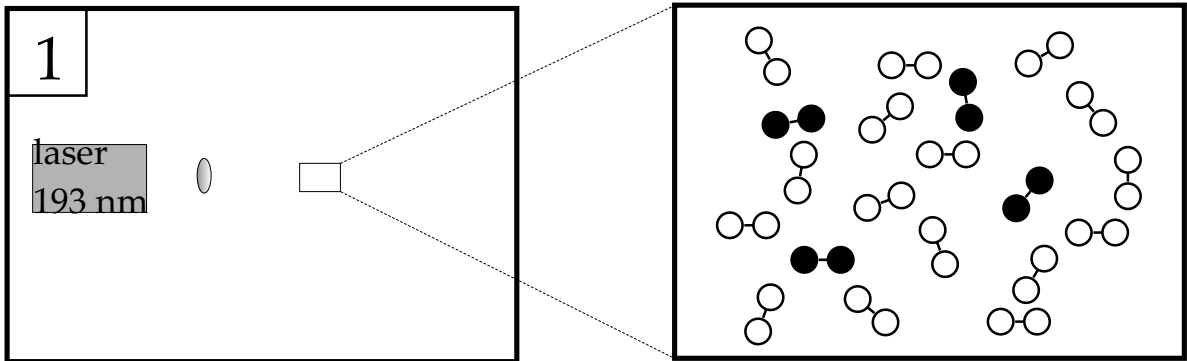
Figuur B.10: *Een schematische voorstelling van de VLLAM-techniek. In tekening 1 is aan de linkerkant de laser te zien met een lens. We vergroten een klein deel van de lucht (de rechthoek), zodat we wat moleculen zien. De witte bolletjes stellen stikstofmoleculen voor en de zwarte bolletjes stellen zuurstofmoleculen voor. Als nu in tekening 2 de laser wordt aangezet, wordt de laserbundel in het brandpunt geknepen, net als bij een loep en zonlicht. De luchtmoleculen worden door die laser kapot geschoten en vormen nieuwe moleculen. Deze combinatie van een wit en een zwart bolletje is een stikstofoxidemolecuul. Ook zie je nog wat stukgeschoten bolletjes rondvliegen, maar die zullen snel samengaan met een ander eenzaam bolletje. In tekening 3 wordt de tweede laser gevuurd, waarbij we in het rechterkader aan de linkerkant een pijl zien die de energie van die laserbundel voorstelt. Ook staan de energieladders van de drie moleculen erbij. De pijl van de laser past alleen bij de stikstofoxidemoleculen en daar zal dus licht vandaan komen en niet van de andere twee moleculen. In tekening 4 is dan ook te zien dat er een oplichtende lijn verschijnt die gekronkeld is, omdat de lucht wat aan het bewegen is. In het rechterkader kunnen we dan zien dat alleen de stikstofoxidemoleculen dit licht uitzenden (gekronkelde pijl). In het proefschrift kun je bij Figuur 1.1 een iets gedetailleerdere versie van dit schema bekijken.*
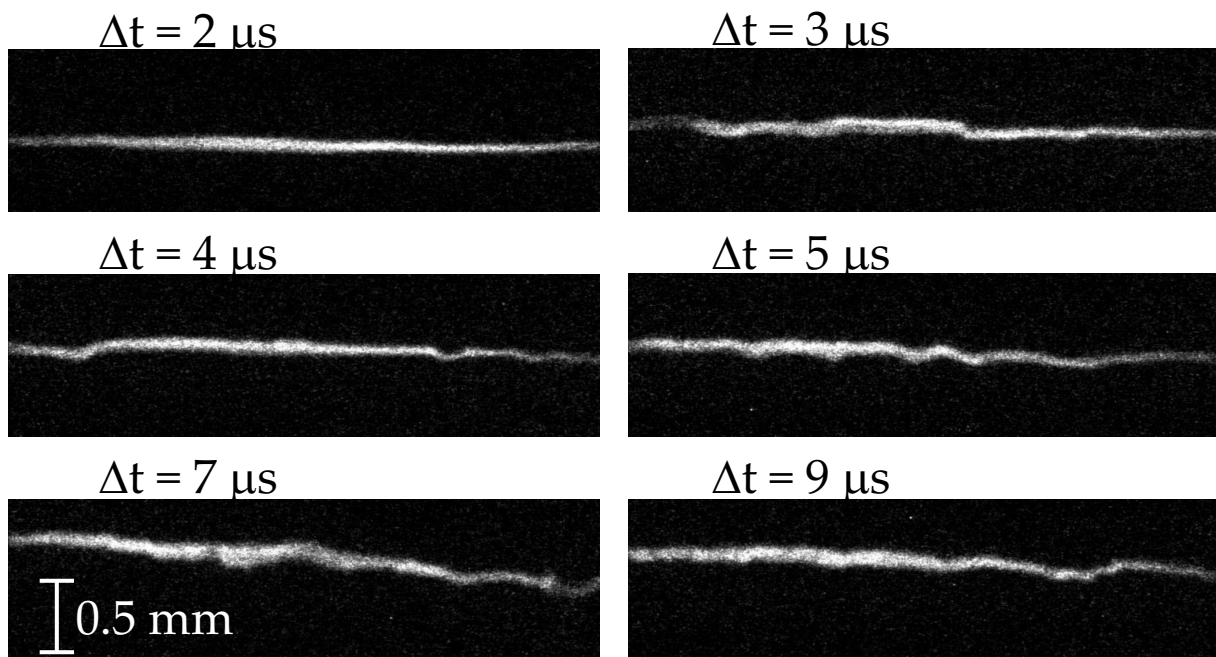
Figuur B.11: *Enkele voorbeeldplaatjes van stikstofoxide-lijnen die zichtbaar zijn gemaakt in een stroming van 40 m/s met behulp van de techniek VLLAM. Door de verplaatsing van de lijn bij bijvoorbeeld 9 μs (0,000009 s) ten opzichte van een beginlijn (bijvoorbeeld de horizontale lijn bij 2 μs) te meten en te delen door de tijd van verplaatsing (9−2 = 7 μs) kan de snelheid voor ieder punt op de lijn worden berekend. Zie voor een ander voorbeeld Figuur 1.2.*
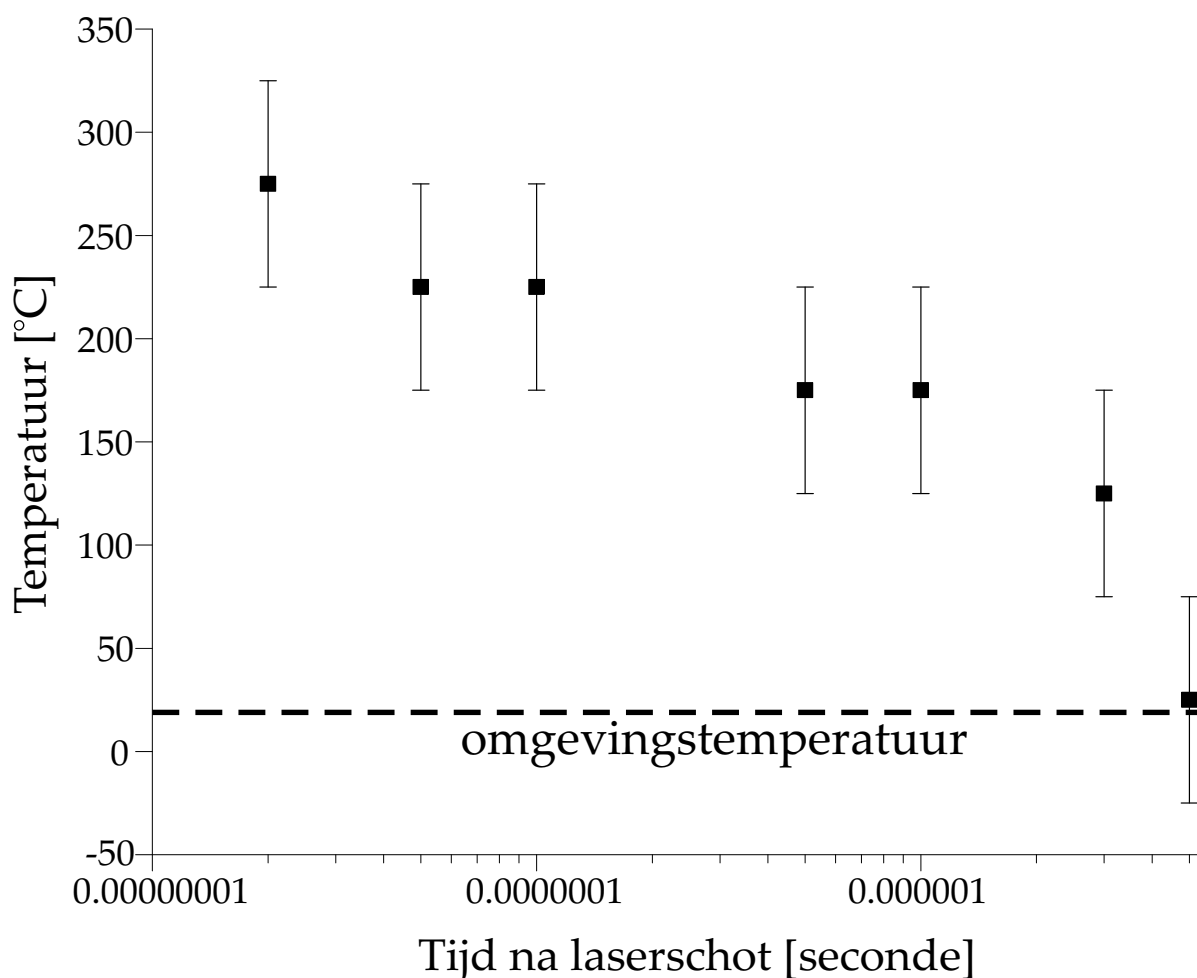
Figuur B.12: *Een grafiek van de temperatuur in het brandpunt, nadat de laser is gevuurd (zie ook Figuur 2.8). Helemaal in het begin zien we dat de temperatuur vrij hoog is, maar deze daalt ook weer heel snel.*

B.3 Wat heb ik met deze methode gedaan?

De VLLAM-techniek heeft de basis gevormd voor mijn proefschrift, wat is opgedeeld in meerdere hoofdstukken. In de eerste paar hoofdstukken staan een inleiding en een beschrijving van alle apparatuur die gebruikt is. In de volgende hoofdstukken beschrijf ik de toepassing van de techniek in twee extreme omstandigheden: onder hoge druk en in een vlam. Uiteindelijk probeer ik in het laatste stuk te begrijpen, wat er gebeurt in het brandpunt van de laser waar de nieuwe stikstofoxidemoleculen worden gemaakt.

B.3.1 Overzicht

De inleiding en beschrijving van apparatuur in het eerste deel is deels al eerder in deze vereenvoudigde beschrijving behandeld. Wat nog wel interessant is, is een meting van de temperatuurstijging in het brandpunt van de laser. Omdat daar heel veel energie samenkomt en de lucht deels wordt stukgeschoten, kan de temperatuur ook stijgen. Hierdoor kan de lucht ook sneller gaan stromen en dat wil je juist voorkomen met deze techniek. Om een idee te krijgen hoeveel de temperatuur stijgt, is hier een meting aan gedaan.

Temperatuur

De hoeveelheid licht die moleculen uitzenden nadat ze in een hogere energietoestand zijn gebracht (fluorescentie), is ook afhankelijk van de temperatuur. Door die hoeveelheid licht te meten, konden we dus de temperatuur bepalen (zie Figuur B.12). Hieruit bleek dat deze in het brandpunt stijgt tot ongeveer 600 K (300 °C), maar dat deze ook weer daalt tot omgevingstemperatuur binnen 3 microseconden (drie miljardste seconde). Dit lijkt heel snel, maar in vergelijking met de tijdschalen van onze experimenten (tientallen microseconden), is dat nog wel merkbaar. Voor een beschrijving van de temperatuurmetingen uit mijn proefschrift zie Hoofdstuk 2.4.

Meetafstand

In een ander experiment hebben we de werkafstand of meetafstand vergroot. De werkafstand is de afstand van alle apparatuur (lasers en camera) tot aan de plek waar het experiment plaats vindt. Om de VLLAM-techniek te kunnen gebruiken in industriële opstellingen, zoals windtunnels, is het belangrijk om alle apparatuur buiten die windtunnels te hebben staan. Anders loop je het risico de apparatuur te beschadigen of de stroming te beïnvloeden. Tijdens mijn metingen stond normaal gesproken alle belangrijke apparatuur (camera en lens) op ongeveer 25 centimeter van waar we wilden meten. Nadat we alles verplaatst hadden tot een werkafstand van ongeveer 1 meter, hebben we laten zien dat de techniek ook op die afstand werkt, zoals te zien is in Figuur 2.7. Dat is natuurlijk nog niet genoeg voor windtunnels, die soms wel tientallen meters groot kunnen zijn, maar het is een flinke verbetering. Voor een beschrijving van de experimenten op grotere werkafstanden kun je Hoofdstuk 2.3 lezen.

B.3.2 Toepassing

Hoge druk

Om te laten zien dat onze techniek niet alleen goed werkt in een normale omgeving hebben we ook gekeken naar een hoge druk. In een vat van ongeveer 10 liter hebben we de druk gevarieerd tussen 1 bar (normale luchtdruk) en 80 bar en we hebben de verhouding tussen zuurstof en stikstof (normaal 1:4) veranderd. Hieruit bleek dat de techniek beter werkt als er bij hogere drukken minder zuurstof toegevoegd wordt, zodat in plaats van 20 % zuurstof in normale lucht maar 1 % zuurstof bij 10 bar wordt gebruikt. Dit komt omdat zuurstof heel makkelijk het licht van de laserbundel in zich opneemt, waardoor er
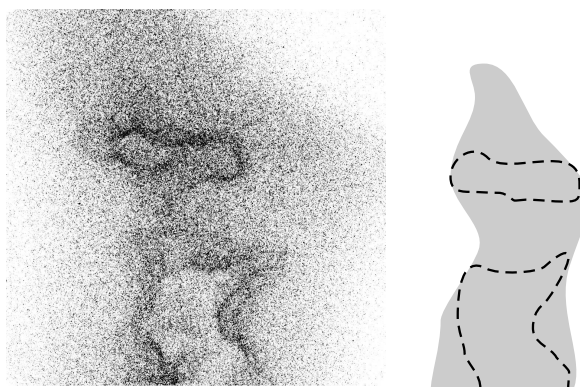
Figuur B.13: *Als we met een speciale camera naar deze vlam kijken, zien we een soort ballonvorm, die het vlamfront voorstelt. Dit is het gedeelte waarin de verbranding plaats vindt. Aan de rechterkant staat een schematische tekening van een vlam met de ballonvormen ingetekend.*

heel snel kleine explosies en bliksemflitsjes kunnen ontstaan in ons brandpunt. Dit willen we vermijden om zo goed mogelijk te kunnen meten.

Als we naar de lijn van NO-moleculen kijken, zien we dat deze breder wordt, omdat de nieuwe moleculen zich vermengen met de luchtmoleculen. Bij een hogere druk verwachten we dat die verbreding minder zal zijn, wat we ook zien in Figuur 3.4.

Hoge temperatuur

Een andere extreme omgeving is hoge temperatuur met verbranding, oftewel een vlam. Hierbij hebben we gekeken of we bij twee speciale branders (zie Figuren 2.5 en 2.6) de snelheid van de gasstroming konden meten. Dit lukte over het algemeen goed, behalve als we naar het vlamfront (zie Figuur B.13 en 4.11) keken. Het vlamfront is het gebied waar de verbranding van zuurstof en brandstof plaatsvindt en dat is meestal het blauwe gebied in een vlam. In dit vlamfront hebben we gezien dat onze techniek niet zo goed werkt, hoogstwaarschijnlijk omdat daar geen zuurstof meer aanwezig is, die wel nodig is om stikstofoxide te kunnen maken.

B.3.3 Bestudering

Om de techniek beter te maken dan hij is, moeten we er voor zorgen dat er een maximale hoeveelheid licht van de stikstofoxidemoleculen afkomt. Dit kunnen we doen door zoveel mogelijk van die moleculen te maken met onze laser, want hoe meer moleculen, hoe meer licht, des te makkelijker is het meten. Als we weten welk proces belangrijk is bij het maken van de nieuwe stikstofoxidemoleculen kunnen we deze kennis gebruiken. De zuurstof- en stikstofmoleculen worden niet gewoon stukgeschoten. Doordat ze een bepaalde energie opnemen, gebeurt er nog wat meer met ze. Omdat dat proces erg complex is, moeten we het in kleine stapjes gaan ontleden. Dat kunnen we het beste doen,
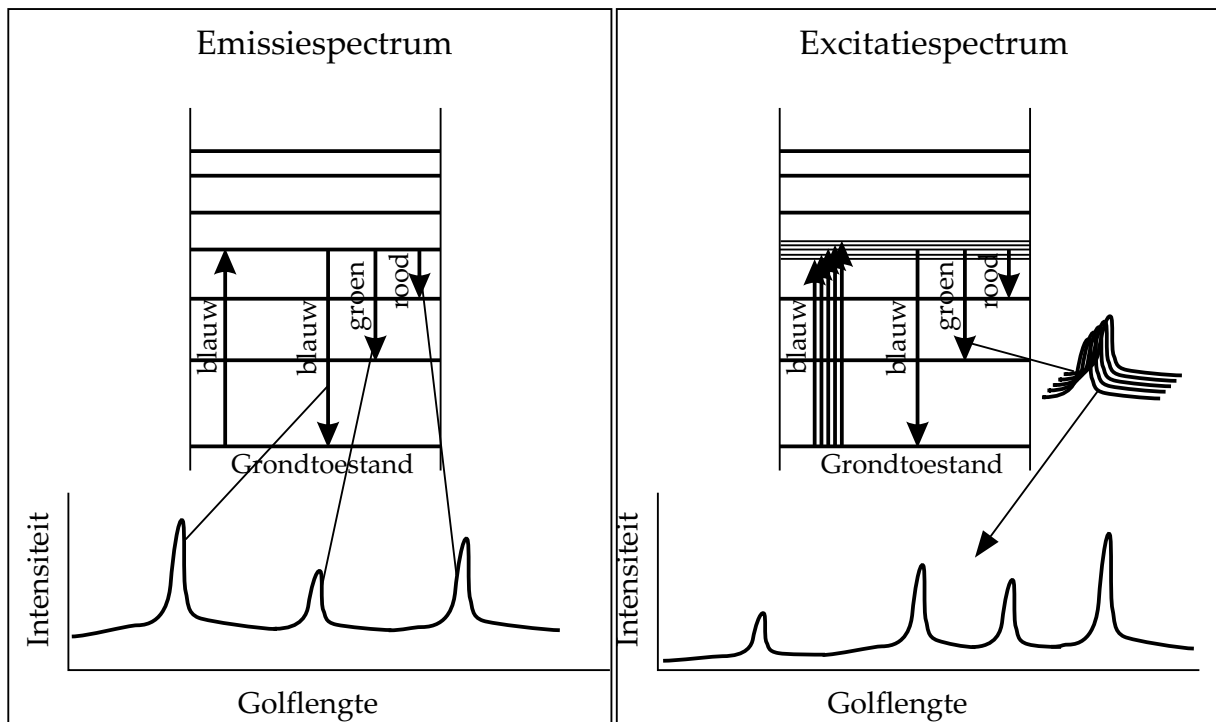
Figuur B.14: *In deze tekening staan de principes van een emissiespectrum en een excitatiespectrum. In het emissiespectrum links wordt met één kleur licht op een aantal moleculen geschoten en dan wordt gekeken naar het licht wat terugkomt (in dit voorbeeld blauw, groen en rood). Als al die kleuren tegelijk in een plaatje met golflengte (kleur) en intensiteit (lichtintensiteit) worden gezet, krijg je een emissiespectrum. Voor het excitatiespectrum rechts wordt de kleur licht die op de moleculen wordt geschoten een klein beetje veranderd. Tegelijkertijd kijken we naar de lichtintensiteit van één kleur die terugkomt (in dit voorbeeld naar groen). Als je met het licht wat je erop schiet precies twee treden van de ladder verbindt, zal die lichtintensiteit groter worden. Als je al die lichtintensiteiten in een grafiek zet met golflengte (kleur van het laserlicht) en intensiteit, krijg je een excitatiespectrum.*

door afzonderlijk te kijken naar de twee moleculen die betrokken zijn bij het maken van de stikstofoxidemoleculen: zuurstof en stikstof. Dit doen we op twee manieren:

1. We schieten met de laser op de moleculen en bestuderen de kleuren van het licht dat door deze moleculen wordt uitgezonden. Het verschil tussen die kleuren geeft ons een beeld van het onderste deel van de ladder uit Figuur B.14. Dit kleurenspectrum noemen we een emissiespectrum en de afstand tussen de pieken in het emissiespectrum geeft aan hoe het onderste deel van de ladder eruitziet.

2. We veranderen de kleur van de laser een heel klein beetje, waardoor we als het ware het molecuul langzaam langs de ladder omhoog duwen, om te zien welke treden we tegenkomen (Figuur B.14). Als we één van de bovenliggende treden
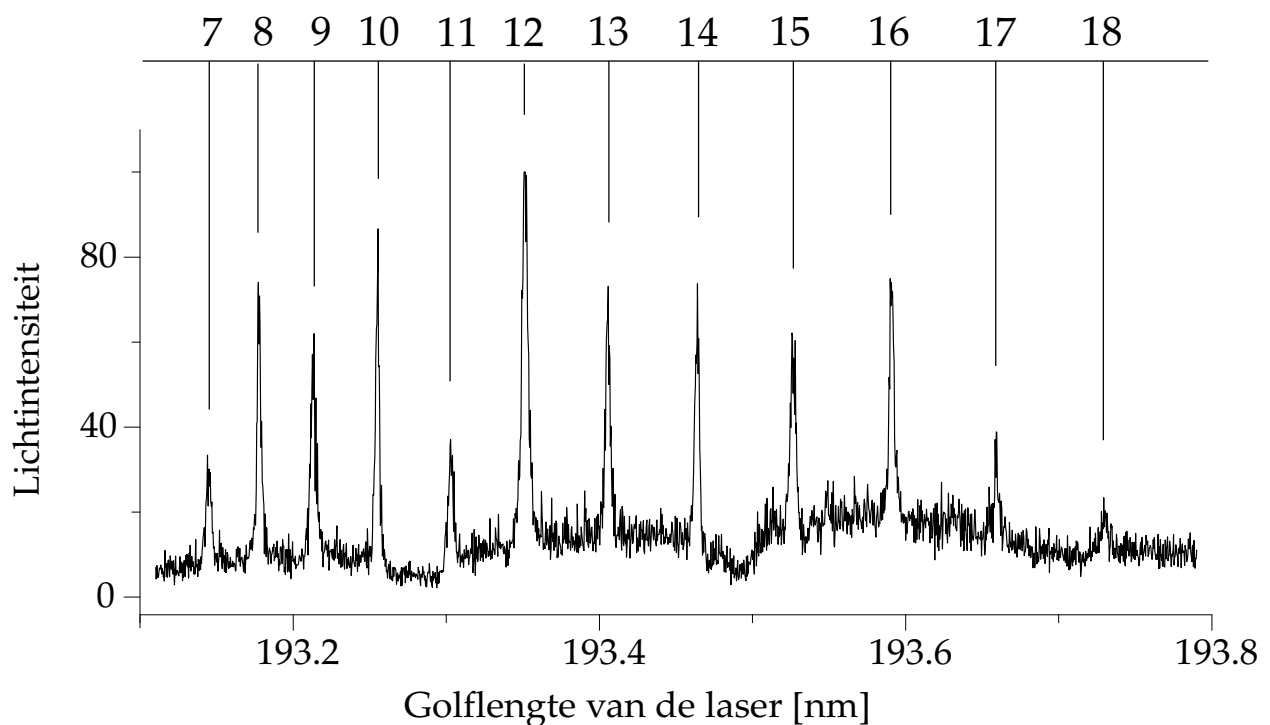
Figuur B.15: *Dit is het excitatiespectrum van stikstof. De getalletjes die er boven staan geven aan dat we herkend hebben van welk deel van de ladder van stikstof dit spectrum vandaan komt. In het proefschrift is deze grafiek te vinden als Figuur 5.4.*

precies bereiken zien we ineens dat het terugkerende licht feller wordt. Op die manier tasten we af hoe het bovenste deel van de ladder eruitziet door te kijken naar de lichtintensiteit van het terugkomende licht. Het spectrum van licht dat daarbij ontstaat noemen we een excitatiespectrum.

Als we dan een beter beeld hebben van hoe de ladders van stikstof en zuurstof eruit zien en naar welk deel van de ladders we kijken met onze laser, hebben we al veel informatie over het proces.

Stikstof

Bij het bestuderen van stikstof hebben we een spectrum gevonden wat al ooit eerder door iemand gevonden is (zie Figuur 5.2), waardoor we wisten naar welk deel van stikstof we aan het kijken waren. Als we de kleur van de laser een klein beetje veranderden, zagen we een excitatiespectrum dat ons veel moeite heeft gekost om te herkennen. Door alles wat bekend was over de ladder van stikstof heel nauwkeurig te bestuderen, veel artikelen door te zoeken en zo allerlei puzzelstukken bij elkaar te zoeken en aan te leggen hebben we een deel van de ladder ontdekt, dat nog nooit eerder gemeten is (zie Figuur B.15). Het was juist zo moeilijk, omdat we aan het zoeken waren in een deel waar meerdere traptreden heel dicht bij elkaar lagen. Een schematische tekening van deze specifieke ladderstructuur is te zien in Figuur 5.1.
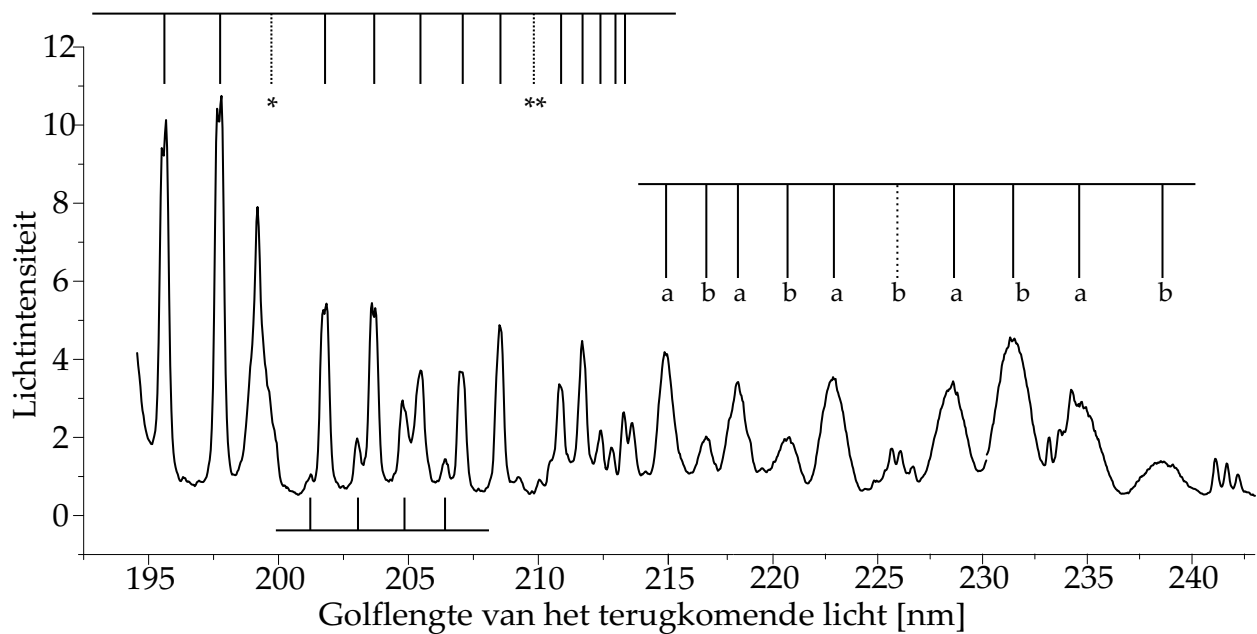
Figuur B.16: *Dit is een deel van het emissiespectrum van zuurstof. Net als bij het exci-tatiespectrum van stikstof (Figuur B.15) hebben we ook hier een deel van de zuurstofladder herkend, wat te zien is aan de verticale lijnen. Deze grafiek staat ook in mijn proefschrift onder Figuren 6.6, 6.7 en 6.12.*

Zuurstof

Bij het bestuderen van zuurstof zagen we ontzettend veel verschillende kleuren licht (zie Figuren 6.4 en 6.5). Hierdoor zijn we tegen een erg ingewikkelde puzzel (zie Figuur B.16 en Figuur 6.7) aangelopen die we ook nog maar deels hebben opgelost. Een paar van de kleuren (het linkerdeel uit Figuur B.16) hebben we uiteindelijk herkend als stappen van en naar bekende laddertreden. In het proefschrift zie je in de Figuren 6.9 en 6.10 weer een schematische voorstelling van het laddersysteem. Hierbij treedt ook nog een verschijnsel op waarbij het gedrag van het zuurstofmolecuul deels verandert in dat van het allersim-pelste atoom, waterstof. Dit extra verschijnsel maakt het begrijpen van zuurstof nog veel moeilijker, omdat er nog meer laddertreden lijken bij te komen.

Een andere set kleuren die we gezien hadden (het rechterdeel van Figuur B.16 en Figuur 6.12), bracht ons tot een heel opmerkelijk resultaat. Normaal zien we bij het bekij-ken van een spectrum de plaats van de laddertreden van een molecuul. Nu keken we toevallig naar een paar heel bijzondere laddertreden, waardoor we een ander resultaat te zien kregen. Iets wat ook bij de quantumfysica hoort is dat de twee atomen niet alleen maar het liefst in één evenwichtstoestand staan (wanneer de veer tussen de atomen in rust is), maar dat er meerdere afstanden tussen de atomen zijn waar het molecuul zich prettig bij voelt. Wat we uiteindelijk in het kleurenspectrum zagen, was een beschrijving van de afstand tussen de twee zuurstofatomen (zie Figuur B.6). Dat je die afstand tussen de twee atomen kunt zien, is heel bijzonder en komt niet vaak voor, omdat je meestal alleen de afstand tussen laddertreden te zien krijgt. In Figuur 6.19 staat een tekening van

deze afstand tussen de atomen. Hierbij is de r op de x-as de afstand tussen de atomen in tienmiljoenste millimeter en de pieken in het plaatje geven aan welke op welke afstand de atomen zich liever bevinden.

Dit resultaat gaf ons al een beter idee van wat er in het brandpunt van de laser gebeurt met zuurstof, maar we hebben het nog steeds niet helemaal kunnen oplossen, omdat het er op lijkt dat we weer een nieuwe laddertrede hebben ontdekt (zie Figuur 6.21), net als bij stikstof.

Gecombineerd

Als we nu de twee moleculen tegelijk gaan bekijken, zien we opeens vreemde dingen gebeuren. De typische ladder van stikstof is opeens verdwenen en we zien in plaats daarvan de typische ladder van zuurstof, zoals te zien is in Figuur 6.3. Dat is heel vreemd, omdat we nog wel naar het licht aan het kijken zijn dat van stikstof afkomstig is. Daarbij verwacht je niet dat opeens de ladder gaat veranderen, zoals wel gebeurt in Figuren 7.7 en 7.8. Wat we hieruit kunnen concluderen is dat er een overdracht is van energie of lading van zuurstof naar stikstof, waarbij de interne energie van zuurstof wordt overgedragen op stikstof. Hierbij neemt stikstof dan tijdelijk de laddereigenschap van zuurstof over. Een schematische tekening van dit proces en andere processen binnen zuurstof en stikstof staat in Figuur 7.10.

Als we de kleur van de laser wat veranderen, zien we ook dat we meer stikstofoxide-moleculen maken. We herkennen hierin weer de ladder van het zuurstofmolecuul zoals te zien is in Figuur 1.3. Een overzicht van de scheikundige reacties die kunnen plaatsvinden in onze techniek is te zien in Tabel 7.1.

B.3.4   Conclusie

We hebben laten zien dat we onze techniek kunnen gebruiken in een hoge-druk- en hoge-temperatuuromgeving. Wat er uiteindelijk precies gebeurt in het proces van het omzetten van lucht in stikstofoxide is nog niet helemaal duidelijk.

Het onderzoek naar wat er met de stikstofmoleculen en zuurstofmoleculen in het brandpunt van de laser gebeurt heeft een aantal interessante resultaten opgeleverd. Bij stikstof vonden we een nieuw deel van de ladder en bij zuurstof hebben we een bijzonder fenomeen waargenomen, waarbij we de mogelijke afstanden tussen de twee zuurstofatomen hebben waargenomen.

In de bestudering van de wisselwerking tussen de moleculen zuurstof en stikstof (lucht) zagen we dat er energie wordt overgedragen van zuurstof naar stikstof, waardoor de ladder van zuurstof bij stikstof te meten was. Ondanks dat we veel moeilijke puzzels hebben ontdekt en maar deels hebben opgelost, hebben we toch een beter idee van wat de basis is van onze VLLAM-techniek.

References

[1] E. W. Rothe, P. Andresen, Application of tunable excimer lasers to combustion diagnostics: a review, Appl. Opt. 36 (1997) 3971.

[2] R. W. B. Pearse, A. G. Gaydon, The identification of molecular spectra, 4th ed. Chapman & Hall, London, 1976.

[3] M. Hippler, J. Pfab, Detection and probing of nitric oxide (NO) by two-colour laser photoionisation (REMPI) spectroscopy on the A←X transition, Chem. Phys. Lett. 243 (1995) 500.

[4] T. Rossmann, M. G. Mungal, R. K. Hanson, Nitric-oxide planar laser-induced fluorescence applied to low-pressure hypersonic flow fields for the imaging of mixture fraction, Appl. Opt. 42 (2003) 6682.

[5] K. Verbiezen, R. J. H. Klein-Douwel, A. J. Donkerbroek, A. P. van Vliet, W. L. Meerts, N. J. Dam, J. J. ter Meulen, Quantitative laser-induced fluorescence measurements of nitric oxide in a heavy-duty diesel engine, Appl. Phys. B 83 (2006) 155.

[6] R. A. L. Tolboom, N. J. Dam, N. M. Sijtsema, J. J. ter Meulen, Quantitative spectrally resolved imaging through a spectrograph, Opt. Lett. 28 (2003) 2046.

[7] R. Evertsen, Cavity ring-down spectroscopy in combustion environments, Ph.D. Thesis at the University of Nijmegen, the Netherlands, 2002.

[8] N. J. Dam, R. J. H. Klein-Douwel, N. M. Sijtsema, J. J. ter Meulen, Nitric oxide flow tagging in unseeded air, Opt. Lett. 26 (2001) 36.

[9] T. Elenbaas, N. M. Sijtsema, R. A. L. Tolboom, N. J. Dam, W. van de Water, J. J. ter Meulen, Characterisation of turbulence by air photolysis and recombination tracking, AIAA Paper, (020694).

[10] W. Demtröder, Laser Spectroscopy: Basic concepts and instrumentation, Springer Verlag Berlin Heidelberg New York, 1981.

[11] A. T. Hartlieb, B. Atakan, K. Kohse-Höinghaus, Temperature measurement in fuel-rich non-sooting low-pressure hydrocarbon flames, Appl. Phys. B 70 (2000) 435.

[12] J. Luque, D. R. Crosley, LIFBASE: Database and spectral simulation (version 1.5), SRI International Report MP 99-009, 1999.

[13] J. Bominaar, M. Pashtrapanska, T. Elenbaas, N. J. Dam, J. ter Meulen, W. van de Water, Writing in turbulent air, Phys. Rev. E 77 (2008) 046312.

[14] T. Elenbaas, Writing lines in turbulent air using Air Photolysis And Recombination Tracking, Ph.D. Thesis at Radboud University of Nijmegen and Technical University Eindhoven, the Netherlands, 2006.

[15] G. Berden, R. Peeters, G. Meijer, Cavity ring-down spectroscopy: Experimental schemes and applications, Int. Reviews in Physical Chemistry 19 (2000) 565.

[16] X. Mercier, Mesure de Concentrations Absolues d'Espèces Réactives Minoritaires dans les Flammes par la Technique d'Absorption Cavity Ring-Down Spectroscopy, Ph.D. Thesis at l'Université des sciences et technologies de Lille, France, 2000.

[17] A. Noullez, G. Wallace, W. Lempert, R. B. Miles, U. Frisch, Transverse velocity increments in turbulent flow using the RELIEF technique, J. Fluid Mech. 339 (1997) 287.

[18] S. T. Acton, J. Tang, Vessel boundary tracking for intra vital microscopy via multiscale gradient vector flow snakes, IEEE Transactions on biomedical engineering 51 (2004) 316.

[19] D. Terzopoulos, M. Kass, A. Witkin, Snakes: Active contour models, Int. J. of Computer Vision 1 (1987) 321.

[20] J. L. Prince, C. Xu, Snakes, shapes and gradient vector flow, IEEE Transactions on pattern analysis and machine intelligence 12 (1998) 855.

[21] M. Olsson, V. Barger, Classical mechanics: A modern perspective, McGraw-Hill Inc., 1973.

[22] M. S. Klassen, D. D. Thomsen, J. R. Reisel, N. M. Laurendeau, Laser-induced fluorescence measurements of nitric oxide formation in high-pressure premixed methane flames, Combust. Sci and Tech. 110 (1995) 229.

[23] J. R. Reisel, N. M. Laurendeau, Laser-induced fluorescence measurements and modeling of nitric oxide formation in high-pressure flames, Combust. Sci and Tech. 98 (1994) 137.

[24] C. H. Sohn, I. M. Jeong, S. H. Chung, Numerical study of the effects of pressure and air-dilution on NO formation in laminar counterflow diffusion flames of methane in high temperature air, Combust. Flame 130 (2002) 83.

[25] D. Charlston-Goch, B. L. Chadwick, R. J. S. Morrison, A. Campisi, D. D. Thomsen, N. M. Larendeau, Laser-induced fluorescence measurements and modeling of nitric oxide in premixed flames of $CO + H_2 + CH_4$ and air at high pressures. 1. Nitrogen fixation, Combust. Flame 125 (2001) 729.

[26] U. Hällsten, P. Lindblom, O. Solin, Oxygen reactions in high-pressure nitrogen gas studied with optical emission spectroscopy, Appl. Radiat. Isot. 60 (2004) 787.

[27] T. Namihira, S. Katsuki, R. Hackam, H. Akiyama, K. Okamoto, Production of nitric oxide using a pulsed arc discharge, IEEE Transactions on plasma science 30 (2002) 1993.

[28] G. C. Goldenbaum, R. R. Dickerson, Nitric oxide production by lightning discharges, J. Geophys. Res. 98 (1993) 18333.

[29] P. K. Kundu, Fluid mechanics, Academic Press, 1990.

[30] S. Chakraborty, S. Chakraborty, Isotopic fractination of the O_3-nitric oxide reaction, Current Science 85 (2003) 1210.

[31] J. M. Diaz Consul, D. Thiele, R. C. Veses, I. M. Baibich, R. M. Dallago, Catalytic decomposition of nitrogen oxides, Quimica Nova 27 (2004) 432.

[32] S. Solomon, Stratospheric ozone depletion: a review of concepts and history, Rev. Geophys. 37 (1999) 275.

[33] R. P. Lindstedt, E. M. Vaos, Transported PDF modeling of high-Reynolds-number premixed turbulent flames, Combust. Flame 145 (2006) 495.

[34] K. Herrmann, K. Boulouchos, Nitric oxide detection in turbulent premixed methane/air flames, Proc. Comb. Inst. 30 (2005) 1517.

[35] M. Tanahashi, S. Murakami, G.-M. Choi, Y. Fukuchi, T. Miyauchi, Simultaneous CH-OH PLIF and stereoscopic PIV measurements of turbulent premixed flames, Proc. Comb. Inst. 30 (2005) 1665.

[36] S. R. Turns, Understanding NOx formation in nonpremixed flames: Experiments and modeling, Prog. Energy Combust. Sci. 21 (1995) 361.

[37] R. Mustata, L. Valiño, C. Jiménez, W. P. Jones, S. Bondi, A probablity density function Eulerian Monte Carlo field method for large eddy simulations: Application to a turbulent piloted methane/air diffusion flame (Sandia D), Combust. Flame 145 (2006) 88.

[38] A. Kempf, F. Flemming, J. Janicka, Investigation of lengthscales, scalar dissipation, and flame orientation in a piloted diffusion flame by LES, Proc. Comb. Inst. 30 (2005) 557.

[39] M. R. H. Sheikhi, T. G. Drozda, P. Givi, F. A. Jaberi, S. B. Pope, Large eddy simulation of a turbulent nonpremixed piloted methane jet flame (Sandia Flame D), Proc. Comb. Inst. 30 (2005) 549.

[40] Y. I. M. Tanahashi, Y. Nada, T. Miyauchi, Local flame structure in the well-stirred reactor regime, Proc. Comb. Inst. 29 (2002) 2041.

[41] T. Takeno, Y. Mizobuchi, Significance of DNS in combustion science, C. R. Mecanique 334 (2006) 517.

[42] N. Peters, Turbulent Combustion, Cambridge University Press, 2000.

[43] L. Gagnepain, Contribution a l'étude de la structure des flammes turbulentes prémélangées pauvres. Determination des échelles caractéristiques de champs dynamique et scalaire, Ph.D. Thesis at University of Orléans, France, 1998.

[44] V. R. Savarianandam, C. J. Lawn, Burning velocity of premixed turbulent flames in the weakly wrinkled regime, Combust. Flame 146 (2006) 1.

[45] Y.-C. Chen, R. W. Bilger, Turbulence measurements in a bunsen burner inserted with perforated plugs of different hole sizes using DPIV, Exp. Therm. Fluid Sci. 27 (2003) 619.

[46] V. Bakić, S. Nemoda, M. Sijerčić, V. Turanjanin, B. Stanković, Experimental and numerical investigation of premixed acetylene flame, Int. J. Heat Mass Transfer 49 (2006) 4023.

[47] S. A. Filatyev, J. F. Driscoll, C. D. Carter, J. M. Donbar, Measured properties of turbulent premixed flames for model assessment, including burning velocities, stretch rates, and surface densities, Combust. Flame 141 (2005) 1.

[48] H. Kobayashi, K. Seyama, H. Hagiwara, Y. Ogami, Burning velocity correlation of methane/air turbulent premixed flames at high pressure and high temperature, Proc. Comb. Inst. 30 (2005) 827.

[49] M. J. Tummers, E. H. van Veen, N. George, R. Rodink, K. Hanjalić, Measurement of velocity-temperature correlations in a turbulent diffusion flame, Exp. Fluids 37 (2004) 364.

[50] R. S. Barlow, J. H. Frank, A. N. Karpetis, J.-Y. Chen, Piloted methane/air flames: Transport effects and aspects of scalar structure, Combust. Flame 143 (2005) 433.

[51] W. Pendleton Jr., P. Erman, M. Larsson, G. Witt, Observation of strong NO gamma-band radiation induced in thin N_2-CO_2 and N_2-H_2O targets by electron impact and its possible relation to the auroral chemistry of NO, Phys. Scr. 28 (1983) 532.

[52] I. Shepherd, L. Gagnepain, I. Gökalp, Micro scalar timescales in premixed turbulent combustion, Proc. Comb. Inst. 28 (2000) 351.

[53] J. Kazenwadel, W. Koban, T. Kunzelmann, C. Schulz, Fluorescence imaging of natural gas/air mixing without tracers added, Chem. Phys. Lett. 345 (2001) 259.

[54] J. Bominaar, C. Schoemaecker, N. J. Dam, J. ter Meulen, G. Groenenboom, (2+1) REMPI on molecular nitrogen through the $^1\Sigma_g^+$(II)-state, Chem. Phys. Lett. 435 (2007) 242.

[55] W. Ubachs, L. Tashiro, R. N. Zare, Study of the N_2 $b^1\Pi_u$ state via 1+1 multiphoton ionization, Chem. Phys. 130 (1989) 1.

[56] J. J. Hopfield, Absorption and emission spectra in the region $\lambda = 600\text{-}1100$, Phys. Rev. 35 (1930) 1133.

[57] R. E. Worley, F. A. Jenkins, A new Rydberg series in N_2, Phys. Rev. 54 (1938) 305.

[58] R. E. Worley, Absorption spectrum of N_2 in the extreme ultraviolet, Phys. Rev. 64 (1943) 207.

[59] T. Takamine, Y. Tanaka, Vibrational structure of the $^2\Sigma_g^+ \leftarrow {}^1\Sigma_g^+$ Rydberg series of N_2, Phys. Rev. 59 (1941) 613.

[60] L.-E. Berg, P. Erman, E. Källne, S. Sorensen, G. Sundström, Studies of photoionization and photodissociation of molecular nitrogen in the 15-30 eV region using intense synchrotron radiation, Phys. Scr. 44 (1991) 131.

[61] M. A. Baig, J. P. Connerade, Autoionising Rydberg series in the spectrum of N_2, J. Phys. B: At. Mol. Phys. 19 (1986) L605.

[62] K. P. Huber, G. Stark, K. Ito, Rotational structure in the Hopfield series of N_2, J. Chem. Phys. 98 (1993) 4471.

[63] J. P. Sprengers, W. Ubachs, K. G. H. Baldwin, B. R. Lewis, W.-Ü. L. Tchang-Brillet, Extreme ultraviolet laser excitation of isotopic molecular nitrogen: The dipole-allowed spectrum of $^{15}N_2$ and $^{14}N^{15}N$, J. Chem. Phys. 119 (2003) 3160.

[64] E. F. McCormack, S. T. Pratt, J. L. Dehmer, P. M. Dehmer, Double-resonance spectroscopy of autoionizing states of N_2 near the ionization threshold, Phys. Rev. A 42 (1990) 5445.

[65] K. Dressler, B. L. Lutz, Optical identification of the 12.28-eV quadrupole transition in molecular nitrogen, Phys. Rev. Lett. 19 (1967) 1219.

[66] H. H. Michels, Identification of two low-lying non-Rydberg states of the nitrogen molecule, J. Chem. Phys. 53 (1970) 841.

[67] W. C. Ermler, A. D. McLean, R. S. Mulliken, *Ab initio* study of valence state potential energy curves of N_2, J. Phys. Chem. 86 (1982) 1305.

[68] W. C. Ermler, J. P. Clark, R. S. Mulliken, *Ab initio* calculations of potential energy curves and transition moments of $^1\Sigma_g^+$ and $^1\Sigma_u^+$ states of N_2, J. Chem. Phys. 86 (1987) 370.

[69] T. F. Hanisco, A. C. Kummel, Resonantly enhanced multiphoton ionization of N_2 $a''^1\Sigma_g^+(v' = v'') \leftarrow X^1\Sigma_g^+(v'' = 0 - 2)$. 1. Determination of rotational populations and virtual state character, J. Phys. Chem. 95 (1991) 8565.

[70] N. M. Sijtsema, N. J. Dam, R. J. H. Klein-Douwel, J. J. ter Meulen, Air Photolysis and Recombination Tracking (APART): A new molecular tagging velocimetry scheme, AIAA J. 40 (2002) 1061.

[71] J. M. Ress, G. Laufer, R. H. Krauss, Laser ion time-of-flight velocity measurements using N_2^+ tracers, AIAA J. 33 (1995) 296.

[72] M. Aldén, W. Wendt, Detection of nitrogen molecules through multi-photon laser excitation and N_2^+ fluorescence, Opt. Commun. 69 (1988) 31.

[73] M. Versluis, M. Ebben, M. Drabbels, J. J. ter Meulen, Frequency calibration in the ArF excimer laser-tuning range using laser-induced fluorescence of NO, Appl. Opt. 30 (1991) 5229.

[74] K. P. Huber, G. Herzberg, Constants of diatomic molecules, Van Nostrand Reinhold, New York, 1979.

[75] R. C. Ekey Jr., E. F. McCormack, A planar jet expansion discharge source of molecular afterglow emission, Chem. Phys. Lett. 381 (2003) 416.

[76] J. Comer, F. H. Read, Electron impact studies of a resonant state of N_2^-, J. Phys. B: At. Mol. Phys. 4 (1971) 1055.

[77] L. Sanche, G. J. Schulz, Electron transmission spectroscopy: core-excited resonances in diatomic molecules, Phys. Rev. A 6 (1972) 69.

[78] A. Lofthus, P. H. Krupenie, The spectrum of molecular nitrogen, J. Phys. Chem. Ref. Data 6 (1977) 113.

[79] S. Sharpe, P. M. Johnson, Triplet Rydberg states in molecular nitrogen, J. Chem. Phys. 85 (1986) 4943.

[80] J. A. Guthrie, X. X. Wang, L. J. Radziemski, Resonance-enhanced multiphoton ionization of N_2 at 193 and 248 nm detected by N_2^+ fluorescence, Chem. Phys. Lett. 170 (1990) 117.

[81] G. Herzberg, Spectra of diatomic molecules p. 169, Van Nostrand Reinhold, New York, 1950.

[82] F. Merkt, T. P. Softley, Rotationally resolved zero-kinetic-energy photoelectron spectrum of nitrogen, Phys. Rev. A 46 (1992) 302.

[83] P. Gürtler, V. Saile, E. E. Koch, High resolution absorption spectrum of nitrogen in the vacuum ultraviolet, Chem. Phys. Lett. 48 (1977) 245.

[84] J. Kaplan, Products of dissociation in nitrogen, Phys. Rev. 42 (1932) 97.

[85] D. T. Colbert, W. H. Miller, A novel discrete variable representation for quantum mechanical reactive scattering via the S-matrix Kohn method, J. Chem. Phys. 96 (1992) 1982.

[86] G. C. Groenenboom, D. T. Colbert, Combining the discrete variable representation with the S-matrix Kohn method for quantum reactive scattering, J. Chem. Phys. 99 (1993) 9681.

[87] W. C. Price, G. Collins, The far ultraviolet absorption spectrum of oxygen, Phys. Rev. 48 (1935) 714.

[88] V. M. Ellsworth, J. J. Hopfield, Oxygen bands in the ultraviolet, Phys. Rev. 29 (1927) 79.

[89] P. M. Dehmer, W. A. Chupka, High resolution study of photoionization processes in O_2^*, J. Chem. Phys. 62 (1975) 4525.

[90] E. Nishitani, I. Tanaka, New vibrational assignments for the autoionization bands of O_2 based on isotope shifts, J. Chem. Phys. 81 (1984) 3429.

[91] F. Merkt, P. M. Guyon, J. Hepburn, High-resolution threshold photoelectron spectrum of molecular oxygen, Chem. Phys. 173 (1993) 479.

[92] K. Ellis, R. I. Hall, L. Avaldi, G. Dawber, A. McConkey, L. Andrić, G. C. King, High resolution threshold photoelectron and photoion spectroscopy of oxygen in the 12-50 eV range, J. Phys. B: At. Mol. Phys. 27 (1994) 3415.

[93] M. Evans, S. Simson, C. Y. Ng, High-resolution pulsed field ionization photoelectron study of O_2: Predissociation lifetimes and high-n Rydberg lifetimes converging to $O_2^+(c^4\Sigma_u^-, v^+=0,1)$, J. Chem. Phys. 109 (1998) 1285.

[94] Y. Lu, Z. X. He, J. N. Curtler, S. H. Southwort, W. C. Stolte, J. A. R. Samson, Dissociative photoionization study of O_2, J. Electron Spectrosc. Relat. Phenom. 94 (1998) 135.

[95] Y. Hikosaka, P. Lablanquie, M. Ahmad, R. I. Hall, J. G. Lambourne, F. Penent, J. H. D. Eland, Competition between autoionization and dissociation in the $[O_2^+(B^2\Sigma_g^-)]nl$ and $[O_2^+(c^4\Sigma_u^-)]nl$ Rydberg states investigated by photon-induced dissociation to neutral fragments, J. Phys. B: At. Mol. Phys. 36 (2003) 4311.

[96] G. Laufer, R. L. McKenzie, W. M. Huo, Radiative processes in air excited by an ArF laser, Opt. Lett. 13 (1988) 99.

[97] S. Yang, W. T. Hill III, S. N. Dixit, Multiphoton dissociative ionization of O_2: Competition between dissociation and ionization in excited states, J. Chem. Phys. 100 (1994) 6434.

[98] B. L. G. Bakker, D. H. Parker, Photophysics of O_2 excited by tunable laser radiation around 193 nm, J. Chem. Phys. 112 (2000) 4037.

[99] C. Y. R. Wu, Assignments of autoionization states of O_2^*, J. Quant. Spectros. Radiat. Transfer 37 (1987) 1.

[100] K. Takahashi, T. Nakayama, Y. Matsumi, Vacuum ultraviolet laser-induced fluorescence detection of $O(^1D)$ atom produced in the 193 nm photolysis of ozone, J. Phys. Chem. A 107 (2003) 9368.

[101] P. H. Krupenie, The spectrum of molecular oxygen, J. Phys. Chem. Ref. Data 1 (1972) 423.

[102] M. Versluis, Combustion diagnostics at atmospheric pressures using a tunable excimer laser, Ph.D. Thesis at University of Nijmegen, the Netherlands, 1992.

[103] M. Versluis, G. Meijer, D. W. Chandler, Degenerate four-wave mixing with a tunable excimer laser, Appl. Opt. 33 (1994) 3289.

[104] D. Eisel, D. Zevgolis, W. Demtröder, Sub-Doppler laser spectroscopy of the NaK molecule, J. Chem. Phys. 71 (1979) 2005.

[105] A. S.-C. Cheung, K. Yoshino, W. H. Parkinson, D. E. Freeman, Molecular spectroscopic constants of $O_2(B^3\Sigma_u^-)$: The upper state of the Schumann-Runge bands, J. Mol. Spec. 119 (1986) 1.

[106] W. van der Zande, Energy redistribution in the dissociation of low Rydberg states of HeH and O_2, Ph.D. Thesis at University of Amsterdam, the Netherlands, 1988.

[107] B. R. Lewis, S. T. Gibson, S. S. Banerjee, H. Lefebvre-Brion, Relations between Rydberg-valence interactions in the O_2 molecule, J. Chem. Phys. 113 (2000) 2214.

[108] R. W. Nicholls, Approximate formulas for Franck-Condon factors, J. Chem. Phys. 74 (1981) 6980.

[109] H. A. Sheard, T. Ridley, K. P. Lawley, R. J. Donovan, An optical-optical double–resonance study of the Rydberg states of O_2. I. The ns and nd (*gerade*) states excited via single-rotational levels of the $b^1\Sigma_{0g}^+$ valence state, J. Chem. Phys. 118 (2003) 8781.

[110] E. U. Condon, Nuclear motions associated with electron transitions in diatomic molecules, Phys. Rev. 32 (1928) 858.

[111] E. U. Condon, The Franck-Condon principle and related topics, Am. J. Phys. 15 (1947) 365.

[112] J. Tellinghuisen, E→B Structured continuum in I_2, Phys. Rev. Lett. 34 (1975) 1137.

[113] M. S. Child, H. Essén, R. J. LeRoy, An RKR-like inversion procedure for bound-continuum transition intensities, J. Chem. Phys. 78 (1983) 6732.

[114] R. J. LeRoy, W. J. Keogh, An inversion procedure for oscillatory continuum spectra: Method and application to NaK, J. Chem. Phys. 89 (1988) 4564.

[115] H. H. Michels, Electronic structure of excited states of selected atmospheric gases, Adv. Chem. Phys. 45 (1981) 225.

[116] P. F. Bernath, Spectra of atoms and molecules, Oxford University Press, 1995.

[117] P. Atkins, J. de Paula, Atkins' physical chemistry, Oxford University Press, seventh edition, 2002.

[118] C. H. Bamford, Photochemical proscesses in an oxygen-nitrogen atmosphere, Rep. Prog. Phys. 9 (1942) 75.

[119] V. Aquilanti, M. Bartolomei, D. Cappelletti, E. Carmona-Novillo, F. Pirani, Photodynamics of clusters of the major components of the atmosphere, Int. J. Photoenergy 6 (2004) 53.

[120] J. L. Grenfell, R. Lehmann, P. Mieth, U. Langematz, B. Steil, Chemical reaction pathways affecting stratospheric and mesospheric ozone, J. Geophys. Res.- Atmos. 111 (2006) D17311.

[121] V. Chernyak, L. Kernazhitsky, V. Naumov, G. Puchkovska, V. Yukhymenko, UV-NIR spectroscopy of air plasma in transverse arc discharge, J. Mol. Struct. 744.

[122] E. Kamaratos, Active nitrogen and oxygen: Enhanced emissions and chemical reactions, Chem. Phys. 323 (2006) 271.

[123] A. J. Midey, A. A. Viggiano, P. Zhang, S. Irle, K. Morokuma, A study of the reaction of N^+ with O_2: Experimental quantification of $NO^+(a^3\Sigma^+)$ production (298-500 K) and computational study of the overall reaction pathways, J. Phys. Chem. A 110 (2006) 3080.

[124] S. P. Nandula, R. W. Pitz, J. Bominaar, C. Schoemaecker, N. J. Dam, J. J. ter Meulen, Kinetics of NO tag formation in air for unseeded Molecular Tagging Velocimetry, AIAA 42th Aerospace Sciences Meeting, Paper No. AIAA-2004-0390, Reno, Nevada, January 5-8, 2004.

[125] S. S. Prasad, E. C. Zipf, Photochemical production of odd nitrogen directly from O_2, N_2 principals: Atmospheric implications and related open issues, J. Geophys. Res. 109 (2004) doi:10.1029/2003JD004061.

[126] R. Ono, T. Oda, NO formation in a pulsed spark discharge in $N_2/O_2/Ar$ mixture at atmospheric pressure, J. Phys. D Appl. Phys. 35 (2002) 543.

[127] N. Balakrishnan, A. Dalgarno, Rate coefficients for NO formation in energetic N + O_2 collisions, Chem. Phys. Lett. 302 (1999) 485.

[128] R. Brandenburg, V. A. Maiorov, Y. B. Golubovskii, H.-E. Wagner, J. Behnke, J. F. Behnke, Diffuse barrier discharges in nitrogen with small admixtures of oxygen: discharge mechanism and transition to the filamentary regime, J. Phys. D Appl. Phys. 38 (2005) 2187.

[129] N. R. Tawde, V. S. Patankar, Influence of air-gases on the first and second positive systems of nitrogen, the London, Edinburgh and Dublin philosophical magazine and journal of science 35 (1944) 600.

[130] V. Hrachová, O. Kylián, A. Kaňka, Study of the vacuum purity influence on oxygen and nitrogen spectra properties in DC glow discharge, Vacuum 76 (2004) 433.

[131] J. M. Thomas, F. Kaufman, An upper limit on the formation of NO($X^2\Pi_r$) in the reactions $N_2(A^3\Sigma_u^+) + O(^3P)$ and $N_2(A^3\Sigma_u^+) + O_2(X^3\Sigma_g^-)$ at 298 K, J. Phys. Chem. 100 (1996) 8901.

[132] K. P. Huber, G. Herzberg, Constants of Diatomic Molecules, (data prepared by J. W. Gallagher and R. D. Johnson, III) in NIST Chemistry WebBook, NIST Standard Reference Database Number 69, Eds. P. J. Linstrom and W. G. Mallard, June 2005, National Institute of Standards and Technology, Gaithersburg MD, 20899 (http://webbook.nist.gov).

[133] Y. Tanaka, A. S. Jursa, F. J. LeBlanc, Hopfield's emission bands of O_2 in the region 1900-2350 Å, J. Chem. Phys. 24 (1956) 915.

[134] F. J. LeBlanc, Electronic states of Hopfield's oxygen emission bands, J. Chem. Phys. 38 (1963) 487.

[135] O. Edqvist, E. Lindholm, L. E. Selin, L. Åsbrink, On the photoelectron spectrum of O_2, Phys. Scr. 1 (1970) 25.

[136] J. Schopman, R. Locht, The observation of predissociation in the oxygen molecular ion by low-energy electron impact, Chem. Phys. Lett. 26 (1974) 596.

[137] B. Ramachandran, N. Balakrishnan, A. Dalgarno, Vibrational-rotational distributions of NO formed from N + O_2 reactive collisions, Chem. Phys. Lett. 332 (2000) 562.

[138] M. Braunstein, J. W. Duff, Theoretical study of the $N(^2D) + O_2(X^3\Sigma_g^-) \rightarrow O + NO$ reaction, J. Chem. Phys. 113 (2000) 7406.

[139] M. J. Pinheiro, G. Gousset, A. Granier, C. M. Ferreira, Modelling of low-pressure surface wave discharges in flowing oxygen: I. Electrical properties and species concentrations, Plasma Sources Sci. Technol. 7 (1998) 524.

[140] M. Vialle, M. Touzeau, G. Gousset, C. M. Ferreira, Kinetics of O(^1S) and O(^1D) metastable atoms in a DC oxygen glow discharge, J. Phys. D Appl. Phys. 24 (1991) 301.

[141] L. V. Gatilova, K. Allegraud, J. Guillon, Y. Z. Ionikh, G. Cartry, J. Röpcke, A. Rousseau, NO formation mechanisms studied by infrared laser absorption in a single low-pressure plasma pulse, Plasma Sources Sci. Technol. 16 (2007) S107.

[142] C. D. Pintassilgo, J. Loureiro, V. Guerra, Modelling of a N_2-O_2 flowing afterglow for plasma sterilization, J. Phys. D Appl. Phys. 38 (2005) 417.

[143] B. F. Gordiets, C. M. Ferreira, V. L. Guerra, J. M. A. H. Loureiro, Kinetic model of a low-pressure N_2-O_2 flowing glow discharge, IEEE Transactions on Plasma Science 23 (1995) 750.

[144] A. R. De Souza, G. Gousset, M. Touzeau, T. Khiet, Note on the determination of the efficiency of the reaction $N_2(A^3\Sigma) + O(^3P) \rightarrow N_2 + O(^1S)$, J. Phys. B: At. Mol. Phys. 18 (1985) L661.

[145] R. A. Sultanov, N. Balakrishnan, Quantum mechanical investigation of the $N(^4S)$ + $O_2(X^3\Sigma_g^-) \rightarrow NO(X^2\Pi) + O(^3P)$ reaction, J. Chem. Phys. 124 (2006) 124321.

[146] I. D. Clark, R. P. Wayne, Kinetics of the reaction between atomic nitrogen and molecular oxygen in the ground $(^3\Sigma_g^-)$ and first excited $(^1\Delta_g)$ states, Proc. Roy. Soc. Lond. A 316 (1970) 539.

[147] J. T. Herron, Evaluated chemical kinetics data for reactions of $N(^2D)$, $N(^2P)$, and $N_2(A^3\Sigma_u^+)$ in the gas phase, J. Phys. Chem. Ref. Data 28 (1999) 1453.

[148] C. A. Barth, Nitric oxide in the lower thermosphere, Planet. Space Sci. 40 (1992) 315.

[149] M. Gauthier, D. R. Snelling, Mechanisms of singlet molecular oxygen formation from photolysis of ozone at 2537 Å, J. Chem. Phys. 54 (1971) 4317.

[150] A. A. Frimer, Singlet O_2, Volume I, Physical-Chemical Aspects, CRC Press Inc., 1985.

[151] L. Campbell, D. C. Cartwright, M. J. Brunger, Role of excited N_2 in the production of nitric oxide, J. Geophys. Res. 112 (2007) A08303.

[152] A. T. J. B. Eppink, D. H. Parker, M. H. M. Janssen, B. Buijsse, W. J. van der Zande, Production of maximally aligned $O(^1D)$ atoms from two-step photodissociation of molecular oxygen, J. Chem. Phys. 108 (1998) 1305.

[153] R. E. Falco, D. G. Nocera, Quantitative multipoint measurements and visualization of dense liquid-solid flows using laser induced photochemical anemometry (LIPA); chapter 3, pp 59-126 in: Particulate two-phase flow, Heinemann: Butterworth, 1993.

[154] M. M. Koochesfahani, R. K. Cohn, C. P. Gendrich, D. G. Nocera, Molecular tagging diagnostics for the study of kinematics and mixing in liquid-phase flows; chapter 2, section 1 in: Developments in laser techniques and fluid mechanics, Springer-Verlag, 1997.

[155] C. P. Gendrich, M. M. Koochesfahani, D. G. Nocera, Molecular tagging velocimetry and other novel applications of a new phosphorescent supramolecule, Exp. Fluids 2 (1997) 61.

[156] M. M. Koochesfahani, Molecular Tagging Velocimetry (MTV): Progress and application, AIAA 99-3786.

[157] M. M. Koochesfahani, A. C. Goh, H. J. Schock, Molecular Tagging Velocimetry (MTV) and its automotive applications in: The aerodynamics of heavy vehicles: trucks, buses and trains, lecture notes in Applied and computational mechanics, vol. 19, pages 143-155, Springer-Verlag, 2004.

[158] B. Hiller, R. A. Booman, C. Hassa, R. K. Hanson, Velocity visualization in gas flows using laser-induced phosphorescence of biacetyl, Rev. Sci. Instrum. 55 (1984) 1964.

[159] B. Stier, M. M. Koochesfahani, Molecular Tagging Velocimetry MTV measurements in gas phase flows, Exp. Fluids 26 (1999) 297.

[160] L. Jian-Bang, P. Qi, L. Chang-Sheng, S. Jie-Rong, Principles of flow field diagnostics by laser induced biacetyl phosphorescence, Exp. Fluids 6 (1988) 505.

[161] R. Miles, C. Cohen, J. Conners, P. Howard, S. Huang, E. Markovitz, G. Russel, Velocity measurements by vibrational tagging and fluorescent probing of oxygen, Opt. Lett. 12 (1987) 861.

[162] R. B. Miles, J. Grinstead, R. H. Kohl, G. Diskin, The RELIEF flow tagging technique and its application in engine testing facilities and for helium-air mixing studies, Meas. Sci. Tech. 11 (2000) 1272.

[163] W. R. Lempert, B. Zhang, R. B. Miles, G. S. Diskin, Simplifications of the RELIEF flow tagging system for laboratory use, AIAA Paper, (91-0356).

[164] G. S. Diskin, B. Zhang, W. R. Lempert, R. B. Miles, Stokes seeding of a Raman shifting cell for use in RELIEF velocimetry, AIAA 93-0515.

[165] R. B. Miles, J. J. Connors, E. C. Markovitz, P. J. Howard, G. J. Roth, Instantaneous profiles and turbulence statistics of supersonic free shear layers by Raman excitation plus laser-induced electronic fluorescence (Relief) velocity tagging of oxygen, Exp. Fluids 8 (1989) 17.

[166] R. B. Miles, J. J. Connors, E. C. Markovitz, P. J. Howard, G. J. Roth, Instantaneous supersonic velocity profiles in an underexpanded sonic air jet by oxygen flow tagging, Phys. Fluids 1 (1989) 389.

[167] L. R. Boedeker, Velocity measurement by H_2O photolysis and laser-induced fluorescence of OH, Opt. Lett. 14 (1989) 473.

[168] R. W. Pitz, M. D. Lahr, Z. W. Douglas, J. A. Wehrmeyer, S. T. Hu, C. D. Carter, K. Y. Hsu, C. Lum, M. M. Koochesfahani, Hydroxyl tagging velocimetry in a supersonic flow over a cavity, Appl. Opt. 44 (2005) 6692.

[169] J. A. Wehrmeyer, L. A. Ribarov, D. A. Oguss, R. W. Pitz, Flame flow tagging velocimetry with 193-nm H_2O photodissociation, Appl. Opt. 38 (1999) 6912.

[170] M. D. Lahr, R. W. Pitz, Z. W. Douglas, C. D. Carter, Hydroxyl tagging velocimetry in cavity-piloted Mach 2 combustor, 44th AIAA Aerospace sciences meeting and exhibit, 2006 Reno, Nevada 0040 (2006) 1.

[171] L. A. Ribarov, J. A. Wehrmeyer, R. W. Pitz, R. A. Yetter, Hydroxyl tagging velocimetry (HTV) in experimental air flows, Appl. Phys. B 74 (2002) 175.

[172] L. P. Goss, T. H. Chen, D. D. Trump, B. Sarka, Flow tagging velocimetry using UV-photodissociation of water vapor, AIAA Paper, (910355).

[173] L. A. Ribarov, S. T. Hu, J. A. Wehrmeyer, R. W. Pitz, Hydroxyl tagging velocimetry method optimization: signal intensity and spectroscopy, Appl. Opt. 44 (2005) 6616.

[174] R. W. Pitz, T. M. Brown, S. P. Nandula, P. A. Skaggs, Unseeded velocity measurement by ozone tagging velocimetry, Opt. Lett. 21 (1996) 755.

[175] L. A. Ribarov, J. A. Wehrmeyer, F. Batliwala, R. W. Pitz, P. A. DeBarber, Ozone flow tagging velocimetry using narrowband excimer laser, AIAA J. 37 (1999) 708.

[176] R. W. Pitz, J. A. Wehrmeyer, L. A. Ribarov, D. A. Oguss, F. Batliwala, P. A. DeBarber, S. Deusch, P. E. Dimotakis, Unseeded molecular flow tagging in cold and hot flows using ozone and hydroxyl tagging velocimetry, Meas. Sci. Tech. 11 (2000) 1259.

[177] W. P. N. van der Laan, R. A. L. Tolboom, N. J. Dam, J. J. ter Meulen, Molecular tagging velocimetry in the wake of an object in supersonic flow, Exp. Fluids 34 (2003) 531.

[178] S. Krüger, G. Grünefeld, Stereoscopic flow-tagging velocimetry, Appl. Phys. B 69 (1999) 509.

[179] S. Krüger, G. Grünefeld, Gas-phase velocity field measurements in dense sprays by laser-based flow tagging, Appl. Phys. B 70 (2000) 463.

[180] H. Finke, G. Grünefeld, An experimental investigation of extinction of curved laminar hydrogen diffusion flames, Proc. Comb. Inst. 28 (2000) 2133.

[181] W. R. Lempert, N. Jiang, S. Sethuram, M. Samimy, Molecular tagging velocimetry measurements in supersonic microjets, AIAA J. 40 (2002) 1065.

[182] H. Hu, M. M. Koochesfahani, A novel method for instantaneous, quantitative measurement of molecular mixing in gaseous flows, Exp. Fluids 33 (2002) 202.

[183] P. Barker, A. Thomas, H. Rubinsztein-Dunlop, P. Ljungberg, Velocity measurements by flow tagging employing laser enhanced ionisation and laser induced fluorescence, Spectrochim. Acta Part B 50 (1995) 1301.

[184] H. Rubinsztein-Dunlop, B. Littleton, P. Barker, P. Ljungberg, Y. Halmsten, Ionic strontium fluorescence as a method for flow tagging velocimetry, Exp. Fluids 30 (2000) 36.

[185] P. Barker, A. M. T. an T. J. McIntyre, H. Rubinsztein-Dunlop, Velcoimetry and thermometry of supersonic flow around a cylindrical body, AIAA J. 36 (1998) 1055.

[186] P. Barker, A. Bishop, H. Rubinsztein-Dunlop, Supersonic velocimetry in a shock tube using laser enhanced ionisation and planar laser induced fluorescence, Appl. Phys. B 64 (1997) 369.

[187] C. Orlemann, C. Schulz, J. Wolfrum, NO-flow tagging by photodissociation of NO_2. A new approach for measuring small-scale flow structures, Chem. Phys. Lett. 307 (1999) 15.

[188] P. M. Danehy, S. O'Byrne, A. F. P. Houwing, J. S. F. nd D. R. Smith, Flow-tagging velocimetry for hypersonic flows using fluorescence of nitric oxide, AIAA J. 41 (2003) 263.

Summary

In this thesis a new flow velocimetry technique is described that falls under the category MTV (Molecular Tagging Velocimetry), which, unlike PIV (Particle Image Velocimetry) and LDA (Laser Doppler Anemometry) does not need added tracer particles, but instead visualizes and follows tracer molecules in the flow. To introduce this technique, APART (Air Photolysis And Recombination Tracking), to the industry its effect on the medium and its applicability need to be studied and its signal-to-noise ratio needs to be optimized.

The APART technique consists of creating a line of NO molecules by focusing an ArF excimer laser beam in air, after which the created molecules can be visualized by inducing fluorescence using a Nd:YAG-pumped dye laser. This technique is less intrusive than adding solid particles to the flow, but we have shown that the local temperature increase is approximately 300 K for a period of several microseconds. This temperature increase is probably due not as much to the NO creation process itself, but rather an unavoidable side effect of photodissociation of O_2 by the ArF excimer laser. The amount of NO molecules created was measured to be 5 ppm per laser pulse.

Application of the technique was performed by using it in a high-pressure environment and in a turbulent flame. By increasing the focal distance of the lens and the distance between camera and laser focus we have shown that a working distance of 1 m is feasible since line length and thickness increase with focal distance. The high-pressure study has shown that there is no fundamental problem in applying APART at high pressures. It does, however, benefit from smaller concentrations of oxygen. The use of this technique in a turbulent flame becomes difficult at the flame front where a lack of oxygen prevents optimum NO creation. Inside the flame, however, the technique appears to work.

To improve signal-to-noise ratio of the NO fluorescence the creation process needs to be studied in detail. In fact, the excimer laser focus is a source not only of NO molecules, but also of photon emission by N_2^+-ions, as well as highly excited N_2 and O_2 molecules. The tunability feature of the excimer laser permitted us to plot a wavelength dependence of the NO creation efficiency. This spectral structure was exactly the same when looking at emission of excimer-excited oxygen and nitrogen molecules in air. When we look at the same emission wavelength of nitrogen (B-X of N_2^+) in pure nitrogen a completely different excitation spectrum emerges. This new structure was assigned to rotational structure of the $v' = 32$ level in a two-photon resonance with the double well a$''^1\Sigma_g^+, ^1\Sigma_g^+$(II). A third photon in the relatively long laser pulse then brings the system to the B-state of N_2^+. The double-well state was predicted, but never observed.

The oxygen emission spectrum brings a lot of unknown structure in the 200 to 280 nm range that was found to be reported in literature a few times since 1930, but had resisted assignment. We have partially assigned this structure to emission from a Rydberg state

converging to the $a^4\Pi_u$-state of O_2^+ down to the $B^3\Sigma_u^-$-state of oxygen. Another band that directly connects with the red side of the assigned structure and clearly is linked to this spectrum is ascribed to emission from the same upper Rydberg state to a repulsive curve with a dissociation energy equal to that of the B-state. Since the energy spacing of this band is inverted compared to typical vibrational structure, the spectrum is believed to be the projection of the wavefunction of the upper Rydberg state. The lower-lying repulsive curve is not the repulsive branch of the B-state, but it appears to be unknown up to now.

The nitrogen excitation spectrum in pure nitrogen is completely replaced by one that is equal to the spectrum seen in NO creation and pure oxygen excitation when adding only 8 % of oxygen. This effect is probably caused by an efficient energy/charge transfer between nitrogen and oxygen at the three-photon level, combined with efficient quenching of the two-photon resonant state of nitrogen by oxygen. A chemical treatment of this NO creation problem finally leads to a proposal for a mechanism where N_2 in the $A^3\Sigma_u^+$-state created from relaxing nitrogen ions and oxygen atoms created from single-photon excited oxygen molecules recombine to form NO.

Molecular nitrogen and oxygen undoubtedly belong to the most extensively studied molecules on earth. Nevertheless, the photolysis of these small molecules, when brought to a high excitation level, is found to be largely unknown ground, and to yield many surprises and mysteries.

Samenvatting

In dit proefschrift wordt een nieuwe meettechniek voor stromingssnelheden beschreven die onder de categorie MTV (meettechniek voor stromingssnelheden door het markeren van moleculen) valt. In tegenstelling tot de technieken PIV (meettechniek voor stromingsnelheden door het fotograferen van deeltjes) en LDA (meettechniek voor stromingssnelheden door laser Dopplerverschuiving aan deeltjes) heeft MTV geen toegevoegde deeltjes nodig. In plaats daarvan visualiseert en volgt MTV gemarkeerde moleculen in de stroming. Om deze techniek, APART (het fotodissociëren van lucht en het volgen van de gevormde moleculen) genoemd, te introduceren bij de industrie, moeten het effect van de techniek op het medium en zijn toepasbaarheid bestudeerd zijn en zijn signaal-ruisverhouding geoptimaliseerd zijn.

De APART-techniek bestaat uit het vormen van een lijn van NO-moleculen door een ArF excimerlaserbundel te focusseren in lucht, waarna de gecreëerde moleculen gevisualiseerd worden door fluorescentie te induceren met behulp van een kleurstoflaser gepompt door een Nd:YAG laser. Deze techniek is minder intrusief dan het toevoegen van vaste deeltjes aan de stroming, maar we hebben aangetoond dat de lokale temperatuurstijging ongeveer $300\,K$ is gedurende een periode van enkele microseconden. Deze temperatuurstijging is waarschijnlijk niet veroorzaakt door de NO-vorming zelf, maar door een onvermijdelijk bijeffect van fotodissociatie van O_2 door de ArF excimerlaser. De hoeveelheid gevormde NO-moleculen, is gemeten op $5\,ppm$ per laserpuls.

De APART-techniek is toegepast in een hoge-drukomgeving en in een turbulente vlam. Door de brandpuntsafstand van de lens en de afstand tussen camera en laserbrandpunt te vergroten, hebben we aangetoond dat een werkafstand van $1\,m$ mogelijk is. Omdat de lijnlengte en -dikte groter worden met de brandpuntsafstand, blijft de lijn toch zichtbaar op grotere afstanden. De hoge-drukstudie heeft aangetoond dat er geen fundamenteel probleem bestaat in het toepassen van APART bij hoge drukken. Lagere zuurstofconcentraties dragen wel positief bij. Het gebruik van de techniek in een turbulente vlam is beperkt op de plek van het vlamfront waar een gebrek aan zuurstof optimale NO-vorming bemoeilijkt. Binnenin de vlam werkt de techniek echter wel.

Om signaal-ruisverhouding van de NO-fluorescentie te verbeteren, moet het creatie-proces in detail bestudeerd worden. In feite is het brandpunt van de excimerlaser niet alleen een bron van NO-moleculen, maar ook van fotonemissie door N_2^+-ionen en van hooggeëxciteerde N_2- en O_2-moleculen. Omdat de excimerlaser in golflengte afstembaar is, konden we een golflengteafhankelijkheid van de NO-vorming uitzetten. De resulterende spectrale structuur was exact dezelfde als de emissie van excimer-geëxciteerde zuurstof en stikstof moleculen in lucht. Als we naar dezelfde emissiegolflengte van stikstof (B-X van N_2^+) in pure stikstof kijken, zien we een compleet nieuw excitatiespectrum

verschijnen. Deze nieuwe structuur is toegekend aan rotationele structuur van het $v' = 32$-niveau in een tweefoton-resonantie met de dubbele put $a''^1\Sigma_g^+, ^1\Sigma_g^+(\text{II})$. Een derde foton in de relatief langdurende laserpuls brengt dan het systeem naar de B-toestand van N_2^+. De dubbele-puttoestand was voorspeld, maar is pas voor het eerst in deze studie gezien.

Het zuurstof-emissiespectrum geeft een heleboel onbekende structuur in het 200 tot 280 nm-gebied, die sinds 1930 al een aantal keren gerapporteerd is in de literatuur, maar nog nooit is toegekend. We hebben deze structuur deels toegekend aan emissie van een Rydbergtoestand, die convergeert naar de $a^4\Pi_u$-toestand van O_2^+, naar de $B^3\Sigma_u^-$-toestand van zuurstof. Een andere emissieband die direct aansluit op het rode deel van de toegekende structuur en daar duidelijk aan gekoppeld is, is toegekend aan emissie van dezelfde bovenste Rydbergtoestand naar een repulsieve kromme met dezelfde dissociatie-energie als die van de B-toestand. Omdat de energie-afstanden van deze band geïnverteerd zijn ten opzichte van typische vibrationele structuur, is het spectrum toegekend aan een projectie van de golffunctie van de bovenste Rydbergtoestand. De lager gelegen repulsieve kromme is niet het repulsieve deel van de B-toestand, maar is tot op heden nog onbekend.

Bijmengen van slechts 8 % zuurstof verandert het pure stikstof-excitatiespectrum in één dat gelijk is aan het spectrum dat te zien is bij NO-vorming en excitatie van puur zuurstof. Dit effect wordt waarschijnlijk veroorzaakt door een efficiënte energie- of ladingsoverdracht tussen stikstof en zuurstof op het drie-fotonniveau, gecombineerd met een efficiënte uitdoving van de tweefoton-resonante toestand van stikstof door zuurstof. Een chemische behandeling van dit NO-vormingsprobleem leidt uiteindelijk tot een voorstel voor een mechanisme waar N_2 in de $A^3\Sigma_u^+$-toestand, gecreëerd door relaxerende stikstofionen, en zuurstofatomen, gemaakt door één-fotongeëxciteerde zuurstofmoleculen, samen NO vormen.

Moleculair stikstof en zuurstof behoren zonder twijfel tot de meest uitgebreid bestudeerde moleculen op aarde. De fotolyse van deze moleculen, wanneer ze sterk aangeslagen worden, brengt desondanks vele verrassingen en mysteries met zich mee.

Curriculum Vitae

Jeroen Bominaar was born on June 20 1979 in Roosendaal, a town in the province Noord-Brabant. He attended the St. Gertrudislyceum in Roosendaal and started his studies Physics in 1997 at the Catholic University of Nijmegen. In August of 2002 Jeroen got his degree after finishing internships at the Photo Acoustics group in Nijmegen and at Philips Research in Eindhoven. During his internship in Nijmegen he used a laser system, that accurately detects trace gases to measure the influence of UV radiation on skin where the sun usually does not shine. Together with fellow student Bas Moeskops they were their own best test subjects. At Philips Research Jeroen worked on an optical technique that visualizes capillaries close to the skin. The purpose of that study was to perform non-intrusive inline diagnostics on blood. In between these internships he also tasted from High Energy Physics during a summer course at the international institute CERN in Geneva.

Immediately after finishing the studies of Physics Jeroen started his PhD at the group Applied Molecular Physics, also in Nijmegen. An extended description of the research performed during this time can be found in the previous pages of this book. On September 9 2008 he finalized his PhD in a public defense at the Radboud University Nijmegen. Since June 2007, Jeroen has returned to his home province, Noord-Brabant, to work on immersion systems at ASML in Veldhoven.

THE END